Factorization at the LHC: From PDFs to Initial State Jets

by

Wouter J. Waalewijn

Submitted to the Department of Physics
in partial fulfillment of the requirements for the degree of

Doctor of Philosophy in Physics

at the

MASSACHUSETTS INSTITUTE OF TECHNOLOGY

June 2010

Author . . . .
Department of Physics
May 12, 2010

Certified by. . . . .
Iain W. Stewart
Associate Professor
Thesis Supervisor

Accepted by . . . .
Krishna Rajagopal
Associate Department Head for Education

Factorization at the LHC: From PDFs to Initial State Jets

by

Wouter J. Waalewijn

Abstract

New physics searches at the LHC or Tevatron typically look for a certain number of hard jets, leptons and photons. The constraints on the hadronic final state lead to large logarithms, which need to be summed to obtain reliable theory predictions. These constraints are sensitive to the strong initial-state radiation and resolve the colliding partons inside initial-state jets. We find that the initial state is properly described by "beam functions".

We introduce an observable called "beam thrust" τ_B, which measures the hadronic radiation relative to the beam axis. By requiring $\tau_B \ll 1$, beam thrust can be used to impose a central jet veto, which is needed to reduce the large background in $H \to WW \to \ell\nu\ell\bar{\nu}$ from $t\bar{t} \to WWb\bar{b}$. We prove a factorization theorem for "isolated" processes, $pp \to XL$ where the hadronic final state X is restricted by $\tau_B \ll 1$ and L is non-hadronic. This factorization theorem enables us to sum large logarithms $\alpha_s^n \ln^m \tau_B$ in the cross section and involves beam functions. The beam thrust spectrum allows us to study initial-state radiation in perturbation theory, which can be compared with experiment and Monte Carlo. We present results for the beam thrust cross section for Drell-Yan and Higgs production through gluon fusion at next-to-next-to-leading-logarithmic order.

The beam functions depend on the momentum fraction x and the (transverse) virtuality t of the colliding partons. The t dependence can be calculated in perturbation theory by matching beam functions onto the parton distribution functions (PDFs) at an intermediate scale $\mu_B \sim \sqrt{t}$. We calculate all the one-loop matching coefficients. Below μ_B we have the usual DGLAP evolution for the PDFs. Above μ_B, the evolution of the beam function is in t and does not change x or the parton type.

We introduce the event shape "N-jettiness" τ_N, which generalizes beam thrust to events with N signal jets. Requiring $\tau_N \ll 1$ restricts radiation between the signal jets and vetoes additional undesired jets. This yields a factorization formula with inclusive beam and jet functions and allows us to sum the large logarithms $\alpha_s^n \ln^m \tau_N$ from the phase space restriction.

Thesis Supervisor: Iain W. Stewart
Title: Associate Professor

Acknowledgments

It has been a pleasure to work under the supervision of Prof. Iain Stewart, and I want to thank him for all the advice and time he has given me. The work in this thesis has been done in collaboration with Dr. Frank Tackmann, who I would like to thank for many enjoyable discussions and for sharing some of his physical intuition and passion for physics. I also want to thank Dr. Carola Berger and Claudio Marcantonini with whom I collaborated on some of the research presented in this thesis. Thanks go to my thesis committee members Prof. Robert Jaffe and Prof. Allan Adams. I have enjoyed and benefitted from being part of a research group that has included Dr. Keith Lee, Dr. Chris Arnesen, Dr. Ambar Jain, Dr. Massimiliano Procura, Riccardo Abbate, Teppo Jouttenus and Roberto Sanchis.

I am very grateful for the love and support of my parents Caspar and Heleen and my family. I especially want to thank my wife Eileen. Her love, care and encouragement have been a joy and help throughout my PhD. The MIT Graduate Christian Fellowship has been a great place of friendship, fun and growth, in particular the Sidney-Pacific bible study group. I am thankful for the many friends, both in an outside of the Center of Theoretical Physics that have been part of my life during my time at MIT. I realize that all my gifts and talents are not something I deserve, and I am grateful to God for this opportunity as well as the results.

Contents

List of Figures

List of Tables

Chapter 1

Introduction

1.1 Effective Physics

Over the centuries we have been studying the world around us, discovering new physics at new length scales. Starting from our everyday experience which ranges from scales of about 10^3 to 10^{-3} meters (m), we encounter phenomena like gravity, contact forces, fluid dynamics and light. When we move on to the smaller scales of cells at 10^{-5} m or molecules and atoms around 10^{-10} m, we pass entire fields of science such as biology and chemistry. It is surprising that the underlying physics that leads to this rich variety of phenomena is simply (quantum) electrodynamics. The nucleus of the atom at scales of 10^{-15} m is made of protons and neutrons and is held together by the nuclear force. This is a residual force coming from the strong force, also known as Quantum Chromodynamics (QCD). QCD is responsible for confining the quarks to protons and neutrons. The remaining force that is part of the well established Standard Model of particle physics is the weak force, which for example plays a role in some hadron decays.

With the Large Hadron Collider (LHC) at CERN starting to take data, we will be probing nature at smaller length scales than before and hope to discover new physics. In order to reconstruct new short distance physics from the measured leptons and QCD radiation, one typically looks for a signal with a certain number of jets of energetic hadrons. This thesis explores the effect of such restrictions on the hadronic final state in theoretical calculations, with an emphasis on the 0-jet case which allows us to study initial-state radiation. An introduction to the work in this thesis can be found in the next section.

Our current understanding of nature as the strong, weak and electromagnetic force,

together with gravity, is beautiful in its simplicity as a theory. Yet its computational complexity makes it ill-suited to describe most phenomena in nature. In practice one adopts an effective description appropriate for the length scale one is looking at. We are already used to doing this in much simpler theories such as Newtonian gravity, where for our everyday purposes a constant gravitational acceleration is an appropriate description. Effectively we are treating the earth as an infinite plane, which is a reasonable approximation given that we are small compared to the size of the earth. If we instead would try to describe the motion of the planets in our solar system, the size of the planets and the sun becomes negligibly small and we can treat them as points.

We encounter a similar situation in electrostatics, when we want to determine the electric field due to an object at a distance r that is large compared to the size s of the object. We can start by approximating the object as a point with a total charge Q and systematically improve this result by using the so-called multipole expansion. This is an expansion in $s/r \ll 1$, where each next order contains more details of the charge distribution. The first correction comes from the dipole moment $\vec{p}$ of the configuration and is suppressed by a factor of s/r. The next correction comes from the quadrupole moment Q_{ij} and is suppressed by s^2/r^2 etc. We have thus found an effective description of the charge configuration, where the details of the full charge configuration are captured by only a few constants: Q, $\vec{p}$, etc.

This simplification to an effective description, where the relevant details of the complete physical picture are condensed into just a few constants, will be a theme that continues as we study effective descriptions of quantum field theories. In this thesis we will use Soft-Collinear Effective Theory (SCET) , which describes initial and final state radiation and provides us with a powerful tool for studying processes at the LHC. In the next section we will present an introduction to the work in this thesis. In Sec. 1.3 we will look at an effective description for a decay involving the weak force, which will allow us to discuss general features of effective field theories. We present an intuitive introduction to Soft-Collinear Effective Theory in Sec. 1.4.

1.2 Predicting Collisions at the LHC

In this section we introduce the work described in this thesis. Starting with a schematic picture of proton-proton collisions, we review the topic of factorization and discuss the
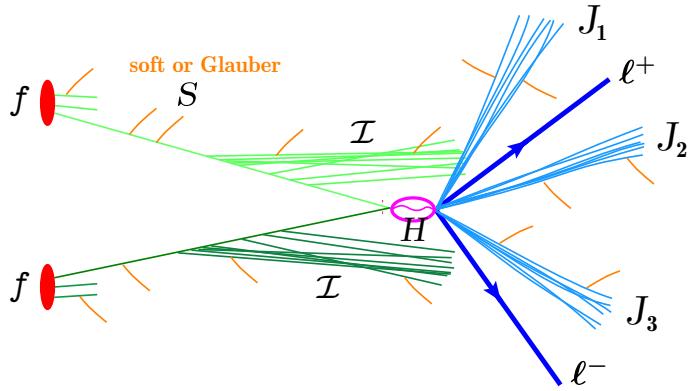
Figure 1-1: Schematic picture of a collision at the LHC or Tevatron. It shows the evolution in time from left to right, starting with the proton and (anti)proton in the initial state and ending with jets, leptons and soft radiation in the final state.

relevance of experimental restrictions on the hadronic final state. Our work focusses on how such constraints can be incorporated into factorization theorems and we give a preview of our results.

The primary goal of the experiments at the LHC and Tevatron is to search for the Higgs particle and physics beyond the Standard Model through collisions at the energy frontier. The fact that the short-distance processes of interest are interlaced with QCD interactions complicates the search. A schematic picture of a proton-proton collision is displayed in Fig. 1-1. A quark or gluon is extracted from each proton (the red circles labeled f), and emits strong initial-state radiation ($\mathcal{I}$) prior to the hard short-distance collision (at H). The hard collision produces strongly interacting partons which hadronize into collimated jets of hadrons ($J_{1,2,3}$), as well as non-strongly interacting particles (represented in the figure by the $\ell^+\ell^-$). Finally, all the strongly interacting particles, including the spectators in the proton, interact with low-momentum soft gluons and can exchange perpendicular momentum by Glauber gluons (both indicated by the short orange lines labeled S).

Factorization is one of the most fundamental concepts in the theoretical description of these collisions. It is the statement that the cross section can be computed as a product of probability functions, each describing a part of Fig. 1-1. For a review of factorization see Ref. [77], for examples of factorization theorems see Sec. 2.1. Factorization allows one to separate the new hard physics from the array of QCD interactions in the initial and final states and is therefore key in the search for new physics. It is also necessary for controlling QCD effects. For example, the momentum distributions of the colliding partons

in the protons are nonperturbative, but factorization can imply that these are described by universal distributions which have been measured in earlier experiments.

Monte Carlo programs are a widely used numerical method and employ notions from factorization and properties of QCD in the soft and collinear limits to model the ingredients in the full cross section, $d\sigma = H \otimes f \otimes f \otimes \mathcal{I} \otimes \mathcal{I} \otimes \prod_i J_i \otimes S$. They have the virtue of providing a general tool for any observable, but have the disadvantage of making model-dependent assumptions to combine all the ingredients and to calculate some of them. When a factorization theorem for a specific observable is available this provides a better approach, since the various ingredients are defined and combined in a rigorous way.

In order to probe the physics of the hard interaction, measurements often impose restrictions on the hadronic final state, requiring a certain number of hard leptons or jets [1, 2, 38, 39]. For example, a typical new physics search looking for missing transverse energy may also require a minimum number of jets with p_T above some threshold. To identify the new physics and determine the masses of new-physics particles, one has to reconstruct decay chains with a certain number of jets and leptons in the final state.

However, for the majority of processes of interest at hadron colliders where one distinguishes properties of the hadronic final state, so far no rigorous field-theoretic derivation of a factorization theorem to all orders in perturbation theory exists. The most well-known factorization theorem is

$$d\sigma = \sum_{i,j} d\sigma_{ij}^{\text{part}} \otimes f_i(\xi_a) \otimes f_j(\xi_b) \,. \tag{1.1}$$

Here f_i and f_j are the standard parton distribution functions (PDFs) that describe the probability to extract a parton $i, j = \{g, u, \bar{u}, d, \ldots\}$ out of the proton, with a fraction $\xi_{a,b}$ of the proton momentum. The hard scattering of i and j is described by the partonic cross section $d\sigma_{ij}^{\text{part}}$ calculated in fixed-order perturbation theory. In Eq. (1.1), the hadronic final state is treated as fully inclusive. Hence, in the presence of experimental restrictions that make a process less inclusive, Eq. (1.1) is a priori not applicable.

Factorization theorems for processes near threshold are a well-studied case where Eq. (1.1) can be extended to sum large phase-space logarithms [42, 53, 63, 66, 73, 118, 121, 132, 165]. (We discuss large logarithms in Sec. 1.3.) However, threshold production requires the limit $\xi_{a,b} \to 1$. The PDFs fall off steeply in this limit, so this is not as relevant for the LHC [62].

(a) 3 central jets.

(b) $\ell^+\ell^-$ + 0 central jets.
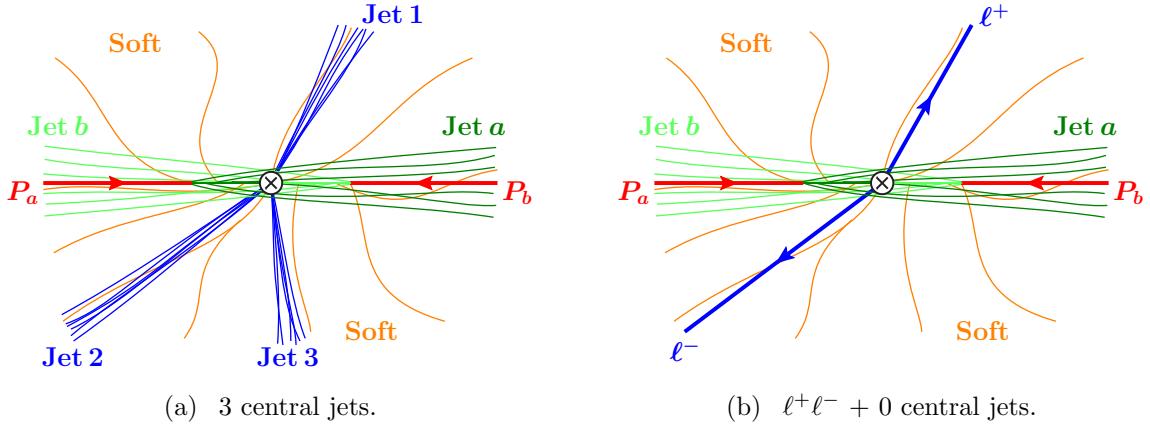
Figure 1-2: Examples of events at the LHC. The $P_{a,b}$ denote the incoming protons. Jet a and b are due to initial-state radiation.

Our goal is to study factorization for a situation where the hard interaction occurs between partons with momentum fractions away from the limit $\xi_{a,b} \to 1$, and where the hadronic final state is measured and restricted by constraints on certain event shapes. These restrictions allow one to probe more details about the final state and may be used experimentally to control backgrounds.

A typical event at the LHC with three high-p_T jets is illustrated in Fig. 1-2(a). There are several complications one has to face when trying to derive a factorization theorem in this situation. First, experimentally the number and properties of the final-state jets are determined with a jet algorithm. Second, to enhance the ratio of signal over background, the experimental analyses have to apply kinematic selection cuts. Third, in addition to the jets produced by the hard interaction, there is soft radiation everywhere (which is part of what is sometimes called the "underlying event"). Fourth, a (large) fraction of the total energy in the final state is deposited near the beam axes at high rapidities. Some of this radiation can contribute to measurements, and when it does, it cannot be neglected in the factorization. In this thesis we focus on the last three items. In chapter 10 we take some steps towards resolving the first item. Methods for including jet algorithms in factorization have been studied in Refs. [32, 121, 173]

To explore the implications of restrictions on the hadronic final state, we consider the simpler situation shown in Fig. 1-2(b) where there are no hard central jets. This is already interesting for $h \to WW$ decaying non-hadronically, since it could help reduce the background from top quarks decaying into a W plus b-jet. We will now construct an observable

that we use in our analysis to impose this central jet veto. We define two hemispheres, a and b, orthogonal to the beam axis and two unit lightlike vectors n_a and n_b along the beam axis pointing into each hemisphere. Taking the beam axis along the z direction, hemisphere a is defined as $z > 0$ with $n_a^\mu = (1, 0, 0, 1)$, and hemisphere b as $z < 0$ with $n_b^\mu = (1, 0, 0, -1)$. We now divide the total momentum p_X of the hadronic final state into the contributions from particles in each hemisphere, $p_X = p_{X_a} + p_{X_b}$. We measure the components B_a^+ and B_b^+ of the hemisphere momenta defined by

$$B_a^+ = n_a \cdot p_{X_a}, \qquad B_b^+ = n_b \cdot p_{X_b}. \qquad (1.2)$$

Because of the dot product with n_a or n_b, energetic particles near the beam axes only give small contributions to B_a^+ or B_b^+. In particular, any contributions from particles at very large rapidities outside the detector reach, including the remnant of unscattered partons in the proton, are negligible. Demanding that $B_{a,b}^+$ are small only allows highly energetic particles inside jets along the beam directions labeled "Jet a" and "Jet b" in Fig. 1-2(b). Hence, measuring and constraining $B_{a,b}^+$ provides a theoretically clean method to control the remaining particles in the hadronic final state.

In this thesis, we will prove a factorization theorem for Drell-Yan $pp \to X\ell^+\ell^-$ where X is allowed to have hard jets close to the beam but no hard central jets, corresponding to Fig. 1-2(b). We call this "isolated Drell-Yan". Our proof of factorization uses Soft-Collinear Effective Theory (SCET) [29, 31, 35, 37] plus additional arguments to rule out effects of Glauber gluons based in part on Refs. [22, 78]. Our factorization theorem applies to processes $pp \to XL$, were the lepton pair is replaced by other non-strongly interacting particles, such as Higgs or Z' decaying non-hadronically. This is particularly interesting for $H \to W^+W^- \to \ell^+\nu\ell^-\bar{\nu}$ where a central jet veto is required to remove the large background from top quarks decaying into a W plus a b-jet. We will also write down a factorization formula with beam functions for processes with hard central jets. This is not as rigorous as the 0-jet case, in particular we have not yet shown the cancellation of Glauber gluons.

Our main result is to show that process-independent "beam functions", $B_i(t, x)$ with $i = \{g, u, \bar{u}, d, \ldots\}$, are required to properly describe the initial state. Generically, by restricting X one performs an indirect measurement of the proton prior to the hard collision. At this point, the proton is resolved into a colliding hard parton inside a cloud of collinear

and soft radiation. The proper description of this initial-state jet is given by a beam function in conjunction with a soft function describing the soft radiation in the event.

One might worry that the collision of partons inside initial-state jets rather than partons inside protons could drastically change the physical picture. The changes are not dramatic but there are important implications. The beam functions can be computed in an operator product expansion, giving

$$B_i(t, \xi, \mu_B) = \delta(t) \, f_i(\xi, \mu_B) + \mathcal{O}[\alpha_s(\mu_B)] \,, \tag{1.3}$$

where μ_B is an intermediate perturbative scale and t is an invariant-mass variable closely related to the off-shellness of the colliding parton (and the Mandelstam variable t). Thus, the beam functions reduce to standard PDFs at leading order. For what we call the gluon beam function, this was already found in Ref. [96], where the same matrix element of gluon fields appeared in their computation of $\gamma \, p \to J/\psi X$ using SCET.

Equation (1.3) implies that the momentum fractions $\xi_{a,b}$ are determined by PDFs evaluated at the scale $\mu_B \ll Q$, which is parametrically smaller than the scale Q of the partonic hard interaction. The renormalization group evolution (RGE) for the initial state now proceeds in two stages. For scales $\mu < \mu_B$, the RGE is given by the standard PDF evolution [9, 89, 104, 107, 109], which redistributes the momentum fractions in the proton to lower ξ values and mixes the gluon and quark PDFs. For scales $\mu > \mu_B$, the jet-like structure of the initial state becomes relevant and its evolution is properly described by the RGE of the beam function. In contrast to the PDF, the evolution of the beam function does not involve mixing between quarks and gluons and only changes t. In addition to the change in evolution, the transition from PDFs to beam functions at the scale μ_B also involves explicit $\alpha_s(\mu_B)$ corrections as indicated in Eq. (1.3). These include mixing effects, such as a gluon from the proton pair-producing a quark that goes on to initiate the hard interaction and an antiquark that is radiated into the final state. For our observables such fluctuations are not fully accounted for by the PDF evolution. These beam effects must be taken into account, which can be done by perturbative calculations. Fortunately, the standard PDFs are still sufficient to describe the nonperturbative information required for the initial state.

One should ask whether the description of the initial state by beam functions, as well as their interplay with the soft radiation, are properly captured by current Monte Carlo

programs used to simulate events at the LHC and Tevatron, such as Pythia [159, 160] and Herwig [23, 80]. In these event generators the corresponding effects should be described at leading order by the initial-state parton shower in conjunction with models for the underlying event [24, 60, 161, 162]. We will see that the initial-state parton shower is in fact closer to factorization with beam functions than to the inclusive factorization formula in Eq. (1.1). In particular, the physical picture of off-shell partons that arises from the factorization with beam functions has a nice correspondence with the picture adopted for initial-state parton showers a long time ago [45, 158]. Experimentally, measurements of the isolated Drell-Yan cross section provide a simple obsevable that can rigorously test the accuracy of the initial-state shower in Monte Carlo programs, by contrasting it with our analytic results.

1.3   Weak Interactions and Effective Field Theory

Many physical processes involve several scales and perturbative calculations typically lead to logarithms of the ratios of these scales, e.g. $\alpha_s \ln \mu_1/\mu_2$. If the scales are widely separated $\mu_1 \gg \mu_2$ the logarithms become large and perturbation theory breaks down. We will see in this section how effective field theories conveniently solve this problem by factoring a process into separate pieces, each corresponding to only one of the scales. For an introduction to effective field theories see for example Refs. [102, 137, 141, 156].

As an example we will study the decay of a D meson to a K^- and a π^+ meson. A review of effective field theories for weak decays can be found in Refs. [58, 59]. At the parton level we can understand this process as $c \to su\bar{d}$ along with a spectator $\bar{u}$ quark, which is mediated by a W boson of the weak force. The tree level diagram is shown in Fig. 1-3(a) and given by

$$\left(\frac{\mathrm{i}g_2}{\sqrt{2}}\right)^2 V_{cs}^* V_{ud} \, \frac{-\mathrm{i}}{k^2 - m_W^2}\left(g^{\mu\nu} - \frac{k^\mu k^\nu}{m_W^2}\right)\bar{u}_s\gamma_\mu P_L u_c \, \bar{u}_u\gamma_\nu P_L u_d \,. \tag{1.4}$$

Here the g_2 is the coupling of the weak interactions, V_{ij} are elements of the CKM matrix from the weak interaction and u_i is the spinor for an external quark of flavor i. The quarks are confined to the mesons, implying that the momentum $k^\mu \ll m_W$. We can therefore
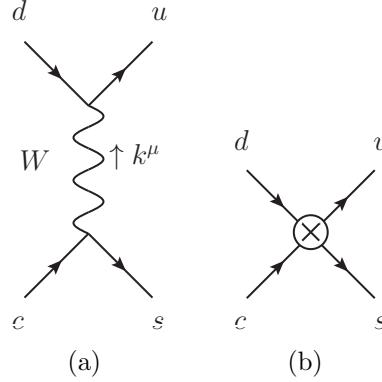
Figure 1-3: The tree-level process in the full theory (a) and effective theory (b).

expand the propagator as

$$\frac{-\mathrm{i}}{k^2 - m_W^2}\Big(g^{\mu\nu} - \frac{k^\mu k^\nu}{m_W^2}\Big) = \frac{\mathrm{i}}{m_W^2}\Big[1 + \mathcal{O}\Big(\frac{k^2}{m_W^2}\Big)\Big]. \tag{1.5}$$

This removes the W boson as a dynamical degree of freedom and replaces the tree-level process in Fig. 1-3(a) by the four-fermion interaction in Fig. 1-3(b). The W propagator gets shrunk to a point because we no longer resolve the short distance physics.

The dominant corrections to this tree-level diagram come from the strong force, which we now consider. The systematic approach to include these corrections in the Lagrangian of the effective theory is called "matching" and is based on the operator product expansion (OPE) [175]. First we write down all interactions in the low energy theory that are allowed by symmetries. The matching will occur at a scale $\mu \sim m_W$, so we can treat the c, s, d and u quarks as massless and use the corresponding chiral symmetry to constrain possible terms. Using Fierz identities for spin and color, we are left with just two terms in our effective Lagrangian

$$\mathcal{L}_W^{\text{eff}} = -\frac{4G_F}{\sqrt{2}}V_{cs}^*V_{ud}\left[C_1(\mu)\mathcal{O}_1(\mu) + C_2(\mu)\mathcal{O}_2(\mu)\right],$$

$$\mathcal{O}_1 = \bar{s}_j\gamma^\mu P_L c_j\,\bar{u}_k\gamma_\mu P_L d_k\,, \quad \mathcal{O}_2 = \bar{s}_j\gamma^\mu P_L c_k\,\bar{u}_k\gamma_\mu P_L d_j\,, \tag{1.6}$$

where $G_F = \sqrt{2}g_2^2/(8m_W^2)$ is the Fermi constant and j and k are color indices. Since we are working at leading order in k^μ/m_W, we do not include terms with derivatives that one would get from higher order terms of the expansion in Eq. (1.5). To determine the coefficients $C_i(\mu)$ we calculate some physical quantity in both the full theory and the effective theory
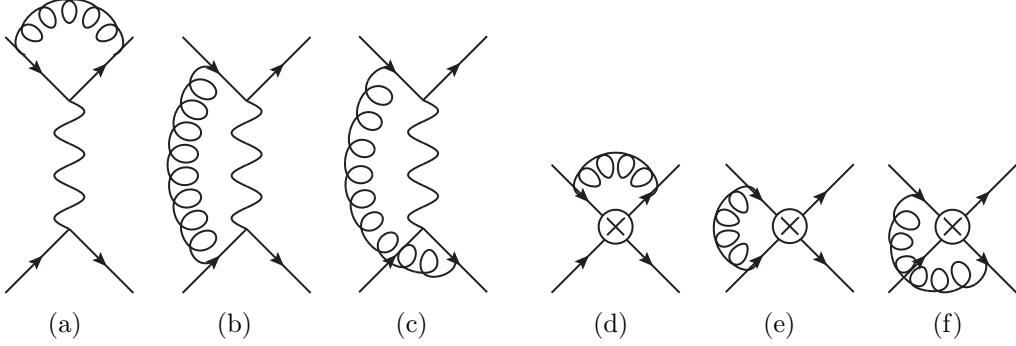
Figure 1-4: The one-loop QCD corrections in the full theory (a)-(c) and effective theory (d)-(f). These diagrams have symmetric counterparts.

and match. A common choice is renormalized matrix elements, where we are free to choose any on-shell or off-shell states since the effective theory should completely reproduce the low energy limit of the full theory. From our tree-level calculation in Eqs. (1.4) and (1.5) we know that $C_1^{(0)}(\mu) = 1$ and $C_2^{(0)}(\mu) = 0$ (the superscript (n) denotes terms of order α_s^n).

Moving on to the α_s corrections, the one-loop diagrams that contribute to the matrix element with external free quarks are shown in Fig. 1-4 for the full theory and for the effective theory. The ultraviolet(UV) divergences we encounter in these calculations are regularized using dimensional regularization (DR) and renormalized in the modified minimal subtraction scheme ($\overline{\text{MS}}$). Performing the matching onto the effective theory at order α_s

$$\langle su\bar{d}|\mathrm{i}\mathcal{L}_W^{\text{full}}|c\rangle^{(1)} = \langle su\bar{d}|\mathrm{i}\mathcal{L}_W^{\text{eff}}|c\rangle^{(1)}$$
$$= -\mathrm{i}\frac{4G_F}{\sqrt{2}}V_{cs}^*V_{ud}\sum_{i=1,2}C_i(\mu)^{(0)}\langle su\bar{d}|\mathcal{O}_i|c\rangle^{(1)} + C_i(\mu)^{(1)}\langle su\bar{d}|\mathcal{O}_i|c\rangle^{(0)}, \quad (1.7)$$

results in

$$C_1(\mu) = 1 + \frac{3}{N_c}\frac{\alpha_s(\mu)}{4\pi}\ln\frac{m_W^2}{\mu^2},$$
$$C_2(\mu) = -3\frac{\alpha_s(\mu)}{4\pi}\ln\frac{m_W^2}{\mu^2}. \quad (1.8)$$

Here $N_c = 3$ is the number of colors in QCD. It is worth pointing out that the full theory and effective theory results depend on the momenta p^μ of the external quarks (which we took to all be equal), but that this dependence cancels in the matching. This is an explicit check that effective theory reproduces the full theory in the low energy limit.

We now take a closer look at the full theory calculation. Schematically it has the following structure

$$\langle su\bar{d}|i\mathcal{L}_W^{\text{full}}|c\rangle = 1 + \alpha_s L + \alpha_s^2 L^2 + \alpha_s^3 L^3 + \dots$$
$$\alpha_s + \alpha_s^2 L + \alpha_s^3 L^2 + \dots$$
$$\alpha_s^2 + \alpha_s^3 L + \dots, \quad (1.9)$$

where 1 denotes the tree level result and $L = \ln(-m_W^2/p^2)$. For our D meson decay the momentum $p^\mu \ll m_W$, which implies that L is large and logarithmic terms such as $\alpha_s L$ are more important than the finite (non-logarithmic) α_s corrections. Assuming that $L \sim 1/\alpha_s$, the terms on the first row would all be of $\mathcal{O}(1)$ and thus need to be summed to get the correct treelevel amplitude. This is called leading logarithmic (LL) resummation. The finite α_s correction (first term on the second row) is of the same order as the logarithmic terms $\alpha_s^{n+1} L^n$ on the second row. Summing these terms corresponds to next-to-leading logarithmic (NLL) resummation. We will see how this resummation can be achieved in the effective field theory.

Large logarithms are a generic feature of theories with disparate scales. Our effective field theory approach allows us to separate these scales and the corresponding physics:

$$\langle su\bar{d}|i\mathcal{L}_W^{\text{full}}|c\rangle = 1 + \alpha_s \ln\frac{m_W^2}{-p^2} + \dots$$
$$= \underbrace{\left(1 + \alpha_s \ln\frac{m_W^2}{\mu^2} + \dots\right)}_{C_i(\mu)} \underbrace{\left(1 + \alpha_s \ln\frac{\mu^2}{-p^2} + \dots\right)}_{\langle c\bar{u}d|\mathcal{O}_i(\mu)|b\rangle} = \langle su\bar{d}|i\mathcal{L}_W^{\text{eff}}|c\rangle. \quad (1.10)$$

The physics associated with m_W can only enter in the Wilson coefficients. The low energy physics remains as dynamical degrees of freedom in the effective theory and drops out in the matching. The large logarithms can now be avoided by evaluating the matching coefficients in Eq. (1.8) at a scale $\mu \sim m_W$ and the matrix elements at a scale $\mu \sim \sqrt{p^2}$.

We can use the renormalization group evolution (RGE) [61, 101, 170, 171, 174] to run the Wilson coefficients $C_i(\mu)$ from a scale $\mu \sim m_W$ down to $\mu \sim \sqrt{p^2}$. The renormalization scale μ can roughly be interpreted as the scale at which the UV divergences are cut off. Lowering μ thus corresponds to reducing the degrees of freedom in the effective theory and absorbing the corresponding change in the Wilson coefficients C_i. With this picture in mind

	matching	running	
		anom. dim.	$\beta(\alpha_s)$
LO	0-loop	-	-
NLO	1-loop	-	-
NNLO	2-loop	-	-
LL	0-loop	1-loop	1-loop
NLL	1-loop	2-loop	2-loop
NNLL	2-loop	3-loop	3-loop

Table 1.1: Order counting for fixed and resummed perturbation theory with single logarithms.

it makes sense that we should match at $\mu \sim m_W$ and then run down to $\mu \sim \sqrt{p^2}$. The full theory calculation contained no UV divergences in the final answer, because the mass of the W acted as a UV cutoff. In our effective theory we are expanding about the limit $m_W \to \infty$ and hence $\ln -m_W^2/p^2$ leads to UV divergences, which is what allows us to factor and resum these large logarithms.

We will now see explicitly how the RGE resums the large logarithms in our example. The UV divergences from the one-loop effective theory diagrams in Fig. 1-4(d)-(f) lead to the following RGE

$$\mu \frac{\mathrm{d}}{\mathrm{d}\mu} C_i(\mu) = \gamma_{ij}(\mu) C_j(\mu), \qquad \gamma_{ij}(\mu) = \frac{\alpha_s(\mu)}{2\pi} \begin{pmatrix} 3/N_c & -3 \\ -3 & 3/N_c \end{pmatrix}. \qquad (1.11)$$

This can be solved by diagonalizing

$$C_\pm = C_1 \pm C_2, \quad C_\pm(\mu) = C_\pm(m_W) \left[\frac{\alpha_s(m_W)}{\alpha_s(\mu)} \right]^{\gamma_\pm/(2\beta_0)}, \quad \gamma_\pm = \pm 6 \frac{N_c \mp 1}{N_c}, \qquad (1.12)$$

where $\beta_0 = (11C_A - 4T_F n_f)/3$ is the lowest order coefficient in the running of α_s. As a consequence, even though $C_2(m_W) = 0$ at tree level a non-zero $C_2(\mu)$ gets generated through the RGE. By expanding we explicitly see how the RGE sums the LL series

$$\left[\frac{\alpha_s(m_W)}{\alpha_s(\mu)} \right]^{\gamma_\pm/(2\beta_0)} = \exp\left[-\gamma_\pm \frac{\alpha_s(\mu)}{4\pi} \ln \frac{m_W}{\mu} \right] \sim 1 + \alpha_s L + \alpha_s^2 L^2 + \dots. \qquad (1.13)$$

Resummed perturbation theory is powerful because it captures the most important pieces of higher loop diagrams, without having to calculate them. The above resummed result contains for example $\alpha_s^2 L^2$ which in a full theory calculation would only show up at two

loops. The appropriate resummation when we match at order α_s is NLL resummation, for which the running is determined from the UV divergences of two-loop diagrams. The running is generally at one higher loop that the matching, as is shown in Table 1.1.

After matching and running, the final step to calculate the $D \to K^+\pi^-$ decay consists of determining the matrix elements $\langle K^+\pi^- | \mathcal{O}_i(\mu) | D \rangle$ at $\mu \sim \sqrt{p^2}$. For some electroweak decays Heavy Quark Effective Theory (HQET) [91, 103, 108] allows you to exploit some further symmetries, but at the end of the day this is a non-perturbative matrix element that needs to be determined using either lattice QCD, modeling or experiments. The good news is that in effective field theories the non-perturbative matrix elements are often universal: they can be extracted from some experiment and used in a different one. The PDFs that we encountered in the previous section are an example of this.

The weak decay we have studied captures the generic situation in effective field theories: a large separation of scales allows us to expand onto an effective theory but also leads to large logarithms. These large logarithms are factored in the effective theory. The Wilson coefficients $C_i(\mu)$ contain the effects of physics at the high scale and the operators $\mathcal{O}_i(\mu)$ describe the dynamics of the low energy physics. The renormalization scale μ can be thought of as the scale that separates what goes into $C_i(\mu)$ and what is described by $\mathcal{O}_i(\mu)$. The large logarithms are resummed by calculating $C_i(\mu)$ at the high scale ("matching") and using the RGE to run it down to the low scale ("running"). The relevant matrix elements of the operator $\mathcal{O}_i(\mu)$ at the low scale may be non-perturbative, in which case they should be extracted from experiment or may be determined using lattice QCD.

We conclude this section with a somewhat technical point related to our choice of renormalization scheme. For this we will look at the running of the electromagnetic coupling in $\overline{\text{MS}}$ and the off-shell momentum subtraction (ms) scheme. The one-loop contribution from the electron with mass m leads to

$$\mu \frac{\mathrm{d}}{\mathrm{d}\mu} e(\mu) = \beta(\mu) e(\mu) \,,$$

$$\beta^{\overline{\text{MS}}}(\mu) = \frac{e^3(\mu)}{12\pi^2} \,, \quad \beta^{\text{ms}}(\mu) = \frac{e^3(\mu)}{2\pi^2} \int_0^1 \mathrm{d}x \, \frac{x^2(1-x)^2\mu^2}{m^2 + x(1-x)\mu^2} \,. \tag{1.14}$$

For $\mu \gg m$ we have $\beta^{\text{ms}}(\mu) = \beta^{\overline{\text{MS}}}(\mu)$, but

$$\beta^{\text{ms}}(\mu) = \frac{e^3(\mu)}{60\pi^2} \frac{\mu^2}{m^2} \qquad \text{for } \mu \ll m \,. \tag{1.15}$$

So below the electron mass the effect of the electron decouples from the running, with a smooth transition through $\mu = m$. By contrast, the electron doesn't decouple in the $\overline{\text{MS}}$ scheme ($\beta^{\overline{\text{MS}}}$ doesn't depend on m at all). As this example illustrates, adopting a so-called physical renormalization scheme causes high energy degrees of freedom to decouple naturally. However, the expressions become much more involved (compare β^{ms} with $\beta^{\overline{\text{MS}}}$), which is why we prefer to use the $\overline{\text{MS}}$ scheme and manually perform the decoupling by matching and running.

1.4   Soft-Collinear Effective Theory

In a typical event at the LHC the final state contains photons, leptons and hadrons (see Fig. 1-2(a)). The energetic hadrons generically come in collimated jets and there are also much less energetic hadrons everywhere. These two types are referred to as "collinear" and "soft" radiation and are enhanced due to the presence of collinear and soft infrared(IR) singularities in QCD. SCET is an effective theory of QCD describing these modes [29, 31, 35, 37]. In this section we present an intuitive introduction to SCET. We start by introducing light-cone coordinates and describing the degrees of freedom in SCET. We will discuss the matching onto SCET, reparametrization invariance (RPI), the factorization of soft and collinear degrees of freedom and the resummation of large logarithms.

It is convenient to use light-cone coordinates to describe jets of energetic hadrons. Choose a light-cone vector n^μ vector pointing in the direction of one of the energetic jets and an additional light-cone vector $\bar{n}^\mu$ such that $n \cdot \bar{n} = 2$. For $n^\mu = (1, \vec{n})$ a common choice is $\bar{n}^\mu = (1, -\vec{n})$, where of course $\vec{n}^2 = 1$. We can then decompose any four-vector $p^\mu = (p^+, p^-, p_\perp^\mu)$ as

$$p^\mu = p^+ \frac{\bar{n}^\mu}{2} + p^- \frac{n^\mu}{2} + p_\perp^\mu, \qquad p^+ = n \cdot p, \qquad p^- = \bar{n} \cdot p. \qquad (1.16)$$

The momenta of energetic hadrons in the jet along the n^μ direction are parametrically

$$p^\mu = (p^+, p^-, p_\perp^\mu) \sim Q(\lambda^2, 1, \lambda) \qquad \text{(collinear)}, \qquad (1.17)$$

where Q is the scale of the hard collision and $\lambda \sim p_\perp/p^- \ll 1$ characterizes the size of the jet. The power counting in Eq. (1.17) corresponds to a particle with virtuality $p^2 \sim \lambda^2 Q^2$
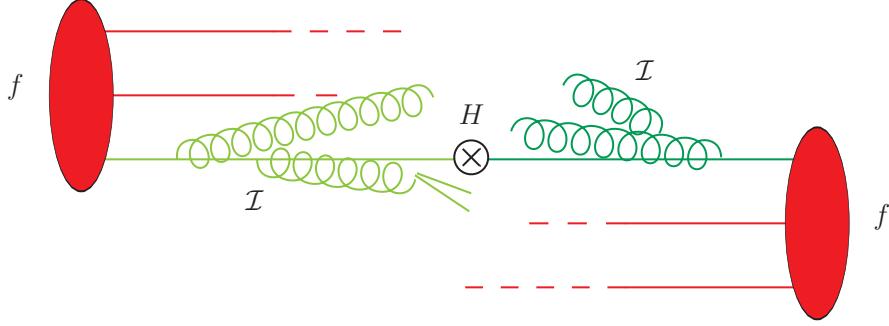
Figure 1-5: Schematic diagram of a proton-(anti)proton collision up to the hard interaction. A quark or gluon is taken out of each of the protons f and propagates while emitting initial-state radiation $\mathcal{I}$ until it enters the hard interaction H. The two shades of green correspond to the two collinear modes. For our observables the proton remnant is much more collinear and goes straight down the beam pipe.

that is boosted in the n^μ direction (we consider light particles whose mass we can ignore).

For the isolated Drell-Yan process shown in Fig. 1-2(b), we have two jets from initial-state radiation corresponding to the directions $n_a^\mu = (1,0,0,1)$ and $n_b^\mu = (1,0,0,-1)$. We thus have two collinear modes

$$p_a^\mu = (p_a^+, p_a^-, p_{a\perp}^\mu) \sim Q(\lambda^2, 1, \lambda) \qquad (n_a \text{ collinear}),$$
$$p_b^\mu = (p_b^-, p_b^+, p_{b\perp}^\mu) \sim Q(1, \lambda^2, \lambda) \qquad (n_b \text{ collinear}), \tag{1.18}$$

where we take $n_b = \bar{n}_a$ and $n_a = \bar{n}_b$ for convenience. By convention the $p_{a,b}^-$ will always correspond to the large light-cone component. Each of the two initial-state jets originates from a single quark or gluon coming out of the proton, which propagates and radiates until it enters the hard interaction, as shown schematically in Fig. 1-5.

Since the final state hadrons are colorless, there must be some degrees of freedom connecting the jets that carry color charge. The collinear modes cannot interact directly because that would lead to a momentum

$$p_a^\mu + p_b^\mu \sim Q(\lambda^2, 1, \lambda) + Q(1, \lambda^2, \lambda) = Q(1, 1, \lambda), \qquad (p_a + p_b)^2 \sim Q^2. \tag{1.19}$$

In SCET we have integrated out the hard interaction and so the corresponding modes with virtuality Q^2 are no longer dynamical degrees of freedom. The interactions between the collinear modes is provided by additional "soft" degrees of freedom which have the

$$= \mathrm{i}g\frac{\not{n}}{2}\,n^{\mu}T^{a}$$
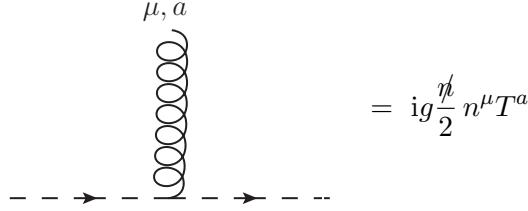
Figure 1-6: Feynman rule for the interaction between an n-collinear quark (dashed line) and a soft gluon, at leading order in the power counting.

following power counting[1]

$$p_{s}^{\mu} = (p_{s}^{+}, p_{s}^{-}, p_{s\perp}^{\mu}) \sim Q(\lambda^{2}, \lambda^{2}, \lambda^{2}) \qquad (\text{soft})\,. \tag{1.20}$$

They describe much less energetic radiation $E \sim \lambda^{2}Q$ without a preferred direction and correspond to long range fluctuations since their virtuality $p^{2} \sim Q\lambda^{4}$ is smaller. At a more technical level we expand the collinear momenta $p^{\mu} = \tilde{p}^{\mu} + p_{r}^{\mu}$ into a discrete large momentum $\tilde{p}^{\mu} = (0, \tilde{p}^{-}, \tilde{p}_{\perp}^{\mu}) \sim Q(0, 1, \lambda)$ and a small residual momentum $p_{r}^{\mu} \sim Q\lambda^{2}$ that can be exchanged with the soft radiation. The interaction between a soft and a collinear mode at leading order in the power counting is shown in Fig. 1-6.

SCET differs in several ways from effective theories where a heavy particle has been integrated out (such as the W boson in the previous section). The expansion parameter λ is not set by the mass of a heavy particle and there are different modes corresponding to the same particles, e.g. we have both collinear gluons and soft gluons. We thus have to be careful not to double count degrees of freedom, which can be removed through so-called zero-bin subtractions [140].

One might wonder if there are any other degrees of freedom that we should include in our effective theory. The answer to this question depends on the observable you want to study. For the weak decay in the previous section the small external momenta told us that we did not need to treat the W boson as a dynamical degree of freedom in our effective theory. For the isolated Drell-Yan process the invariant mass of the leptons sets the scale of the hard interaction Q. Measuring the B_{a}^{+} and B_{b}^{+} variables introduced in Eq. (1.2) and restricting $B_{a,b}^{+} \ll Q$ implies that energetic radiation is restricted to be along the beam axis. This is what leads to the two collinear modes in Eq. (1.18) with $\lambda^{2} \sim B_{a,b}^{+}/Q$. The

---

[1]In the literature these are sometimes referred to as ultrasoft modes, where soft is reserved for modes with power counting $(p^{+}, p^{-}, p_{\perp}^{\mu}) \sim Q(\lambda, \lambda, \lambda)$. As discussed below Eq. (1.21), we do not need these modes.

contribution to B_a^+ and B_b^+ from the soft radiation is of the same parametric size as that of the collinear radiation, so we need to include the soft degrees of freedom.

In principle you could imagine including modes with a scaling such as

$$
\begin{aligned}
(a) \qquad & p \sim Q(\lambda, \lambda, \lambda)\,, \\
(b) \qquad & p \sim Q(\lambda^4, \lambda^4, \lambda^4)\,, \\
(c) \qquad & p \sim Q(\lambda^4, 1, \lambda^2)\,, \\
(d) \qquad & p \sim Q(\lambda^2, \lambda^2, \lambda)\,.
\end{aligned}
\tag{1.21}
$$

In (a) we are considering a mode with virtuality $p^2 \sim \lambda^2 Q^2$ that, like the soft radiation, has no preferred direction. This mode would lead to contributions of order λQ to $B_{a,b}^+$. However, our measurement demands $B_{a,b}^+ \sim \lambda^2 Q$ and so (a) is ruled out in final state radiation. We now address virtual contributions from (a), by arguing that these modes cannot couple to the collinear and soft degrees of freedom. Attempting to couple (a) to collinear modes leads to a virtuality $p^2 \sim \lambda Q^2$, which is too large and has been integrated out. The momentum components of (a) are all larger than those of the soft modes in Eq. (1.20), and so these short range fluctuations are not resolved by our soft modes. There is no coupling between (a) and the soft degrees of freedom in the leading order Lagrangian.

The degrees of freedom in (b) correspond to a soft mode with virtuality $p^2 \sim \lambda^8 Q^2$ and is already contained in our soft degrees of freedom. Alternatively, the contribution of (b) to B_a^+ and B_b^+ is power suppressed, so there is no need to separately include them. The same is true for (c), which is a collinear mode with a smaller virtuality than in Eq. (1.17) and is therefore already contained in our existing collinear degrees of freedom.

Gluons with a scaling as in (d) are called Glauber gluons. They cannot enter in the final state since they are offshell modes, but they can mediate perpendicular momentum transfer between the two different collinear sectors in Eq. (1.18). In particular they could connect the active parton from one proton with a quark or gluon in the remnant of the other proton. As a consequence the proton remnant no longer goes straight down the beam pipe and contributes to $B_{a,b}^+$, see Fig. 1-7. We will discuss below how to factorize the soft and the various collinear degrees of freedom. If Glauber gluons need to be taken into account, this factorization breaks down. In Sec. 7.3.4 we show that the contribution from Glauber gluons cancels out for our factorization theorem.
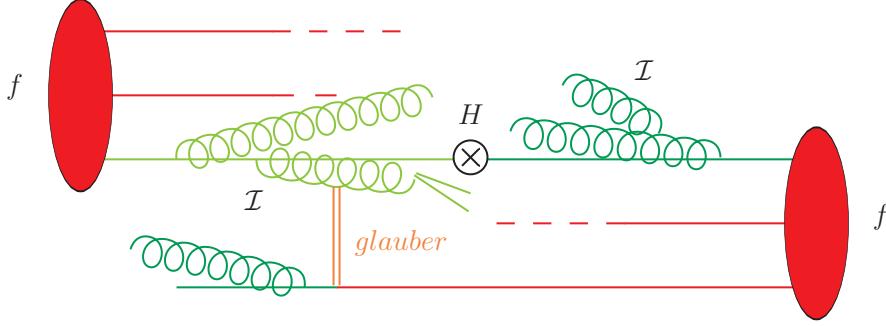
Figure 1-7: Schematic diagram of a proton-(anti)proton collision up to the hard interaction. Glauber gluons (double line) can couple an active parton with a spectator from the other proton. The spectator was very collinear and would have gone straight down the beam pipe but the Glauber gluon kicks it into active region, where it contributes to $B_{a,b}^+$.

To summarize, identifying the relevant modes is really the art of effective field theories. Including any unnecessary degrees of freedom is permitted and will not affect the outcome, as long as one avoids double counting by appropriate zero-bin subtractions. However, it will dramatically increase the computational effort required.

We now discuss the matching onto SCET in which we integrate out the hard interaction [30]. In the previous section our effective Lagrangian only contained two terms $\mathcal{L}_W^{\text{eff}} = \sum_{i=1,2} C_i \mathcal{O}_i$, because the weak interaction is insensitive to the details of our external states. In SCET the collinear degrees of freedom have large $p^- \sim Q$ components, which enter in the hard interaction. Matching onto SCET thus yields Wilson coefficients and operators that depend on both the direction n^μ and size $\tilde{p}^-$ of these large components,

$$\mathcal{L}^{\text{eff}} = \sum_i \sum_{n_a, n_b} \int \mathrm{d}\tilde{p}_a^- \int \mathrm{d}\tilde{p}_b^- \, C_i(n_a, \tilde{p}_a^-, n_b, \tilde{p}_b^-) \mathcal{O}_i(n_a, \tilde{p}_a^-, n_b, \tilde{p}_b^-) \,. \tag{1.22}$$

As an example we show the matching for Higgs production through gluon fusion in Fig. 1-8. The collinear directions are fixed by the directions of the protons and $\tilde{p}_{a,b}^-$ are related to the virtuality and rapidity of the Higgs by momentum conservation.

Collinear gluons have the scaling $A_n^\mu = (A_n^+, A_n^-, A_{n\perp}^\mu) \sim (\lambda^2, 1, \lambda)$, which e.g. follows from the homogenous power counting of the covariant derivative. This implies that we can add arbitrary many collinear $\bar{n} \cdot A_n$ fields in the matching at the same order in the power counting, see Fig. 1-8(c) and (d). Fortunately gauge invariance restricts these operators, organizing these gluons into collinear Wilson lines W_n [37].
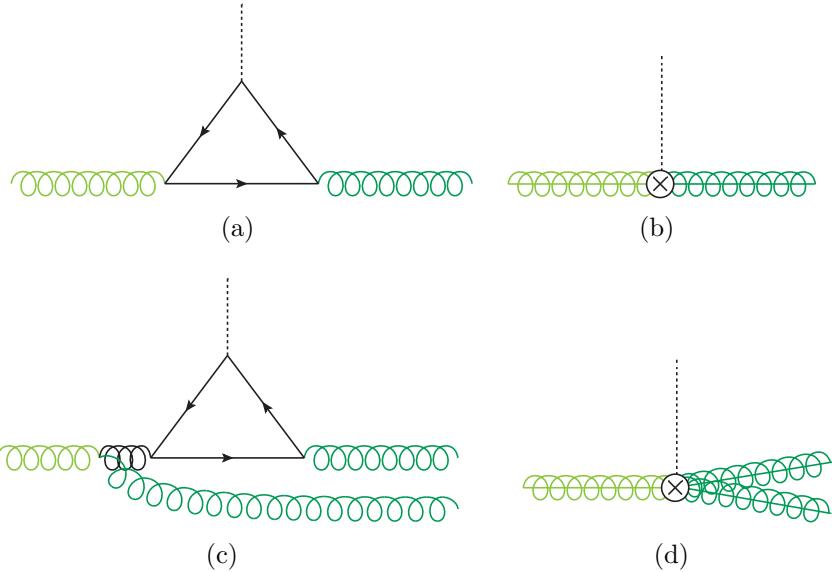
Figure 1-8: The matching for Higgs production through gluon fusion. The full theory diagram (a) gets matched onto the effective interaction (b). Springs with a line through them are collinear gluons. The different shades of green correspond to the two collinear modes and the solid black lines with the hard degrees of freedom that get integrated out. In (c) we consider the emission of an additional $\bar{n} \cdot A$ which is at the same order in the power counting and gets matched onto (d). Including arbitrary many emissions of $\bar{n} \cdot A$ gluons generates a collinear Wilson line W_n in SCET.

There was some arbitrariness in our choice of n^μ and $\bar{n}^\mu$, since the light-cone vector n^μ only needs to point roughly in the direction of the jet and we can choose any $\bar{n}^\mu$ that satisfies $n \cdot \bar{n} = 2$. The precise choice of these parameters should not affect our calculations, providing us with additional symmetries known as reparametrization invariance (RPI) [139]. We will often use RPI-III that transforms $n^\mu \to e^\alpha n^\mu$ and $\bar{n}^\mu \to e^{-\alpha} \bar{n}^\mu$. As an example, an RPI-III invariant function $f(p^+, p^-)$ can only depend on the invariant combination $p^+ p^-$.

We now discuss the factorization of the soft and various collinear degrees of freedom. It turns out that at leading order in the power counting the coupling of soft degrees of freedom to any collinear sector organizes itself into a Wilson line Y of soft gluons [35], as shown in Fig. 1-9. This is due to the simple coupling between soft and collinear degrees of freedom in Fig. 1-6 and their relative power counting in Eqs. (1.17) and (1.20). By factoring out this soft Wilson line from the collinear quark and gluon field ξ_n and A_n^μ

$$\xi_{n,\tilde{p}}(x) = Y(x)\, \xi_{n,\tilde{p}}^{(0)}(x)\,,$$
$$A_{n,\tilde{p}}^\mu(x) = Y(x)\, A_{n,\tilde{p}}^{\mu(0)}(x)\, Y^\dagger(x)\,, \qquad (1.23)$$
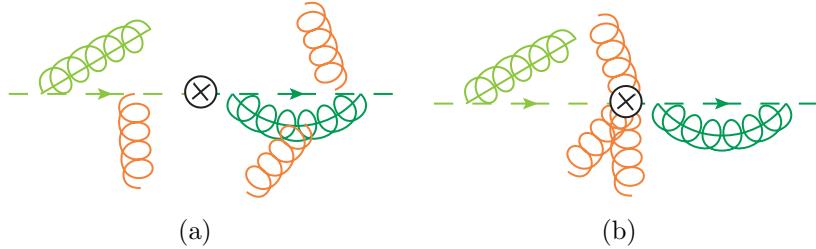
Figure 1-9: The soft radiation in (a) organizes itself into emissions from soft Wilson lines shown in (b). The dashed lines correspond to collinear quarks, and the springs with (without) a solid line through them correspond to collinear (soft) gluons.

we get collinear fields $\xi_n^{(0)}, A_n^{\mu(0)}$ that are decoupled from the soft degrees of freedom at leading order in the power counting. This is known as the BPS field redefinition.

We conclude this section by discussing the resummation of large logarithms. Our measurement sets the expansion parameter $\lambda^2 \sim B_a^+/Q \ll 1$ and SCET will allow us to resum the corresponding large logarithms $L = \ln B_a^+/Q$. However, rather than single logarithms $\alpha_s L$ we now encounter double logarithms $\alpha_s L^2$ which leads to a different structure than in Eq. (1.9)

$$\sigma \sim 1 + \alpha_s L^2 + \alpha_s^2 L^4 + \alpha_s^3 L^6 + \dots$$
$$\alpha_s L + \alpha_s^2 L^3 + \alpha_s^3 L^5 + \dots$$
$$\alpha_s + \alpha_s^2 L^2 + \alpha_s^3 L^4 + \dots . \tag{1.24}$$

If we assume $L \sim 1/\alpha_s$, getting the correct tree level result requires us to sum the first row, the second row, everything on the third row except for the first term etc. This looks complicated, but once these logarithms are factored in SCET the story is very similar to that in Sec. 1.3. Each factor only depends on one physical scale and by evaluating it at this scale we avoid large logarithms. We then use the RGE to evolve all the factors to a common scale μ, which resums the logarithms in Eq. (1.24). The evolution of a factor has the following parametric structure

$$U(\mu_0, \mu) \sim \exp\left[\sum_k (\alpha_s L)^k L + (\alpha_s L)^k + \alpha_s(\alpha_s L)^k + \dots\right]. \tag{1.25}$$

The first term, $\sum_k (\alpha_s L)^k L$, was not present for the weak decays in Eq. (1.13). It is due to the cusp anomalous dimension which comes from the cusp of Wilson lines. This term is

| | matching | running | | |
		non-cusp	cusp	$\beta(\alpha_s)$
LO	0-loop	-	-	-
NLO	1-loop	-	-	-
NNLO	2-loop	-	-	-
LL	0-loop	0-loop	1-loop	1-loop
NLL	0-loop	1-loop	2-loop	2-loop
NNLL	1-loop	2-loop	3-loop	3-loop

Table 1.2: Order counting for fixed and resummed perturbation theory with double logarithms.

related to the different structure of the logarithms in Eq. (1.24), as is clear from expanding $U(\mu_0, \mu)$. Assuming $L \sim 1/\alpha_s$, we need the first two terms of the exponent in Eq. (1.25) to get the correct tree level result, which requires the two-loop cusp anomalous dimension. The non-cusp piece of the anomalous dimension does not contribute to the first term of the exponent in Eq. (1.25) and is only needed at one-loop. The general counting for fixed order and resummed perturbation theory is shown in Table 1.2. We will not consider LL resummation because this does not include the $\sum_k (\alpha_s L)^k$ term in the exponent in Eq. (1.25), which parametrically contributes at $\mathcal{O}(1)$.

1.5 Outline

Chapter 2 provides an introduction to beam functions and factorization for isolated processes, in which we discuss our main results. The goal of this chapter is to give a thorough discussion of the physical picture behind our results which is accessible to non-expert readers. We define the "beam thrust" event shape that we use to impose the central vet jeto in isolated Drell-Yan, and we present the factorization theorem. The renormalization of the beam functions and the relationship between the beam functions and the PDFs is discussed, and we make the comparison with the initial-state parton shower. We compare our factorization theorem for isolated Drell-Yan to the fixed-order calculation and discuss its RGE structure. For convenience we have included a quick overview of our notation and symbols in App. A. In App. B we list the plus distribution definitions and identities that we use, as well as identities for discontinuties needed in the calculations in Ch. 4 and Ch. 5.

In chapter 3 we discuss several formal aspects of the quark and gluon beam functions, including their definition in terms of matrix elements of operators in SCET, their renor-

malization, their analytic structure, and the operator product expansion relating the beam functions to PDFs. In particular, we show that the beam functions have the same RGE as the jet functions to all orders in perturbation theory. (Part of the proof is relegated to App. C.)

We perform the one-loop matching of the quark beam function onto quark and gluon PDFs in Ch. 4. Using an offshellness IR regulator we give explicit details of the calculations for the quark beam function and PDF. We verify explicitly that the IR singularities cancel in the matching and extract results for the next-to-leading order (NLO) matching coefficients. In App. D we repeat the matching calculation for the quark beam function in pure dimensional regularization. The calculation of the one-loop matching coefficients for the gluon beam function is performed in Ch. 5. In chapter 6, we show and discuss plots for the quark and gluon beam function at NLO in fixed-order perturbation theory and next-to-next-to-leading logarithmic (NNLL) order in resummed perturbation theory.

In chapter 7, we derive in detail the factorization theorem for isolated processes $pp \to XL$ using SCET, and apply it to the case of Drell-Yan.

Plots for the beam thrust cross section for Drell-Yan at NLO and NNLL are shown and discussed in Ch. 8. In Ch. 9 we apply our factorization theorem to Higgs production through gluon fusion and show results for the corresponding beam thrust cross section. The necessary ingredients for evaluating these cross sections at NNLL are collected in App. E.

In Ch. 10 we extend our work to final state jets. For a signal with N jets we define a global event shape called "N-jettiness" to veto any unwanted additional jets. We describe theoretical and experimental benefits of our approach and present a factorization formula for the corresponding N-jet cross section. We conclude in Ch. 11.

Chapter 2

Introduction to Beam Functions and Isolated Drell-Yan

This chapter provides an extensive discussion of how factorization with beam functions works, including the necessary kinematic definitions for the variables that constrain the hadronic final state. In the interest of avoiding technical details, we only discuss the physics contained in the factorization theorems. Readers interested in the field-theoretic definitions for the beam functions are referred to Ch. 3, while those interested in the derivation of the factorization theorem in SCET and explicit definitions for all its ingredients are referred to Ch. 7. The work in this chapter was first presented in Ref. [166].

In Sec. 2.1, we review the factorization theorems for inclusive Drell-Yan and threshold Drell-Yan, and then explain the factorization theorem for our isolated Drell-Yan process. We use a simple setup where measurements on the final-state hadrons use hemispheres orthogonal to the beam. These observables are generalized in Sec. 2.2 to uniformly account for measurements that sample over a wide variety of boosts between the hadronic and partonic center-of-mass frames. We explain the relation between beam functions and parton distribution functions in Sec. 2.3. We compare the beam-function renormalization group evolution to initial-state parton showers in Sec. 2.4. In Sec. 2.5, we show how the various pieces in the factorization theorem arise from the point of view of a fixed-order calculation. In Sec. 2.6, we compare the structure of large logarithms and their resummation for the different factorization theorems. This yields an independent argument for the necessity of beam functions.

2.1 Drell-Yan Factorization Theorems

To describe the Drell-Yan process $pp \to X\ell^+\ell^-$ or $p\bar{p} \to X\ell^+\ell^-$, we take

$$P_a^\mu + P_b^\mu = p_X^\mu + q^\mu \,, \tag{2.1}$$

where $P_{a,b}^\mu$ are the incoming (anti)proton momenta, $E_{\rm cm} = \sqrt{(P_a + P_b)^2}$ is the total center-of-mass energy, and q^μ is the total momentum of the $\ell^+\ell^-$ pair. We also define

$$\tau = \frac{q^2}{E_{\rm cm}^2} \,, \qquad Y = \frac{1}{2}\ln\frac{P_b \cdot q}{P_a \cdot q} \,, \qquad x_a = \sqrt{\tau}e^Y \,, \qquad x_b = \sqrt{\tau}e^{-Y} \,, \tag{2.2}$$

where Y is the total rapidity of the leptons with respect to the beam axis, and x_a and x_b are in one-to-one correspondence with τ and Y. Their kinematic limits are

$$0 \leq \tau \leq 1 \,, \qquad 2|Y| \leq -\ln\tau \,, \qquad \tau \leq x_a \leq 1 \,, \qquad \tau \leq x_b \leq 1 \,. \tag{2.3}$$

The invariant mass of the hadronic final state is bounded by

$$m_X^2 = p_X^2 \leq E_{\rm cm}^2 (1 - \sqrt{\tau})^2 \,. \tag{2.4}$$

In Drell-Yan

$$Q = \sqrt{q^2} \gg \Lambda_{\rm QCD} \tag{2.5}$$

plays the role of the hard interaction scale. In general, for factorization to be valid at some leading level of approximation with a perturbative computation of the hard scattering, the measured observable must be infrared safe and insensitive to the details of the hadronic final state.

For inclusive Drell-Yan, illustrated in Fig. 2-1(a), one sums over all hadronic final states X allowed by Eq. (2.4) without imposing any cuts. Hence, the measurement is insensitive to any details of X because one sums over all possibilities. In this situation there is a rigorous derivation of the classic factorization theorem [52, 75, 78]

$$\frac{1}{\sigma_0}\frac{{\rm d}\sigma}{{\rm d}q^2 {\rm d}Y} = \sum_{i,j}\int\frac{{\rm d}\xi_a}{\xi_a}\frac{{\rm d}\xi_b}{\xi_b}\,H_{ij}^{\rm incl}\Big(\frac{x_a}{\xi_a},\frac{x_b}{\xi_b},q^2,\mu\Big)\,f_i(\xi_a,\mu)\,f_j(\xi_b,\mu)\Big[1+\mathcal{O}\Big(\frac{\Lambda_{\rm QCD}}{Q}\Big)\Big]\,, \tag{2.6}$$

(a) Inclusive Drell-Yan. (b) Drell-Yan near threshold. (c) Isolated Drell-Yan.

(d) Dijet near threshold. (e) Isolated dijet production.
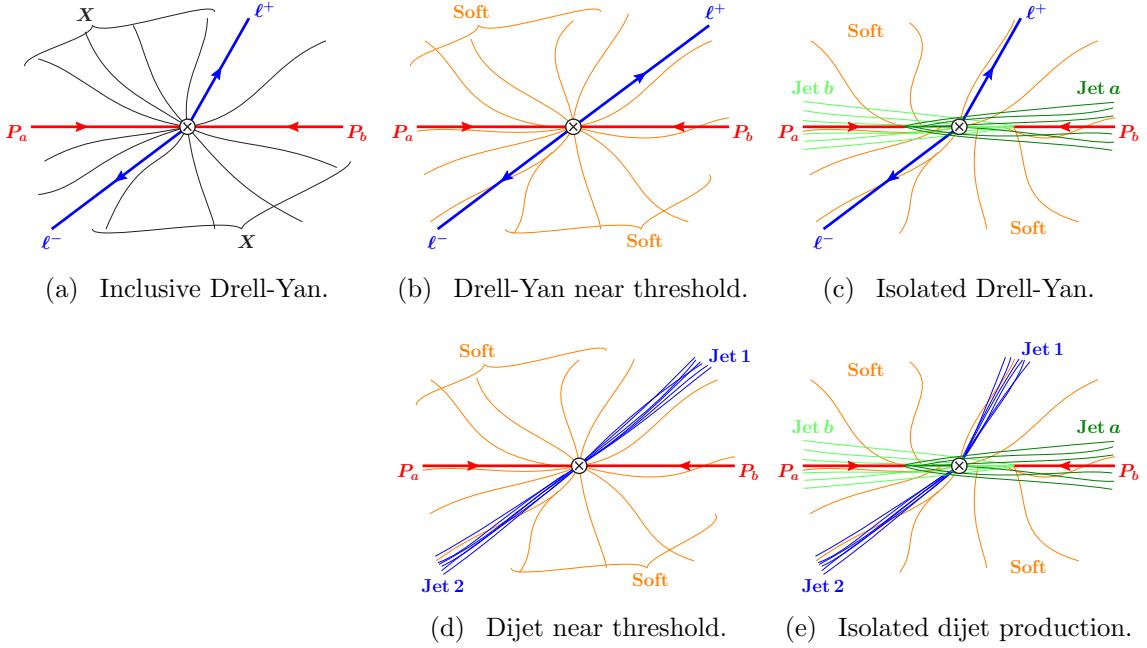
Figure 2-1: Different final-state configurations for pp collisions. The top row corresponds to Drell-Yan factorization theorems for the (a) inclusive, (b) threshold, and (c) isolated cases. The bottom row shows the corresponding pictures with the lepton pair replaced by dijets.

where $\sigma_0 = 4\pi\alpha_{\rm em}^2/(3N_c E_{\rm cm}^2 q^2)$, and the integration limits are $x_a \leq \xi_a \leq 1$ and $x_b \leq \xi_b \leq 1$. The sum is over partons $i,j = \{g, u, \bar{u}, d, \ldots\}$, and $f_i(\xi_a)$ is the parton distribution function for finding parton i inside the proton with light-cone momentum fraction ξ_a along the proton direction. Note that $\xi_{a,b}$ are partonic variables, whereas $x_{a,b}$ are leptonic, and the two are only equal at tree level. The inclusive hard function $H_{ij}^{\rm incl}$ can be computed in fixed-order perturbative QCD as the partonic cross section to scatter partons i and j [corresponding to $d\sigma_{ij}^{\rm part}$ in Eq. (1.1)] and is known to two loops [8, 14, 15, 110, 113].

For threshold Drell-Yan, one imposes strong restrictions to only allow soft hadronic final states with $m_X \ll Q$, as illustrated in Fig. 2-1(b). Using Eq. (2.4), this can be ensured by forcing $(1 - \sqrt{\tau})^2 \ll \tau$, so that one is close to the threshold $\tau \to 1$. In this case, there are large double logarithms that are not accounted for by the parton distributions. Furthermore, since

$$1 \geq \xi_{a,b} \geq x_{a,b} \geq \tau \to 1 \,, \tag{2.7}$$

a single parton in each proton carries almost all of the energy, $\xi_{a,b} \to 1$. The partonic analog

of τ is the variable

$$z = \frac{q^2}{\xi_a \xi_b E_{\text{cm}}^2} = \frac{\tau}{\xi_a \xi_b} \leq 1\,, \tag{2.8}$$

and $\tau \to 1$ implies the partonic threshold limit $z \to 1$. As Eq. (2.3) forces $Y \to 0$ for $\tau \to 1$, it is convenient to integrate over Y and consider the $\tau \to 1$ limit for $\mathrm{d}\sigma/\mathrm{d}q^2$. The relevant factorization theorem in this limit is [63, 165]

$$\frac{1}{\sigma_0} \frac{\mathrm{d}\sigma}{\mathrm{d}q^2} = \sum_{ij} H_{ij}(q^2, \mu) \int \frac{\mathrm{d}\xi_a}{\xi_a} \frac{\mathrm{d}\xi_b}{\xi_b}\, f_i(\xi_a, \mu)\, f_j(\xi_b, \mu)$$
$$\times\, Q\, S_{\text{thr}}\Big[Q\Big(1 - \frac{\tau}{\xi_a \xi_b}\Big), \mu\Big]\Big[1 + \mathcal{O}\Big(\frac{\Lambda_{\text{QCD}}}{Q}, 1 - \tau\Big)\Big]\,, \tag{2.9}$$

where we view Eq. (2.9) as a hadronic factorization theorem in its own right, rather than simply a refactorization of H_{ij}^{incl} in Eq. (2.6). This Drell-Yan threshold limit has been studied extensively [42, 44, 68, 118, 126, 136, 150]. Factorization theorems of this type are the basis for the resummation of large logarithms in near-threshold situations. In contrast to Eq. (2.6), the sum in Eq. (2.9) only includes the dominant $q\bar{q}$ terms for various flavors, $ij = \{u\bar{u}, \bar{u}u, d\bar{d}, \ldots\}$. Other combinations are power-suppressed and only appear at $\mathcal{O}(1 - \tau)$ or higher. The threshold hard function $H_{ij} \sim |C_i C_j^*|$ is given by the square of Wilson coefficients in SCET, and can be computed from the timelike quark form factor. The threshold Drell-Yan soft function S_{thr} is defined by a matrix element of Wilson lines and contains both perturbative and nonperturbative physics. If it is treated purely in perturbation theory at the soft scale $Q(1 - \tau)$, there are in principle additional power corrections of $\mathcal{O}[\Lambda_{\text{QCD}}/Q(1 - \tau)]$ in Eq. (2.9) [125].

Our goal is to describe the isolated Drell-Yan process shown in Fig. 2-1(c). Here, the colliding partons in the hard interaction are far from threshold as in the inclusive case, but we impose a constraint that does not allow central jets. Soft radiation still occurs everywhere, including the central region. Away from threshold, the hard interaction only carries away a fraction of the total energy in the collision. The majority of the remaining energy stays near the beam. The colliding partons emit collinear radiation along the beams that can be observed in the final state, shown by the green lines labeled "Jet a" and "Jet b" in Fig. 2-1(c). This radiation cannot be neglected in the factorization theorem and necessitates the beam functions. In the threshold case, these jets are not allowed by the

limit $\tau \to 1$, which forces all available energy into the leptons and leaves only soft hadronic radiation.[1] In the inclusive case there are no restrictions on additional hard emissions, in which case initial-state radiation is included in the partonic cross section in H_{ij}^{incl}.

Also shown in Fig. 2-1(c) is the fact that the leptons in isolated Drell-Yan need not be back to back, though they are still back to back in the transverse plane [see Sec. 7.2]. In this regard, isolated Drell-Yan is in-between the threshold case, where the leptons are fully back to back with $Y \approx 0$, and the inclusive case, where they are unrestricted.

In Figs. 2-1(d) and 2-1(e) we show analogs of threshold Drell-Yan and isolated Drell-Yan with the leptons replaced by final-state jets. We will discuss the extension to jets in Ch. 10.

To formulate isolated Drell-Yan we must first discuss how to veto hard emissions in the central region. For this purpose, it is important to use an observable that covers the full phase space. Jet algorithms are good tools to identify jets, but not necessarily to veto them. Imagine we use a jet algorithm and require that it does not find any jets in the central region. Although this procedure covers the full phase space, the restrictions it imposes on the final state depend in detail on the algorithm and its criteria to decide if something is considered a jet or not. It is very hard to incorporate such restrictions into explicit theoretical calculations, and in particular into a rigorous factorization theorem. Even if possible in principle, the resulting beam and soft functions would be very complicated objects, and it would be difficult to systematically resum the large logarithms arising at higher orders from the phase-space restrictions. Therefore, to achieve the best theoretical precision, it is important to implement the central jet veto using an inclusive kinematic variable. This allows us to derive a factorization theorem with analytically manageable ingredients, which can then be used to sum large phase-space logarithms. For a clean theoretical description, this observable must be chosen carefully such that it is infrared safe and sensitive to emissions everywhere in phase space. Observables satisfying these criteria for hadron colliders have been classified and studied in Refs. [27, 28], and are referred to as global event shapes. (Issues related to non-global observables have been discussed for example in Refs. [20, 46, 82, 97].)

---

[1]Note that the proof of factorization for the partonic cross section in the partonic threshold limit $z \to 1$ is not sufficient to establish the factorization of the hadronic cross section, unless one takes the limit $\tau \to 1$. The hadronic factorization theorem assumes that all real radiation is soft with only virtual hard radiation in the hard function. The weaker limit $z \to 1$ still allows the incoming partons to emit energetic real radiation that cannot be described by the threshold soft function. Only the $\tau \to 1$ limit forces the radiation to be soft. This point is not related to whether or not the threshold terms happen to dominate numerically away from $\tau \to 1$ due to the shape of the PDFs or other reasons.
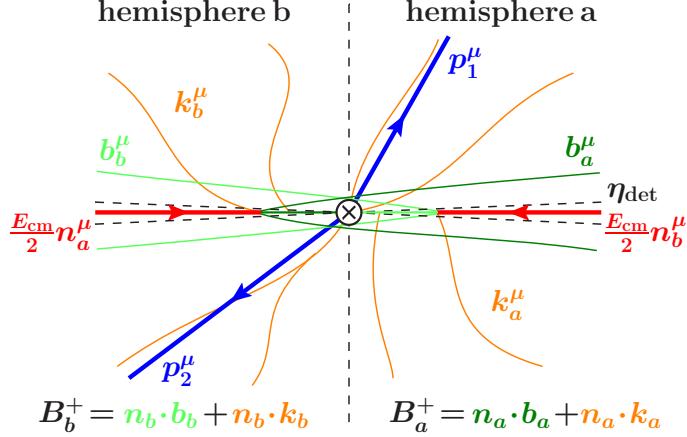
Figure 2-2: Definition of hemispheres and kinematic variables for isolated Drell-Yan.

We will consider a simple kinematic variable that fulfills the above criteria, leaving the discussion of more sophisticated generalizations to the next section. The key variables for the isolated Drell-Yan process are shown in Fig. 2-2. The proton momenta P_a^μ and P_b^μ are used to define lightlike vectors n_a^μ and n_b^μ,

$$P_a^\mu = \frac{E_{\rm cm}}{2}\, n_a^\mu\,, \qquad P_b^\mu = \frac{E_{\rm cm}}{2}\, n_b^\mu\,, \tag{2.10}$$

where the protons are massless and $n_a^2 = 0$, $n_b^2 = 0$, and $n_a \cdot n_b = 2$. Using the beam axis, we define two hemispheres a and b opposite to the incoming protons. We then divide up the total hadronic momentum as

$$p_X^\mu = B_a^\mu + B_b^\mu\,, \tag{2.11}$$

where $B_a^\mu = p_{X_a}^\mu$ and $B_b^\mu = p_{X_b}^\mu$ are the total final-state hadronic momenta in hemispheres a and b. Of these, we consider the components

$$B_a^+ = n_a \cdot B_a = B_a^0 (1 + \tanh y_a)\, e^{-2y_a}\,, \qquad B_b^+ = n_b \cdot B_b = B_b^0 (1 + \tanh y_b)\, e^{-2y_b}\,, \tag{2.12}$$

where $B_{a,b}^0$ are the energy components and $y_{a,b}$ are the total rapidities of $B_{a,b}^\mu$ with respect to the forward direction $n_{a,b}$ for each hemisphere. Here, $\lim_{y\to\infty}(1 + \tanh y) = 2$ and $1 + \tanh y \geq 1.8$ for $y \geq 1$, so $B_{a,b}^+$ scale exponentially with the rapidities $y_{a,b}$.

In terms of the measured particle momenta p_k in hemisphere a,

$$B_a^+ = \sum_{k \in a} n_a \cdot p_k = \sum_{k \in a} E_k (1 + \tanh \eta_k) e^{-2\eta_k} . \tag{2.13}$$

Here, E_k and η_k are the experimentally measured energy and pseudorapidity with respect to $\vec{n}_a$, and we neglect the masses of final-state hadrons. An analogous formula applies for B_b^+. Hence, B_a^+ and B_b^+ receive large contributions from energetic particles in the central region, while contributions from particles in the forward region are suppressed. Thus, requiring small $B_{a,b}^+ \ll Q$ is an effective way to restrict the energetic radiation in each hemisphere as a smooth function of rapidity, allowing forward jets and disallowing central jets. At the same time, soft radiation with energies $\ll Q$ is measured, but not tightly constrained.

As an example, consider the cut

$$B_{a,b}^+ \leq Q \, e^{-2y_{\text{cut}}} . \tag{2.14}$$

This constraint vetoes any events with a combined energy deposit of more than $Q/2$ per hemisphere in the central rapidity region $|y| \leq y_{\text{cut}}$. In the smaller region $|y| \leq y_{\text{cut}} - 1$, the energy allowed by Eq. (2.14) is reduced by a factor of $e^2 \simeq 7$, essentially vetoing any jets there. In the larger region $|y| \leq y_{\text{cut}} + 1$, it is increased by the same factor, so beyond $y_{\text{cut}} + 1$ the hadronic final state is essentially unconstrained. Thus, a typical experimental value might be $y_{\text{cut}} = 2$, which vetoes energetic jets in the central region $|y| \leq 1$. The precise value of the cut on $B_{a,b}^+$ will of course depend on the requirements of the experimental analyses.

Note that the variable B_a^+ is similar to the total transverse energy in hemisphere a, defined as

$$E_{Ta} = \sum_{k \in a} \frac{E_k}{\cosh \eta_k} = \sum_{k \in a} E_k (1 + \tanh \eta_k) e^{-\eta_k} . \tag{2.15}$$

B_a^+ has two advantages over E_{Ta}. First, the exponential sensitivity to rapidity is much stronger for B_a^+, which means it provides a stronger restriction on jets in the central region and at the same time is less sensitive to jets in the forward region. Second, since B_a^+ is a specific four-momentum component and linear in four-momentum, $(p_1 + p_2)^+ = p_1^+ + p_2^+$, it is much simpler to work with and to incorporate into the factorization theorem. It is clear that the isolated Drell-Yan factorization theorem discussed here can be extended to

observables with other exponents, $e^{-a\eta_k}$, much like the angularity event shapes in e^+e^- [47].

One should ask, down to what values can $B_{a,b}^+$ be reliably measured experimentally? In principle, particles at any rapidity contribute to $B_{a,b}^+$, but the detectors only have coverage up to a maximum pseudorapidity η_{det}, as indicated in Fig. 2-2. For the hadron calorimeters at the LHC $\eta_{\mathrm{det}} \simeq 5$ and at the Tevatron $\eta_{\mathrm{det}} \simeq 4$. In the hadronic center-of-mass frame, the unscattered partons inside the proton have plus components of $\mathcal{O}(\Lambda_{\mathrm{QCD}}^2/E_{\mathrm{cm}})$, so any contributions from the unmeasured proton remnants are always negligible. The question then is, what is the maximal contribution to $B_{a,b}^+$ from initial-state radiation that is missed as it is outside the detector? In the extreme scenario where all proton energy is deposited right outside η_{det}, we would have $B_{a,b}^+ = 14\,\mathrm{TeV}e^{-10} = 0.6\,\mathrm{GeV}$ at the LHC and $B_{a,b}^+ = 2\,\mathrm{TeV}e^{-8} = 0.7\,\mathrm{GeV}$ at the Tevatron. In more realistic scenarios, the contribution from such radiation is suppressed by at least another factor of 10 or more. Therefore, the finite detector range is clearly not an issue for measuring values $B_{a,b}^+ \gtrsim 2\,\mathrm{GeV}$, and the relevant limitation will be the experimental resolution in $B_{a,b}^+$.

The factorization theorem for isolated Drell-Yan, which we prove in Ch. 7, reads

$$\frac{1}{\sigma_0}\frac{\mathrm{d}\sigma}{\mathrm{d}q^2\mathrm{d}Y\mathrm{d}B_a^+\mathrm{d}B_b^+} = \sum_{ij} H_{ij}(q^2,\mu)\int \mathrm{d}k_a^+\,\mathrm{d}k_b^+\,q^2 B_i[\omega_a(B_a^+ - k_a^+), x_a, \mu]$$

$$\times B_j[\omega_b(B_b^+ - k_b^+), x_b, \mu]S_{\mathrm{ihemi}}(k_a^+, k_b^+, \mu)\left\{1 + \mathcal{O}\left[\frac{\Lambda_{\mathrm{QCD}}}{Q}, \frac{\omega_{a,b}B_{a,b}^+}{Q^2}\right]\right\}. \qquad (2.16)$$

The physical interpretation of Eq. (2.16) is that we take partons i and j out of the initial-state jets B_i, B_j and hard-scatter them to final state particles with H_{ij}, while including S_{ihemi} to describe the accompanying soft radiation. The hard function H_{ij} is identical to the one in the threshold factorization theorem in Eq. (2.9), and the sum in Eq. (2.16) is again only over $ij = \{u\bar{u}, \bar{u}u, d\bar{d}, \ldots\}$. The quark and antiquark beam functions B_q and $B_{\bar{q}}$ describe the effects of the incoming jets and have replaced the PDFs. The variables $\omega_{a,b} = x_{a,b}E_{\mathrm{cm}}$. The hard partons are taken from initial-state jets rather than protons, so unlike in the threshold case the gluon PDF now contributes via the beam functions. We will see how this works in more detail in Sec. 2.3. Finally, S_{ihemi} is the initial-state hemisphere soft function.

The kinematic variables in Eq. (2.16) are displayed in Fig. 2-2. The soft function depends on the momenta $k_a^+ = n_a \cdot k_a$ and $k_b^+ = n_b \cdot k_b$ of soft particles in hemispheres a and b,

respectively. Much like PDFs, the beam functions $B_i(t_a, x_a, \mu)$ and $B_j(t_b, x_b, \mu)$ depend on the momentum fractions x_a and x_b of the active partons i and j participating in the hard collision. In addition, they depend on invariant-mass variables

$$t_a = \omega_a b_a^+ \geq 0\,, \qquad t_b = \omega_b b_b^+ \geq 0\,, \tag{2.17}$$

where $\omega_{a,b} = x_{a,b} E_{\mathrm{cm}}$ are the hard momentum components and $b_a^+ = n_a{\cdot}b_a$. The momentum b_a^μ is defined as the total momentum of the energetic particles radiated into hemisphere a, as shown in Fig. 2-2, and similarly for b_b^+. (The kinematics are shown in more detail in Fig. 7-1.) Before the hard interaction, the momentum of the active quark can be written as

$$\omega_a \frac{n_a^\mu}{2} - b_a^+ \frac{n_b^\mu}{2} - b_{a\perp}^\mu\,. \tag{2.18}$$

The first term is its hard momentum along the proton direction, and the last two terms are from the momentum it lost to radiation, where $b_{a\perp}^2 = -\vec{b}_{aT}^2$ contains the transverse components. The quark's spacelike invariant mass is $-\omega_a b_a^+ - \vec{b}_{aT}^2 = -t_a - \vec{b}_{aT}^2$. The beam function B_i for hemisphere a depends on $t_a = \omega_a b_a^+ = x_a E_{\mathrm{cm}} b_a^+$, which is the negative of the quark's transverse virtuality. (When the distinction is unimportant we will usually refer to t simply as the quark's virtuality.) By momentum conservation $b_a^+ = B_a^+ - k_a^+$, leading to the convolution of the beam and soft functions as shown in Eq. (2.16). Physically, the reason we have to subtract the soft momentum from B_a^+ is that the beam function only properly describes the collinear radiation, while the soft radiation must be described by the soft function. An analogous discussion applies to B_j and t_b for hemisphere b. The convolutions in the factorization theorem thus encode the cross talk between the soft radiation and energetic collinear radiation from the beams.

By measuring and constraining B_a^+ we essentially measure the virtuality of the hard parton in the initial state. As the proton cannot contain partons with virtualities larger than Λ_{QCD}^2, the initial state at that point must be described as an incoming jet containing the hard off-shell parton. This is the reason why beam functions describing these initial-state jets must appear in Eq. (2.16). It also follows that since $t \gg \Lambda_{\mathrm{QCD}}^2$ we can calculate the beam functions perturbatively in terms of PDFs, which we discuss further in Sec. 2.3.

It is convenient to consider a cumulant cross section, including all events with $B_{a,b}^+$ up to some specified value, as in Eq. (2.14). Integrating Eq. (2.16) over $0 \leq B_{a,b}^+ \leq B_{\mathrm{max}}^+$ we

obtain

$$\frac{1}{\sigma_0}\frac{d\sigma}{dq^2 dY}(B_{\max}^+) = \sum_{ij} H_{ij}(q^2,\mu)\int dk_a^+ \, dk_b^+ \, \widetilde{B}_i[\omega_a(B_{\max}^+ - k_a^+), x_a, \mu]$$

$$\times \widetilde{B}_j[\omega_b(B_{\max}^+ - k_b^+), x_b, \mu] S_{\mathrm{ihemi}}(k_a^+, k_b^+, \mu)\left\{1 + \mathcal{O}\left[\frac{\Lambda_{\mathrm{QCD}}}{Q}, \frac{\omega_{a,b}B_{\max}^+}{Q^2}\right]\right\}, \quad (2.19)$$

where the soft function S_{ihemi} is the same as in Eq. (2.16), and we defined the integrated beam function

$$\widetilde{B}_i(t_{\max}, x, \mu) = \int dt \, B_i(t, x, \mu)\,\theta(t_{\max} - t). \quad (2.20)$$

The cut $B_{a,b}^+ \leq B_{\max}^+$ implies the limit $b_{a,b}^+ \leq B_{\max}^+ - k_{a,b}^+$ and $t_{a,b} \leq \omega_{a,b}(B_{\max}^+ - k_{a,b}^+)$, leading to the convolutions in Eq. (2.19).

The factorization theorem Eq. (2.16) and its integrated version Eq. (2.19) are valid in the limit $t_{a,b}/Q^2 \simeq B_{a,b}^+/Q \equiv \lambda^2 \ll 1$, and receive power corrections of $\mathcal{O}(\lambda^2)$. Thus, for $B_{\max}^+ = Q e^{-2y_{\mathrm{cut}}}$ with $y_{\mathrm{cut}} = 1$, we expect the power corrections not to exceed $e^{-2} \sim 10\%$. This is not a fundamental limitation, because the power corrections can be computed in SCET if necessary. If the soft function is treated purely perturbatively, there are additional power corrections of $\mathcal{O}(\Lambda_{\mathrm{QCD}}/B_{a,b}^+)$, which account for soft singularities as $B_{a,b}^+ \to 0$. The variables $B_{a,b}^+$ are infrared safe with respect to collinear splittings [164].

The hard function receives perturbative α_s corrections at the hard scale $\mu_H \simeq Q$, the beam functions have α_s corrections at the intermediate beam scale $\mu_B^2 \simeq t_{\max} \simeq Q B_{\max}^+$, and the soft function at the soft scale $\mu_S \simeq B_{\max}^+$. For example, for $Q \simeq 1\,\mathrm{TeV}$ and $y_{\mathrm{cut}} = 2$ we have $\mu_B \simeq 140\,\mathrm{GeV}$ and $\mu_S \simeq 20\,\mathrm{GeV}$. Even with a very small $Q \simeq 100\,\mathrm{GeV}$, perhaps for Higgs production, $\mu_B \simeq 14\,\mathrm{GeV}$ and $\mu_S \simeq 2\,\mathrm{GeV}$ are still perturbative (although at this point nonperturbative contributions $\sim \Lambda_{\mathrm{QCD}}/\mu_S$ to the soft function might no longer be small and may be incorporated with the methods in Refs. [117, 135]). In fixed-order perturbation theory, the cross section contains large single and double logarithms, $\ln(B_{\max}^+/Q) \simeq -4$ and $\ln^2(B_{\max}^+/Q) \simeq 16$, invalidating a fixed-order perturbative expansion. The factorization theorem allows us to systematically resum these logarithms to all orders in perturbation theory, which is discussed in more detail in Sec. 2.6.

The factorization theorem Eq. (2.16) also applies to other non-hadronic final states such as $Z' \to \ell^+\ell^-$, or Higgs production with $H \to \gamma\gamma$ or $H \to ZZ^* \to 4\ell$. In each case, q^2 and Y are the total non-hadronic invariant mass and rapidity, and central jets are

46

vetoed with a cut on $B_{a,b}^+$. The only dependence on the process is in the hard function, which must be replaced appropriately and can be taken directly from the corresponding threshold factorization theorem. One may also consider W production with $W \to \ell\bar\nu$, with an appropriate replacement of q^2 and Y with the charged lepton's rapidity. For a light Higgs with $Q \sim m_H$, the isolated Drell-Yan factorization theorem applies to Higgs production through gluon fusion $gg \to H$ and Higgs-strahlung $q\bar q \to VH$, which are the dominant production channels at the LHC and Tevatron, respectively.[2] For a generic process $pp \to XL$, the sum over $ij = \{gg, u\bar u, \bar u u, d\bar d, \ldots\}$ includes a gluon-gluon contribution, but still no cross terms between different parton types, and there will be two independent soft functions $S_{\mathrm{ihemi}}^{q\bar q}$ and S_{ihemi}^{gg}. [As shown in Ch. 7, only the $q\bar q$ soft function contributes to isolated Drell-Yan, so the labels were omitted in Eq. (2.16).] Indeed, the gluon-gluon contribution involving the gluon beam and soft functions, B_g and S_{ihemi}^{gg}, gives the dominant contribution in the case of Higgs production.

With the above physical picture, we can understand why the gluon beam function appeared in $\gamma p \to J/\psi X$ in the analysis of Ref. [96] in the limit where $E_{J/\psi} \to E_\gamma$. Taking p_X as the total momentum of final-state hadrons other than the J/ψ, one has $n \cdot p_X \sim E_{\mathrm{cm}}(1 - E_{J/\psi}/E_\gamma)$, where n is the proton direction. For $E_{J/\psi}$ close to E_γ, energetic radiation in the final state is restricted to a jet close to the n direction. Just as for our $B_{a,b}^+$, the measurement of $E_{J/\psi}$ probes the radiation emitted by the colliding gluon in the initial state. Thus, the proton is broken apart prior to the hard collision, and the gluon beam function is required to describe the initial state.

2.2   Generalized Observables

The factorization theorem in Eq. (2.16) applies for $t_a \ll q^2$ and $t_b \ll q^2$. This includes the situation where in the hadronic center-of-mass frame there is a numerically significant asymmetry $\omega_a = x_a E_{\mathrm{cm}} > \omega_b = x_b E_{\mathrm{cm}}$. This means that the boost between the hadronic and partonic center-of-mass frames, given by the leptonic $Y = \ln \sqrt{\omega_a/\omega_b} = \ln \sqrt{x_a/x_b}$, is significantly different from zero. We explore the implications of this here.

If there is no hierarchy, $\omega_a \approx \omega_b \approx \sqrt{\omega_a \omega_b} = Q$, corresponding to $Y \approx 0$, we can define

---

[2]In vector-boson fusion and associated production $gg \to t\bar tH$, the situation is more complicated and one has to explicitly consider the process $pp \to XjjH$ with two forward (top) jets.

a simple variable to constrain both hemispheres simultaneously,

$$\widehat{B} = \frac{B_a^+ + B_b^+}{Q} \,. \tag{2.21}$$

From Eq. (2.16), this gives

$$\frac{1}{\sigma_0} \frac{d\sigma}{dq^2 dY d\widehat{B}} = \sum_{ij} H_{ij}(q^2, \mu) \int dt_a \, dt_b \, B_i(t_a, x_a, \mu) \, B_j(t_b, x_b, \mu)$$
$$\times Q \, S_B\Big(Q\widehat{B} - \frac{t_a}{\omega_a} - \frac{t_b}{\omega_b}, \mu\Big), \tag{2.22}$$

where the soft function is defined as

$$S_B(k^+, \mu) = \int dk_a^+ dk_b^+ \, S_{\text{ihemi}}(k_a^+, k_b^+, \mu) \, \delta(k^+ - k_a^+ - k_b^+) \,. \tag{2.23}$$

The advantage of using $\widehat{B}$ is that the soft function now only depends on the single variable $k^+ = k_a^+ + k_b^+$, much like the soft function for thrust in e^+e^- collisions.

If we have a hierarchy $\omega_b < Q < \omega_a$, the final state has a substantial boost in the n_a direction, as shown in Fig. 2-3. In this case, the energetic radiation will generically be much closer to the beam axis in hemisphere a than in hemisphere b. To take this into account, it is natural to impose different cuts on B_a^+ and B_b^+. Using the boost-invariant combinations $\omega_a B_a^+/q^2$ and $\omega_b B_b^+/q^2$ to define the cut, we obtain

$$\frac{\omega_a B_a^+}{q^2} = \frac{B_a^+}{\omega_b} \le e^{-2y_{\text{cut}}}, \qquad \frac{\omega_b B_b^+}{q^2} = \frac{B_b^+}{\omega_a} \le e^{-2y_{\text{cut}}}, \tag{2.24}$$

so B_a^+ has a tighter constraint than B_b^+, as desired. If we simply replace $\widehat{B}$ by $B_a^+/\omega_b + B_b^+/\omega_a$, the soft function analogous to S_B in Eq. (2.23) will depend on $(\omega_a k_a^+ + \omega_b k_b^+)/Q^2$.

However, we should also adjust the hemispheres themselves to take into account the significant boost of the partonic center-of-mass frame. We therefore define a generalized hemisphere a as $y > Y$ and hemisphere b as $y < Y$, as shown in Fig. 2-3. The corresponding total hemisphere momenta are denoted as $B_{a,b}^+(Y)$ and the soft hemisphere momenta as $k_{a,b}^+(Y)$. The original definitions in Fig. 2-2 correspond to $B_{a,b}^+(0) \equiv B_{a,b}^+$ and $k_{a,b}^+(0) \equiv k_{a,b}^+$. The generalization of $\widehat{B}$ is given by the boost-invariant combination

$$\tau_B = \frac{\omega_a B_a^+(Y) + \omega_b B_b^+(Y)}{q^2} \,. \tag{2.25}$$
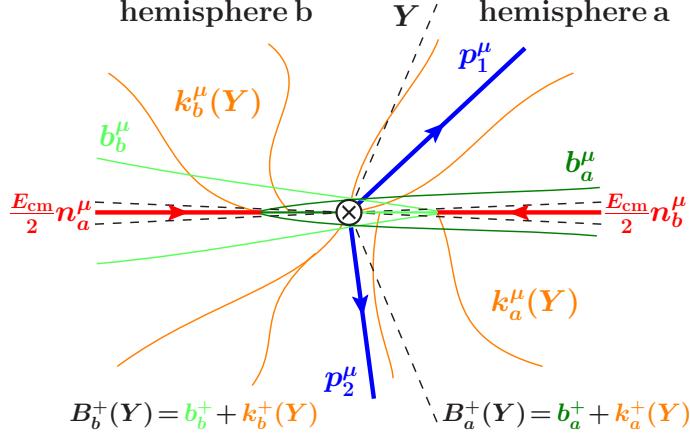
Figure 2-3: Generalized definition of hemispheres. The total rapidity of the leptons is Y, $b_{a,b}^+ = n_{a,b} \cdot b_{a,b}$, and $k_{a,b}^+(Y) = n_{a,b} \cdot k_{a,b}(Y)$.

With the generalized definition of the hemispheres, $B_{a,b}^+(Y)$ and $\omega_{a,b}$ transform under a boost by y in the n_a direction as

$$B_a^+(Y) \to B_a^{+\prime}(Y+y) = e^{-y}B_a^+(Y) \,, \qquad B_b^+(Y) \to B_b^{+\prime}(Y+y) = e^{y}B_b^+(Y) \,,$$

$$\omega_a \to \omega_a' = e^{y}\omega_a \,, \qquad\qquad\qquad \omega_b \to \omega_b' = e^{-y}\omega_b \,. \qquad (2.26)$$

Thus, boosting by $y = -Y$ from the hadronic to the partonic center-of-mass frame gives

$$\tau_B = \frac{\omega_a' B_a^{+\prime}(0) + \omega_b' B_b^{+\prime}(0)}{q^2} = \frac{B_a^{+\prime}(0) + B_b^{+\prime}(0)}{Q} \,. \qquad (2.27)$$

In the partonic center-of-mass frame we have $\omega_a' = \omega_b' = Q$, so there is no hierarchy. Correspondingly, the generalized hemispheres in this frame are again perpendicular to the beam axis, so Eq. (2.27) has the same form as $\widehat{B}$.

Note that for $e^+e^- \to$ jets, one can use the thrust axis to define two hemispheres with $n_{a,b}$ analogous to our case. In the 2-jet limit, thrust is then given by $1 - T = (Q\, n_a \cdot p_{X_a} + Q\, n_b \cdot p_{X_b})/2Q^2$. Hence, we can think of τ_B as the analog of thrust for incoming jets. For this reason we will call τ_B the "beam thrust".

In analogy to Eqs. (2.14) and (2.24), we define the cutoff on τ_B by

$$\tau_B \le e^{-2y_B^{\mathrm{cut}}} \,. \qquad (2.28)$$

49

For $\tau_B \to 0$ or equivalently $y_B^{\text{cut}} \to \infty$ the jets along the beam axes become pencil-like, while for generic y_B^{cut} we allow energetic particles up to rapidities $y \lesssim y_B^{\text{cut}}$ (with y measured in the partonic center-of-mass frame).

The beam functions are boost-invariant along the beam axis, so the different hemisphere definitions do not affect them. The soft function is boost-invariant up to the hemisphere definition, which defines its arguments $k_{a,b}^+$. Hence, boosting by $-Y$ we have $S_{\text{ihemi}}[e^Y k_a^+, e^{-Y} k_b^+; Y] = S_{\text{ihemi}}[k_a^+, k_b^+; 0] = S_{\text{ihemi}}(k_a^+, k_b^+)$, where the third argument denotes the definition of the hemispheres. This implies that the soft function for τ_B is the same as in Eq. (2.23). The factorization theorem for τ_B following from Eq. (2.16) is

$$\frac{1}{\sigma_0} \frac{\mathrm{d}\sigma}{\mathrm{d}q^2 \mathrm{d}Y \mathrm{d}\tau_B} = \sum_{ij} H_{ij}(q^2, \mu) \int \mathrm{d}t_a \, \mathrm{d}t_b \, B_i(t_a, x_a, \mu) \, B_j(t_b, x_b, \mu)$$
$$\times Q \, S_B\left(Q\tau_B - \frac{t_a + t_b}{Q}, \mu\right). \tag{2.29}$$

Integrating over $0 \le \tau_B \le \exp(-2y_B^{\text{cut}})$ we obtain

$$\frac{\mathrm{d}\sigma}{\mathrm{d}q^2 \mathrm{d}Y}(y_B^{\text{cut}}) = \int_0^{\exp(-2y_B^{\text{cut}})} \mathrm{d}\tau_B \, \frac{\mathrm{d}\sigma}{\mathrm{d}q^2 \mathrm{d}Y \mathrm{d}\tau_B} \, . \tag{2.30}$$

We will use Eqs. (2.29) and (2.30) to show plots of our results in chapters 8 and 9.

2.3   Relating Beam Functions and PDFs

The beam functions can be related to the PDFs by performing an operator product expansion, because $t_{a,b} \gg \Lambda_{\text{QCD}}^2$. This yields the factorization formula

$$B_i(t, x, \mu) = \sum_j \int_x^1 \frac{\mathrm{d}\xi}{\xi} \, \mathcal{I}_{ij}\left(t, \frac{x}{\xi}, \mu\right) f_j(\xi, \mu) \left[1 + \mathcal{O}\left(\frac{\Lambda_{\text{QCD}}^2}{t}\right)\right], \tag{2.31}$$

where we sum over partons $j = \{g, u, \bar{u}, d, \ldots\}$, $\mathcal{I}_{ij}$ are perturbatively calculable Wilson coefficients, and f_j is the standard PDF for parton j. The $\mathcal{O}(\Lambda_{\text{QCD}}^2/t)$ power corrections in Eq. (2.31) involve proton structure functions at subleading twist. Further mathematical details on Eq. (2.31) are discussed in Ch. 3, whereas here we focus on the physical ramifications.

The interpretation of Eq. (2.31) is illustrated in Fig. 2-4. At a hadronic scale $\mu_\Lambda \sim$
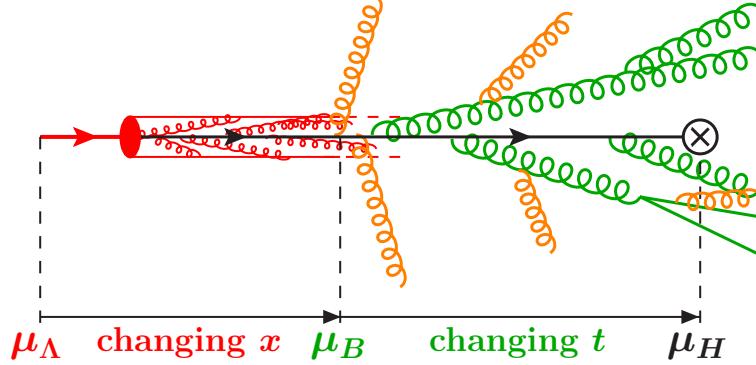
Figure 2-4: Evolution of the initial state. Starting from the low scale μ_Λ, the incoming proton is described by the x-dependent evolution of the PDFs, which redistributes the total momentum of the proton between its constituents. At the scale μ_B, the proton is probed by measuring the radiation in the final state and breaks apart. This is the scale where the PDFs are evaluated and the x-dependent evolution stops. Above μ_B, the proton has ceased to exist, and the initial state behaves like an incoming jet, whose evolution is governed by the virtuality t of the off-shell spacelike parton that eventually enters the hard interaction at the scale μ_H.

$1\,\mathrm{GeV}$, the initial conditions for the PDFs f_j can be specified, and one has the standard DGLAP evolution up to the scale μ_B,

$$\mu \frac{\mathrm{d}}{\mathrm{d}\mu} f_j(\xi, \mu) = \sum_{j'} \int \frac{\mathrm{d}\xi'}{\xi'} P_{jj'}\left(\frac{\xi}{\xi'}, \mu\right) f_{j'}(\xi', \mu) \,. \tag{2.32}$$

The anomalous dimensions $P_{jj'}$ are the standard QCD splitting functions for quarks, antiquarks, and gluons (including the color factors and coupling constant). Equation (2.31) applies at the scale $\mu = \mu_B$, since this is the scale at which a measurement on the proton is performed by observing the soft and collinear radiation contributing to $B^+_{a,b}$. At this scale, a parton j with momentum fraction ξ is taken out of the incoming proton according to the probability distribution $f_j(\xi, \mu)$. As the parton continues to propagate and evolve with $\mu > \mu_B$, it is modified by virtual radiation and by the emission of real radiation, which forms a jet. The evolution in this region no longer depends on ξ, but instead on the virtuality t. This evolution occurs with fixed x and fixed parton type i, via the beam function RGE

$$\mu \frac{\mathrm{d}}{\mathrm{d}\mu} B_i(t, x, \mu) = \int \mathrm{d}t' \, \gamma^i_B(t - t', \mu) \, B_i(t', x, \mu) \,. \tag{2.33}$$

This result for initial-state jet evolution has the same structure as the evolution for final-

state jets. In fact, the anomalous dimension γ_B^q is identical to that for the quark jet function to all orders in perturbation theory. We further discuss the renormalization of the beam function and prove this correspondence with the jet function in Sec. 3.2.

The effect of initial-state real and virtual radiation is described by the perturbatively calculable Wilson coefficients $\mathcal{I}_{ij}(t, x/\xi, \mu)$ at the scale $\mu = \mu_B$. They encode several physical effects. The virtual loop corrections contribute to the $\mathcal{I}_{ii}$ and modify the effective strength of the various partons. If the radiation is real, it has physical timelike momentum. Hence, it pushes the active parton in the jet off shell with spacelike virtuality $-t < 0$ and reduces its light-cone momentum fraction from ξ to x.

In addition, the real radiation can change the identity of the colliding parton, giving rise to the sum over j in Eq. (2.31). For example, an incoming quark can radiate an energetic gluon which enters the hard interaction, while the quark itself goes into the final state. This gives a contribution of the quark PDF to the gluon beam function through $\mathcal{I}_{gq}$. Similarly, an incoming gluon can pair-produce, with the quark participating in the hard interaction and the antiquark going into the final state. This gives a contribution of the gluon PDF to the quark beam function through $\mathcal{I}_{qg}$. There are also of course real radiation contributions to the diagonal terms, $\mathcal{I}_{qq}$ and $\mathcal{I}_{gg}$, where the parton in the PDF and the parton participating in the hard interaction have the same identity.

At lowest order in perturbation theory, the parton taken out of the proton directly enters the hard interaction without emitting radiation,

$$\mathcal{I}_{ij}^{\text{tree}}\left(t, \frac{x}{\xi}, \mu\right) = \delta_{ij} \, \delta(t) \, \delta\left(1 - \frac{x}{\xi}\right). \tag{2.34}$$

Thus at tree level, the beam function reduces to the PDF

$$B_i^{\text{tree}}(t, x, \mu) = \delta(t) \, f_i(x, \mu). \tag{2.35}$$

Beyond tree level, $\mathcal{I}_{ij}(t, x/\xi, \mu)$ can be determined perturbatively as discussed in more detail in Ch. 3, where we give precise field-theoretic definitions of the beam functions. We calculate the one-loop coefficients $\mathcal{I}_{ij}$ for the quark beam function in Ch. 4 and for the gluon beam function in Ch. 5.

Interestingly, in the threshold factorization theorem Eq. (2.9), cross terms between quark and gluon PDFs are power suppressed, so the gluon PDF does not contribute at leading

order. In the inclusive case Eq. (2.6), such cross terms are leading order in the power counting. For isolated Drell-Yan, there are no cross terms between quark and gluon beam functions, but there are leading-order cross terms between different PDFs, which appear via the contributions of different PDFs to a given beam function in Eq. (2.31). Thus, the isolated case is again in-between the inclusive and threshold cases.

2.4 Comparison with Initial-State Parton Shower

The physical situation associated with the beam evolution has an interesting correspondence with that of initial-state parton showers. As pictured in the region between μ_B and μ_H in Fig. 2-4, the parton in the beam function evolves forward in time while emitting a shower of radiation into the final state governed by the anomalous dimension $\gamma_B^i(t-t',\mu)$ in Eq. (2.33). This equation has no parton mixing. Each emission by the radiating parton increases the magnitude of its spacelike virtuality $-t < 0$, pushing it further off-shell in a spacelike direction. At the time the parton is annihilated in the hard collision, it has evolved to some t with $|t| \ll q^2$, so the large momentum transfer q^2 guarantees that no partons in the final state are spacelike. This description agrees quite well with the physical picture associated with the evolution of the primary parton in an initial-state parton shower, as summarized in Ref. [159].

Differences in the description arise when one considers the initial-state parton shower in more detail (for simplicity we focus on the so-called longitudinal evolution). The shower is based on the evolution equation for the PDFs in Eq. (2.32). An evolution forward in time is not practical because of the lack of prior knowledge of the scale of the hard interaction, so the shower uses backward evolution starting at a given partonic hard scale Q [158]. Knowing the identity of the final parton i, the shower evolves based on the probability $\mathrm{d}\mathcal{P}_i/\mathrm{d}t$ that parton i is unresolved into parton j via the splitting $j \to ij'$ at an earlier (lower) scale t. The evolution equation is [159]

$$\frac{\mathrm{d}\mathcal{P}_i(x, t_{\max}, t)}{\mathrm{d}t} = \left[\sum_{jj'} \int_x^{z_{\max}} \frac{\mathrm{d}z}{z} P_{j\to ij'}(z,t) \frac{f_j(x/z, t)}{f_i(x,t)} \right] \frac{1}{t} \mathcal{P}_i(x, t_{\max}, t), \qquad (2.36)$$

where $\mathcal{P}_i(x, t_{\max}, t)$ is the shower Sudakov exponential, which is interpreted as the probability for no emissions to occur between the initial value $t_{\max}$ and t. The evolution variable t,

which determines the scale of the splitting, is usually chosen as the virtuality or transverse momentum of the parton.

The mixing of partons in the PDF evolution influences the shower. In particular, the evolution kernel depends on the PDF $f_j(x/z, t)$, which determines the number density of partons of type j at the scale t, and inversely on the PDF $f_i(x, t)$. Thus, unlike in the beam evolution in Eq. (2.33), the shower evolution in Eq. (2.36) still knows the identity of the initial-state hadron. Double logarithms in the initial-state parton shower are generated in $q \to qg$ and $g \to gg$ splittings because of the soft-gluon singularity $\sim 1/(1-z)$ in the splitting functions. This singularity is regulated [159] by the upper cutoff $z_{\max} = x/(x+x_\epsilon)$, where x_ϵ provides a lower cutoff on the gluon energy in the rest frame of the hard scattering, $E_g \geq x_\epsilon \gamma E_{\rm cm}/2 \simeq 2\,{\rm GeV}$ (where γ is the boost factor of the hard scattering). Hence, one logarithm, $\ln x_\epsilon$, is generated by the z integration, and one logarithm, $\ln t$, by the collinear $1/t$ singularity. In contrast, the beam function contains double logarithms $\ln^2 t$ similar to a final-state parton shower, where the z integration yields a kernel $\sim (\ln t)/t$ that produces a double logarithm $\ln^2 t$ via the t evolution.

The above comparison is very rough. For example, the influence of soft radiation on both the shower and on the isolated factorization theorem was not compared and is likely to be important. Furthermore, the goal of the shower is to provide a universal method for populating fully exclusive final states, while the beam function applies for a more inclusive situation with a particular measurement. Note that just the presence of mixing in the initial-state parton shower and absence of mixing in the beam-function evolution does not imply an inconsistency. For example, it is well known that the final-state parton shower reproduces the correct double logarithms for e^+e^- event shapes [64], even though there is no parton mixing in the evolution of the corresponding hard, jet, and soft functions. In the future it would be interesting to test in detail the correspondence between the double logarithms generated by the initial-state parton shower and those predicted by our factorization theorem for the isolated Drell-Yan process.

2.5 Relation to Fixed-Order Calculation

The factorization theorem for the cross section in Eq. (2.16) and the factorization for the beam function in Eq. (2.31) together allow us to describe in more detail how various Feyn-
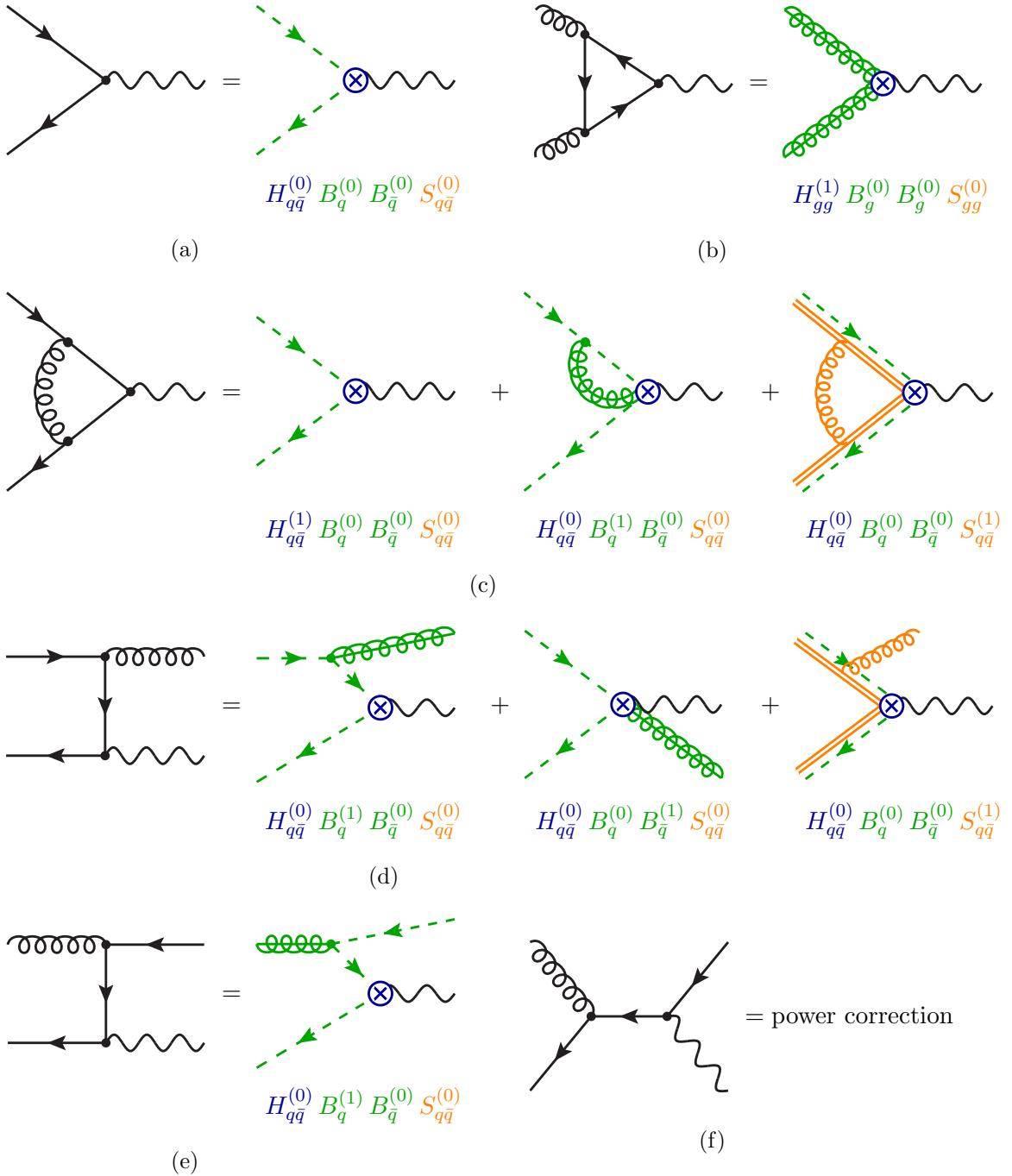
Figure 2-5: Factorization for isolated Drell-Yan in pictures. The left-hand side of each equality are graphs in QCD, while the right-hand side shows the sum of the corresponding SCET diagrams. Dashed lines are collinear quarks, and springs with a line through them are collinear gluons. The double lines denote soft Wilson lines, and the gluons attached to them are soft.

man diagrams that would appear in a fixed-order calculation contribute to the cross section in our kinematic region. Various examples are shown in Fig. 2-5.

In Fig. 2-5(a), we have the tree-level $q\bar{q}$ annihilation producing a γ or Z, which involves the tree-level $\mathcal{O}(\alpha_s^0)$ hard function, beam functions, and soft function, denoted by a superscript (0) in the figure. In Fig. 2-5(b), initial-state gluons couple to a quark loop (e.g. a top quark), which subsequently annihilates into a γ, Z, or Higgs. The quarks in this loop are far off shell, so they can be integrated out and appear as one-loop corrections, $H_{gg}^{(1)}$, to the hard coefficient in the factorization theorem. Other possibilities for this graph are power suppressed.

The situation for the vertex correction in Fig. 2-5(c) is more involved. If the gluon in the loop is hard, all particles in the loop are far off shell and can be integrated out, giving the one-loop hard function $H_{q\bar{q}}^{(1)}$ shown as the first term on the right-hand side. In the second term, the gluon is collinear to the incoming quark beam and gives a virtual one-loop contribution to the quark beam function, $B_q^{(1)}$. The third term is the analog of the second, but now with the gluon collinear to the incoming antiquark. Finally in the fourth term, the gluon is soft, communicating between the incoming collinear beams. Here, the eikonal approximation holds for describing the quark propagators. The generalization of this to all orders in α_s leads to the fact that the soft function is a matrix element of Wilson lines. Although a single loop graph contributes in several different places in the factorization theorem, all of these contributions have a precise separation in SCET. We will use this separation in Ch. 7 to prove the isolated Drell-Yan factorization theorem.

An interesting contribution occurs in Fig. 2-5(d), where a gluon is radiated into the final state. Because of the kinematic restrictions in isolated Drell-Yan, this gluon can only be collinear to the incoming quark, collinear to the incoming antiquark, or soft, and these three possibilities are represented by the diagrams on the right-hand side of the equality. In the first case, we have a real-emission correction to the quark beam function, $B_q^{(1)}$. In the second case, the intermediate quark is far off shell and can be integrated out, and the gluon collinear to the antiquark arises from a collinear Wilson line contribution in $B_{\bar{q}}^{(1)}$. The third case gives a real-emission correction to the soft function, $S_{q\bar{q}}^{(1)}$. The full-theory graph in Fig. 2-5(d) has a t-channel singularity. An important fact about the isolated Drell-Yan factorization theorem is that it fully captures the dominant parts of this singularity, and allows a simple framework for a resummation of higher order α_s corrections enhanced by large double logarithms due to this singularity. For threshold Drell-Yan, the kinematic restrictions are stronger and only allow the third graph with soft initial-state radiation. In

inclusive Drell-Yan, the gluon is treated as hard, and the graph in Fig. 2-5(d) only corrects $H_{q\bar{q}}^{\mathrm{incl}}$, without providing a framework for summing the large double logarithms that appear when we make a global measurement of the radiation in each hemisphere defined by the beams.

The situation is a bit simpler for Figs. 2-5(e) and 2-5(f). In Fig. 2-5(e), the incoming collinear gluon from the PDF pair-produces a quark and antiquark both collinear to this beam direction, and the quark enters the hard interaction. Therefore, this is a one-loop correction to the quark beam function, $B_q^{(1)}$, proportional to the gluon PDF f_g. The beam functions again allow us to resum the possibly large logarithms due to this t-channel singularity. Other possibilities for the final-state antiquark in Fig. 2-5(e) lead to power-suppressed contributions. Similarly, the s-channel graph in Fig. 2-5(f), which has the same initial and final states as Fig. 2-5(e), has no leading-power contribution and only contributes to Eq. (2.16) in the power-suppressed terms. The same is also true for Drell-Yan in the threshold region. Only inclusive Drell-Yan receives a leading-order hard contribution from the s-channel graph, which is then treated as of the same size as the t-channel graphs.

2.6   Renormalization Group Evolution

In this section, we discuss and compare the structure of large logarithms in the cross sections for inclusive, threshold, and isolated Drell-Yan. These large logarithms may be summed using the renormalization group evolution of the individual functions appearing in the factorization theorems. In fact, the structure of large logarithms in the differential $B_{a,b}^+$ cross section allows us to infer the necessity of the beam functions in the isolated factorization theorem. This procedure provides a method of determining whether beam functions enter for other observables or processes than those studied here. The consistency of the RGE was used to provide a similar consistency check in Ref. [93] when deriving a new factorization theorem for the invariant-mass distribution of jets initiated by a massive quark in e^+e^- collisions. In that case, the RGE consistency provided important constraints on the structure of the factorization theorem at scales below the heavy-quark mass.

In inclusive Drell-Yan, the hard functions H_{ij}^{incl} are sensitive to the scale $\mu_H \simeq Q$ of the hard interaction, and the proton mass defines a low scale $\mu_\Lambda \simeq 1\,\mathrm{GeV} \gtrsim \Lambda_{\mathrm{QCD}}$ (which is still large enough so perturbation theory can be applied for the PDF evolution). The
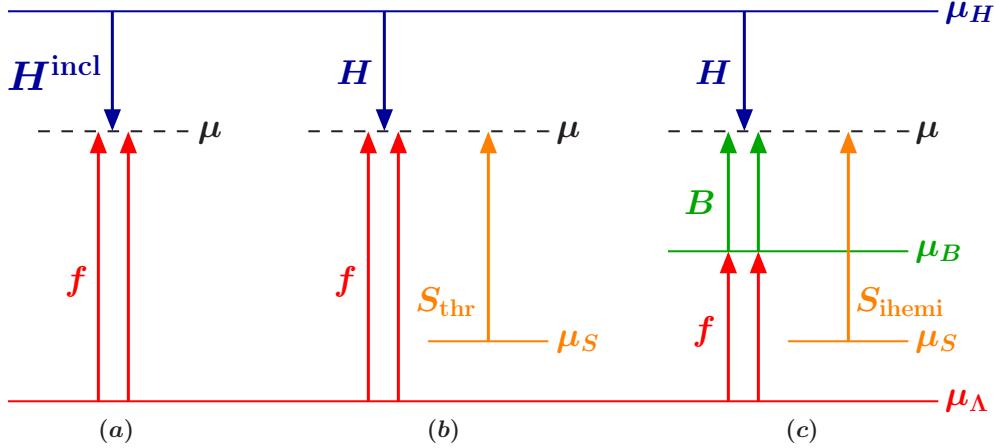
Figure 2-6: RGE running for different Drell-Yan scenarios. Case (a) corresponds to the inclusive case. Case (b) corresponds to the threshold case, where the kinematics forces all hadrons in the final state to be soft. Case (c) corresponds to the isolated case. Here, the PDFs freeze out at the intermediate beam scale μ_B, above which they are replaced by beam functions.

measurement of q^2 and Y in this case does not introduce additional scales, and thus does not influence the structure of the logarithms. Thus, we have the hierarchy $\mu_\Lambda \ll \mu_H$, and the large logarithms are $L = \ln(\mu_\Lambda/\mu_H)$. Here, only single-logarithmic series, $(\alpha_s L)^k$, are generated at higher orders in perturbation theory. The logarithms are factorized as $\ln(\mu/\mu_H) + \ln(\mu_\Lambda/\mu)$ in the factorization theorem in Eq. (2.6) and may then be resummed. The general form of the running is pictured in Fig. 2-6(a). The logarithms $\ln(\mu_\Lambda/\mu)$ are summed by evolving the PDFs $f_i(\xi_a, \mu)$ and $f_j(\xi_b, \mu)$ from μ_Λ up to the common scale μ. The inclusive hard function, $H^{\mathrm{incl}}(x_a/\xi_a, x_b/\xi_b, q^2, \mu)$, is evolved from μ_H down to μ, summing the logarithms $\ln(\mu/\mu_H)$. The choice of μ is arbitrary. Taking $\mu \simeq \mu_H$ corresponds to only running the PDFs up, while for $\mu \simeq \mu_\Lambda$ only H^{incl} runs down. The equivalence of these two choices implies that H^{incl} must be convoluted with the two PDFs and exhibit a factorized structure for logarithms in the a and b variables.

For threshold Drell-Yan, the kinematic restrictions only allow soft radiation in the final state. This induces additional large logarithms $\ln(1 - \tau)$. These can be written in terms of a ratio of scales $\ln(\mu_S/\mu_H)$, where the soft scale $\mu_S \simeq Q(1 - \tau)$ is another important scale in the analysis. The logarithms $L = \ln(\mu_S/\mu_H)$ appear as double-logarithmic series $(\alpha_s L^2)^k$ in the cross section. In the threshold factorization theorem in Eq. (2.9), these double logarithms can be summed by evolving the PDFs and the threshold soft and hard

functions, S_{thr} and H, to a common scale μ, as shown in Fig. 2-6(b). Since $\xi_{a,b} \to 1$, the logarithms $\ln(1 - \xi_a)$ and $\ln(1 - \xi_b)$ are also large. The RGE for the PDFs must be expanded, and the result sums a double-logarithmic series of $\ln^2(1-\xi)$ terms. The threshold soft function sums double logarithms $\ln^2(\mu/\mu_S)$ between μ_S and μ, while the threshold hard function sums double logarithms $\ln^2(\mu/\mu_H)$ between μ_H and μ. The RG equations are

$$
\mu \frac{\mathrm{d}}{\mathrm{d}\mu} H(q^2, \mu) = \gamma_H(q^2, \mu) \, H(q^2, \mu) \,,
$$
$$
\mu \frac{\mathrm{d}}{\mathrm{d}\mu} f_i(\xi, \mu) = \int \frac{\mathrm{d}\xi'}{\xi'} \, P_{ii}^{\text{expanded}} \left(\frac{\xi}{\xi'}, \mu \right) f_i(\xi', \mu) \,, \tag{2.37}
$$
$$
\mu \frac{\mathrm{d}}{\mathrm{d}\mu} S_{\text{thr}}(k, \mu) = \int \mathrm{d}k'_s \, \gamma_{S_{\text{thr}}}(k - k', \mu) \, S_{\text{thr}}(k', \mu) \,.
$$

The consistency of the RGE at the scale μ shown in Fig. 2-6(b) implies that the double logarithms in f_i, f_j, and S_{thr} combine in such a way that the RGE of the convolution $f_i f_j \otimes S_{\text{thr}}$ is identical to that of H, and hence only depends on q^2.

For isolated Drell-Yan, the kinematic restrictions allow both soft and collinear initial-state radiation, and induce an invariant-mass scale for each beam function, $\mu_B^2 \simeq x_a E_{\text{cm}} B_a^+$ and $\mu_B^2 \simeq x_b E_{\text{cm}} B_b^+$, and a soft scale $\mu_S \simeq B_{a,b}^+$. For simplicity, we use a common scale μ_B for both beam functions in our discussion here. (Since the evolution of the two beam functions is independent, one can just as easily implement two independent beam scales.) As we saw in Sec. 2.1, at partonic center-of-mass energies of a hundred GeV to a few TeV there is a large hierarchy between the different scales, $\mu_\Lambda \ll \mu_S \ll \mu_B \ll \mu_H$, and correspondingly large double and single logarithms of the ratios of these scales. The RGE running for this case is shown in Fig. 2-6(c). Here, the PDFs are not restricted to their endpoints, so their evolution is given by Eq. (2.32), which involves the unexpanded and nondiagonal $P_{ij}(\xi/\xi')$ and sums single logarithms, $(\alpha_s L)^k$. For each f_j this evolution joins at $\mu = \mu_B$ with the Wilson coefficients $\mathcal{I}_{ij}$ in the beam function factorization $B_i = \mathcal{I}_{ij} \otimes f_j$ of Eq. (2.31). The $\mathcal{I}_{ij}$ cancel the ξ-dependent evolution of f_j, and turn it into the t-dependent evolution of B_i, which sums a double-logarithmic series. The objects meeting at the common scale μ in Fig. 2-6(c) are the hard function (same as threshold case) and the beam and soft functions,

$$
\mu \frac{\mathrm{d}}{\mathrm{d}\mu} B_i(t, x, \mu) = \int \mathrm{d}t' \, \gamma_B^i(t - t', \mu) \, B_i(t', x, \mu) \,,
$$
$$
\mu \frac{\mathrm{d}}{\mathrm{d}\mu} S_{\text{ihemi}}(k_a^+, k_b^+, \mu) = \int \mathrm{d}k'_a \, \mathrm{d}k'_b \, S_{\text{ihemi}}(k_a^+, k_b^+, \mu) \gamma_{S_{\text{ihemi}}}(k_a^+ - k'_a, k_b^+ - k'_b, \mu) \,. \tag{2.38}
$$

The consistency of the RGE at μ now implies that the double-logarithmic running in the different variables for B_i, B_j, and S_{ihemi} cancels such that the convolution $B_i B_j \otimes S_{\text{ihemi}}$ has an RGE identical to H, which only depends on q^2. (A detailed discussion of this consistency can be found in Ref. [94] for the analogous case of two jet functions and the final-state hemisphere soft function, $JJ \otimes S_{\text{hemi}}$.) It is important that this cancellation would not be possible if we tried to replace B_i by f_i in the isolated factorization theorem. Given the type of double logarithms in the cross section, the single logarithms summed by the PDFs at generic x cannot combine with the double logarithms in S_{ihemi} to give a result in agreement with the double logarithms in H. Thus, the structure of double logarithms necessitates the presence of beam functions in the isolated factorization theorem.

By the same argument we can conclude that for all processes involving a threshold-type hard function H with double logarithms, and with $x_{a,b}$ away from one, the description of the initial-state radiation will require beam functions B_i. This includes all situations where H is the square of Wilson coefficients of SCET operators, $H = \sum_k |C_k|^2$ (for example when the energetic partons in the hard collision all have distinct collinear directions). In particular, the theoretical description of any threshold process with $x \to 1$ can be extended to a factorization theorem for the respective isolated case with x away from one. This is achieved by adding variables $B_{a,b}^+$, replacing the PDFs by beam functions, and replacing the threshold soft function by an appropriate soft function for the isolated case.

Thus, beam functions are quite prevalent for cross sections that one may wish to study at the LHC. In situations where the hadronic final state is constrained with variables that are more complicated than $B_{a,b}^+$, one generically expects to find different beam functions and different soft functions encoding these constraints. This extension is analogous to how the choice of jet algorithm modifies the definition of the jet and soft functions for central jets produced by the hard collision [32]. Even with this generalization, the beam and soft functions will both sum double-logarithmic series, and we expect that the factorization relating the beam function to the PDFs will carry through, just with different Wilson coefficients $\mathcal{I}_{ij}$.

Chapter 3

Beam Functions

We discuss several formal aspects of the quark and gluon beam functions in this chapter, which were first reported in Ref. [168]. The beam functions are defined in Sec. 3.1 as matrix elements of operators in SCET. We include a brief review of the necessary SCET ingredients. In Sec. 3.2 we work out the renormalization of the beam functions and show they have the same RGE as jet functions to all-orders in perturbation theory. We relate beam functions to PDFs in Sec. 3.3 by performing an OPE, and calculate the tree-level matching coefficients in Sec. 3.4. Finally, in Sec. 3.5 we discuss the analytic structure of the beam functions and derive a relationship with matrix elements of time-ordered products of fields. This allows us to use the usual Feynman rules when we calculate the beam functions in the next chapters.

3.1 Definition

In this section we discuss the definition of the quark and gluon beam functions in terms of matrix elements of operators in SCET, and compare them to the corresponding definition of the PDF. The operator language will be convenient to elucidate the renormalization structure and relation to jet functions in the following section.

We first discuss some SCET ingredients that are relevant later on. We introduce light-cone vectors n^μ and $\bar{n}^\mu$ with $n^2 = \bar{n}^2 = 0$ and $n \cdot \bar{n} = 2$ that are used to decompose four-vectors into light-cone coordinates $p^\mu = (p^+, p^-, p_\perp^\mu)$, where $p^+ = n \cdot p$, $p^- = \bar{n} \cdot p$ and $p_\perp^\mu$ contains the components perpendicular to n^μ and $\bar{n}^\mu$.

In SCET, the momentum p^μ of energetic collinear particles moving close to the n direc-

tion is separated into large and small parts

$$p^\mu = \tilde{p}^\mu + p_r^\mu = \bar{n} \cdot \tilde{p}\, \frac{n^\mu}{2} + \tilde{p}_{n\perp}^\mu + p_r^\mu \,. \tag{3.1}$$

The large part $\tilde{p}^\mu = (0, \tilde{p}^-, \tilde{p}_{n\perp})$ has components $\tilde{p}^- = \bar{n} \cdot \tilde{p}$ and $\tilde{p}_{n\perp} \sim \lambda \tilde{p}^-$, and the small residual piece $p_r^\mu = (p_r^+, p_r^-, p_{r\perp}^\mu) \sim \tilde{p}^-(\lambda^2, \lambda^2, \lambda^2)$ with $\lambda \ll 1$. The corresponding n-collinear quark and gluon fields are multipole expanded (with expansion parameter λ). This means particles with different large components are described by separate quantum fields, $\xi_{n,\tilde{p}}(y)$ and $A_{n,\tilde{p}}(y)$, which are distinguished by explicit momentum labels on the fields (in addition to the n label specifying the collinear direction). We use y to denote the position of the fields in the operators to reserve x for the parton momentum fractions.

Interactions between collinear fields cannot change the direction n but change the momentum labels to satisfy label momentum conservation. Since the momentum labels are changed by interactions, it is convenient to use the short-hand notations

$$\xi_n(y) = \sum_{\tilde{p} \neq 0} \xi_{n,\tilde{p}}(y)\,, \qquad A_n^\mu(y) = \sum_{\tilde{p} \neq 0} A_{n,\tilde{p}}^\mu(y)\,. \tag{3.2}$$

The sum over label momenta explicitly excludes the case $\tilde{p}^\mu = 0$ to avoid double-counting the soft degrees of freedom (described by separate soft quark and gluon fields). In practice when calculating matrix elements, this is implemented using zero-bin subtractions [140] or alternatively by dividing out matrix elements of Wilson lines [120, 134]. The dependence on the label momentum is obtained using label momentum operators $\overline{\mathcal{P}}_n$ or $\mathcal{P}_{n\perp}^\mu$ which return the sum of the minus or perpendicular label components of all n-collinear fields on which they act.

The decomposition into label and residual momenta is not unique. Although the explicit dependence on the vectors n^μ and $\bar{n}^\mu$ breaks Lorentz invariance, the theory must still be invariant under changes to n^μ and $\bar{n}^\mu$ which preserve the power counting of the different momentum components and the defining relations $n^2 = \bar{n}^2 = 0$, $n \cdot \bar{n} = 2$. This reparametrization invariance (RPI) [69, 139] can be divided into three types. RPI-I and RPI-II transformations correspond to rotations of n and $\bar{n}$. We will mainly use RPI-III under which n^μ and $\bar{n}^\mu$ transform as

$$n^\mu \to e^\alpha n^\mu\,, \qquad \bar{n}^\mu \to e^{-\alpha} \bar{n}^\mu\,, \tag{3.3}$$

62

which implies that the vector components transform as $p^+ \to e^\alpha p^+$ and $p^- \to e^{-\alpha} p^-$. In this way, the vector p^μ stays invariant and Lorentz symmetry is restored within a cone about the direction of n^μ. Since Eq. (3.3) only acts in the n-collinear sector, it is not equivalent to a spacetime boost of the whole physical system.

We now define the following bare operators

$$\widetilde{\mathcal{O}}_q^{\text{bare}}(y^-, \omega) = e^{-i\hat{p}^+ y^-/2} \, \bar{\chi}_n\left(y^- \frac{n}{2}\right) \frac{\bar{n}\!\!\!/}{2} \big[\delta(\omega - \overline{\mathcal{P}}_n)\chi_n(0)\big] \,,$$

$$\widetilde{\mathcal{O}}_{\bar{q}}^{\text{bare}}(y^-, \omega) = e^{-i\hat{p}^+ y^-/2} \, \text{tr}\left\{ \frac{\bar{n}\!\!\!/}{2} \chi_n\left(y^- \frac{n}{2}\right) \big[\delta(\omega - \overline{\mathcal{P}}_n)\bar{\chi}_n(0)\big]\right\} \,,$$

$$\widetilde{\mathcal{O}}_g^{\text{bare}}(y^-, \omega) = -\omega \, e^{-i\hat{p}^+ y^-/2} \, \mathcal{B}_{n\perp\mu}^c\left(y^- \frac{n}{2}\right) \big[\delta(\omega - \overline{\mathcal{P}}_n)\mathcal{B}_{n\perp}^{\mu c}(0)\big] \,. \qquad (3.4)$$

Their renormalization will be discussed in the next section. The corresponding renormalized operators are denoted as $\widetilde{\mathcal{O}}_i(y^-, \omega, \mu)$ and are defined in Eq. (3.21) below. Here, $\hat{p}^+$ is the momentum operator of the residual plus momentum and acts on everything to its right. The overall phase is included such that the Fourier-conjugate variable to y^- corresponds to the plus momentum of the initial-state radiation, see Eq. (3.9) below. The operator $\delta(\omega - \overline{\mathcal{P}}_n)$ only acts inside the square brackets and forces the total sum of the minus labels of all fields in $\chi_n(0)$ and $\mathcal{B}_{n\perp}(0)$ to be equal to ω. The color indices of the quark fields are suppressed and summed over, c is an adjoint color index that is summed over, and the trace in $\widetilde{\mathcal{O}}_{\bar{q}}$ is over spin. The operators are RPI-III invariant, because the transformation of the $\delta(\omega - \overline{\mathcal{P}}_n)$ is compensated by that of the $\bar{n}\!\!\!/$ in $\widetilde{\mathcal{O}}_{q,\bar{q}}$ and the overall ω in $\widetilde{\mathcal{O}}_g$.

The fields

$$\chi_n(y) = W_n^\dagger(y) \, \xi_n(y) \,, \qquad \mathcal{B}_{n\perp}^\mu = \frac{1}{g}\big[W_n^\dagger(y) \, iD_{n\perp}^\mu W_n(y)\big] \,, \qquad (3.5)$$

with $iD_{n\perp}^\mu = \mathcal{P}_{n\perp}^\mu + gA_{n\perp}^\mu$, are composite SCET fields of n-collinear quarks and gluons. In Eq. (3.4) they are at the positions $y^\mu = y^- n^\mu/2$ and $y^\mu = 0$. The Wilson lines

$$W_n(y) = \left[\sum_{\text{perms}} \exp\left(-\frac{g}{\overline{\mathcal{P}}_n} \, \bar{n}\!\cdot\! A_n(y)\right)\right] \qquad (3.6)$$

are required to make $\chi_n(y)$ and $\mathcal{B}_{n\perp}^\mu(y)$ gauge invariant with respect to collinear gauge transformations [31, 37]. They are Wilson lines in label momentum space consisting of $\bar{n}\!\cdot\! A_n(y)$ collinear gluon fields. They sum up arbitrary emissions of n-collinear gluons from

an n-collinear quark or gluon, which are $\mathcal{O}(1)$ in the SCET power counting. Since $W_n(y)$ is localized with respect to the residual position y, $\chi_n(y)$ and $\mathcal{B}^\mu_{n\perp}(y)$ are local operators for soft interactions. The fields in Eqs. (3.4) and (3.5) are those after the field redefinition [35] decoupling soft gluons from collinear particles. Thus at leading order in the power counting these collinear fields do not interact with soft gluons through their Lagrangian and no longer transform under soft gauge transformations. Hence, the operators in Eq. (3.4) are gauge invariant under both soft and collinear gauge transformations. The soft interactions with collinear particles are factorized into a soft function, which is a matrix element of soft Wilson lines (see Sec. 7.3.3).

Note that our fields in Eq. (3.4) have continuous labels and hence are not the standard SCET fields with discrete labels. They only depend on the minus coordinate, y^-, corresponding to the residual plus momentum, p_r^+, and not a full four-vector y^μ. As discussed in detail in the derivation of the factorization theorem in Ch. 7, it is convenient to absorb the residual minus and perpendicular components into the label momenta which then become continuous variables. For example, for the minus momentum (suppressing the perpendicular dependence)

$$\sum_{\tilde{p}^-} e^{-i\tilde{p}^- y^+/2} \chi_{n,\tilde{p}^-}(y^-,y^+) = \sum_{\tilde{p}^-} \int \mathrm{d}p_r^- \, e^{-i(\tilde{p}^- + p_r^-)y^+/2} \chi_{n,p^-}(y^-)$$

$$= \int \mathrm{d}p^- \, e^{-ip^- y^+/2} \chi_{n,p^-}(y^-) \, . \tag{3.7}$$

In this case, $W_n(y^- n/2)$ can also be written in position space where all gluon fields sit at the same residual minus coordinate, y^-, and are path ordered in the plus coordinate (corresponding to the label minus momentum) from y^+ to infinity.

Next, we introduce the Fourier-transformed operators

$$\mathcal{O}_i^{\text{bare}}(\omega b^+, \omega) = \frac{1}{2\pi} \int \frac{\mathrm{d}y^-}{2|\omega|} e^{ib^+ y^-/2} \, \widetilde{\mathcal{O}}_i^{\text{bare}}(y^-, \omega) \, . \tag{3.8}$$

For example, for the quark operator

$$\mathcal{O}_q^{\text{bare}}(\omega b^+, \omega) = \frac{1}{2\pi} \int \frac{\mathrm{d}y^-}{2|\omega|} e^{i(b^+ - \hat{p}^+)y^-/2} \left(e^{i\hat{p}^+ y^-/2} \bar{\chi}_n(0) e^{-i\hat{p}^+ y^-/2} \right) \frac{\bar{\slashed{n}}}{2} \left[\delta(\omega - \overline{\mathcal{P}}_n) \chi_n(0) \right]$$

$$= \bar{\chi}_n(0) \, \delta(\omega b^+ - \omega \hat{p}^+) \frac{\bar{\slashed{n}}}{2} \left[\delta(\omega - \overline{\mathcal{P}}_n) \chi_n(0) \right] \, . \tag{3.9}$$

In the first step we used residual momentum conservation to shift the position of the field. Here we see that the overall phase in Eq. (3.4) allows us to write the b^+ dependence in terms of $\delta(\omega b^+ - \omega \hat{p}^+)$, which means that b^+ measures the plus momentum of any intermediate state that is inserted between the fields. For the corresponding renormalized operators $\mathcal{O}_i(\omega b^+, \omega, \mu)$ see Eq. (3.22) below.

We divide by $|\omega|$ in Eq. (3.8) to make the integration measure of the Fourier transform RPI-III invariant. (Taking the absolute value $|\omega|$ ensures that the definition of the Fourier transform does not depend on the sign of ω.) As a result, the Fourier-transformed operators are still RPI-III invariant and only depend on b^+ through the RPI-III invariant combination $t = \omega b^+$. The beam functions are defined as the proton matrix elements of the renormalized operators $\mathcal{O}_i(t, \omega, \mu)$,

$$B_i(t, x = \omega/P^-, \mu) = \langle p_n(P^-) | \theta(\omega) \mathcal{O}_i(t, \omega, \mu) | p_n(P^-) \rangle. \tag{3.10}$$

The matrix elements are always averaged over proton spins, which we suppress in our notation. Note that part of the definition in Eq. (3.10) is the choice of the direction n such that the proton states have no perpendicular momentum, $P^\mu = P^- n^\mu/2$, which is why we write $|p_n(P^-)\rangle$. By RPI-III invariance, the beam functions can then only depend on the RPI-III invariant variables $t = \omega b^+$ and $x = \omega/P^-$. The restriction $\theta(\omega)$ on the right-hand side of Eq. (3.10) is included to enforce that the $\chi_n(0)$, $\bar{\chi}_n(0)$, or $\mathcal{B}_{n\perp}(0)$ fields annihilate a quark, antiquark, or gluon out of the proton, as we discuss further at the start of Sec. 3.5.

The definition of the beam functions can be compared with that of the quark and gluon PDFs. In SCET, the PDFs are defined [30] in terms of the RPI-III invariant operators

$$\begin{aligned}
\mathcal{Q}_q^{\text{bare}}(\omega') &= \theta(\omega') \, \bar{\chi}_n(0) \frac{\bar{\slashed{n}}}{2} \big[\delta(\omega' - \overline{\mathcal{P}}_n) \chi_n(0) \big], \\
\mathcal{Q}_{\bar{q}}^{\text{bare}}(\omega') &= \theta(\omega') \, \text{tr}\Big\{ \frac{\bar{\slashed{n}}}{2} \chi_n(0) \big[\delta(\omega' - \overline{\mathcal{P}}_n) \bar{\chi}_n(0) \big] \Big\}, \\
\mathcal{Q}_g^{\text{bare}}(\omega') &= -\omega' \theta(\omega') \, \mathcal{B}_{n\perp\mu}^c(0) \big[\delta(\omega' - \overline{\mathcal{P}}_n) \mathcal{B}_{n\perp}^{\mu c}(0) \big],
\end{aligned} \tag{3.11}$$

as the proton matrix elements of the corresponding renormalized operators $\mathcal{Q}_i(\omega', \mu)$ defined in Eq. (3.14) below,

$$f_i(\omega'/P^-, \mu) = \langle p_n(P^-) | \mathcal{Q}_i(\omega', \mu) | p_n(P^-) \rangle. \tag{3.12}$$

By RPI-III invariance, the PDFs can only depend on the momentum fraction $\xi = \omega'/P^-$. Beyond tree level ξ or ω' are not the same as x or ω, which is why we denote them differently. Without the additional $\theta(\omega')$ in the operators in Eq. (3.11) the quark and anti-quark PDFs would combine into one function, with the quark PDF corresponding to $\omega > 0$ and the antiquark PDF to $\omega < 0$. We explicitly separate these pieces to keep analogous definitions for the PDFs and beam functions.

It is important to note that the collinear fields in Eq. (3.11) do not require zero-bin subtractions, because as is well-known, the soft region does not contribute to the PDFs. If one makes the field redefinitions $\xi_n \to Y\xi_n$ and $A_n \to YA_nY^\dagger$ to decouple soft gluons, then the soft Wilson lines Y cancel in Eq. (3.11). Equivalently, if the fields in Eq. (3.11) include zero-bin subtractions then the subtractions will cancel in the sum of all diagrams, just like the soft gluons. (This is easy to see by formulating the zero-bin subtraction as a field redefinition [134] analogous to the soft one but with Wilson lines in a different light-cone direction.) In contrast, the collinear fields in the beam function operator in Eq. (3.4) must include zero-bin subtractions. We will see this explicitly at one loop in our PDF and beam function calculations in Ch. 4.

The SCET definitions of the PDFs are equivalent to the standard definition in terms of full QCD quark fields ψ in position space. For example, the quark PDF in QCD is defined as [74]

$$
f_q(\omega'/P^-,\mu) = \theta(\omega') \int \frac{\mathrm{d}y^+}{4\pi}\, e^{-i\omega'y^+/2} \Big\langle p_n(P^-) \Big| \Big[\bar{\psi}\Big(y^+\frac{\bar{n}}{2}\Big) W\Big(y^+\frac{\bar{n}}{2},0\Big) \frac{\slashed{\bar{n}}}{2}\psi(0) \Big]_\mu \Big| p_n(P^-) \Big\rangle .
$$
(3.13)

The square brackets denote the renormalized operator. Here, the fields are separated along the $\bar{n}$ direction and the lightlike Wilson line $W(y^+\bar{n}/2,0)$ is required to render the product of the fields gauge invariant. The relation to the SCET definition is that the SCET fields in Eq. (3.11) (without zero-bin subtractions) involve a Fourier transform of ψ in y^+ to give the conjugate variable ω'. The corresponding Wilson lines in Eq. (3.12) are precisely the W_n contained in the definitions of χ_n and $\mathcal{B}_{n\perp}^\mu$. Hence, the QCD and SCET definitions of the PDF are equivalent (provided of course that one uses the same renormalization scheme, which we do).

Comparing to Eq. (3.4), the difference between the beam functions and PDFs is that for the beam functions the fields are additionally separated along the n light-cone, with a large

66

separation $y^- \gg y^+$ corresponding to the small momentum $b^+ \ll \omega$. Thus, formulating equivalent definitions of the beam functions directly in QCD would be more challenging, as it would require QCD fields that are simultaneously separated in the n and $\bar{n}$ directions. For this case, it is not clear a priori how to obtain an unambiguous gauge-invariant definition, because Wilson lines connecting the fields along different paths are not equivalent. This ambiguity is resolved in SCET, where the multipole expansion distinguishes the different scales and divides the possible gauge transformations into global, collinear, and soft transformations, allowing one to treat the separations along the two orthogonal light-cones independently. The large y^- separation corresponds to soft Wilson lines and soft gauge transformations that are independent from collinear gauge transformations corresponding to the small y^+ dependence. As already mentioned, the operators in Eq. (3.4) are separately gauge invariant under both types of gauge transformations.

3.2   Renormalization and RGE

The beam functions and PDFs are defined as the matrix elements of renormalized operators. The renormalization of the operators immediately yields that of the functions defined by their matrix elements. In this section we derive the RG equations and show that the anomalous dimensions of the beam and jet functions are the same to all orders in perturbation theory.

We start by considering the known renormalization of the PDF, but in the SCET operator language. The renormalized PDF operators are given in terms of the bare operators in Eq. (3.11) as

$$\mathcal{Q}_i^{\text{bare}}(\omega) = \sum_j \int \frac{\mathrm{d}\omega'}{\omega'} \, Z_{ij}^f\Big(\frac{\omega}{\omega'},\mu\Big)\mathcal{Q}_j(\omega',\mu)\,. \tag{3.14}$$

In general, operators with different i and ω can (and will) mix into each other, so the renormalization constant $Z_{ij}^f(\omega/\omega',\mu)$ is a matrix in i,j and ω,ω'. RPI-III invariance then restricts the integration measure to be $\mathrm{d}\omega'/\omega'$ and $Z_{ij}^f(\omega/\omega',\mu)$ to only depend on the ratio ω/ω'. Hence, the form of Eq. (3.14) is completely specified by the SCET symmetries. The μ independence of the bare operators $\mathcal{Q}_i^{\text{bare}}(\omega)$ yields an RGE for the renormalized operators

in $\overline{\text{MS}}$

$$\mu \frac{\mathrm{d}}{\mathrm{d}\mu} \mathcal{Q}_i(\omega, \mu) = \sum_j \int \frac{\mathrm{d}\omega'}{\omega'} \gamma_{ij}^f \left(\frac{\omega}{\omega'}, \mu\right) \mathcal{Q}_j(\omega', \mu),$$

$$\gamma_{ij}^f(z, \mu) = -\sum_k \int \frac{\mathrm{d}z'}{z'} (Z^f)_{ik}^{-1} \left(\frac{z}{z'}, \mu\right) \mu \frac{\mathrm{d}}{\mathrm{d}\mu} Z_{kj}^f(z', \mu), \tag{3.15}$$

where the inverse $(Z^f)_{ik}^{-1}(z, \mu)$ is defined as

$$\sum_k \int \frac{\mathrm{d}z'}{z'} (Z^f)_{ik}^{-1} \left(\frac{z}{z'}, \mu\right) Z_{kj}^f(z', \mu) = \delta_{ij}\, \delta(1-z). \tag{3.16}$$

Taking the proton matrix element of Eq. (3.15) yields the RGE for the PDFs

$$\mu \frac{\mathrm{d}}{\mathrm{d}\mu} f_i(\xi, \mu) = \sum_j \int \frac{\mathrm{d}\xi'}{\xi'} \gamma_{ij}^f \left(\frac{\xi}{\xi'}, \mu\right) f_j(\xi', \mu). \tag{3.17}$$

The solution of this RGE can be written in terms of an evolution function U^f which acts on the initial PDF $f_j(\xi', \mu_0)$ and takes it to $f_i(\xi, \mu)$,

$$f_i(\xi, \mu) = \int \frac{\mathrm{d}\xi'}{\xi'} U_{ij}^f \left(\frac{\xi}{\xi'}, \mu, \mu_0\right) f_j(\xi', \mu_0). \tag{3.18}$$

From Eq. (3.17) we can identify the anomalous dimensions $\gamma_{ij}^f(z)$ in terms of the QCD splitting functions. For example, in dimensional regularization in the $\overline{\text{MS}}$ scheme, the one-loop anomalous dimensions for the quark PDF are the standard ones

$$\gamma_{qq}^f(z, \mu) = \frac{\alpha_s(\mu)C_F}{\pi} \theta(z) P_{qq}(z), \qquad \gamma_{qg}^f(z, \mu) = \frac{\alpha_s(\mu)T_F}{\pi} \theta(z) P_{qg}(z), \tag{3.19}$$

with the $q \to qg$ and $g \to q\bar{q}$ splitting functions

$$P_{qq}(z) = \mathcal{L}_0(1-z)(1+z^2) + \frac{3}{2}\delta(1-z) = \left[\theta(1-z)\frac{1+z^2}{1-z}\right]_+,$$

$$P_{qg}(z) = \theta(1-z)\left[(1-z)^2 + z^2\right]. \tag{3.20}$$

The plus distribution $\mathcal{L}_0(x) = [\theta(x)/x]_+$ is defined as usual, see Eq. (B.2). For later convenience we do not include the overall color factors in the definitions in Eq. (3.20).

We now go through an analogous discussion for the beam functions. The renormalized

operators $\widetilde{\mathcal{O}}_i(y^-, \omega, \mu)$ are given in terms of the bare operators in Eq. (3.4) by

$$\widetilde{\mathcal{O}}_i^{\text{bare}}(y^-, \omega) = \widetilde{Z}_B^i\left(\frac{y^-}{2\omega}, \mu\right) \widetilde{\mathcal{O}}_i(y^-, \omega, \mu),\tag{3.21}$$

where $\widetilde{Z}_B^i(y^-/2\omega, \mu)$ is the position-space renormalization constant. In App. C, we give an explicit proof that the beam function renormalization is multiplicative in this way to all orders in perturbation theory. The underlying reason is that the renormalization of the theory should preserve locality, so renormalizing the nonlocal beam function operator should not affect the y^- separation between the fields. For example, mixing between operators with different y^- would destroy locality at distance scales within the validity range of the effective theory. RPI-III invariance then implies that $\widetilde{Z}_B^i$ can only depend on the ratio $y^-/2\omega$ (the factor of $1/2$ is for convenience). In principle, one might think there could also be mixing between operators with different i or ω in Eq. (3.21) [as was the case for the PDFs in Eq. (3.14)]. Our derivation in App. C shows that this is not the case.

Taking the Fourier transform of Eq. (3.21) according to Eq. (3.8), we find

$$\mathcal{O}_i^{\text{bare}}(t, \omega) = \int \mathrm{d}t'\, Z_B^i(t - t', \mu)\, \mathcal{O}_i(t', \omega, \mu),$$
$$Z_B^i(t, \mu) = \frac{1}{2\pi} \int \frac{\mathrm{d}y^-}{2|\omega|}\, e^{ity^-/2\omega}\, \widetilde{Z}_B^i\left(\frac{y^-}{2\omega}, \mu\right).\tag{3.22}$$

Since the bare operator is μ independent, taking the derivative with respect to μ, we find the RGE for the renormalized operator

$$\mu\frac{\mathrm{d}}{\mathrm{d}\mu}\mathcal{O}_i(t, \omega, \mu) = \int \mathrm{d}t'\gamma_B^i(t - t', \mu)\, \mathcal{O}_i(t', \omega, \mu),$$
$$\gamma_B^i(t, \mu) = -\int \mathrm{d}t'\, (Z_B^i)^{-1}(t - t', \mu)\, \mu\frac{\mathrm{d}}{\mathrm{d}\mu}Z_B^i(t', \mu),\tag{3.23}$$

where the inverse of $Z_B^i(t, \mu)$ is defined as usual,

$$\int \mathrm{d}t'\, (Z_B^i)^{-1}(t - t', \mu)\, Z_B^i(t', \mu) = \delta(t).\tag{3.24}$$

Taking the proton matrix element of Eq. (3.23) we obtain the corresponding RGE for the beam function,

$$\mu\frac{\mathrm{d}}{\mathrm{d}\mu}B_i(t, x, \mu) = \int \mathrm{d}t'\, \gamma_B^i(t - t', \mu)\, B_i(t', x, \mu).\tag{3.25}$$

As discussed in App. C, to all orders in perturbation theory the anomalous dimension has the form

$$\gamma_B^i(t, \mu) = -2\Gamma_{\text{cusp}}^i(\alpha_s) \frac{1}{\mu^2} \mathcal{L}_0\left(\frac{t}{\mu^2}\right) + \gamma_B^i(\alpha_s)\,\delta(t)\,, \tag{3.26}$$

where $\mathcal{L}_0(x) = [\theta(x)/x]_+$ is defined in Eq. (B.2), $\Gamma_{\text{cusp}}^i(\alpha_s)$ is the cusp anomalous dimension for quarks/antiquarks ($i = q$) or gluons ($i = g$), and $\gamma_B^i(\alpha_s)$ denotes the non-cusp part. Since there is no mixing between operators $\mathcal{O}_i(t, \omega, \mu)$ with different i or ω, the beam function RGE only changes the virtuality t but not the momentum fraction x and does not mix quark and gluon beam functions. By rescaling the plus distribution,

$$\frac{1}{\mu^2}\mathcal{L}_0\left(\frac{t}{\mu^2}\right) = \frac{1}{\mu_0^2}\mathcal{L}_0\left(\frac{t}{\mu_0^2}\right) - 2\ln\frac{\mu}{\mu_0}\,\delta(t) \tag{3.27}$$

we can see that $\gamma_B^i(t, \mu)$ has logarithmic μ-dependence, which means that the RGE sums Sudakov double logarithms.

The solution of the RGE in Eq. (3.25) with the form of the anomalous dimension in Eq. (3.26) is known [26, 94, 151]. It takes the form

$$B_i(t, x, \mu) = \int dt'\, B_i(t - t', x, \mu_0)\, U_B^i(t', \mu_0, \mu)\,, \tag{3.28}$$

where the evolution kernel can be written as [135]

$$U_B^i(t, \mu_0, \mu) = \frac{e^{K_B^i - \gamma_E \eta_B^i}}{\Gamma(1 + \eta_B^i)}\left[\frac{\eta_B^i}{\mu_0^2}\mathcal{L}^{\eta_B^i}\left(\frac{t}{\mu_0^2}\right) + \delta(t)\right]. \tag{3.29}$$

The distribution $\mathcal{L}^\eta(x)$ is defined in Eq. (B.2), and the RGE functions $K_B^i \equiv K_B^i(\mu_0, \mu)$ and $\eta_B^i \equiv \eta_B^i(\mu_0, \mu)$ are given in Eq. (E.8).

The SCET quark, antiquark, and gluon jet functions are given by [35, 95]

$$J_q(\omega p^+ + \omega_\perp^2, \mu) \tag{3.30}$$

$$= \frac{(2\pi)^2}{N_c}\int \frac{dy^-}{2|\omega|}\, e^{ip^+ y^-/2}\, \text{tr}\left\langle 0\left| \left[\frac{\bar{\slashed{n}}}{2}\chi_n\left(y^-\frac{n}{2}\right)\left[\delta(\omega + \overline{\mathcal{P}}_n)\delta^2(\omega_\perp + \mathcal{P}_{n\perp})\bar{\chi}_n(0)\right]\right]_\mu\right|0\right\rangle,$$

$$J_{\bar{q}}(\omega p^+ + \omega_\perp^2, \mu)$$

$$= \frac{(2\pi)^2}{N_c}\int \frac{dy^-}{2|\omega|}\, e^{ip^+ y^-/2}\left\langle 0\left| \left[\bar{\chi}_n\left(y^-\frac{n}{2}\right)\frac{\bar{\slashed{n}}}{2}\left[\delta(\omega + \overline{\mathcal{P}}_n)\delta^2(\omega_\perp + \mathcal{P}_{n\perp})\chi_n(0)\right]\right]_\mu\right|0\right\rangle,$$

$$J_g(\omega p^+ + \omega_\perp^2, \mu)$$

$$= -\frac{(2\pi)^2}{N_c^2 - 1} \omega \int \frac{\mathrm{d}y^-}{2|\omega|} e^{\mathrm{i}p^+ y^- / 2} \left\langle 0 \left| \left[\mathcal{B}_{n\perp\mu}^c \left(y^- \frac{n}{2} \right) \left[\delta(\omega + \overline{\mathcal{P}}_n) \delta^2(\omega_\perp + \mathcal{P}_{n\perp}) \mathcal{B}_{n\perp}^{\mu c}(0) \right] \right]_\mu \right| 0 \right\rangle,$$

where the notation $[\ldots]_\mu$ again denotes the renormalized operators. Here, we used the same conventions as for the beam functions where the large label momenta ω and $\omega_\perp$ are continuous, so the only position dependence of the fields is in the minus component. RPI invariance requires that the jet function only depends on the total invariant mass of the jet, $p^2 = \omega p^+ + \omega_\perp^2$. When the jet function appears in a factorization theorem, the direction of the jet is either measured (e.g. by measuring the thrust axis in $e^+ e^- \to 2$ jets) or fixed by kinematics (e.g. in $B \to X_s \gamma$ the jet direction is fixed by the direction of the photon) and n is chosen along the jet direction, so one typically has $\omega_\perp = 0$. Taking the vacuum matrix element of $\mathcal{O}_q^{\mathrm{bare}}(t, \omega)$, we get

$$\frac{(2\pi)^2}{N_c} \langle 0 | \mathcal{O}_q^{\mathrm{bare}}(-t, -\omega) | 0 \rangle$$

$$= \frac{(2\pi)^2}{N_c} \int \mathrm{d}^2\omega_\perp \frac{1}{2\pi} \int \frac{\mathrm{d}y^-}{2|\omega|} e^{\mathrm{i}ty^- / (2\omega)} \left\langle 0 \left| \bar{\chi}_n \left(y^- \frac{n}{2} \right) \frac{\bar{\slashed{n}}}{2} \delta(\omega + \overline{\mathcal{P}}_n) \delta^2(\omega_\perp - \mathcal{P}_{n\perp}) \chi_n(0) \right| 0 \right\rangle$$

$$= \int \mathrm{d}^2\vec{\omega}_\perp J_{\bar{q}}^{\mathrm{bare}}(t - \vec{\omega}_\perp^2) \equiv \widehat{J}_{\bar{q}}^{\mathrm{bare}}(t) = \widehat{J}_q^{\mathrm{bare}}(t). \tag{3.31}$$

In the last step we used that the quark and antiquark jet functions are the same. The analogous relation holds for the antiquark operator, $\mathcal{O}_{\bar{q}}(t, \omega, \mu)$. The $\vec{\omega}_\perp$ integral is bounded and does not lead to new UV divergences, because the jet function only has support for nonnegative argument, $0 < \vec{\omega}_\perp^2 < t$, and t is fixed. Similarly, for the gluon operator we have

$$\frac{(2\pi)^2}{N_c^2 - 1} \langle 0 | \mathcal{O}_g^{\mathrm{bare}}(-t, -\omega) | 0 \rangle = \int \mathrm{d}^2\vec{\omega}_\perp J_g^{\mathrm{bare}}(t - \vec{\omega}_\perp^2, \mu) \equiv \widehat{J}_g^{\mathrm{bare}}(t). \tag{3.32}$$

The renormalization of $J_i^{\mathrm{bare}}(t)$ does not depend on the choice of $\omega_\perp$ in Eq. (3.30). Since $\widehat{J}_i^{\mathrm{bare}}(t)$ is simply an average over different choices for $\omega_\perp$ it has the same renormalization. Hence $J_i(t, \mu)$ and $\widehat{J}_i(t, \mu)$ have the same anomalous dimension,

$$\mu \frac{\mathrm{d}}{\mathrm{d}\mu} \widehat{J}_i(t, \mu) = \int \mathrm{d}^2\vec{\omega}_\perp \, \mathrm{d}s \, \gamma_J^i(t - \vec{\omega}_\perp^2 - s, \mu) \, J_i(s, \mu) = \int \mathrm{d}t' \gamma_J^i(t - t', \mu) \int \mathrm{d}^2\vec{\omega}_\perp \, J_i(t' - \vec{\omega}_\perp^2, \mu)$$

$$= \int \mathrm{d}t' \, \gamma_J^i(t - t', \mu) \, \widehat{J}_i(t', \mu). \tag{3.33}$$

On the other, Eq. (3.31) says that $\widehat{J}_i^{\mathrm{bare}}(t)$ is a matrix element of the same operator as the beam function, whose general renormalization was given in Eq. (3.22). We thus conclude that the beam and jet function anomalous dimensions are identical to all orders in perturbation theory,

$$\gamma_J^i(t,\mu) = \gamma_B^i(t,\mu). \tag{3.34}$$

For the cusp part this result already follows from our explicit one-loop calculation, since Γ_{cusp}^i is universal and its coefficients are the same at one loop. Our one-loop result provides a cross check for the identity of the one-loop non-cusp part of the anomalous dimension, which agree. Furthermore, $\gamma_J^q(\alpha_s)$ and hence $\gamma_B^q(\alpha_s)$ can be obtained to three loops from Refs. [147, 148], and for completeness the result is given in App. E.

3.3 Operator Product Expansion

The difference between the beam function operators in Eq. (3.4) and the PDF operators in Eq. (3.11) is the additional separation in the y^- coordinate between the fields. Hence, by performing an operator product expansion about the limit $y^- \to 0$ we can expand the renormalized operators $\widetilde{\mathcal{O}}_i(y^-, \omega, \mu)$ in terms of a sum over $\mathcal{Q}_i(\omega', \mu)$,

$$\widetilde{\mathcal{O}}_i(y^-, \omega, \mu) = \widetilde{J}_i\Big(\frac{y^-}{2\omega}, \mu\Big)1 + \sum_j \int \frac{\mathrm{d}\omega'}{\omega'} \widetilde{\mathcal{I}}_{ij}\Big(\frac{y^-}{2\omega}, \frac{\omega}{\omega'}, \mu\Big)\mathcal{Q}_j(\omega', \mu) + \mathcal{O}\Big(\frac{y^-}{\omega}\Big). \tag{3.35}$$

For completeness we included the identity operator on the right-hand side. The form of the matching coefficients $\widetilde{\mathcal{I}}_{ij}$ and $\widetilde{J}_i$ is again constrained by RPI-III invariance so the structure of the OPE is completely determined by the SCET symmetries.

Fourier transforming both sides of Eq. (3.35) with respect to y^- we get

$$\mathcal{O}_i(t, \omega, \mu) = \widehat{J}_i(-t, \mu)1 + \sum_j \int \frac{\mathrm{d}\omega'}{\omega'} \mathcal{I}_{ij}\Big(t, \frac{\omega}{\omega'}, \mu\Big)\mathcal{Q}_j(\omega', \mu) + \mathcal{O}\Big(\frac{y^-}{\omega}\Big). \tag{3.36}$$

Taking the vacuum matrix element of both sides, and using $\langle 0|\mathcal{Q}_j|0\rangle = 0$, we just get the coefficient of the identity operator on the right-hand side, which from Eqs. (3.31) and (3.32) is thus given by $\widehat{J}_i(-t, \mu)$. Taking the proton matrix element of Eq. (3.36) with $\omega > 0$ according to Eq. (3.10), this first term drops out, because the jet functions only have support for $-\omega > 0$ (or alternatively because the corresponding diagrams are disconnected),

72

and we obtain the OPE for the beam function

$$B_i(t, x, \mu) = \sum_j \int \frac{d\xi}{\xi} \mathcal{I}_{ij}\left(t, \frac{x}{\xi}, \mu\right) f_j(\xi, \mu) \left[1 + \mathcal{O}\left(\frac{\Lambda_{\mathrm{QCD}}^2}{t}\right)\right]. \tag{3.37}$$

For B_g this equation was already derived in Ref. [96] using a moment-space OPE for the matrix element (modulo missing the mixing contribution from the quark PDF). The higher-order power corrections in Eq. (3.37) must scale like $1/t$ and are therefore of $\mathcal{O}(\Lambda_{\mathrm{QCD}}^2/t)$ where Λ_{QCD}^2 is the typical invariant mass of the partons in the proton. (Equivalently, one can think of the scaling as $(\Lambda_{\mathrm{QCD}}^2/\omega)/b^+$ where $\Lambda_{\mathrm{QCD}}^2/\omega$ is the typical plus momentum of the parton in the proton.) They are given in terms of higher-twist proton structure functions. Since Eq. (3.36) is valid for $t \gg \Lambda_{\mathrm{QCD}}^2$, this also means that we can calculate the matching coefficients in perturbation theory at the beam scale $\mu_B^2 \simeq t$. This matching calculation is carried out in the usual way by computing convenient matrix elements of the operators on both sides of Eq. (3.36) and extracting the matching coefficients from the difference. This is carried out at tree level in the next section, while the full one-loop matching calculation for the quark beam function is given in Ch. 4 and for the gluon beam function in Ch. 5. On the other hand, for $t \sim \Lambda_{\mathrm{QCD}}^2$ the beam functions are nonperturbative and the OPE would require an infinite set of higher-twist proton structure functions. In this case, the beam functions essentially become nonperturbative b^+-dependent PDFs.

The physical interpretation of the beam function OPE in Eq. (3.37) leads exactly to the physical picture shown in Fig. 2-4 and discussed in the introduction. At the beam scale $\mu_B \simeq t$, the PDFs are evaluated and a parton j with momentum fraction ξ is taken out of the proton. It then undergoes further collinear interactions, which are described by the perturbative Wilson coefficients $\mathcal{I}_{ij}(t, z, \mu)$. By emitting collinear radiation it looses some of its momentum, and the final momentum fraction going into the hard interaction is $x < \xi$. In addition, the sum on j indicates that there is a mixing effect from terms without large logarithms, e.g. the quark beam function gets contributions from the quark, gluon, and antiquark PDFs. For example, when an incoming gluon from the proton pair-produces, with the quark participating in the hard interaction and the antiquark going into the beam remnant, then this is a mixing of the gluon PDF into the quark beam function. These are the physical effects that would usually be described by the PDF evolution. The difference is that once we are above the beam scale these effects only cause non-logarithmic perturbative

corrections, which means the parton mixing and x-reshuffling now appears in the matching, while the RG evolution of the beam function only changes t, as we saw above. In Ch. 6 we will see that these matching corrections are still important numerically and must be taken into account. For example, since the gluon PDF at small ξ is very large compared to the quark and antiquark PDFs, it still gives an important contribution to the quark and antiquark beam functions.

The consistency of the RGE requires that the μ dependence of the Wilson coefficients $\mathcal{I}_{ij}(t, z, \mu)$ turns the RG running of the PDFs into the proper RG running of the beam functions. Taking the μ derivative of Eq. (3.37) we find the evolution equation for the Wilson coefficients

$$\mu \frac{\mathrm{d}}{\mathrm{d}\mu} \mathcal{I}_{ij}(t, z, \mu) = \sum_k \int \mathrm{d}t' \frac{\mathrm{d}z'}{z'} \mathcal{I}_{ik}\left(t - t', \frac{z}{z'}, \mu\right) \left[\gamma_B^i(t', \mu)\, \delta_{kj}\delta(1 - z') - \delta(t')\gamma_{kj}^f(z', \mu)\right].$$

(3.38)

The solution to this RGE can be easily obtained in terms of the evolution factors for the PDF and beam function in Eqs. (3.18) and (3.29),

$$\mathcal{I}_{ij}(t, z, \mu) = \sum_k \int \mathrm{d}t' \frac{\mathrm{d}z'}{z'} \mathcal{I}_{ik}\left(t - t', \frac{z}{z'}, \mu_0\right) U_B^i(t', \mu_0, \mu)\, U_{kj}^f(z', \mu_0, \mu).$$

(3.39)

Hence as expected, the RGE running of $\mathcal{I}_{ij}(t, z, \mu)$ cancels the running of the PDFs and adds in the running of the beam function.

3.4 Tree-level Matching onto PDFs

To illustrate the application of the OPE, we will calculate the Wilson coefficients $\mathcal{I}_{ij}$ at tree level, starting with $\mathcal{I}_{qq}$. We can use any external states for the computation of the Wilson coefficient as long as they have nonzero overlap with our operator. Thus, we pick the simplest choice, n-collinear quark and gluon states, $|q_n(p)\rangle$ and $|g_n(p)\rangle$, with momentum $p^\mu = (p^+, p^-, 0)$ where $p^- > 0$ is the large momentum. In the following section we will use a small $p^+ < 0$ as an IR regulator, but otherwise p^+ is set to zero. The tree-level diagrams with an external quark for the quark PDF and beam function are shown in Figs. 3-1(a) and
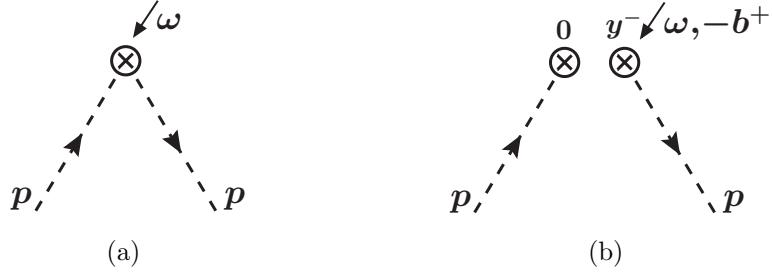
Figure 3-1: Tree-level diagram for the quark PDF (a) and the quark beam function (b). For the latter, the y^- coordinate separation in the operator is indicated by drawing separated vertices for each field.

3-1(b). They give

$$\big\langle q_n(p)\big|\mathcal{Q}_q(\omega',\mu)\big|q_n(p)\big\rangle^{(0)} = \theta(\omega')\,\bar{u}_n(p)\delta(\omega'-p^-)\frac{\slashed{\bar{n}}}{2}u_n(p) = \theta(\omega')\,\delta(1-\omega'/p^-)\,,$$

$$\big\langle q_n(p)\big|\mathcal{O}_q(t,\omega,\mu)\big|q_n(p)\big\rangle^{(0)} = \bar{u}_n(p)\,\delta(t)\,\delta(\omega-p^-)\frac{\slashed{\bar{n}}}{2}u_n(p) = \delta(t)\,\delta(1-\omega/p^-)\,. \qquad (3.40)$$

Here and in the following the superscript (i) indicates the $\mathcal{O}(\alpha_s^i)$ contribution. Note that the results in Eq. (3.40) are the same whether we use a state with fixed spin and color or whether we average over spin and color. Taking the matrix element of both sides of Eq. (3.36) and using Eq. (3.40), we can read off the tree-level matching coefficient

$$\mathcal{I}_{qq}^{(0)}(t,z,\mu) = \mathcal{I}_{\bar{q}\bar{q}}^{(0)}(t,z,\mu) = \delta(t)\,\delta(1-z)\,. \qquad (3.41)$$

Similarly, the tree-level results for the gluon PDF and beam function are

$$\big\langle g_n(p)\big|\mathcal{Q}_g(\omega',\mu)\big|g_n(p)\big\rangle^{(0)} = \theta(\omega')\,\delta(1-\omega'/p^-)\,,$$

$$\big\langle g_n(p)\big|\mathcal{O}_g(t,\omega,\mu)\big|g_n(p)\big\rangle^{(0)} = -\omega\,\varepsilon^*\!\cdot\!\varepsilon\,\delta(t)\,\delta(\omega-p^-) = \delta(t)\,\delta(1-\omega/p^-)\,, \qquad (3.42)$$

leading to

$$\mathcal{I}_{gg}^{(0)}(t,z,\mu) = \delta(t)\,\delta(1-z)\,. \qquad (3.43)$$

Since at tree level the quark (gluon) matrix elements of the gluon (quark) operators vanish,

$$\big\langle g_n(p)\big|\mathcal{Q}_g(\omega',\mu)\big|g_n(p)\big\rangle^{(0)} = \big\langle q_n(p)\big|\mathcal{Q}_q(\omega',\mu)\big|q_n(p)\big\rangle^{(0)} = 0\,,$$

$$\big\langle g_n(p)\big|\mathcal{O}_q(t,\omega,\mu)\big|g_n(p)\big\rangle^{(0)} = \big\langle q_n(p)\big|\mathcal{O}_g(t,\omega,\mu)\big|q_n(p)\big\rangle^{(0)} = 0\,, \qquad (3.44)$$

we obtain

$$\mathcal{I}_{qg}^{(0)}(t, z, \mu) = \mathcal{I}_{gq}^{(0)}(t, z, \mu) = 0 \,. \tag{3.45}$$

To summarize, the complete tree-level results are

$$\mathcal{I}_{ij}^{(0)}(t, z, \mu) = \delta_{ij}\delta(t)\,\delta(1 - z)\,, \qquad B_i^{(0)}(t, x, \mu) = \delta(t)f_i(x, \mu)\,. \tag{3.46}$$

The interpretation is simply that at tree level the parton taken out of the proton goes straight into the hard interaction. However, even at tree level the OPE already provides nontrivial information. From our general discussion we know that the matching should be performed at the beam scale $\mu_B^2 \simeq t$ to avoid large logarithms in the $\mathcal{O}(\alpha_s)$ terms, and this determines the scale at which the PDFs must be evaluated to be $\mu = \mu_B$.

3.5   Analytic Structure and Time-Ordered Products

In this section we discuss the analytic structure of the beam functions. For the OPE matching calculation we want to calculate partonic matrix elements of $\mathcal{O}_q(t, \omega, \mu)$. For this purpose it is convenient to relate the matrix elements of the products of fields in $\mathcal{O}_q(t, \omega, \mu)$ to discontinuities of matrix elements of time-ordered products of fields, since the latter are easily evaluated using standard Feynman rules. For notational simplicity we only consider the quark operator $\mathcal{O}_q(t, \omega)$ and suppress the spin indices and μ dependence. The discussion for the antiquark and gluon operators are analogous.

We are interested in the forward matrix element of $\mathcal{O}_q(t, \omega)$ between some n-collinear state $|p_n\rangle \equiv |p_n(p^+, p^-)\rangle$ with large momentum p^- and small residual momentum p^+. Inserting a complete set of states $\sum_X |X\rangle\langle X|$, we get

$$\langle p_n|\mathcal{O}_q(t, \omega)|p_n\rangle = \sum_X \Big\langle p_n\Big|\bar{\chi}_n(0)\frac{\slashed{\bar{n}}}{2}\,\delta(t - \omega\hat{p}^+)\Big|X\Big\rangle\langle X|\big[\delta(\omega - \overline{\mathcal{P}}_n)\chi_n(0)\big]|p_n\rangle \tag{3.47}$$

$$= \sum_X \delta(t - \omega p_X^+)\,\delta(\omega - p^- + p_X^-)\Big\langle p_n\Big|\bar{\chi}_n(0)\frac{\slashed{\bar{n}}}{2}\Big|X\Big\rangle\langle X|\chi_n(0)|p_n\rangle\,.$$

The $\delta(\omega - \overline{\mathcal{P}}_n)$ by definition only acts on the field inside the square bracket, returning its minus momentum, which by momentum conservation must be equal to the difference of the minus momenta of the external states. Since $\omega = p^- - p_X^-$, requiring $\omega > 0$ implies $p_X^- < p^-$. This means that the action of the field reduces the momentum of the initial state

so it effectively annihilates a parton in the initial state $|p_n\rangle$. Similarly, for $\omega < 0$ we would have $p_X^- > p^-$ and the field would effectively create an antiquark in $\langle X|$. Also, since $|X\rangle$ are physical states, we have $p_X^\pm \geq 0$ so $\omega \leq p^-$ and $t = \omega p_X^+$ and ω have the same sign.

Hence, for the beam function, where $|p_n\rangle \equiv |p_n(P^-)\rangle$ is the proton state, the restriction to $\omega > 0$ in its definition, Eq. (3.10), enforces that we indeed take a quark out of the proton. (Note that $\omega < 0$ does not correspond to the anti-quark beam function.) Taking the states $|X\rangle$ to be a complete set of physical hadronic states, the beam function has the physical support

$$ 0 < x < 1 - \frac{p_{X\min}^-}{P^-} < 1 \,, \qquad t > \omega\, p_{X\min}^+ > 0 \,, \tag{3.48} $$

where $p_{X\min}^\pm > 0$ are the smallest possible hadronic momenta (which are strictly positive because with an incoming proton $|X\rangle$ can neither be massless nor the vacuum state). For the jet function the external state is the vacuum $|p_n\rangle = |0\rangle$ yielding $\delta(\omega + p_X^-)$, so the matrix element in Eq. (3.47) vanishes for $\omega > 0$.

Next, consider the following time-ordered analog of $\langle p_n | \mathcal{O}_q(t, \omega) | p_n \rangle$,

$$ \langle p_n | T_q(\omega b^+, \omega) | p_n \rangle = \frac{1}{2\pi} \int \frac{\mathrm{d}y^-}{2|\omega|} \, e^{\mathrm{i}(b^+ - p^+)y^-/2} \Big\langle p_n \Big| T\Big\{ \bar{\chi}_n\Big(y - \frac{n}{2}\Big) \frac{\bar{\slashed{n}}}{2} \big[\delta(\omega - \overline{\mathcal{P}}_n)\chi_n(0) \big] \Big\} \Big| p_n \Big\rangle. \tag{3.49} $$

Writing out the time-ordering,

$$ T\Big\{ \bar{\chi}_n\Big(y - \frac{n}{2}\Big) \frac{\bar{\slashed{n}}}{2} \big[\delta(\omega - \overline{\mathcal{P}}_n)\chi_n(0) \big] \Big\} $$
$$ = \theta(y^-) \bar{\chi}_n\Big(y - \frac{n}{2}\Big) \frac{\bar{\slashed{n}}}{2} \big[\delta(\omega - \overline{\mathcal{P}}_n)\chi_n(0) \big] - \theta(-y^-)\big[\delta(\omega - \overline{\mathcal{P}}_n)\chi_n(0) \big] \bar{\chi}_n\Big(y - \frac{n}{2}\Big) \frac{\bar{\slashed{n}}}{2} \,, \tag{3.50} $$

using

$$ \theta(\pm y^-) = \frac{\mathrm{i}}{2\pi} \int \mathrm{d}\kappa \, \frac{e^{\mp \mathrm{i}\kappa y^-}}{\kappa + \mathrm{i}0} \,, \tag{3.51} $$

inserting a complete set of states, and translating the fields to spacetime position zero,

$$ \langle p_n | T_q(\omega b^+, \omega) | p_n \rangle $$
$$ = \frac{\mathrm{i}}{(2\pi)^2} \int \frac{\mathrm{d}y^-}{2|\omega|} \frac{\mathrm{d}\kappa}{\kappa + \mathrm{i}0} \sum_X \Big[e^{\mathrm{i}(b^+ - p_X^+ - \kappa)y^-/2} \, \delta(\omega - p^- + p_X^-) \Big\langle p_n \Big| \bar{\chi}_n(0) \frac{\bar{\slashed{n}}}{2} \Big| X \Big\rangle \langle X | \chi_n(0) | p_n \rangle $$
$$ + e^{\mathrm{i}(b^+ + p_X^+ + \kappa)y^-/2} \, \delta(\omega + p^- - p_X^-) \langle p_n | \chi_n(0) | X \rangle \Big\langle X \Big| \bar{\chi}_n(0) \frac{\bar{\slashed{n}}}{2} \Big| p_n \Big\rangle \Big] $$
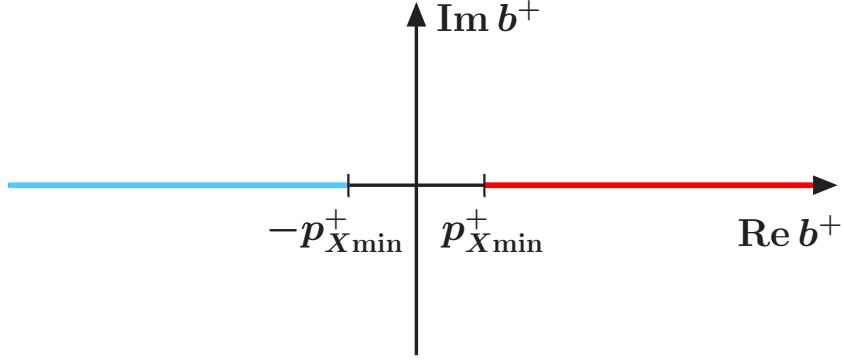
Figure 3-2: Cuts in the complex b^+ plane for the time-ordered product in Eq. (3.52).

$$
= \frac{\mathrm{i}}{2\pi|\omega|} \sum_X \left[\frac{\delta(\omega - p^- + p_X^-)}{b^+ - p_X^+ + \mathrm{i}0} \left\langle p_n \left| \bar{\chi}_n(0) \frac{\slashed{\bar{n}}}{2} \right| X \right\rangle \left\langle X \left| \chi_n(0) \right| p_n \right\rangle \right.
$$
$$
\left. - \frac{\delta(\omega + p^- - p_X^-)}{b^+ + p_X^+ - \mathrm{i}0} \left\langle p_n \left| \chi_n(0) \right| X \right\rangle \left\langle X \left| \bar{\chi}_n(0) \frac{\slashed{\bar{n}}}{2} \right| p_n \right\rangle \right] . \tag{3.52}
$$

The first term creates a cut in the complex b^+ plane for $b^+ \geq p_{X\min}^+$. This cut is shown as the dark red line in Fig. 3-2. The second term produces a cut at $b^+ \leq -p_{X\min}^+$, shown as the light blue line in Fig. 3-2.

The beam function matrix element in Eq. (3.47) can be identified as precisely the discontinuity of the first term in Eq. (3.52) with respect to b^+. Thus, for the beam function we have

$$
B_q(\omega b^+, \omega) = \mathrm{Disc}_{b^+ > 0} \left\langle p_n(P^-) \left| \theta(\omega) T_q(\omega b^+, \omega) \right| p_n(P^-) \right\rangle . \tag{3.53}
$$

Taking the discontinuity only for $b^+ > 0$ ensures that we only pick out the cut due to the first term in Eq. (3.52). Here, the discontinuity of a function $g(x)$ for $x > x_0$ is defined as

$$
\mathrm{Disc}_{x > x_0} g(x) = \lim_{\beta \to 0} \theta(x - x_0) \left[g(x + \mathrm{i}\beta) - g(x - \mathrm{i}\beta) \right] , \tag{3.54}
$$

and we used Eq. (B.7) to take the discontinuity of $1/(b^+ - p_X^+)$,

$$
\mathrm{Disc}_{b^+ > 0} \frac{\mathrm{i}}{2\pi|\omega|} \frac{1}{b^+ - p_X^+} = \frac{1}{|\omega|} \delta(b^+ - p_X^+) = \delta(\omega b^+ - \omega p_X^+) . \tag{3.55}
$$

Since we explicitly specify how to take the discontinuity, we can drop the i0 prescription in the denominators. (Alternatively, we could multiply by i and take the imaginary part using the i0 prescription.) Since we are eventually only interested in the case $\omega > 0$ anyway,

we may as well restrict the matrix elements to $\omega > 0$ from the very beginning and instead simply take the discontinuity in t for $t = \omega b^+ > 0$, so

$$\langle p_n | \theta(\omega) \mathcal{O}_q(t, \omega) | p_n \rangle = \mathrm{Disc}_{t>0} \langle p_n | \theta(\omega) T_q(t, \omega) | p_n \rangle. \tag{3.56}$$

For the matching calculation $|p_n\rangle$ is a partonic quark or gluon state. For any contributions with real radiation in the intermediate state, i.e. diagrams where the two χ_n or $\mathcal{B}_{n\perp}$ fields in the operator $\mathcal{O}_i$ are joined by a series of propagators and vertices, we can use the standard Feynman rules to evaluate the time-ordered matrix element of $T_q(t, \omega)$. However, with partonic external states, we can also have the vacuum state as an intermediate state, because the fields in the operator are spacetime separated. For such purely virtual contributions it is simpler to directly start from $\mathcal{O}_q(t, \omega)$, insert the vacuum state between the fields, and then use standard Feynman rules to separately compute the two pieces $\langle p_n | \bar{\chi}_n(0) \bar{\not{n}}/2 | 0 \rangle$ and $\langle 0 | \chi_n(0) | p_n \rangle$. In fact, this is exactly what we already did in our tree-level calculation in Sec. 3.4, and we will see another example in Ch. 4. Thus, we will obtain the total partonic matrix element as

$$\begin{aligned} \langle p_n | \theta(\omega) \mathcal{O}_q(t, \omega) | p_n \rangle &= \langle p_n | \theta(\omega) \mathcal{O}_q(t, \omega) | p_n \rangle_{\mathrm{virtual}} + \langle p_n | \theta(\omega) \mathcal{O}_q(t, \omega) | p_n \rangle_{\mathrm{radiation}} \\ &= \delta(t)\, \delta(\omega - p^-) \left\langle p_n \left| \bar{\chi}_n(0) \frac{\bar{\not{n}}}{2} \right| 0 \right\rangle_{\mathrm{connected}} \langle 0 | \chi_n(0) | p_n \rangle_{\mathrm{connected}} \\ &\quad + \mathrm{Disc}_{t>0} \langle p_n | \theta(\omega) T_q(t, \omega) | p_n \rangle_{\mathrm{connected}}. \end{aligned} \tag{3.57}$$

The virtual contribution must be kept, since it only looks superficially disconnected because the operator itself is spacetime separated. As always, we still disregard genuinely disconnected diagrams, e.g. diagrams involving vacuum bubbles, when calculating the matrix elements in the second line.

Chapter 4

The Quark Beam Function

In this chapter we compute the matching coefficients $\mathcal{I}_{qq}(t, z, \mu)$ and $\mathcal{I}_{qg}(t, z, \mu)$ in the OPE for the quark beam function to next-to-leading order in $\alpha_s(\mu)$, first reported in Ref. [168].

As explained in Sec. 3.3 and Sec. 3.4, the matching can be done by computing the partonic matrix elements of both sides of Eq. (3.36) to NLO. We use the same n-collinear quark and gluon states, $|q_n\rangle \equiv |q_n(p)\rangle$ and $|g_n\rangle \equiv |g_n(p)\rangle$, as in the tree-level matching in Sec. 3.4, with momentum $p^\mu = (p^+, p^-, 0)$. Since only $\mathcal{I}_{qq}(t, z, \mu)$ is nonzero at leading order, we will only need the NLO matrix elements of the quark operators, $\mathcal{O}_q(t, \omega, \mu)$ and $\mathcal{Q}_q(\omega, \mu)$. We will write all the matrix elements in terms of the RPI-III invariant variables

$$ t = b^+ \omega \,, \qquad t' = -p^+ \omega = -z p^+ p^- \,, \qquad z = \frac{\omega}{p^-} \,. \tag{4.1} $$

Here, z is the partonic momentum fraction of the quark annihilated by the operator relative to the momentum of the incoming quark or gluon, and will coincide with the argument of the Wilson coefficients $\mathcal{I}_{ij}(t, z, \mu)$.

To regulate the UV we use dimensional regularization with $d = 4 - 2\epsilon$ dimensions and renormalize using the $\overline{\text{MS}}$ scheme. Since the matching coefficients in the OPE must be IR finite, the matrix elements of $\mathcal{O}_q$ and $\mathcal{Q}_q$ must have the same IR divergences, i.e., the beam function must contain the same IR divergences as the PDF. To explicitly check that this is the case, we separate the UV and IR divergences by regulating the IR with a small $p^+ < 0$. This forces the external states to have a small offshellness $p^+ p^- < 0$, and since $p^+ p^- = -t'/z$ the IR divergences will appear as $\ln t'$. This also allows us to directly obtain the one-loop renormalization constants and anomalous dimensions for $\mathcal{O}_q$ and $\mathcal{Q}_q$ from their
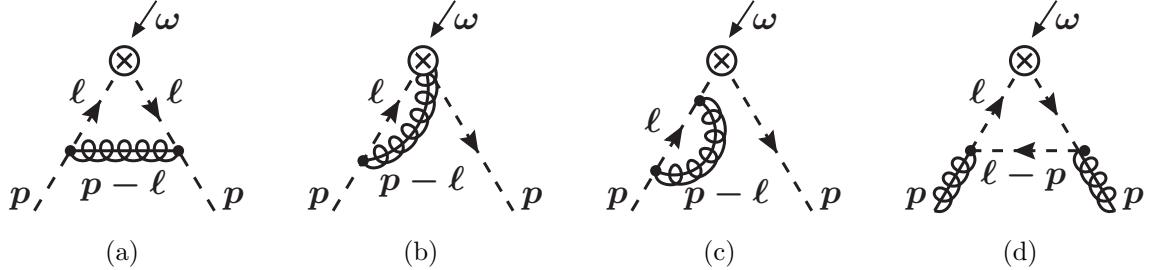
Figure 4-1: Nonzero one-loop diagrams for the quark PDF. The minus momentum ω enters the vertex through its outgoing fermion line and leaves through its incoming fermion line. Diagram (c) represents the inclusion of the wave-function renormalization constant for the renormalized fields together with the corresponding residue factor in the LSZ formula for the S-matrix. Diagrams (b) and (c) have symmetric counterparts which are included in their computation.

one-loop matrix elements.

We first compute the renormalized one-loop matrix elements of the quark PDF operator $\mathcal{Q}_q$ in Sec. 4.1. This calculation of the PDF for general x using the SCET operator definition and with an offshellness IR regulator is quite instructive, both by itself and in comparison to the beam function calculation, which is why we give it in some detail. In Sec. 4.2, we compute the renormalized one-loop matrix elements of the quark beam function operator $\mathcal{O}_q$. We use these results to extract expressions for $\mathcal{I}_{qq}(t, z, \mu)$ and $\mathcal{I}_{qg}(t, z, \mu)$ valid to NLO in Sec. 4.3.

Assuming that the IR divergences in the beam function and PDF will cancel, the matching calculation can be performed more easily using dimensional regularization for both UV and IR. We do this as an illustrative exercise in App. D, which, as it should, yields the same result for the matching coefficients.

4.1 Quark PDF with Offshellness IR Regulator

We start by calculating the bare S-matrix elements

$$\left\langle q_n(p) \middle| \mathcal{Q}_q^{\text{bare}}(\omega) \middle| q_n(p) \right\rangle, \qquad \left\langle g_n(p) \middle| \mathcal{Q}_q^{\text{bare}}(\omega) \middle| g_n(p) \right\rangle, \tag{4.2}$$

using Feynman gauge to compute the gauge-invariant sum of all diagrams. The relevant one-loop diagrams are shown in Fig. 4-1. Since $\mathcal{Q}_q$ is a local SCET operator, we can use the usual time-ordered Feynman rules in SCET (without any of the complications discussed in

Sec. 3.5 for $\mathcal{O}_q$). The collinear $q_n q_n g_n$ vertex factor is

$$\mathrm{i}g\, T^a V_n^\mu(p,\ell)\frac{\bar{\slashed{n}}}{2} \qquad \text{with} \qquad V_n^\mu(p,\ell) = n^\mu + \frac{\slashed{p}_\perp \gamma_\perp^\mu}{p^-} + \frac{\gamma_\perp^\mu \slashed{\ell}_\perp}{\ell^-} - \frac{\slashed{p}_\perp \slashed{\ell}_\perp}{p^- \ell^-}\bar{n}^\mu, \qquad (4.3)$$

where p^μ and ℓ^μ are the label momenta of the outgoing and incoming quark lines. (Because we have a single collinear direction the computation can also be done with QCD Feynman rules, still accounting for zero-bin subtractions, with the only difference being the Dirac algebra in the numerator of the loop integral. We checked that the final results for each diagram are indeed the same either way.)

The diagram in Fig. 4-1(a) is

$$\langle q_n | \mathcal{Q}_q^{\text{bare}}(\omega) | q_n \rangle^{(a)}$$
$$= -\mathrm{i}\left(\frac{e^{\gamma_E}\mu^2}{4\pi}\right)^\epsilon g^2 C_F \int \frac{\mathrm{d}^d\ell}{(2\pi)^d} \frac{\bar{u}_n(p) V_n^\mu(p,\ell) V_{n\mu}(\ell,p)\frac{\bar{\slashed{n}}}{2} u_n(p)(\ell^-)^2}{(\ell^2+\mathrm{i}0)^2[(\ell-p)^2+\mathrm{i}0]}\,\delta(\ell^- - \omega), \qquad (4.4)$$

where $g \equiv g(\mu)$ is the renormalized $\overline{\text{MS}}$ coupling. The Dirac algebra for the numerator gives

$$\bar{u}_n(p) V_n^\mu(p,\ell) V_{n\mu}(\ell,p)\frac{\bar{\slashed{n}}}{2} u_n(p)(\ell^-)^2 = \bar{u}_n(p)\gamma_\perp^\mu \slashed{\ell}_\perp \slashed{\ell}_\perp \gamma_{\perp\mu}\frac{\bar{\slashed{n}}}{2} u_n(p) = p^-(d-2)\ell_\perp^2. \qquad (4.5)$$

To compute the loop integral we write $\mathrm{d}^d\ell = \mathrm{d}\ell^+\mathrm{d}\ell^-\mathrm{d}^{d-2}\vec{\ell}_\perp/2$, where $\vec{\ell}_\perp$ is Euclidean, so $\ell_\perp^2 = -\vec{\ell}_\perp^2$. The ℓ^+ integral is done by contour integration as follows. For $\ell^- < 0$ all poles are above the axis and for $\ell^- > p^-$ all poles are below the axis, so both cases give zero. Hence, the ℓ^- integration range is restricted to $0 < \ell^- < p^-$, where there is a double pole below the axis from the $1/(\ell^2+\mathrm{i}0)^2$ and a single pole above the axis from the $1/[(\ell-p)^2+\mathrm{i}0]$. Taking the single pole above amounts to replacing the second denominator by $2\pi\mathrm{i}/(\ell^- - p^-)$ and setting $\ell^+ = p^+ - \vec{\ell}_\perp^2/(p^- - \ell^-)$ everywhere else. After performing the contour integral the i0 have served their purpose and can be set to zero everywhere. The ℓ^- integral is trivial using the $\delta(\ell^- - \omega)$ and turns the ℓ^- limits into an overall $\theta(\omega)\theta(p^- - \omega)$. The remaining $\vec{\ell}_\perp$ integration is done in $d - 2 = 2(1-\epsilon)$ Euclidean dimensions as usual. Putting everything together, we obtain

$$\langle q_n | \mathcal{Q}_q^{\text{bare}}(\omega) | q_n \rangle^{(a)}$$
$$= \left(\frac{e^{\gamma_E}\mu^2}{4\pi}\right)^\epsilon g^2 C_F\, \theta(\omega)\theta(p^- - \omega)\,\frac{(d-2)(p^- - \omega)}{4\pi\, p^-}\int \frac{\mathrm{d}^{d-2}\vec{\ell}_\perp}{(2\pi)^{d-2}}\,\frac{\vec{\ell}_\perp^2}{[\vec{\ell}_\perp^2 + (1-z)t']^2}$$

83

$$= \frac{\alpha_s(\mu)C_F}{2\pi}\,\theta(z)\theta(1-z)\,\Gamma(\epsilon)\Big(\frac{e^{\gamma_E}\mu^2}{t'}\Big)^{\epsilon}(1-z)^{1-\epsilon}(1-\epsilon)^2$$

$$= \frac{\alpha_s(\mu)C_F}{2\pi}\,\theta(z)\theta(1-z)\,(1-z)\Big\{\frac{1}{\epsilon} - \ln\frac{t'}{\mu^2} - \ln(1-z) - 2\Big\}, \qquad (4.6)$$

where in the last line we expanded in ϵ.

In the diagram in Fig. 4-1(b), the gluon is annihilated by the Wilson line inside one of the χ_n fields. The contraction with the one in $\bar{\chi}_n$ is $\propto \delta(\ell^- - \omega)$ and the contraction with the one in χ_n is $\propto \delta(p^- - \omega)$. The $1/\overline{\mathcal{P}}_n$ in the Wilson lines [see Eq. (3.6)] contributes a factor $1/(\ell^- - p^-)$ with a relative minus sign between the two contractions. (There is also a diagram where the gluon connects both Wilson lines which vanishes because the Wilson lines only contain $\bar{n}\cdot A$ gluons and we use Feynman gauge.) Adding Fig. 4-1(b) and its mirror graph, which gives an identical contribution, we get

$$\langle q_n|\mathcal{Q}_q^{\text{bare}}(\omega)|q_n\rangle^{(b)}$$

$$= 2\mathrm{i}\Big(\frac{e^{\gamma_E}\mu^2}{4\pi}\Big)^{\epsilon}g^2 C_F \int \frac{\mathrm{d}^d\ell}{(2\pi)^d}\,\frac{\bar{n}_\mu\bar{u}_n(p)V_n^{\mu}\frac{\slashed{\bar{n}}}{2}u_n(p)\ell^-}{(\ell^- - p^-)(\ell^2 + \mathrm{i}0)[(\ell-p)^2 + \mathrm{i}0]}\,[\delta(\ell^- - \omega) - \delta(p^- - \omega)]$$

$$= \frac{\alpha_s(\mu)C_F}{\pi}\,\Gamma(\epsilon)\Big(\frac{e^{\gamma_E}\mu^2}{-p^+p^-}\Big)^{\epsilon}\int \mathrm{d}\ell^-\,\theta(\ell^-)\,\theta(p^- - \ell^-)\frac{(\ell^-/p^-)^{1-\epsilon}}{(1-\ell^-/p^-)^{1+\epsilon}}\,[\delta(\ell^- - \omega) - \delta(p^- - \omega)]$$

$$= \frac{\alpha_s(\mu)C_F}{\pi}\,\Gamma(\epsilon)\Big(\frac{e^{\gamma_E}\mu^2}{t'}\Big)^{\epsilon}\Big\{\frac{\theta(z)\theta(1-z)z}{(1-z)^{1+\epsilon}} - \delta(1-z)\frac{\Gamma(2-\epsilon)\Gamma(-\epsilon)}{\Gamma(2-2\epsilon)}\Big\}. \qquad (4.7)$$

In the first step we used $\bar{n}_\mu V_n^\mu = 2$ and $\bar{u}_n(p)\slashed{n}u_n(p) = 2p^-$, performed the ℓ^+ integral by contours and did the $\vec{\ell}_\perp$ integral as usual. The ℓ^+ integral has the same pole structure as in Fig. 4-1(a) (except that the double pole at $\ell^+ = 0$ is now a single pole), which restricts the ℓ^- integral to the finite range $0 < \ell^- < p^-$. Expanding Eq. (4.7) in ϵ, using the distribution identity in Eq. (B.3), we get

$$\langle q_n|\mathcal{Q}_q^{\text{bare}}(\omega)|q_n\rangle^{(b)} = \frac{\alpha_s(\mu)C_F}{\pi}\,\Gamma(\epsilon)\Big(\frac{e^{\gamma_E}\mu^2}{t'}\Big)^{\epsilon}\Big\{\theta(z)\Big[-\frac{1}{\epsilon}\delta(1-z) + \mathcal{L}_0(1-z)z - \epsilon\mathcal{L}_1(1-z)z\Big]$$

$$+ \delta(1-z)\Big[\frac{1}{\epsilon} + 1 + \epsilon\Big(2 - \frac{\pi^2}{6}\Big)\Big]\Big\}$$

$$= \frac{\alpha_s(\mu)C_F}{\pi}\,\theta(z)\Big\{\Big(\frac{1}{\epsilon} - \ln\frac{t'}{\mu^2}\Big)\big[\mathcal{L}_0(1-z)z + \delta(1-z)\big] - \mathcal{L}_1(1-z)z$$

$$+ \delta(1-z)\Big(2 - \frac{\pi^2}{6}\Big)\Big\}, \qquad (4.8)$$

where $\mathcal{L}_n(x) = [\theta(x)(\ln^n x)/x]_+$ are the usual plus distributions defined in Eq. (B.2).

In the last step in Eq. (4.7), the ℓ^- integral produces an additional $1/\epsilon$ pole in each of the two terms corresponding to real and virtual radiation from the two different Wilson line contractions. It comes from the singularity at $\ell^- = p^-$, where the gluon in the loop becomes soft. (This soft IR divergence appears as a pole in ϵ because the offshellness only regulates the collinear IR divergence here.) The soft IR divergences cancel in the sum of the virtual and real contributions, as can be seen explicitly in the first line of Eq. (4.8) where the $1/\epsilon$ poles in curly brackets cancel between the two terms. One can already see this in the ℓ^- integral in Eq. (4.7), because for $\ell^- = p^-$ the two δ functions cancel so there is no soft divergence in the total integral. Thus, in agreement with our discussion in Sec. 3.1, we explicitly see that contributions from the soft region drop out in the PDF. As a consequence, the PDF only contains a single $1/\epsilon$ pole and correspondingly its RGE will sum single logarithms associated with this purely collinear IR divergence.

Since the gluon in the loop is supposed to be collinear, the soft gluon region must be explicitly removed from the collinear loop integral, which is the condition $\tilde{p} \neq 0$ in Eq. (3.2). For continuous loop momenta this is achieved by a zero-bin subtraction. However, since the soft region does not contribute to the PDF, it also does not require zero-bin subtractions in SCET. (If we were to include separate zero-bin subtractions for the virtual and real contributions, they would simply cancel each other.) We will see shortly that the situation for the beam function is quite different.

The last diagram with external quarks, Fig. 4-1(c), is

$$\langle q_n | \mathcal{Q}_q^{\text{bare}}(\omega) | q_n \rangle^{(c)} = \delta(1-z)(Z_\xi - 1) = -\frac{\alpha_s(\mu)C_F}{4\pi}\,\delta(1-z)\left\{\frac{1}{\epsilon} - \ln\frac{t'}{\mu^2} + 1\right\}. \quad (4.9)$$

Here we used the result for the one-loop on-shell wave-function renormalization with an offshellness IR regulator, which is the same in SCET and QCD.

Adding up the results in Eqs. (4.6), (4.8), and (4.9) we obtain for the bare one-loop quark matrix element

$$\langle q_n | \mathcal{Q}_q^{\text{bare}}(\omega) | q_n \rangle^{(1)} = \frac{\alpha_s(\mu)C_F}{2\pi}\,\theta(z)\Bigg\{\left(\frac{1}{\epsilon} - \ln\frac{t'}{\mu^2}\right)P_{qq}(z) - \mathcal{L}_1(1-z)(1+z^2)$$
$$+ \delta(1-z)\left(\frac{7}{2} - \frac{\pi^2}{3}\right) - \theta(1-z)2(1-z)\Bigg\}, \quad (4.10)$$

where

$$P_{qq}(z) = \mathcal{L}_0(1-z)(1+z^2) + \frac{3}{2}\delta(1-z) = \left[\theta(1-z)\frac{1+z^2}{1-z}\right]_+ \tag{4.11}$$

is the $q \to qg$ splitting function, see Eq. (3.20).

Next, we consider the matrix element of $\mathcal{Q}_q$ between gluon states $|g_n\rangle \equiv |g_n(p)\rangle$. The only relevant diagram is shown in Fig. 4-1(d),

$$\langle g_n|\mathcal{Q}_q^{\text{bare}}(\omega)|g_n\rangle^{(d)}$$
$$= \mathrm{i}\left(\frac{e^{\gamma_E}\mu^{2\epsilon}}{4\pi}\right)^\epsilon g^2 T_F \int \frac{\mathrm{d}^d\ell}{(2\pi)^d} \frac{(-\varepsilon_\mu^*\varepsilon_\nu)\mathrm{tr}\left[V_n^\mu V_n^\nu \frac{\bar{\not{n}}\not{n}}{4}\right](\ell^-)^2(\ell^- - p^-)}{(\ell^2 + \mathrm{i}0)^2[(\ell-p)^2 + \mathrm{i}0]}\delta(\ell^- - \omega). \tag{4.12}$$

Here $\varepsilon \equiv \varepsilon(p)$, $V_n^\mu \equiv V_n^\mu(\ell - p, \ell)$ and $V_n^\nu \equiv V_n^\nu(\ell, \ell - p)$. Since the physical polarization vector is perpendicular, $n \cdot \varepsilon(p) = \bar{n} \cdot \varepsilon(p) = 0$, we only need the perpendicular parts of the collinear vertices. The numerator then becomes

$$\mathrm{tr}\left[V_n^\mu V_n^\nu \frac{\bar{\not{n}}\not{n}}{4}\right](\ell^-)^2(\ell^- - p^-)$$
$$= \frac{1}{2}\mathrm{tr}\left[\left(\frac{\ell_\perp\gamma_\perp^\mu}{\ell^- - p^-} + \frac{\gamma_\perp^\mu\ell_\perp}{\ell^-}\right)\left(\frac{\ell_\perp\gamma_\perp^\nu}{\ell^-} + \frac{\gamma_\perp^\nu\ell_\perp}{\ell^- - p^-}\right)\right](\ell^-)^2(\ell^- - p^-)$$
$$= 2\frac{(p^-)^2}{\ell^- - p^-}\ell_\perp^2 g_\perp^{\mu\nu} + 8\ell^- \ell_\perp^\mu \ell_\perp^\nu = 2g_\perp^{\mu\nu}p^-\left(\frac{1}{1-z} - \frac{4z}{d-2}\right)\ell_\perp^2. \tag{4.13}$$

In the last step we used that under the integral we can replace $\ell^- = \omega = zp^-$ and $\ell_\perp^\mu \ell_\perp^\nu = \ell_\perp^2 g_\perp^{\mu\nu}/(d-2)$. The remaining loop integral is exactly the same as in Fig. 4-1(a), so the bare one-loop gluon matrix element becomes

$$\langle g_n|\mathcal{Q}_q^{\text{bare}}(\omega)|g_n\rangle^{(1)} = \frac{\alpha_s(\mu)T_F}{2\pi}\theta(z)\,\theta(1-z)\Gamma(\epsilon)\left(\frac{e^{\gamma_E}\mu^2}{t'}\right)^\epsilon(1-z)^{-\epsilon}(1-2z+2z^2-\epsilon)$$
$$= \frac{\alpha_s(\mu)T_F}{2\pi}\theta(z)\left\{\left[\frac{1}{\epsilon} - \ln\frac{t'}{\mu^2} - \ln(1-z)\right]P_{qg}(z) - \theta(1-z)\right\}. \tag{4.14}$$

Here

$$P_{qg}(z) = \theta(1-z)\,(1-2z+2z^2) \tag{4.15}$$

is the $g \to q\bar{q}$ splitting function from Eq. (3.20).

Note that the diagram analogous to Fig. 4-1(d) with the two gluons crossed can be obtained from Fig. 4-1(d) by taking $p^\mu \to -p^\mu$, which takes $z \to -z$. The limits resulting from the ℓ^+ integral are then $-1 \leq z \leq 0$ or $-p^- < \omega < 0$, and since we require $\omega > 0$

for $\mathcal{Q}_q$, this diagram vanishes. The diagram involving the SCET vertex with two collinear gluons vanishes because the ℓ^+ integral does not have poles on both sides of the axis.

From the bare matrix elements in Eqs. (4.10) and (4.14) we can obtain the renormalization of $\mathcal{Q}_q$. Taking parton matrix elements of Eq. (3.14) and expanding to NLO,

$$
\begin{aligned}
&\langle q_n | \mathcal{Q}_q^{\text{bare}}(\omega) | q_n \rangle^{(1)} \\
&= \sum_j \int \frac{\mathrm{d}\omega'}{\omega'} \left[Z_{qj}^{f(1)}\left(\frac{\omega}{\omega'}, \mu\right) \langle q_n | \mathcal{Q}_j(\omega', \mu) | q_n \rangle^{(0)} + Z_{qj}^{f(0)}\left(\frac{\omega}{\omega'}, \mu\right) \langle q_n | \mathcal{Q}_j(\omega', \mu) | q_n \rangle^{(1)} \right] \\
&= Z_{qq}^{f(1)}(z, \mu) + \langle q_n | \mathcal{Q}_q(\omega, \mu) | q_n \rangle^{(1)} , \\
&\langle g_n | \mathcal{Q}_q^{\text{bare}}(\omega) | g_n \rangle^{(1)} \\
&= \sum_j \int \frac{\mathrm{d}\omega'}{\omega'} \left[Z_{qj}^{f(1)}\left(\frac{\omega}{\omega'}, \mu\right) \langle g_n | \mathcal{Q}_j(\omega', \mu) | g_n \rangle^{(0)} + Z_{qj}^{f(0)}\left(\frac{\omega}{\omega'}, \mu\right) \langle g_n | \mathcal{Q}_j(\omega', \mu) | g_n \rangle^{(1)} \right] \\
&= Z_{qg}^{f(1)}(z, \mu) + \langle g_n | \mathcal{Q}_q(\omega, \mu) | g_n \rangle^{(1)} ,
\end{aligned} \tag{4.16}
$$

where we used the tree-level matrix elements in Eqs. (3.40) and (3.44) and $Z_{ij}^{f(0)}(z, \mu) = \delta_{ij}\, \delta(1 - z)$. The $\overline{\text{MS}}$ counter terms required to cancel the $1/\epsilon$ poles in the bare PDF matrix elements are then

$$
Z_{qq}^f(z) = \delta(1 - z) + \frac{1}{\epsilon} \frac{\alpha_s(\mu) C_F}{2\pi} \theta(z) P_{qq}(z) , \qquad Z_{qg}^f(z) = \frac{1}{\epsilon} \frac{\alpha_s(\mu) T_F}{2\pi} \theta(z) P_{qg}(z) . \tag{4.17}
$$

Expanding Eq. (3.15) to NLO, the one-loop anomalous dimensions are obtained by

$$
\gamma_{ij}^f(z, \mu) = -\mu \frac{\mathrm{d}}{\mathrm{d}\mu} Z_{ij}^{f(1)}(z, \mu) , \qquad \mu \frac{\mathrm{d}}{\mathrm{d}\mu} \alpha_s(\mu) = -2\epsilon\, \alpha_s(\mu) + \beta[\alpha_s(\mu)] , \tag{4.18}
$$

which with Eq. (4.17) yields the anomalous dimension for the quark PDF in Eq. (3.19),

$$
\gamma_{qq}^f(z, \mu) = \frac{\alpha_s(\mu) C_F}{\pi} \theta(z) P_{qq}(z) , \qquad \gamma_{qg}^f(z, \mu) = \frac{\alpha_s(\mu) T_F}{\pi} \theta(z) P_{qg}(z) . \tag{4.19}
$$

Finally, the renormalized NLO PDF matrix elements, which we will need for the matching computation in Sec. 4.3 below, are

$$
\begin{aligned}
\langle q_n | \mathcal{Q}_q(\omega, \mu) | q_n \rangle^{(1)} = -\frac{\alpha_s(\mu) C_F}{2\pi} \theta(z) \Bigg\{ &P_{qq}(z) \ln \frac{t'}{\mu^2} + \mathcal{L}_1(1 - z)(1 + z^2) \\
&- \delta(1 - z)\left(\frac{7}{2} - \frac{\pi^2}{3}\right) + \theta(1 - z) 2(1 - z) \Bigg\} ,
\end{aligned}
$$

87

$$\left\langle g_n \middle| \mathcal{Q}_q(\omega, \mu) \middle| g_n \right\rangle^{(1)} = -\frac{\alpha_s(\mu) T_F}{2\pi} \, \theta(z) \left\{ P_{qg}(z) \left[\ln \frac{t'}{\mu^2} + \ln(1-z) \right] + \theta(1-z) \right\}. \quad (4.20)$$

4.2 Quark Beam Function with Offshellness IR Regulator

Next, we calculate the bare beam function S-matrix elements,

$$\left\langle q_n(p) \middle| \theta(\omega) \mathcal{O}_q^{\mathrm{bare}}(t, \omega) \middle| q_n(p) \right\rangle, \qquad \left\langle g_n(p) \middle| \theta(\omega) \mathcal{O}_q^{\mathrm{bare}}(t, \omega) \middle| g_n(p) \right\rangle, \qquad (4.21)$$

to NLO. The corresponding one-loop diagrams are shown in Fig. 4-2. The matrix elements are calculated as explained in Sec. 3.5 in Eq. (3.57): For the virtual diagrams with vacuum intermediate state we explicitly insert the vacuum state, while for the real-emission diagrams we use Eq. (3.56). In the latter case, we first take the Disc, then expand in ϵ to extract the UV divergences, and at last take the $t' \to 0$ limit to isolate the IR divergences into $\ln t'$ terms. Some helpful formulas for calculating the discontinuity and taking the limit $t' \to 0$ are given in App. B.

For the beam function calculation the $p^+ < 0$ actually plays a dual role: For the UV divergent piece we can treat the calculation as in SCET$_\mathrm{I}$, and so $p^+ \sim b^+ \sim \lambda^2 p^-$, which allows us to explicitly check the structure of the convolution in Eq. (3.22). The renormalized result contributes to the matching onto PDFs, matching from SCET$_\mathrm{I}$ onto SCET$_\mathrm{II}$. In the matching, $-p^+ \ll b^+$ plays the role of the IR regulator, since we are required to use the same states as in the PDF calculation. We will see that the IR divergences $\ln t'$ match up with those present in the PDF calculation, and hence drop out in the coefficients $\mathcal{I}_{ij}$.

The diagrams in Fig. 4-2 have the same Dirac and propagator structure and overall factors as the corresponding PDF diagrams in Fig. 4-1, so we can reuse those parts from the previous section. The difference compared to the PDF calculation is that for the real-emission diagrams, instead of doing the ℓ^+ integral by contours, ℓ^+ is fixed by the additional δ function in b^+, and since we use time-ordered perturbation theory we must now take the discontinuity. This also alters the structure of the remaining $\vec{\ell}_\perp$ integral, for which we now use Feynman parameters to combine the denominators. After carrying out the $\vec{\ell}_\perp$ integration, we will need the following two Feynman parameter integrals

$$I_1(A, B, \epsilon) = \int_0^1 \mathrm{d}\alpha \, [(1-\alpha)A - \alpha B]^{-1-\epsilon} = \frac{(-B)^{-\epsilon} - A^{-\epsilon}}{\epsilon(A+B)}, \quad (4.22)$$
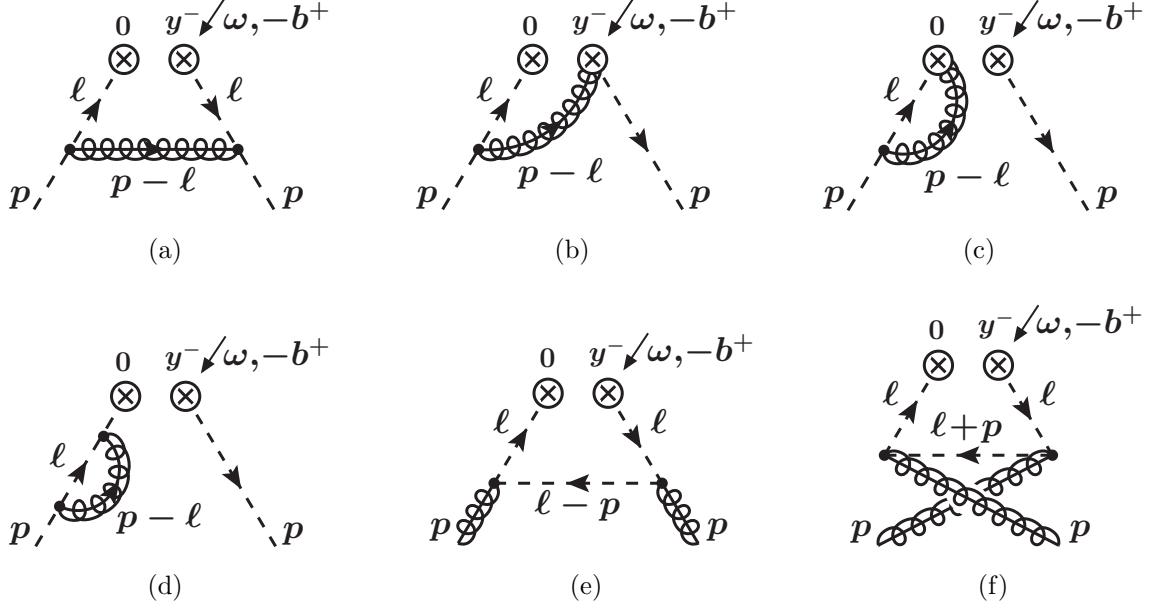
Figure 4-2: One-loop diagrams for the quark beam function. The minus momentum ω is incoming at the vertex and the b^+ momentum is outgoing. Diagram (d) denotes the wave-function contribution. Diagrams (b), (c), and (d) have symmetric counterparts which are equal to the ones shown and included in the computation. Diagram (f) and the diagram with the gluon connecting both vertices vanish.

$$I_2(A, B, \epsilon) = \int_0^1 d\alpha\,(1 - \alpha)[(1 - \alpha)A - \alpha B]^{-1-\epsilon} = -\frac{(-B)^{1-\epsilon} - A^{1-\epsilon}}{\epsilon(1 - \epsilon)(A + B)^2} - \frac{A^{-\epsilon}}{\epsilon(A + B)}\,.$$

The first diagram, Fig. 4-2(a), has real radiation in the final state, so we use Eq. (3.56)

$$\langle q_n | \theta(\omega)\mathcal{O}_q^{\text{bare}}(t, \omega) | q_n \rangle^{(a)}$$

$$= -\mathrm{i}\left(\frac{e^{\gamma_E}\mu^2}{4\pi}\right)^\epsilon g^2 C_F \frac{\theta(\omega)}{\omega} \operatorname{Disc}_{t>0} \int \frac{d^d\ell}{(2\pi)^d} \frac{p^-(d-2)\ell_\perp^2}{(\ell^2 + \mathrm{i}0)^2[(\ell - p)^2 + \mathrm{i}0]} \delta(\ell^- - \omega)\delta(\ell^+ + b^+ - p^+)$$

$$= -\mathrm{i}\left(\frac{e^{\gamma_E}\mu^2}{4\pi}\right)^\epsilon g^2 C_F \frac{\theta(z)(d-2)}{(2\pi)^2 z} \operatorname{Disc}_{t>0} \int_0^1 d\alpha \int \frac{d^{d-2}\vec{\ell}_\perp}{(2\pi)^{d-2}} \frac{(1 - \alpha)\,\vec{\ell}_\perp^2}{[\vec{\ell}_\perp^2 + (1 - \alpha)A - \alpha B]^3}$$

$$= \frac{\alpha_s(\mu)C_F}{2\pi} \frac{\theta(z)}{z} \Gamma(1 + \epsilon)(e^{\gamma_E}\mu^2)^\epsilon(1 - \epsilon)^2 \left[-\frac{\mathrm{i}}{2\pi}\operatorname{Disc}_{t>0} I_2(A, B, \epsilon)\right], \tag{4.23}$$

where we abbreviated

$$A = t + t', \qquad B = \frac{1 - z}{z} t, \qquad A + B = \frac{t}{z} + t'. \tag{4.24}$$

Since $t' > 0$ and $z > 0$, the only discontinuity in $I_2(A, B, \epsilon)$ for $t > 0$ arises from $(-B)$.

89

Using Eq. (B.7) to take the Disc, we obtain

$$-\frac{i}{2\pi}\text{Disc}_{t>0}\, I_2(A,B,\epsilon) = \frac{i}{2\pi}\text{Disc}_{t>0}\frac{(-B)^{1-\epsilon}}{\epsilon(1-\epsilon)(A+B)^2} = \theta(t)\frac{\sin\pi\epsilon}{\pi\epsilon(1-\epsilon)}\frac{\theta(B)B^{1-\epsilon}}{(A+B)^2},$$

$$= \theta\Big(\frac{1-z}{z}\Big)\theta(t)\frac{\sin\pi\epsilon}{\pi\epsilon(1-\epsilon)}\frac{[(1-z)t]^{1-\epsilon}z^{1+\epsilon}}{(t+zt')^2}. \tag{4.25}$$

Note that there is only a discontinuity for $B > 0$, so taking the discontinuity for $t > 0$ requires $(1-z)/z > 0$, and since $z > 0$ we obtain the expected limit $z < 1$. Since there are no UV divergences, we can let $\epsilon \to 0$, and Eq. (4.23) becomes

$$\langle q_n|\theta(\omega)\mathcal{O}_q^{\text{bare}}(t,\omega)|q_n\rangle^{(a)} = \frac{\alpha_s(\mu)C_F}{2\pi}\theta(z)\theta(1-z)(1-z)\frac{\theta(t)\,t}{(t+zt')^2}. \tag{4.26}$$

The above result has a collinear IR singularity for $t \to 0$ which is regulated by the nonzero t'. We can isolate the IR singularity using Eqs. (B.2) and (B.5) by letting $\beta \equiv zt'/\mu^2 \to 0$ while holding $\tilde{t} = t + zt'$ fixed[1],

$$\lim_{t'\to 0}\frac{\theta(t)\,t}{(t+zt')^2} = \lim_{zt'/\mu^2\to 0}\left[\frac{\theta(\tilde{t}-zt')}{\tilde{t}} - \frac{\theta(\tilde{t}-zt')zt'}{\tilde{t}^2}\right] = \frac{1}{\mu^2}\mathcal{L}_0\Big(\frac{\tilde{t}}{\mu^2}\Big) - \delta(\tilde{t})\Big(\ln\frac{zt'}{\mu^2}+1\Big). \tag{4.27}$$

The final result for Fig. 4-2(a) is thus

$$\langle q_n|\theta(\omega)\mathcal{O}_q^{\text{bare}}(t,\omega)|q_n\rangle^{(a)} = \frac{\alpha_s(\mu)C_F}{2\pi}\theta(z)\theta(1-z)(1-z)\left\{\frac{1}{\mu^2}\mathcal{L}_0\Big(\frac{\tilde{t}}{\mu^2}\Big) - \delta(\tilde{t})\Big(\ln\frac{zt'}{\mu^2}+1\Big)\right\}. \tag{4.28}$$

Next, we consider the real-emission diagram in Fig. 4-2(b). It corresponds to the $\delta(\ell^--\omega)$ term in Eq. (4.7). Together with its mirror graph, giving an identical contribution, we obtain

$$\langle q_n|\theta(\omega)\mathcal{O}_q^{\text{bare}}(t,\omega)|q_n\rangle^{(b)}$$

$$= 2i\Big(\frac{e^{\gamma_E}\mu^2}{4\pi}\Big)^{\epsilon}g^2 C_F\frac{\theta(\omega)}{\omega}\text{Disc}_{t>0}\int\frac{d^d\ell}{(2\pi)^d}\frac{2p^-\ell^-\,\delta(\ell^--\omega)\,\delta(\ell^++b^+-p^+)}{(\ell^--p^-)(\ell^2+i0)[(\ell-p)^2+i0]}$$

$$= \frac{\alpha_s(\mu)C_F}{\pi}\frac{\theta(z)}{1-z}\Gamma(1+\epsilon)(e^{\gamma_E}\mu^2)^{\epsilon}\Big[-\frac{i}{2\pi}\text{Disc}_{t>0}\, I_1(A,B,\epsilon)\Big]$$

$$= \frac{\alpha_s(\mu)C_F}{\pi}\theta(z)\Gamma(1+\epsilon)\Big(\frac{e^{\gamma_E}\mu^2}{t}\Big)^{\epsilon}\frac{\sin\pi\epsilon}{\pi\epsilon}\frac{\theta(t)}{t+zt'}\frac{\theta(1-z)z^{1+\epsilon}}{(1-z)^{1+\epsilon}}, \tag{4.29}$$

where in the second step we performed the loop integral as before, and in the last step we

---

[1]We keep the dependence on $\tilde{t}$ in our calculation as it will be useful for checking the structure of the renormalization in the following section.

used Eq. (B.7) to take the discontinuity. As for Fig. 4-2(a), the loop integral produces no UV divergence. However, as in the PDF calculation for Fig. 4-1(b), there is a soft gluon IR divergence at $z \to 1$ or $\ell^- \to p^-$ producing a $\delta(1-z)/\epsilon$ IR pole when expanding the last factor using Eq. (B.3). In contrast to the PDF calculation, the soft gluon region must now be explicitly excluded from the collinear loop integral. In dimensional regularization with an offshellness IR regulator the relevant zero-bin integral is scaleless and vanishes. Thus, including the zero-bin subtraction removes the $1/\epsilon$ IR divergence and replaces it by an equal $1/\epsilon$ UV divergence such that all $1/\epsilon$ poles in the final result are UV divergences. Expanding in ϵ, we have

$$\langle q_n | \theta(\omega) \mathcal{O}_q^{\text{bare}}(t, \omega) | q_n \rangle^{(b)} = \frac{\alpha_s(\mu) C_F}{\pi} \theta(z) \frac{\theta(t)}{t + zt'} \left\{ \delta(1-z) \left(-\frac{1}{\epsilon} + \ln \frac{t}{\mu^2} \right) + \mathcal{L}_0(1-z) z \right\},$$
(4.30)

and taking the same limit as in Eq. (4.27) to isolate the IR divergences,

$$\lim_{t' \to 0} \frac{\theta(t)}{t + zt'} = \lim_{zt'/\mu^2 \to 0} \frac{\theta(\tilde{t} - zt')}{\tilde{t}} = \frac{1}{\mu^2} \mathcal{L}_0 \left(\frac{\tilde{t}}{\mu^2} \right) - \delta(\tilde{t}) \ln \frac{zt'}{\mu^2}, \qquad (4.31)$$

$$\lim_{t' \to 0} \frac{\theta(t)}{t + zt'} \ln \frac{t}{\mu^2} = \lim_{zt'/\mu^2 \to 0} \frac{\theta(\tilde{t} - zt')}{\tilde{t}} \ln \frac{\tilde{t} - zt'}{\mu^2} = \frac{1}{\mu^2} \mathcal{L}_1 \left(\frac{\tilde{t}}{\mu^2} \right) - \delta(\tilde{t}) \left(\frac{1}{2} \ln^2 \frac{zt'}{\mu^2} + \frac{\pi^2}{6} \right),$$

the final result for Fig. 4-2(b) is

$$\langle q_n | \theta(\omega) \mathcal{O}_q^{\text{bare}}(t, \omega) | q_n \rangle^{(b)}$$

$$= \frac{\alpha_s(\mu) C_F}{\pi} \theta(z) \left\{ \left[\frac{1}{\mu^2} \mathcal{L}_0 \left(\frac{\tilde{t}}{\mu^2} \right) - \delta(\tilde{t}) \ln \frac{zt'}{\mu^2} \right] \left[-\frac{1}{\epsilon} \delta(1-z) + \mathcal{L}_0(1-z) z \right] \right.$$

$$\left. + \left[\frac{1}{\mu^2} \mathcal{L}_1 \left(\frac{\tilde{t}}{\mu^2} \right) - \delta(\tilde{t}) \left(\frac{1}{2} \ln^2 \frac{t'}{\mu^2} + \frac{\pi^2}{6} \right) \right] \delta(1-z) \right\}. \qquad (4.32)$$

For the diagram in Fig. 4-2(c) (and its mirror diagram) we insert the vacuum intermediate state between the fields in $\mathcal{O}_q$ as in Eq. (3.57), resulting in a one-loop virtual diagram involving a single field. The calculation is exactly the same as for the $\delta(p^- - \omega)$ term in Eq. (4.7) times an overall $\delta(t)$,

$$\langle q_n | \theta(\omega) \mathcal{O}_q^{\text{bare}}(t, \omega) | q_n \rangle^{(c)}$$

$$= -2\mathrm{i} \left(\frac{e^{\gamma_E} \mu^2}{4\pi} \right)^{\epsilon} g^2 C_F \, \delta(t) \delta(p^- - \omega) \int \frac{\mathrm{d}^d \ell}{(2\pi)^d} \frac{2p^- \ell^-}{(\ell^- - p^-)(\ell^2 + \mathrm{i}0)[(\ell - p)^2 + \mathrm{i}0]}$$

$$= -\frac{\alpha_s(\mu) C_F}{\pi} \Gamma(\epsilon) \left(\frac{e^{\gamma_E} \mu^2}{t'} \right)^{\epsilon} \delta(t) \delta(1-z) \frac{\Gamma(2-\epsilon) \Gamma(-\epsilon)}{\Gamma(2 - 2\epsilon)}$$

91

$$= \frac{\alpha_s(\mu)C_F}{\pi} \delta(\tilde{t})\delta(1-z)\left\{\frac{1}{\epsilon^2} + \frac{1}{\epsilon}\left(1 - \ln\frac{t'}{\mu^2}\right) + \frac{1}{2}\ln^2\frac{t'}{\mu^2} - \ln\frac{t'}{\mu^2} + 2 - \frac{\pi^2}{12}\right\}. \quad (4.33)$$

In the last step we expanded in ϵ and took the IR limit. To be consistent we have to use the same IR limit in the virtual diagrams as in the real-emission diagrams above, which simply turns the overall $\delta(t)$ into a $\delta(\tilde{t})$,

$$\lim_{t'\to 0}\delta(t) = \lim_{zt'/\mu^2\to 0}\delta(\tilde{t} - zt') = \delta(\tilde{t}). \quad (4.34)$$

As in the PDF calculation, the UV divergence in the loop produces a $\Gamma(\epsilon)$ and the soft IR divergence a $\Gamma(-\epsilon)$. The latter is converted by the zero-bin subtraction into a UV divergence, producing the $1/\epsilon^2$ pole. The $1/\epsilon^2$ poles do not cancel anymore between Figs. 4-2(b) and 4-2(c) as they did for the PDF in Fig. 4-1(b), because the phase space of the real emission in Fig. 4-2(b) is now restricted by the measurement of b^+ via the $\delta(\ell^+ + b^+ - p^+)$. For the same reason Fig. 4-2(a) has no UV divergence anymore, while Fig. 4-1(a) did. The $(1/\epsilon)\ln t'$ terms in Eqs. (4.32) and (4.33), which are a product of UV and collinear IR divergences, still cancel between the real and virtual diagrams, ensuring that the UV renormalization is independent of the IR, as should be the case.

The final one-loop contribution to the quark matrix element, Fig. 4-2(d) and its mirror diagram, comes from wave-function renormalization,

$$\langle q_n|\theta(\omega)\mathcal{O}_q^{\mathrm{bare}}(t,\omega)|q_n\rangle^{(d)} = \delta(t)\delta(1-z)(Z_\xi - 1)$$
$$= -\frac{\alpha_s(\mu)C_F}{4\pi}\delta(\tilde{t})\delta(1-z)\left\{\frac{1}{\epsilon} - \ln\frac{t'}{\mu^2} + 1\right\}. \quad (4.35)$$

Adding up the results in Eqs. (4.28), (4.32), (4.33), and (4.35), we obtain the bare beam function quark matrix element at one loop,

$$\langle q_n|\theta(\omega)\mathcal{O}_q^{\mathrm{bare}}(t,\omega)|q_n\rangle^{(1)} = \frac{\alpha_s(\mu)C_F}{2\pi}\theta(z)\left\{\left[\delta(\tilde{t})\left(\frac{2}{\epsilon^2} + \frac{3}{2\epsilon}\right) - \frac{2}{\epsilon}\frac{1}{\mu^2}\mathcal{L}_0\left(\frac{\tilde{t}}{\mu^2}\right)\right]\delta(1-z)\right.$$
$$+ \frac{2}{\mu^2}\mathcal{L}_1\left(\frac{\tilde{t}}{\mu^2}\right)\delta(1-z) + \frac{1}{\mu^2}\mathcal{L}_0\left(\frac{\tilde{t}}{\mu^2}\right)\mathcal{L}_0(1-z)(1+z^2) \quad (4.36)$$
$$\left. - \delta(\tilde{t})\left[P_{qq}(z)\ln\frac{zt'}{\mu^2} - \delta(1-z)\left(\frac{7}{2} - \frac{\pi^2}{2}\right) + \theta(1-z)(1-z)\right]\right\}.$$

We now consider the beam function matrix element with external gluons. The corresponding diagrams are shown in Figs. 4-2(e) and 4-2(f). For Fig. 4-2(e), which is analogous

to Fig. 4-1(d), we find

$$
\begin{aligned}
&\langle g_n | \theta(\omega) \mathcal{O}_q^{\mathrm{bare}}(t,\omega) | g_n \rangle^{(e)} \\
&= \mathrm{i} \Big(\frac{e^{\gamma_E} \mu^{2\epsilon}}{4\pi} \Big)^\epsilon g^2 T_F \frac{\theta(\omega)}{\omega} \, 2p^- \Big(\frac{1}{1-z} - \frac{4z}{d-2} \Big) \mathrm{Disc}_{t>0} \int \frac{\mathrm{d}^d \ell}{(2\pi)^d} \frac{\vec{\ell}_\perp^2 \, \delta(\ell^- - \omega) \delta(\ell^+ + b^+ - p^+)}{(\ell^2 + \mathrm{i}0)^2 [(\ell - p)^2 + \mathrm{i}0]} \\
&= \frac{\alpha_s(\mu) T_F}{2\pi} \frac{\theta(z)}{z} \, \Gamma(1+\epsilon)(e^{\gamma_E} \mu^2)^\epsilon \Big(\frac{1-\epsilon}{1-z} - 2z \Big) \Big[-\frac{\mathrm{i}}{2\pi} \mathrm{Disc}_{t>0} \, I_2(A, B, \epsilon) \Big] \\
&= \frac{\alpha_s(\mu) T_F}{2\pi} \theta(z) P_{qg}(z) \frac{\theta(t)t}{(t+zt')^2} \, .
\end{aligned}
\tag{4.37}
$$

The loop integral and discontinuity are exactly the same as for Fig. 4-2(a). The diagram in Fig. 4-2(f) does not contribute to the quark beam function. It can be obtained from Eq. (4.37) by replacing $p^\mu \to -p^\mu$, which takes $t' \to -t'$ and $z \to -z$. Doing so, the only contribution to the discontinuity is still from $B = -(1+z)t/z$ for $B > 0$, which for $t > 0$ requires $-1 < z < 0$. Hence, Fig. 4-2(f) does not contribute. Using Eq. (4.27) to take $t' \to 0$ in Eq. (4.37), we get the final result for the bare one-loop gluon matrix element

$$
\langle g_n | \theta(\omega) \mathcal{O}_q^{\mathrm{bare}}(t,\omega) | g_n \rangle^{(1)} = \frac{\alpha_s(\mu) T_F}{2\pi} \theta(z) P_{qg}(z) \Big\{ \frac{1}{\mu^2} \mathcal{L}_0 \Big(\frac{\tilde{t}}{\mu^2} \Big) - \delta(\tilde{t}) \Big(\ln \frac{zt'}{\mu^2} + 1 \Big) \Big\} \, .
\tag{4.38}
$$

As for Fig. 4-2(a), it has no UV divergences because of the measurement of b^+, which means that the renormalization does not mix $\mathcal{O}_q$ and $\mathcal{O}_g$.

4.3 Renormalization and Matching

Using the bare matrix elements calculated in the previous section, we can extract the renormalization of $\mathcal{O}_q$. We first take $\tilde{t} = t + zt' \to t$ in the bare matrix elements. Then, expanding the quark matrix element of Eq. (3.22) to one-loop order,

$$
\begin{aligned}
&\langle q_n | \mathcal{O}_q^{\mathrm{bare}}(t,\omega) | q_n \rangle^{(1)} \\
&= \int \mathrm{d}t' \Big[Z_B^{q(1)}(t-t',\mu) \langle q_n | \mathcal{O}_q(t',\omega,\mu) | q_n \rangle^{(0)} + Z_B^{q(0)}(t-t',\mu) \langle q_n | \mathcal{O}_q(t',\omega,\mu) | q_n \rangle^{(1)} \Big] \\
&= Z_B^{q(1)}(t,\mu) \, \delta(1-z) + \langle q_n | \mathcal{O}_q(t,\omega,\mu) | q_n \rangle^{(1)} \, ,
\end{aligned}
\tag{4.39}
$$

we can then read off the $\overline{\mathrm{MS}}$ renormalization constant from Eq. (4.36)

$$Z_B^q(t,\mu) = \delta(t) + \frac{\alpha_s(\mu)C_F}{2\pi}\left[\delta(t)\left(\frac{2}{\epsilon^2} + \frac{3}{2\epsilon}\right) - \frac{2}{\epsilon}\frac{1}{\mu^2}\mathcal{L}_0\left(\frac{t}{\mu^2}\right)\right]. \qquad (4.40)$$

The fact that the gluon matrix element is UV finite and the UV divergences in the quark matrix element are proportional to $\delta(1-z)$ confirms at one loop our general result that the renormalization of the beam function does not mix quarks and gluons or change the momentum fraction.

In Eqs. (4.39) and (4.40) we used that we already know the structure of the renormalization from our general arguments in Sec. 3.2, i.e. that Z_B^q only depends on the difference $t - t'$. Alternatively, we can also use the dependence on z and the finite dependence on t' via $\tilde{t}$ to explicitly check the structure of the renormalization. In this case, we must use the same IR limit also for the tree-level result in Eq. (3.40), which using Eq. (4.34) becomes

$$\left\langle q_n\big|\theta(\omega)\mathcal{O}_q(t,\omega,\mu)\big|q_n\right\rangle^{(0)} = \lim_{t'\to 0}\delta(t)\,\delta(1-z) = \delta(\tilde{t})\,\delta(1-z). \qquad (4.41)$$

Taking $Z_B^q(t,t',\omega/\omega',\mu)$ to be a general function of t, t' and ω/ω', we now get for Eq. (4.39)

$$\left\langle q_n\big|\mathcal{O}_q^{\mathrm{bare}}(t,\omega)\big|q_n\right\rangle^{(1)}$$
$$= \int \mathrm{d}t''\frac{\mathrm{d}\omega'}{\omega'}\,Z_B^{q(1)}\left(t,t'',\frac{\omega}{\omega'},\mu\right)\delta(t''+z't')\,\delta\left(1-\frac{\omega'}{p^-}\right) + \left\langle q_n\big|\mathcal{O}_q(t,\omega,\mu)\big|q_n\right\rangle^{(1)}$$
$$= Z_B^{q(1)}(t,-t',z) + \left\langle q_n\big|\mathcal{O}_q(t,\omega,\mu)\big|q_n\right\rangle^{(1)}. \qquad (4.42)$$

In the first step we used Eq. (4.41) and $Z_B^{q(0)}(t,t',z) = \delta(t-t')\delta(1-z)$. From Eq. (4.36) we now find

$$Z_B^q(t,t',z,\mu) = \left\{\delta(t-t') + \frac{\alpha_s(\mu)C_F}{2\pi}\left[\delta(t-t')\left(\frac{2}{\epsilon^2}+\frac{3}{2\epsilon}\right) - \frac{2}{\epsilon}\frac{1}{\mu^2}\mathcal{L}_0\left(\frac{t-t'}{\mu^2}\right)\right]\right\}\delta(1-z), \quad (4.43)$$

thus explicitly confirming at one loop that $Z_B^q(t,t',z,\mu) \equiv Z_B^q(t-t',\mu)\,\delta(1-z)$.

The one-loop anomalous dimension for the quark beam function follows from Eq. (4.40),

$$\gamma_B^q(t,\mu) = -\mu\frac{\mathrm{d}}{\mathrm{d}\mu}Z_B^{q(1)}(t,\mu) = \frac{\alpha_s(\mu)C_F}{\pi}\left[-\frac{2}{\mu^2}\mathcal{L}_0\left(\frac{t}{\mu^2}\right) + \frac{3}{2}\delta(t)\right]. \qquad (4.44)$$

It is identical to the one-loop anomalous dimension of the quark jet function. The coefficient

of $\mathcal{L}_0(t/\mu^2)/\mu^2$ can be identified as the one-loop expression for $-2\Gamma^q_{\rm cusp}$. Thus, Eq. (4.44) explicitly confirms the general results in Eqs. (3.26) and (3.34) at one loop.

Taking the bare matrix elements in Eqs. (4.36) and (4.38) and subtracting the UV divergences using Eqs. (4.39) and (4.40) gives the renormalized one-loop beam function matrix elements,

$$
\langle q_n|\theta(\omega)\mathcal{O}_q(t,\omega,\mu)|q_n\rangle^{(1)} = \frac{\alpha_s(\mu)C_F}{2\pi}\,\theta(z)\bigg\{\frac{2}{\mu^2}\mathcal{L}_1\Big(\frac{t}{\mu^2}\Big)\delta(1-z)+\frac{1}{\mu^2}\mathcal{L}_0\Big(\frac{t}{\mu^2}\Big)\mathcal{L}_0(1-z)(1+z^2)
$$
$$
- \delta(t)\bigg[P_{qq}(z)\ln\frac{zt'}{\mu^2}-\delta(1-z)\Big(\frac{7}{2}-\frac{\pi^2}{2}\Big)+\theta(1-z)(1-z)\bigg]\bigg\},
$$
$$
\langle g_n|\theta(\omega)\mathcal{O}_q(t,\omega,\mu)|g_n\rangle^{(1)} = \frac{\alpha_s(\mu)T_F}{2\pi}\,\theta(z)P_{qg}(z)\bigg\{\frac{1}{\mu^2}\mathcal{L}_0\Big(\frac{t}{\mu^2}\Big)-\delta(t)\Big(\ln\frac{zt'}{\mu^2}+1\Big)\bigg\}. \quad (4.45)
$$

For the matching onto the PDFs, we must take $t' \to 0$ and have therefore set $\tilde{t} = t$ everywhere, only keeping t' in the IR divergent $\ln t'$ terms.

Expanding the OPE for the quark beam function, Eq. (3.37), to one loop, we have

$$
\langle q_n|\theta(\omega)\mathcal{O}_q(t,\omega,\mu)|q_n\rangle^{(1)}
$$
$$
= \sum_j \int \frac{d\omega'}{\omega'}\bigg[\mathcal{I}^{(1)}_{qj}\Big(t,\frac{\omega}{\omega'},\mu\Big)\langle q_n|\mathcal{Q}_j(\omega',\mu)|q_n\rangle^{(0)} +\mathcal{I}^{(0)}_{qj}\Big(t,\frac{\omega}{\omega'},\mu\Big)\langle q_n|\mathcal{Q}_j(\omega',\mu)|q_n\rangle^{(1)}\bigg]
$$
$$
= \mathcal{I}^{(1)}_{qq}(t,z,\mu) + \delta(t)\langle q_n|\mathcal{Q}_q(\omega,\mu)|q_n\rangle^{(1)},
$$
$$
\langle g_n|\theta(\omega)\mathcal{O}_q(t,\omega,\mu)|g_n\rangle^{(1)}
$$
$$
= \sum_j \int \frac{d\omega'}{\omega'}\bigg[\mathcal{I}^{(1)}_{qj}\Big(t,\frac{\omega}{\omega'},\mu\Big)\langle g_n|\mathcal{Q}_j(\omega',\mu)|g_n\rangle^{(0)} +\mathcal{I}^{(0)}_{qj}\Big(t,\frac{\omega}{\omega'},\mu\Big)\langle g_n|\mathcal{Q}_j(\omega',\mu)|g_n\rangle^{(1)}\bigg]
$$
$$
= \mathcal{I}^{(1)}_{qg}(t,z,\mu) + \delta(t)\langle g_n|\mathcal{Q}_q(\omega,\mu)|g_n\rangle^{(1)}. \quad (4.46)
$$

Thus, the one-loop matching coefficients, $\mathcal{I}^{(1)}_{qi}(t,z,\mu)$, are obtained by subtracting the renormalized PDF matrix elements in Eq. (4.20) from those in Eq. (4.45). Doing so, we see that the $\ln t'$ IR divergences in Eqs. (4.20) and (4.45) precisely cancel, as they must, such that the matching coefficients are independent of the IR regulator and only involve large logarithms that are minimized at the scale $\mu^2 \simeq t$.

The final result for the NLO matching coefficients is given by

$$\mathcal{I}_{qq}(t, z, \mu) = \delta(t)\,\delta(1-z) \tag{4.47}$$
$$+ \frac{\alpha_s(\mu)C_F}{2\pi}\,\theta(z)\left\{\frac{2}{\mu^2}\mathcal{L}_1\left(\frac{t}{\mu^2}\right)\delta(1-z) + \frac{1}{\mu^2}\mathcal{L}_0\left(\frac{t}{\mu^2}\right)\left[P_{qq}(z) - \frac{3}{2}\delta(1-z)\right]\right.$$
$$\left. + \delta(t)\left[\mathcal{L}_1(1-z)(1+z^2) - \frac{\pi^2}{6}\delta(1-z) + \theta(1-z)\left(1 - z - \frac{1+z^2}{1-z}\ln z\right)\right]\right\},$$
$$\mathcal{I}_{qg}(t, z, \mu) = \frac{\alpha_s(\mu)T_F}{2\pi}\,\theta(z)\left\{\frac{1}{\mu^2}\mathcal{L}_0\left(\frac{t}{\mu^2}\right)P_{qg}(z) + \delta(t)\left[P_{qg}(z)\left(\ln\frac{1-z}{z} - 1\right) + \theta(1-z)\right]\right\}.$$

Chapter 5

The Gluon Beam Function

In this chapter we compute the matching coefficients for the gluon beam function at one loop. We determine the renormalization group equation for the gluon beam function and verify that its anomalous dimension equals that of the gluon jet function. These calculations will appear in Ref. [48].

The matrix element which defines the gluon beam function first appeared in Ref. [96] and was named the gluon beam function in Ref. [166]. In Ref. [142] the impact-parameter gluon beam function was introduced, which differs from the gluon beam function in Eqs. (3.4) and (3.10) because the Lorentz indices on the two $\mathcal{B}_{n\perp}^{\mu}$ fields are not contracted and the fields have an additional separation in the residual perpendicular coordinate $y_\perp$. In Refs. [96] and [142] only the matching onto gluon PDFs was considered and there is a discrepancy in one of the terms. Our results agree with those presented in [142] and we also determine the matching onto quark PDFs.

In our calculation we will regularize both the UV and the IR using dimensional regularization and employ the $\overline{\text{MS}}$ renormalization scheme. To perform the renormalization of the beam function and calculate the matching coefficients we replace the external proton states by free quarks or gluons, as was explained in Sec. 3.2 for the tree-level matching. In our partonic calculations we will abbreviate the matrix element notation used in the calculation of the quark beam function in Ch. 4 by writing $f_{i/j}(z,\mu)$ and $B_{i/j}(t,z,\mu)$ to indicate that the proton is replaced by a parton of type j in the PDF or beam functions, i.e.

$$B_{g/j}(\omega b^+, \omega/p^-) = -\theta(\omega) \int \frac{dy^-}{4\pi} \, e^{ib^+ y^-/2} \Big\langle j_n(p^-) \Big| \mathcal{B}_{n\perp\mu}^c \Big(y^- \frac{n}{2} \Big) \delta(\omega - \overline{\mathcal{P}}_n) \, \mathcal{B}_{n\perp}^{c\,\mu}(0) \Big| j_n(p^-) \Big\rangle,$$

$$f_{g/j}(\omega'/p^-) = -\theta(\omega')\omega' \left\langle j_n(p^-) \Big| \mathcal{B}^c_{n\perp\mu}(0)\, \delta(\omega' - \overline{\mathcal{P}}_n)\, \mathcal{B}^{c\,\mu}_{n\perp}(0) \Big| j_n(p^-) \right\rangle. \tag{5.1}$$

We start in Sec. 5.1 with recalling the known results for the partonic PDF for our choice of regulator and scheme. In Sec. 5.2 we list the necessary Feynman rules, for which we introduce some shorthand notation. We calculate the one-loop gluon beam function in Sec. 5.3 and extract the results in Sec. 5.4.

5.1 The Gluon PDF at One Loop

At tree level the partonic PDF is normalized to

$$f^{(0)}_{i/j}(z,\mu) = \delta_{ij}\,\delta(1-z)\,. \tag{5.2}$$

The renormalization of the PDF in the $\overline{\text{MS}}$ scheme is given by

$$f^{\text{bare}}_i(\xi) = \sum_j \int \frac{\mathrm{d}\xi'}{\xi'}\, Z^f_{ij}\left(\frac{\xi}{\xi'},\mu\right) f_j(\xi',\mu) = \sum_j \int \frac{\mathrm{d}z}{z}\, Z^f_{ij}(z,\mu) f_j\left(\frac{\xi}{z},\mu\right), \tag{5.3}$$

where we sum over parton species $j = q, \bar{q}, g$, and the entries in the matrix Z^f are a series of $1/\epsilon$ poles with coefficients in terms of the renormalized coupling $\alpha_s(\mu)$. At one-loop, the results for the standard gluon PDF are [9],

$$
\begin{aligned}
Z^f_{gg}(z,\mu) &= \delta(1-z) + \frac{1}{\epsilon}\frac{\alpha_s(\mu)}{2\pi}\,\theta(z)\left[C_A P_{gg}(z) + \frac{1}{2}\beta_0\,\delta(1-z)\right], \\
Z^f_{gq}(z,\mu) &= \frac{1}{\epsilon}\frac{\alpha_s(\mu)C_F}{2\pi}\,\theta(z)\,P_{gq}(z)\,,
\end{aligned}
\tag{5.4}
$$

where $\beta_0 = (11C_A - 4n_f T_f)/3$, is the lowest order coefficient of the QCD β function. The splitting functions are given by

$$
\begin{aligned}
P_{gg}(z) &= 2\mathcal{L}_0(1-z)z + 2\theta(1-z)\left[\frac{1-z}{z} + z(1-z)\right] \\
&= 2\theta(1-z)\left[\frac{z}{(1-z)_+} + \frac{1-z}{z} + z(1-z)\right], \\
P_{gq}(z) &= \theta(1-z)\,\frac{1+(1-z)^2}{z}\,.
\end{aligned}
\tag{5.5}
$$

We will extract the one-loop partonic gluon PDF from the above results. With our

Figure 5-1: The SCET Feynman diagrams for the gluon field strength at $\mathcal{O}(g^0)$ (a) and $\mathcal{O}(g)$ (b) given by the Feynman rules in Eq. (5.9) and Eq. (5.10), respectively.

choice of dimensional regularization as IR regulator, the only Lorentz invariant quantity they can depend on is z. This is dimensionless, so all diagrams contributing to the PDF calculation vanish. Hence, the one-loop PDF has IR divergences with signs opposite to the UV divergences. The UV divergences follow from Eq. (5.4) by looking at the renormalization of the partonic gluon PDF at one-loop

$$
\begin{aligned}
f_{g/g}^{\text{bare}\,(1)}(z) &= \sum_j \int \frac{\mathrm{d}z'}{z'} \left[Z_{gj}^{f(1)}\left(\frac{z}{z'},\mu\right) f_{j/g}^{(0)}(z',\mu) + Z_{gj}^{f(0)}\left(\frac{z}{z'},\mu\right) f_{j/g}^{(1)}(z',\mu) \right] \\
&= Z_{gg}^{f(1)}(z,\mu) + f_{g/g}^{(1)}(z,\mu)\,, \\
f_{g/q}^{\text{bare}\,(1)}(z) &= \sum_j \int \frac{\mathrm{d}z'}{z'} \left[Z_{gj}^{f(1)}\left(\frac{z}{z'},\mu\right) f_{j/q}^{(0)}(z',\mu) + Z_{gj}^{f(0)}\left(\frac{z}{z'},\mu\right) f_{j/q}^{(1)}(z',\mu) \right] \\
&= Z_{gq}^{f(1)}(z,\mu) + f_{g/q}^{(1)}(z,\mu)\,.
\end{aligned}
\tag{5.6}
$$

This implies that the UV divergent part of the partonic $f_{i/j}^{(1)}(z,\mu)$ is just $Z_{ij}^{f(1)}(z,\mu)$. We thus obtain the renormalized PDF

$$
\begin{aligned}
f_{g/g}^{(1)}(z,\mu) &= -\frac{1}{\epsilon}\frac{\alpha_s(\mu)}{2\pi}\,\theta(z)\left[C_A P_{gg}(z) + \frac{1}{2}\beta_0\,\delta(1-z) \right], \\
f_{g/q}^{(1)}(z,\mu) &= -\frac{1}{\epsilon}\frac{\alpha_s(\mu)C_F}{2\pi}\,\theta(z)P_{qg}(z)\,.
\end{aligned}
\tag{5.7}
$$

5.2   SCET Feynman Rules

We now list the SCET Feynman rules necessary for the calculations. The Feynman rules for the gluon field strength, $\mathcal{B}_{n\perp}^\mu$,

$$
\mathcal{B}_{n\perp}^\mu = \frac{1}{g}\left[W_n^\dagger\, \mathrm{i}D_{n\perp}^\mu W_n \right]
\tag{5.8}
$$

are illustrated in Fig. 5-1. The Feynman rule at order $\mathcal{O}(g^0)$ is

$$\text{Fig. 5-1(a)} = \delta^{ca}\left(g_\perp^{\mu\alpha} - \frac{p_\perp^\mu \bar{n}^\alpha}{\bar{n}\cdot p}\right) \equiv \delta^{ca}\mathcal{B}_{n\perp}^{(0)\,\mu\alpha}(p)\,, \tag{5.9}$$

and at $\mathcal{O}(g)$ it is given by

$$\text{Fig. 5-1(b)} = \mathrm{i}gf^{cab}\left[\frac{g_\perp^{\mu\beta}\bar{n}^\alpha}{\bar{n}\cdot p} - \frac{g_\perp^{\mu\alpha}\bar{n}^\beta}{\bar{n}\cdot q} + \left(\frac{p_\perp^\mu}{\bar{n}\cdot q} - \frac{q_\perp^\mu}{\bar{n}\cdot p}\right)\frac{\bar{n}^\alpha\bar{n}^\beta}{\bar{n}\cdot(p+q)}\right] \equiv \mathrm{i}gf^{cab}\mathcal{B}_{n\perp}^{(1)\,\mu\alpha\beta}(p,q)\,. \tag{5.10}$$

We abbreviate the collinear quark-gluon vertex as

$$\mathrm{i}g\,T^a\left(n^\mu + \frac{\slashed{p}_\perp\gamma_\perp^\mu}{\bar{n}\cdot p} + \frac{\gamma_\perp^\mu\slashed{q}_\perp}{\bar{n}\cdot q} - \frac{\slashed{p}_\perp\slashed{q}_\perp}{\bar{n}\cdot p\,\bar{n}\cdot q}\,\bar{n}^\mu\right)\frac{\slashed{\bar{n}}}{2} \equiv \mathrm{i}g\,T^a V_n^\mu(p,q)\,\frac{\slashed{\bar{n}}}{2}\,, \tag{5.11}$$

where p and q are the momenta of the outgoing and incoming quark lines, so the gluon carries incoming momentum $p - q$. Finally, we abbreviate the triple gluon vertex by

$$gf^{abc}V_3^{\mu\nu\rho}(p_1,p_2,p_3) \equiv gf^{abc}[g^{\mu\nu}(p_1 - p_2)^\rho + g^{\nu\rho}(p_2 - p_3)^\mu + g^{\rho\mu}(p_3 - p_1)^\nu]\,, \tag{5.12}$$

where all momenta are incoming and momentum conservation holds, $p_1 + p_2 + p_3 = 0$.

5.3 The Gluon Beam Function at One Loop

We now turn to the calculation of the partonic gluon beam function. The beam function was defined in Eq. (3.10) such that at tree level it is normalized to

$$B_{i/j}^{(0)}(t, z, \mu) = \delta_{ij}\,\delta(t)\delta(1 - z)\,, \tag{5.13}$$

The one-loop Feynman diagrams for the partonic calculation are shown in Fig. 5-2. Since we regulate both the UV and IR with dimensional regularization, the virtual diagrams in Figs. 5-2(d) and 5-2(e) vanish because there is only the p^- momentum of the external gluon flowing into the loop, which is insufficient to give a nonzero Lorentz-invariant result for the loop integral. This means that the UV divergences cancel the IR divergences. Performing the wave function renormalization in the on shell scheme, both the wave function renormalization Z_ψ as well as the residue R_ψ that enters in LSZ are equal to one. (A different
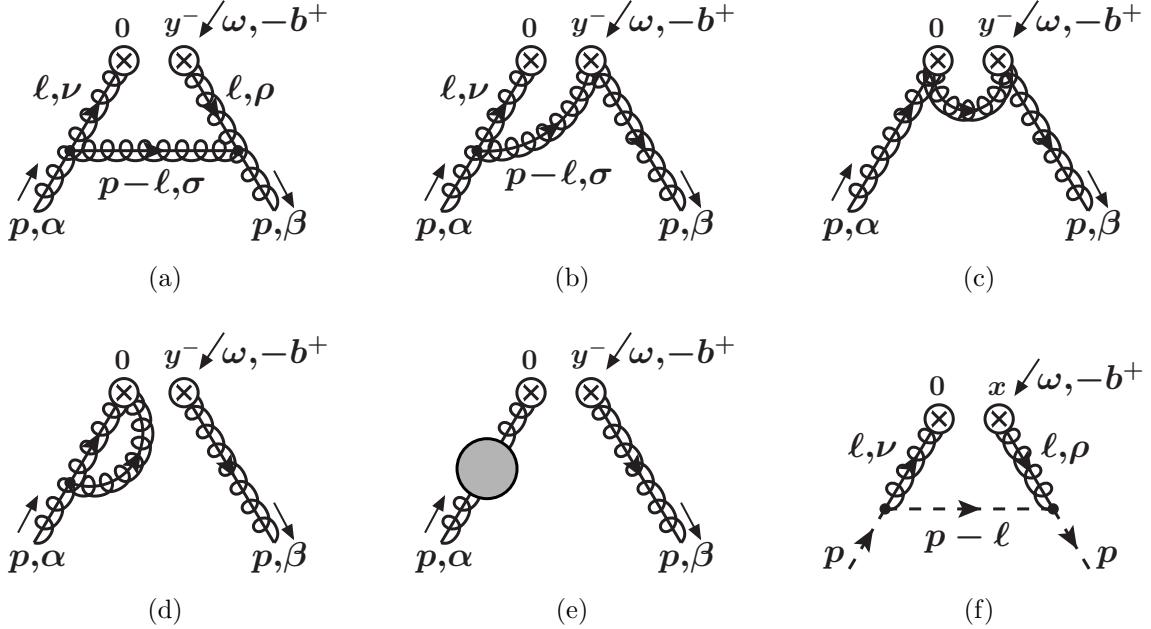
Figure 5-2: One-loop diagrams for the gluon beam function. The minus momentum ω is incoming at the vertex and the b^+ momentum is outgoing. Graphs (b), (d), and (e) have symmetric counterparts which are equal to the ones shown and included in the computation. The diagrams with the external lines crossed vanish and are not shown.

scheme would lead to contributions to Z_ψ and R_ψ that cancel each other in the final result.)

To compute the one-loop real radiation diagrams for the gluon beam function, we use the relationship with the matrix element of the time-ordered product in Eq. (3.56). We always average over the polarizations of the external gluons, and since their momentum is $p^\mu = p^- n^\mu/2$ this gives us the rule

$$\frac{1}{d-2} \sum_{\text{pol}} \varepsilon^\alpha \, \varepsilon^{*\beta} \to -\frac{g_\perp^{\alpha\beta}}{d-2} \, , \tag{5.14}$$

where $d = 4 - 2\epsilon$. We also average over the color of the external gluons (which is trivial). This choice for the polarizations and colors of the external states is just a matter of calculational convenience, in order to determine the renormalization and matching all we need is states with non-zero overlap with the operator.

Let us start with the diagram in Fig. 5-2(a). To make our expressions more palatable, we first perform the color algebra, which simply yields

$$\frac{\delta^{ab}}{N_c^2 - 1} f^{aec} f^{bde} \delta^{fc} \delta^{fd} = -C_A \, . \tag{5.15}$$

101

The diagram is then given by

Fig. 5-2(a)   (5.16)

$$
= -\mathrm{i}\Big(\frac{e^{\gamma_E}\mu^2}{4\pi}\Big)^\epsilon g^2 C_A\,\theta(\omega)\,\mathrm{Disc}_{t>0}\int\frac{\mathrm{d}^d\ell}{(2\pi)^d}\frac{\delta(\ell^- - \omega)\delta(\ell^+ + b^+)}{(\ell^2 + \mathrm{i}0)^2[(\ell-p)^2 + \mathrm{i}0]}
$$

$$
\times\frac{g^\beta_{\perp\alpha}}{d-2}V_3^{\alpha\sigma\nu}(p,\ell-p,-\ell)V_{3\,\beta\rho\sigma}(-p,\ell,p-\ell)\,\mathcal{B}^{(0)}_{n\perp\mu\nu}(\ell)\,\mathcal{B}^{(0)\,\mu\rho}_{n\perp}(-\ell)
$$

$$
= -\mathrm{i}\Big(\frac{e^{\gamma_E}\mu^2}{4\pi}\Big)^\epsilon\frac{g^2 C_A}{(2\pi)^2}\,\theta(z)\,\mathrm{Disc}_{t>0}\int_0^1\mathrm{d}\alpha\,(1-\alpha)\int\frac{\mathrm{d}^{d-2}\vec{\ell}_\perp}{(2\pi)^{d-2}}\frac{(5+4/z^2)\,\vec{\ell}_\perp^2 + (1+1/z)t}{(\vec{\ell}_\perp^2 + \Delta)^3}
$$

$$
= \frac{\alpha_s(\mu)C_A}{2\pi}\,\theta(z)\theta(1-z)2\Big[\frac{1-z}{z} + z(1-z) + \frac{z}{2}\Big]\Gamma(1+\epsilon)(e^{\gamma_E}\mu^2)^\epsilon\frac{\sin\pi\epsilon}{\pi\epsilon}\frac{\theta(t)}{t^{1+\epsilon}}\Big(\frac{z}{1-z}\Big)^\epsilon,
$$

with $\Delta = t(1-\alpha/z)$. To derive the second equality we integrated l^+ and l^- using the delta functions and applied a Feynman parametrization. The last line follows from performing the $\vec{\ell}_\perp$ integral and using the discontinuities listed in App. B. By expanding in ϵ we find

Fig. 5-2(a)   (5.17)

$$
= \frac{\alpha_s(\mu)C_A}{2\pi}\,\theta(z)\theta(1-z)2\Big[\frac{1-z}{z} + z(1-z) + \frac{z}{2}\Big]\Big[\delta(t)\Big(-\frac{1}{\epsilon} + \ln\frac{1-z}{z}\Big) + \frac{1}{\mu^2}\mathcal{L}_0\Big(\frac{t}{\mu^2}\Big)\Big],
$$

where the plus distribution $\mathcal{L}_0(x)$ is defined in Eq. (B.2). The color structure for the diagram in Fig. 5-2(b) yields

$$
\frac{\delta^{ab}}{N_c^2 - 1}f^{aec}\delta^{fc}f^{feb} = -C_A. \tag{5.18}
$$

Including a factor of two for its mirror graph, we get

$$
\text{Fig. 5-2(b)} = -2\mathrm{i}\Big(\frac{e^{\gamma_E}\mu^2}{4\pi}\Big)^\epsilon g^2 C_A\,\theta(\omega)\,\mathrm{Disc}_{t>0}\int\frac{\mathrm{d}^d\ell}{(2\pi)^d}\frac{\delta(\ell^- - \omega)\delta(\ell^+ + b^+)}{(\ell^2 + \mathrm{i}0)\,[(\ell-p)^2 + \mathrm{i}0]}
$$

$$
\times\frac{g^\beta_{\perp\alpha}}{d-2}V_3^{\alpha\sigma\nu}(p,\ell-p,-\ell)\,\mathcal{B}^{(0)}_{n\perp\,\mu\nu}(\ell)\,\mathcal{B}^{(1)\mu}_{n\perp\,\,\sigma\beta}(p-\ell,-p)
$$

$$
= -\mathrm{i}\Big(\frac{e^{\gamma_E}\mu^2}{4\pi}\Big)^\epsilon\frac{g^2 C_A}{(2\pi)^2}\,\theta(z)\frac{1+z}{1-z}\,\mathrm{Disc}_{t>0}\int_0^1\mathrm{d}\alpha\int\frac{\mathrm{d}^{d-2}\vec{\ell}_\perp}{(2\pi)^{d-2}}\frac{1}{(\vec{\ell}_\perp^2 + \Delta)^2}
$$

$$
= \frac{\alpha_s(\mu)C_A}{2\pi}\,\theta(z)(1+z)z^{1+\epsilon}\frac{\theta(1-z)}{(1-z)^{1+\epsilon}}\,\Gamma(1+\epsilon)(e^{\gamma_E}\mu^2)^\epsilon\frac{\sin\pi\epsilon}{\pi\epsilon}\frac{\theta(t)}{t^{1+\epsilon}}, \tag{5.19}
$$

using the relations listed in App. B. Expanding in ϵ yields

Fig. 5-2(b) (5.20)

$$
\begin{aligned}
= \frac{\alpha_s(\mu)C_A}{2\pi}\,\theta(z)\Bigg\{ &\left[-\frac{1}{\epsilon}\delta(t)+\frac{1}{\mu^2}\mathcal{L}_0\Big(\frac{t}{\mu^2}\Big)\right]\left[-\frac{2}{\epsilon}\delta(1-z)+\mathcal{L}_0(1-z)z(1+z)\right] \\
&+\frac{2}{\mu^2}\mathcal{L}_1\Big(\frac{t}{\mu^2}\Big)\delta(1-z)+\delta(t)z(1+z)\left[\mathcal{L}_1(1-z)-\mathcal{L}_0(1-z)\ln z-\frac{\pi^2}{12}\delta(1-z)\right]\Bigg\}.
\end{aligned}
$$

The diagram in Fig. 5-2(c) is zero. Because the external gluons have perpendicular polarization, contracting the two $\mathcal{B}^{(1)}_{n\perp}$ in Eq. (5.10) leads to $\bar{n}\cdot\bar{n}=0$ in the numerator.

Crossing the external lines of these diagrams corresponds to $p\to -p$ (the polarization and color are symmetric and hence unaffected). By changing $\ell\to-\ell$ this yields the same as the original diagram but with $\delta(\ell^- -\omega)\delta(\ell^+ +b^+)\to\delta(\ell^- +\omega)\delta(\ell^+ -b^+)$ and thus

$$
\Delta=\Big(1-\frac{\alpha}{z}\Big)t\to\Big(1+\frac{\alpha}{z}\Big)t\,. \tag{5.21}
$$

Since $\alpha,z>0$ the discontinuity for $t>0$ vanishes for these graphs. Other one-loop real radiation diagrams, like the one involving a four gluon vertex, vanish because their discontinuity vanishes. All cuts of these diagrams involve cutting one of the external lines, which sets $\Delta=t$ in the loop integral and leads to a vanishing discontinuity for $t>0$.

Adding up the two non-vanishing diagrams in Figs. 5-2(a) and 5-2(b), we find

$$
\begin{aligned}
B^{\mathrm{bare}(1)}_{g/g}(t,z)=\frac{\alpha_s(\mu)C_A}{2\pi}\,\theta(z)\Bigg(&\left[\frac{2}{\epsilon^2}\delta(t)-\frac{2}{\epsilon}\frac{1}{\mu^2}\mathcal{L}_0\Big(\frac{t}{\mu^2}\Big)\right]\delta(1-z)-\frac{1}{\epsilon}\delta(t)P_{gg}(z) \\
&+\frac{2}{\mu^2}\mathcal{L}_1\Big(\frac{t}{\mu^2}\Big)\delta(1-z)+\frac{1}{\mu^2}\mathcal{L}_0\Big(\frac{t}{\mu^2}\Big)P_{gg}(z) \\
&+\delta(t)\Big\{\Big[\mathcal{L}_1(1-z)-\frac{\theta(1-z)\ln z}{1-z}\Big]\frac{2[1-z(1-z)]^2}{z}-\frac{\pi^2}{6}\delta(1-z)\Big\}\Bigg).
\end{aligned} \tag{5.22}
$$

This expression agrees with the expression found in Ref. [142]. Transforming to moment space, we find agreement with the expression quoted in Ref. [96] up to an extra term of $-\alpha_s C_A\delta(1-z)\pi^2/8$.

We now determine the mixing contribution of the quark PDF to the gluon beam function, which was not calculated in Refs. [96, 142]. The relevant matrix element has external quarks instead of gluons, and the corresponding diagram is shown Fig. 5-2(f). Using fixed spin and color or averaging over them yields again identical results. Here, we average over spins,

using $\frac{1}{2}\sum_{\text{spins}} u_n(p)\bar{u}_n(p) = \frac{1}{2}\not{p}$. The color average gives $(1/N_c)\text{tr}[T^a T^b]\delta^{ab} = C_F$. The diagram is thus given by

Fig. 5-2(f) $\hspace{8cm}$ (5.23)
$$= -\mathrm{i}\Big(\frac{e^{\gamma_E}\mu^2}{4\pi}\Big)^\epsilon g^2 C_F\, \theta(\omega)\, \text{Disc}_{t>0} \int \frac{\mathrm{d}^d\ell}{(2\pi)^d}\, \frac{(p^- - \ell^-)\, \delta(\ell^- - \omega)\delta(\ell^+ + b^+)}{(\ell^2 + \mathrm{i}0)^2[(p-\ell)^2 + \mathrm{i}0]}$$
$$\times\, \bar{u}_n(p)V_n^\rho(p, p-\ell)V_{n\,\nu}(p-\ell, p)\frac{\not{\bar{n}}}{2}u_n(p)\, \mathcal{B}_{n\perp}^{(0)\mu\nu}(\ell)\, \mathcal{B}_{n\perp\mu\rho}^{(0)}(-\ell)$$
$$= \mathrm{i}\Big(\frac{e^{\gamma_E}\mu^2}{4\pi}\Big)^\epsilon \frac{g^2 C_F}{(2\pi)^2}\, \theta(z)\Big(\frac{d-2}{1-z} + \frac{4}{z^2}\Big)\text{Disc}_{t>0} \int_0^1 \mathrm{d}\alpha\,(1-\alpha)\int \frac{\mathrm{d}^{d-2}\vec{\ell}_\perp}{(2\pi)^{d-2}}\, \frac{\vec{\ell}_\perp^2}{(\vec{\ell}_\perp^2 + \Delta)^3}$$
$$= \frac{\alpha_s(\mu)C_F}{2\pi}\, \theta(z)\theta(1-z)\Gamma(1+\epsilon)(e^{\gamma_E}\mu^2)^\epsilon\Big[\frac{1+(1-z)^2}{z} - \epsilon z\Big]\frac{\sin\pi\epsilon}{\pi\epsilon}\frac{\theta(t)}{t^{1+\epsilon}}\Big(\frac{z}{1-z}\Big)^\epsilon.$$

This is the same loop integral and discontinuity as in Fig. 5-2(a). For the crossed graph, where the external lines are interchanged, we change $\ell \to -\ell$ to find the same expression as in Eq. (5.23) with $\delta(\ell^- - \omega)\delta(\ell^+ + b^+) \to \delta(\ell^- + \omega)\delta(\ell^+ - b^+)$. This leads to Eq. (5.21) and a vanishing discontinuity. Expanding in ϵ, we obtain for the bare one-loop quark matrix element

$$B_{g/q}^{\text{bare}(1)}(t, z) \hspace{7cm} (5.24)$$
$$= \frac{\alpha_s(\mu)C_F}{2\pi}\, \theta(z)\bigg\{\frac{1}{\mu^2}\mathcal{L}_0\Big(\frac{t}{\mu^2}\Big)P_{gq}(z) + \delta(t)\Big[P_{gq}(z)\Big(-\frac{1}{\epsilon} + \ln\frac{1-z}{z}\Big) + \theta(1-z)z\Big]\bigg\}.$$

The matrix element with external antiquarks gives the same result, so the mixing contributions from quarks and antiquarks are identical.

5.4 Renormalization, Running and Matching

We know that the anomalous dimension of the gluon beam function equals that of the gluon jet function, and that the IR divergences of the gluon beam function cancel those of the gluon PDF in the matching. Since we regulate both the UV and IR using dimensional regularization, we cannot separate the UV and IR divergences and we can only verify one of these statements in our calculation. We will assume the cancellation of IR divergences, which then allows us to verify that the anomalous dimension equals that of the gluon jet function. Equivalently, we could have taken the anomalous dimension of the gluon jet function for granted and have checked that the IR divergences cancel in the matching.

We denote the counterterm that renormalizes the beam function by $Z_B^g(t - t', \mu)$

$$B_g^{\text{bare}}(t, x, \mu) = \int dt' \, Z_B^g(t - t', \mu) B_g(t', x, \mu) \, . \tag{5.25}$$

In order to extract the renormalization for the beam function from our partonic calculation, we expand this to one-loop order for gluon states

$$
\begin{aligned}
B_{g/g}^{\text{bare}(1)}(t, z) &= \int dt' \left[Z_B^{g(1)}(t - t', \mu) B_{g/g}^{(0)}(t', z, \mu) + Z_B^{g(0)}(t - t', \mu) B_{g/g}^{(1)}(t', z, \mu) \right] \\
&= Z_B^{g(1)}(t, \mu) \delta(1 - z) + B_{g/g}^{(1)}(t, z, \mu) \, . \tag{5.26}
\end{aligned}
$$

Similarly expanding Eq. (3.37) for the matching onto PDFs

$$
\begin{aligned}
B_{g/g}^{(1)}(t, z, \mu) &= \sum_j \int \frac{dz'}{z'} \left[\mathcal{I}_{gj}^{(1)}(t, z', \mu) f_{j/g}^{(0)}\left(\frac{z}{z'}, \mu\right) + \mathcal{I}_{gj}^{(0)}(t, z', \mu) f_{j/g}^{(1)}\left(\frac{z}{z'}, \mu\right) \right] \\
&= \mathcal{I}_{gg}^{(1)}(t, z, \mu) + \delta(t) f_{g/g}^{(1)}(z, \mu) \\
B_{g/q}^{(1)}(t, z, \mu) &= \sum_j \int \frac{dz'}{z'} \left[\mathcal{I}_{gj}^{(1)}(t, z', \mu) f_{j/q}^{(0)}\left(\frac{z}{z'}, \mu\right) + \mathcal{I}_{gj}^{(0)}(t, z', \mu) f_{j/q}^{(1)}\left(\frac{z}{z'}, \mu\right) \right] \\
&= \mathcal{I}_{gq}^{(1)}(t, z, \mu) + \delta(t) f_{g/q}^{(1)}(z, \mu) \, . \tag{5.27}
\end{aligned}
$$

We know that the IR divergences of the PDF cancel those of the beam function in the matching Eq. (5.27). Hence, after subtracting the IR divergences of the gluon PDF in Eq. (5.7) from the gluon beam function in Eqs. (5.22) and (5.24), all remaining divergences are ultraviolet and enter into the renormalization. There is no UV divergence in the mixing graph and hence the RG evolution does not mix the quark and gluon beam functions. Using Eq. (5.26) we conclude that

$$
\begin{aligned}
Z_B^g(t, \mu) &= \delta(t) + \frac{\alpha_s(\mu)}{2\pi} \left\{ 2C_A \left[\frac{1}{\epsilon^2} - \frac{1}{\epsilon} \frac{1}{\mu^2} \mathcal{L}_0\left(\frac{t}{\mu^2}\right) \right] + \frac{1}{2\epsilon} \beta_0 \, \delta(t) \right\} , \\
\gamma_B^{g(1)}(t, \mu) &= -\mu \frac{d}{d\mu} Z_B^{g(1)}(t, \mu) = -\frac{\alpha_s(\mu) C_A}{\pi} \frac{2}{\mu^2} \mathcal{L}_0\left(\frac{t}{\mu^2}\right) + \frac{\alpha_s(\mu) \beta_0}{2\pi} \delta(t) \, . \tag{5.28}
\end{aligned}
$$

We see that our one-loop calculation agrees with the anomalous dimension of the gluon jet function, as it should according to Eq. (3.26).

Since the PDFs in Eq. (5.7) contain no finite pieces, we infer from Eq. (5.27) that the

remaining terms are simply the matching coefficients

$$\mathcal{I}_{gg}(t, z, \mu) = \delta(t)\delta(1 - z) + \frac{\alpha_s(\mu)C_A}{2\pi}\,\theta(z)\left(\frac{2}{\mu^2}\mathcal{L}_1\left(\frac{t}{\mu^2}\right)\delta(1 - z) + \frac{1}{\mu^2}\mathcal{L}_0\left(\frac{t}{\mu^2}\right)P_{gg}(z)\right.$$

$$\left.+ \delta(t)\left\{\left[\mathcal{L}_1(1 - z) - \frac{\theta(1 - z)\ln z}{1 - z}\right]\frac{2[1 - z(1 - z)]^2}{z} - \frac{\pi^2}{6}\delta(1 - z)\right\}\right),$$

$$\mathcal{I}_{gq}(t, z, \mu) = \frac{\alpha_s(\mu)C_F}{2\pi}\,\theta(z)\left\{P_{gq}(z)\left[\frac{1}{\mu^2}\mathcal{L}_0\left(\frac{t}{\mu^2}\right) + \delta(t)\ln\frac{1 - z}{z}\right] + \theta(1 - z)z\,\delta(t)\right\}. \quad (5.29)$$

Chapter 6

Beam Function Plots

We will now compare results for the beam functions at LO and NLO in fixed-order perturbation theory as well as at NLL and NNLL in resummed perturbation theory, which were first reported in Refs. [48, 168]. Our conventions for the α_s loop counting are given in Table 6.1. To evaluate the required convolutions of plus distributions at NNLL we use the identities from App. B of Ref. [135]. We always use the MSTW2008 [143] parton distributions at NLO for $\alpha_s(m_Z) = 0.117$ and with two-loop, five-flavor running for $\alpha_s(\mu)$. The uncertainty bands in the plots show the perturbative uncertainties, which are estimated by varying the appropriate scales as explained in each case. They do not include the additional uncertainties from the PDFs and $\alpha_s(m_Z)$.

The order of the running of $\alpha_s(\mu)$ deserves some comment. Working consistently to NLO in the matching corrections requires us to use NLO PDFs, for which the two-loop running of α_s was used in Ref. [143]. On the other hand, the double-logarithmic running of the beam functions at NNLL requires the three-loop running of α_s, which poses a slight dilemma. Ideally, we would need NLO PDFs using three-loop running for $\alpha_s(\mu)$, which as far as we know are not available. The numerical difference between α_s run at two and three loops is very small, at most 2%. Hence, we use the following compromise. To be consistent

	matching	γ_x	$\Gamma_{\rm cusp}$	β
LO	0-loop	-	-	-
NLO	1-loop	-	-	-
NLL	0-loop	1-loop	2-loop	2-loop
NNLL	1-loop	2-loop	3-loop	3-loop

Table 6.1: Order counting in fixed-order and resummed perturbation theory.

with our PDF set, we use the above $\alpha_s(m_Z)$ and two-loop, five-flavor running to obtain the numerical value of α_s at some required scale, and to be consistent with the RGE, we use the two- and three-loop expression for the QCD β function in the RGE solutions at NLL and NNLL. (For simplicity we use the same NLO PDFs and α_s also at NLL.)

To illustrate the importance of the various contributions to the quark and gluon beam functions, we also consider the beam functions in the threshold limit and without the mixing contribution. In the threshold limit we only keep the terms in Eq. (4.47) and Eq. (5.29) which are singular as $z \to 1$,

$$
\mathcal{I}_{qq}^{\text{thresh}}(t, z, \mu) = \delta(t)\delta(1-z) + \frac{\alpha_s(\mu)C_F}{2\pi}\,\theta(z)\left\{ \frac{2}{\mu^2}\mathcal{L}_1\Big(\frac{t}{\mu^2}\Big)\delta(1-z) + \frac{2}{\mu^2}\mathcal{L}_0\Big(\frac{t}{\mu^2}\Big)\mathcal{L}_0(1-z) \right.
$$
$$
\left. + \delta(t)\Big[2\mathcal{L}_1(1-z) - \frac{\pi^2}{6}\delta(1-z)\Big] \right\},
$$
$$
\mathcal{I}_{gg}^{\text{thresh}}(t, z, \mu) = \delta(t)\delta(1-z) + \frac{\alpha_s(\mu)C_A}{2\pi}\,\theta(z)\left\{ \frac{2}{\mu^2}\mathcal{L}_1\Big(\frac{t}{\mu^2}\Big)\delta(1-z) + \frac{2}{\mu^2}\mathcal{L}_0\Big(\frac{t}{\mu^2}\Big)\mathcal{L}_0(1-z) \right.
$$
$$
\left. + \delta(t)\Big[2\mathcal{L}_1(1-z) - \frac{\pi^2}{6}\delta(1-z)\Big] \right\},
$$
$$
\mathcal{I}_{qg}^{\text{thresh}}(t, z, \mu) = \mathcal{I}_{gq}^{\text{thresh}}(t, z, \mu) = 0\,. \tag{6.1}
$$

The mixing terms $\mathcal{I}_{qg}$ and $\mathcal{I}_{gq}$ contain no threshold terms (which reflects the fact that in threshold Drell-Yan the gluon PDF does not contribute). For the results without mixing contributions we keep the full $\mathcal{I}_{ii}$ but set $\mathcal{I}_{ij}$ to zero for $i \neq j$, which corresponds to adding the remaining non-threshold terms in $\mathcal{I}_{ii}$ to the threshold result. In the plots below, the results in the threshold limit are shown by a dotted line and are labeled "$x \to 1$", and the results without the mixing contribution are shown by a dashed line and are labeled "no g" for the quark beam functions and "no q" for the gluon beam function. The full results are shown by a solid line. Hence, the size of the non-threshold terms in $\mathcal{I}_{ii}$, and therefore the applicability of the threshold limit, is seen by the shift from the dotted to the dashed line, and the effect of the mixing is given by the shift from the dashed to the solid line.

To be able to plot the beam functions as a function of the momentum fraction x including the virtual terms proportional to $\delta(t)$, we integrate over t up to some maximum $t_{\max}$,

$$
\widetilde{B}_i(t_{\max}, x, \mu) = \int \mathrm{d}t\, B_i(t, x, \mu)\theta(t_{\max} - t)\,, \tag{6.2}
$$

where $B_i(t, x, \mu)$ is given by Eqs. (3.28) and (3.37). In the plots, we always choose $t_{\max} =$
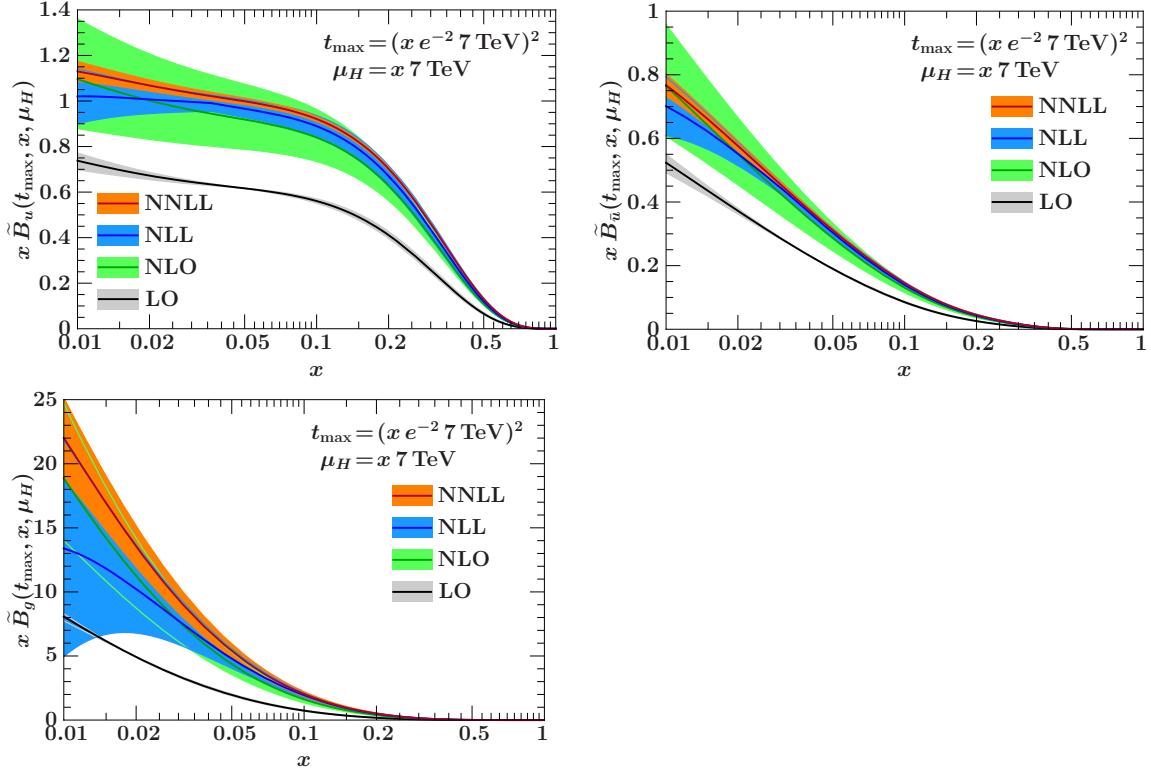
Figure 6-1: The u (upper left), $\bar{u}$ (upper right) and g (lower left) beam functions at the hard scale $\mu_H = x\,7\,\text{TeV}$ at LO, NLO, NLL, and NNLL, integrated up to $t_{\max} = (x\,e^{-2}\,7\,\text{TeV})^2$. The bands show the perturbative uncertainties estimated by varying μ_H for the fixed-order results and the matching scale $\mu_B^2 \simeq t_{\max}$ for the resummed results, explained in the text.

$(x e^{-2}\,7\,\text{TeV})^2$, which one should think of as $t_{\max} = (e^{-y^{\text{cut}}} x E_{\text{cm}})^2$. Hence, this choice of $t_{\max}$ corresponds to a rapidity cut $y^{\text{cut}} = 2$ for $E_{\text{cm}} = 7\,\text{TeV}$ or equivalently $y^{\text{cut}} = 2.4$ for $E_{\text{cm}} = 10\,\text{TeV}$. This is motivated by the upper bound $y^{\text{cut}} = y_B^{\text{cut}} \pm Y$, which follows from the factorization theorem Eq. (2.29) when we integrate $\tau_B \le \exp(-2y_B^{\text{cut}})$.

Figure 6-1 shows the integrated u, $\bar{u}$ and gluon beam function $x\widetilde{B}_i(t_{\max}, x, \mu_H)$ evaluated at the hard scale $\mu_H = Q = x\,7\,\text{TeV}$. For the fixed-order results at LO (lowest gray band) and NLO (light green band) the perturbative uncertainties are obtained by varying μ_H by factors of two, since this is the scale at which the perturbation series for the matching coefficients in Eq. (3.37) is evaluated. At LO, the resulting variation is entirely due to the scale dependence of the PDF. This is clearly an underestimation, since the perturbative corrections in the NLO beam function contain large single and double logarithms of $t_{\max}/Q^2$, causing a large shift in the NLO central value with large uncertainties. For the gluon beam function the shift and uncertainties are particularly large, due to differences between $\mathcal{I}_{gg}^{(1)}$

and $\mathcal{I}_{qq}^{(1)}$ such as an overall coefficient of C_A instead of C_F.

For the resummed results at NLL (dark blue band) and NNLL (medium orange band) the beam function OPE in Eq. (3.37) is evaluated at the beam scale $\mu_B^2 \simeq t_{\max}$, and the beam function is then evolved to μ_H using its RGE, Eq. (3.28). In this way, the large logarithms of $\mu_B^2/\mu_H^2 \simeq t_{\max}/\mu_H^2 = e^{-4}$ are resummed. The perturbative uncertainties are now evaluated by varying the matching scale μ_B, where the perturbation series is evaluated, while keeping μ_H fixed. The uncertainty bands show the minimum and maximum variation in the interval $\sqrt{t_{\max}}/2 \leq \mu_B \leq 2\sqrt{t_{\max}}$ (which due to the double-logarithmic series do not occur at the edges of the interval) with the central value given by the center of the bands. The NLL result is close to the NLO result, showing that the large logarithms make up the biggest part of the NLO corrections. Consequently, the corrections from NLL to NNLL are within the NLL uncertainties. Resummed perturbation theory is thus well-behaved and should be used for the beam function at the hard scale, rather than fixed-order perturbation theory. The large uncertainty bands for the resummed gluon beam function at small x are due to the strong double logarithmic running. The effect is much larger than for the quark beam functions because C_F gets replaced by C_A, which for the running shows up in the exponent. The effect of the running is enhanced at small x because $\alpha_s(\mu_B)$ becomes large. For $x = 0.01$ we are varying the matching scale μ_B between $5\,\mathrm{GeV}$ and $20\,\mathrm{GeV}$ where α_s is much larger than for the corresponding variation for the fixed order results, where μ_H varies between $35\,\mathrm{GeV}$ and $140\,\mathrm{GeV}$.

To study the perturbative corrections to the beam functions in more detail, we consider them at the scale $\mu_B^2 \simeq t_{\max}$, where there are no large logarithms and we can use fixed-order perturbation theory. The u and d beam functions at LO and NLO are shown in Fig. 6-2, the $\bar{u}$ and $\bar{d}$ beam functions in Fig. 6-3 and the gluon beam function in Fig. 6-4. The left panels show $x\widetilde{B}_i(t_{\max}, x, \mu_B)$. The right panels show the same results but as relative corrections with respect to the LO results. At LO, the only scale variation comes from the PDFs and the minimum and maximum variations are obtained for $\mu_B = \{\sqrt{t_{\max}}/2, 2\sqrt{t_{\max}}\}$ with the central value at $\mu_B = \sqrt{t_{\max}}$. For the NLO results, the maximum variation in the range $\sqrt{t_{\max}}/2 \leq \mu_B \leq 2\sqrt{t_{\max}}$ is approximately attained for $\mu_B = \{0.7\sqrt{t_{\max}}, 2.0\sqrt{t_{\max}}\}$ and the corresponding central value for $\mu_B = 1.4\sqrt{t_{\max}}$. To be consistent we use the same central value $\mu_B = 1.4\sqrt{t_{\max}}$ for the NLO results in the threshold limit and without the mixing contribution. For the quark and anti-quark beam functions the NLO perturbative
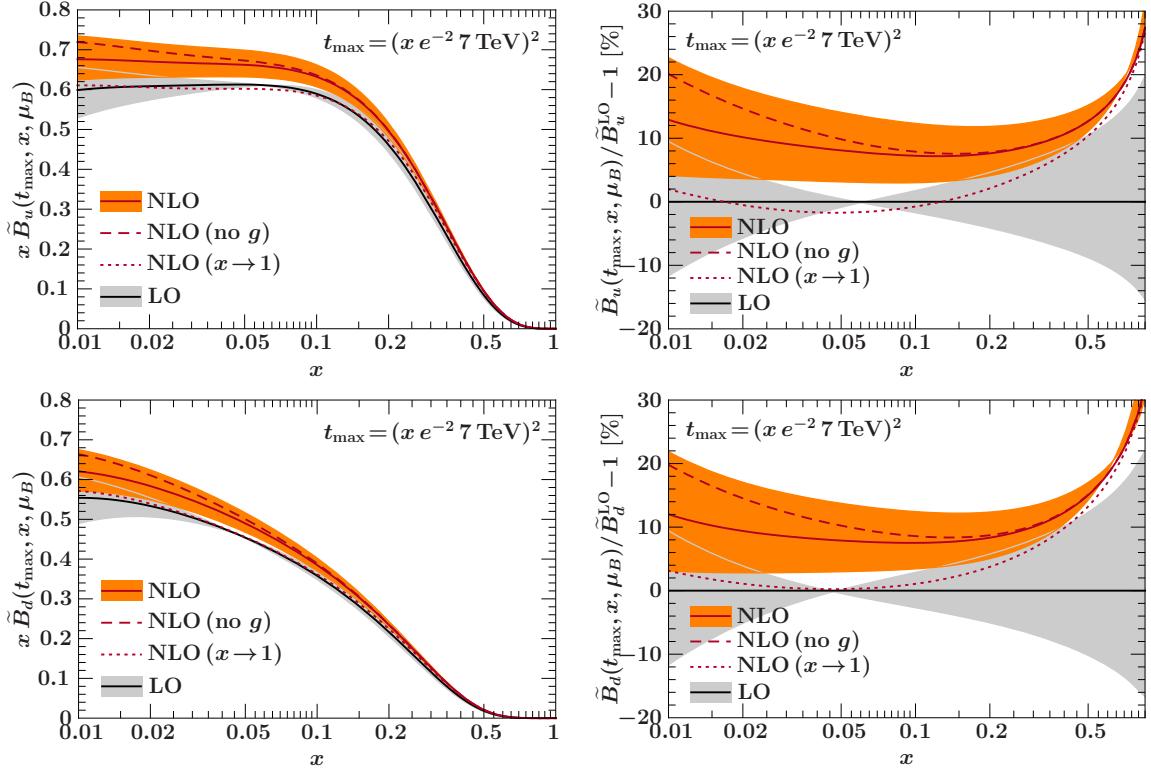
Figure 6-2: The u (top row) and d (bottom row) beam functions at the beam scale $\mu_B^2 \simeq t_{\max}$ at LO and NLO, integrated up to $t_{\max} = (xe^{-2}7\,\text{TeV})^2$. The left column shows the functions times x. The right column shows the relative differences compared to the LO result. Also shown are the NLO beam functions in the threshold limit (dotted) and without the gluon contribution (dashed). The bands show the perturbative scale uncertainties as explained in the text.

corrections are of $\mathcal{O}(10\%)$ and exhibit reasonable uncertainties. The NLO corrections for the gluon beam function are $\mathcal{O}(30\%)$, which is much bigger but still reasonable.

The integration limits $x \leq \xi \leq 1$ in the beam function OPE, Eq. (3.37), force $z = x/\xi \to 1$ in the limit $x \to 1$. Hence, the threshold terms in Eq. (6.1) are expected to dominate over the non-threshold terms at large values of x. This can be seen in Figs. 6-2 and 6-3, where the threshold results shown by the dotted lines approach the full results towards large x values where the beam functions vanish. For the quark beam functions in Fig. 6-2, away from the endpoint, $x \lesssim 0.5$, the threshold corrections give a poor approximation to the full NLO corrections. For the antiquark beam functions in Fig. 6-3, the threshold result turns out to be relatively close to the full result even for small x. However, the reason for this is a relatively strong cancelation between the non-threshold terms in the quark and gluon contributions $\mathcal{I}_{qq}$ and $\mathcal{I}_{qg}$ at one loop. As shown by the result without the gluon
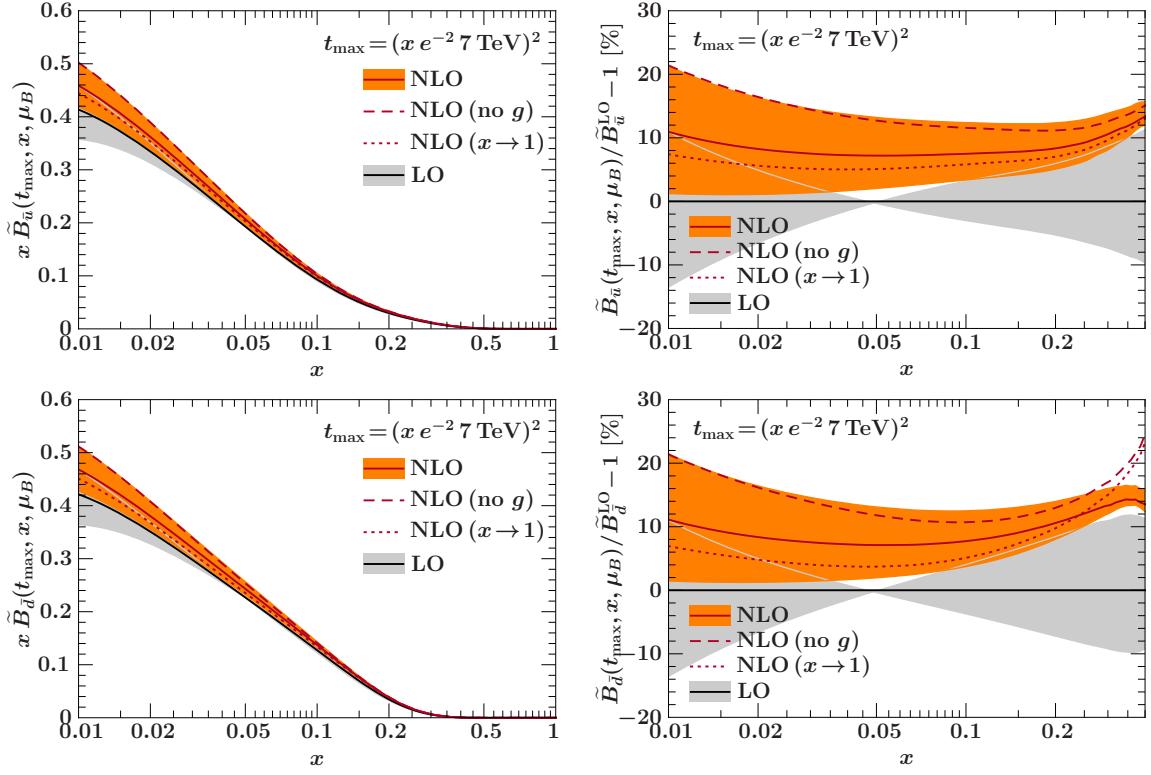
Figure 6-3: The $\bar{u}$ (top row) and $\bar{d}$ (bottom row) beam functions at the beam scale. The meaning of the curves is analogous to Fig. 6-2.
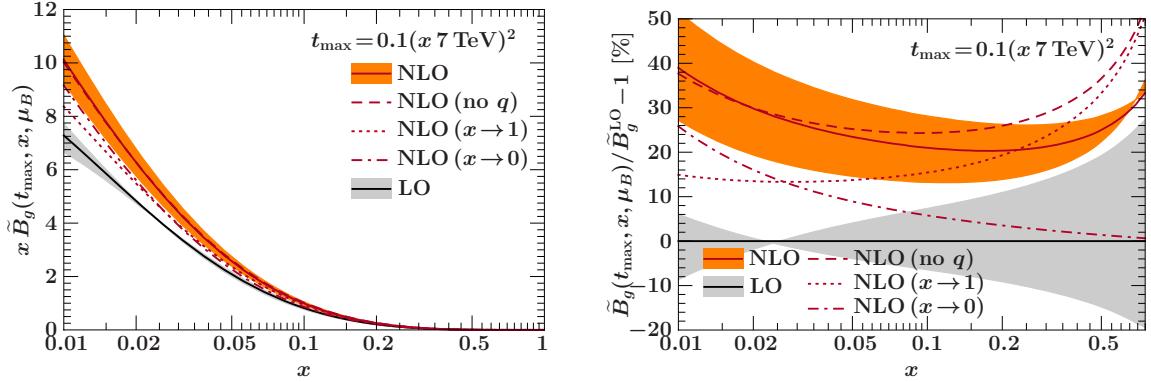
Figure 6-4: The gluon beam function at the beam scale. The meaning of the curves is analogous to Fig. 6-2.

contribution (dashed lines) the non-threshold terms in the quark and gluon contributions each by themselves are of the same size or larger than the threshold contributions. This cancellation appears to be accidental, since it depends on both the relative size of the antiquark and gluon PDFs as well as the relative size of the non-threshold terms in $\mathcal{I}_{qq}$ and $\mathcal{I}_{qg}$. Note also that for the $\bar{d}$ beam function the threshold result approaches the no-

gluon result rather than the full result at large x. This is even more visible for the gluon beam function, where the threshold terms might seem a good approximation around $x \approx 0.2$. However, for large x the threshold terms approach the no-quark result which is very different from the full result.

It has been argued [19, 67] that the steep fall-off of the PDFs causes a systematic enhancement of the partonic threshold region $z \to 1$ even away from the hadronic threshold limit $x \to 1$. This likely explains why the threshold terms in Figs. 6-2 and 6-3 start to dominate already close to the x values where the PDFs are close to zero, rather than strictly near $x = 1$ [42]. However, our results show that the same arguments do not apply in the relevant region of x where the PDFs and beam functions are substantially nonzero.

Chapter 7

Isolated Factorization Theorem

In this chapter we derive the isolated factorization theorem in Eq. (2.16), which was first presented in Ref. [166]. Our analysis is based on factorization in SCET, which rigorously and systematically separates hard, soft and collinear contributions [30, 35, 37]. We make use of a setup with SCET_I and SCET_II [36], carrying out the factorization in two stages at the scales Q^2 and $\omega_{a,b} B_{a,b}^+$ respectively. We have an SCET_I analysis to factorize initial-state jets from soft radiation. The initial-state jets described by beam functions in SCET_I are then matched onto initial-state PDFs with lower offshellness for the collinear particles in SCET_II. In this chapter, we carry out the SCET_I computation, while the matching onto SCET_II was discussed in Ch. 3. Our analysis below uses similar tools as used in the derivation of the factorization theorem for hemisphere invariant masses for $e^+ e^- \to$ dijets in Ref. [93], but differs significantly due to the kinematics, and the fact that we have initial-state rather than final-state jets and a further matching onto SCET_II. The soft dynamics of $e^+ e^- \to$ dijets was studied earlier in SCET in Refs. [33, 34]. We start with a brief overview of the necessary SCET ingredients in Sec. 7.1 and describe the relevant kinematics in Sec. 7.2. We derive the factorization theorem for isolated $pp \to XL$ in Sec. 7.3, including arguments to rule out contributions from so-called Glauber degrees of freedom. Finally in Sec. 7.4, we apply the factorization theorem to $pp \to X\ell^+\ell^-$ and quote final results for the beam thrust cross section with one-loop corrections and logarithmic resummation.

7.1 SCET

Soft-collinear effective theory is an effective field theory of QCD that describes the interactions of collinear and soft particles [29, 31, 35, 37]. Collinear particles are characterized by having large energy and small invariant mass. To separate the large and small momentum components, it is convenient to use light-cone coordinates. We define two light-cone vectors

$$n^\mu = (1, \vec{n}), \qquad \bar{n}^\mu = (1, -\vec{n}), \tag{7.1}$$

with $n^2 = \bar{n}^2 = 0$, $n \cdot \bar{n} = 2$, and $\vec{n}$ is a unit three-vector. Any four-momentum p can then be decomposed as

$$p^\mu = \bar{n}\cdot p\,\frac{n^\mu}{2} + n\cdot p\,\frac{\bar{n}^\mu}{2} + p^\mu_{n\perp}. \tag{7.2}$$

Choosing $\vec{n}$ close to the direction of a collinear particle, its momentum p scales as $(n \cdot p, \bar{n} \cdot p, p_{n\perp}) \sim \bar{n} \cdot p\,(\lambda^2, 1, \lambda)$, with $\lambda \ll 1$ a small parameter. For example, for a jet of collinear particles in the $\vec{n}$ direction with total momentum p_X, $\bar{n}\cdot p_X \simeq 2E_X$ corresponds to the large energy of the jet, while $n \cdot p_X \simeq p_X^2/E_X \ll E_X$, so $\lambda^2 \simeq p_X^2/E_X^2 \ll 1$.

To construct the fields of the effective theory, the momentum is written as

$$p^\mu = \tilde{p}^\mu + k^\mu = \bar{n}\cdot\tilde{p}\,\frac{n^\mu}{2} + \tilde{p}^\mu_{n\perp} + k^\mu \tag{7.3}$$

where $\bar{n} \cdot \tilde{p} \sim Q$ and $\tilde{p}_{n\perp} \sim \lambda Q$ are the large momentum components, where Q is the scale of the hard interaction, while $k \sim \lambda^2 Q$ is a small residual momentum. The effective theory expansion is in powers of the small parameter λ.

The SCET fields for n-collinear quarks and gluons, $\xi_{n,\tilde{p}}(x)$ and $A_{n,\tilde{p}}(x)$, are labeled by the collinear direction n and their large momentum $\tilde{p}$. They are written in position space with respect to the residual momentum and in momentum space with respect to the large momentum components. Frequently, we will only keep the label n denoting the collinear direction, while the momentum labels are summed over and suppressed. Derivatives acting on the fields pick out the residual momentum dependence, $i\partial^\mu \sim k \sim \lambda^2 Q$. The large label momentum is obtained from the momentum operator $\mathcal{P}^\mu_n$, e.g. $\mathcal{P}^\mu_n \xi_{n,\tilde{p}} = \tilde{p}^\mu\,\xi_{n,\tilde{p}}$. If there are several fields, $\mathcal{P}_n$ returns the sum of the label momenta of all n-collinear fields. For convenience, we define $\overline{\mathcal{P}}_n = \bar{n} \cdot \mathcal{P}_n$, which picks out the large minus component.

Collinear operators are constructed out of products of fields and Wilson lines that are

116

invariant under collinear gauge transformations [31, 37]. The smallest building blocks are collinearly gauge-invariant quark and gluon fields, defined as

$$
\chi_{n,\omega}(x) = \left[\delta(\omega - \overline{\mathcal{P}}_n)\, W_n^\dagger(x)\, \xi_n(x) \right] ,
$$
$$
\mathcal{B}_{n,\omega\perp}^\mu(x) = \frac{1}{g} \left[\delta(\omega + \overline{\mathcal{P}}_n)\, W_n^\dagger(x)\, \mathrm{i}D_{n\perp}^\mu W_n(x) \right] , \tag{7.4}
$$

where

$$
\mathrm{i}D_{n\perp}^\mu = \mathcal{P}_{n\perp}^\mu + gA_{n\perp}^\mu \tag{7.5}
$$

is the collinear covariant derivative and

$$
W_n(x) = \left[\sum_{\text{perms}} \exp\left(\frac{-g}{\overline{\mathcal{P}}_n} \bar{n}\cdot A_n(x) \right) \right] . \tag{7.6}
$$

The label operators in Eqs. (7.4) and (7.6) only act inside the square brackets. Here, $W_n(x)$ is a Wilson line of n-collinear gluons in label momentum space. It sums up arbitrary emissions of n-collinear gluons from an n-collinear quark or gluon, which are $\mathcal{O}(1)$ in the power counting. Since $W_n(x)$ is localized with respect to the residual position x, we can treat $\chi_{n,\omega}(x)$ and $\mathcal{B}_{n,\omega}^\mu(x)$ as local quark and gluon fields. The label momentum ω is treated as a continuous variable, which is why we use a δ-function operator in Eq. (7.4). It is set equal to the sum of the minus label momenta of all fields that the δ function acts on, including those in the Wilson lines, while the label momenta of the individual fields are summed over.

In general, the effective theory can contain several collinear sectors, each containing collinear fields along a different collinear direction. To have a well-defined power expansion in this case, the different collinear directions n_i have to be well separated [30],

$$
n_i\cdot n_j \gg \lambda^2 \qquad \text{for} \qquad i \neq j , \tag{7.7}
$$

which is simply the requirement that different collinear sectors are distinct and do not overlap. For $pp \to X\ell^+\ell^-$, we need two collinear sectors, n_a and n_b, along the directions of the two beams. We use a bar to denote the conjugate lightlike vector, so $n_i \cdot \bar{n}_i = 2$. As the beams are back to back, we have $n_a \sim \bar{n}_b$, so $n_a \cdot n_b \sim 2$ and Eq. (7.7) is easily satisfied.

Particles that exchange large momentum of $\mathcal{O}(Q)$ between collinear particles moving in

different directions have to be off shell by an amount of $\mathcal{O}(n_i \cdot n_j Q^2)$. These modes can be integrated out of the theory at the hard scale Q by matching full QCD onto SCET, which yields the hard function. The effective theory below the scale Q then splits into several distinct collinear sectors, where particles in the same collinear sector can still interact with each other, while at leading order in the power counting particles from different collinear sectors can only interact by the exchange of soft particles. This means that before and after the hard interaction takes place, the jets described by the different collinear sectors evolve independently from each other with only soft but no hard interactions between them.

The soft degrees of freedom, responsible for the radiation between collinear jets, are described in the effective theory by soft[1] quark and gluon fields, $q_s(x)$ and $A_s(x)$, which only have residual soft momentum dependence $\mathrm{i}\partial^\mu \sim \lambda^2 Q$. They couple to the collinear sectors via the soft covariant derivative

$$\mathrm{i}D_s^\mu = \mathrm{i}\partial^\mu + g A_s^\mu \tag{7.8}$$

acting on the collinear fields. At leading order in λ, n-collinear particles only couple to the $n \cdot A_s$ component of soft gluons, so the leading-order n-collinear Lagrangian only depends on $n \cdot D_s$. For n-collinear quarks [31, 37]

$$\mathcal{L}_n = \bar{\xi}_n \left(\mathrm{i}n \cdot D_s + g\, n \cdot A_n + \mathrm{i}\slashed{D}_{n\perp} W_n \frac{1}{\overline{\mathcal{P}}_n} W_n^\dagger \mathrm{i}\slashed{D}_{n\perp} \right) \frac{\slashed{\bar{n}}}{2} \xi_n \,. \tag{7.9}$$

The leading-order n-collinear Lagrangian for gluons is given in Ref. [35].

The coupling of soft gluons to collinear particles can be removed at leading order by defining new collinear fields [35]

$$\chi_{n,\omega}^{(0)}(x) = Y_n^\dagger(x)\, \chi_{n,\omega}(x)\,, \tag{7.10}$$

$$\mathcal{B}_{n,\omega\perp}^{\mu(0)}(x) = Y_n^\dagger(x)\, \mathcal{B}_{n,\omega\perp}^\mu(x)\, Y_n(x) = \mathcal{B}_{n,\omega\perp}^{\mu d}(x)\mathcal{Y}_n^{dc}(x)\, T^c,$$

where $Y_n(x)$ and $\mathcal{Y}_n(x)$ are soft Wilson lines in the fundamental and adjoint representations,

$$Y_n(x) = P \exp\left[\mathrm{i}g \int_{-\infty}^0 \mathrm{d}s\, n \cdot A_s(x + s\, n) \right]\,, \qquad T^c \mathcal{Y}_n^{cd}(x) = Y_n(x)\, T^d\, Y_n^\dagger(x)\,. \tag{7.11}$$

---

[1]In some situations it is necessary to distinguish two types of soft sectors, referred to as soft and ultrasoft in the SCET literature. In this paper we only need what are usually called ultrasoft particles, so we will simply refer to these as soft.

$$p^\mu = x E_{\rm cm}\frac{n^\mu}{2} - b^+\frac{\bar{n}^\mu}{2} - b_\perp^\mu$$

$$\xi E_{\rm cm}\frac{n^\mu}{2}$$

$$P^\mu = E_{\rm cm}\frac{n^\mu}{2} \qquad r = (1-\xi) E_{\rm cm}\frac{n^\mu}{2}$$

$$b^\mu = (\xi - x) E_{\rm cm}\frac{n^\mu}{2} + b^+\frac{\bar{n}^\mu}{2} + b_\perp^\mu$$
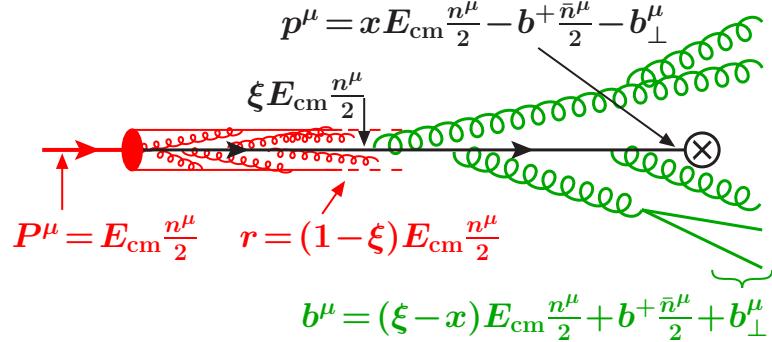
Figure 7-1: Definition of the different collinear momenta related to the incoming beams. The soft radiation is not shown.

The symbol P in Eq. (7.11) denotes the path ordering of the color generators along the integration path. The integral limits in Eq. (7.11) with the reference point at $-\infty$ are the natural choice for incoming particles [70]. The final results are always independent of the choice of reference point, and with the above choice the interpolating fields for the incoming proton states do not introduce additional Wilson lines [21].

After the field redefinition in Eq. (7.10), the leading-order SCET Lagrangian separates into the sum of independent n_i-collinear and soft Lagrangians,

$$\mathcal{L}_{\rm SCET} = \sum_{n_i} \mathcal{L}_{n_i}^{(0)} + \mathcal{L}_s + \cdots , \tag{7.12}$$

with no interactions between any of the collinear and soft sectors. The ellipses denote terms that are subleading in the power counting. This decoupling is what will allow us to factorize the cross section into separate beam and soft functions. The field redefinition in Eq. (7.10) introduces soft Wilson lines in the operators, which because of Eq. (7.12) can be factored out of the matrix element and will make up the soft function.

7.2 Kinematics

Before deriving the factorization theorem, we discuss the relevant kinematics, as illustrated in Fig. 7-1. As already mentioned, we introduce a separate set of collinear fields for each of the beams, with the light-cone vectors n_a and n_b aligned with the beam directions. To derive the factorization theorem we work in the center-of-mass frame of the hadronic collision, so

the momenta of the incoming protons are (neglecting the proton mass)

$$P_a^\mu = E_{\rm cm} \frac{n_a^\mu}{2}\,, \qquad P_b^\mu = E_{\rm cm} \frac{n_b^\mu}{2}\,, \tag{7.13}$$

with $\vec{n}_a = -\vec{n}_b$. In particular, $n_b = \bar{n}_a$ and $n_a \cdot n_b = 2$. We will mostly keep the dependence on the two beam directions explicit, but one should keep in mind that n_a and n_b are related.

The collinear fields in the n_a and n_b directions describe the interactions within each of the beams before and after the collision, and are also responsible for initiating the hard interaction. We define the momenta of the spacelike off-shell partons that go into the hard interaction as

$$p_a^\mu = x_a E_{\rm cm} \frac{n_a^\mu}{2} - b_a^+ \frac{\bar{n}_a^\mu}{2} - b_{a\perp}^\mu\,, \qquad p_b^\mu = x_b E_{\rm cm} \frac{n_b^\mu}{2} - b_b^+ \frac{\bar{n}_b^\mu}{2} - b_{b\perp}^\mu\,, \tag{7.14}$$

where x_a and x_b are the light-cone momentum fractions at which the beam functions will be evaluated. The power-counting parameters for the collinear sectors are

$$\lambda_a^2 \sim \frac{b_a^+}{x_a E_{\rm cm}}\,, \qquad \lambda_b^2 \sim \frac{b_b^+}{x_b E_{\rm cm}}\,, \tag{7.15}$$

where the relevant momenta are those of the off-shell partons in Eq. (7.14), because these are the momenta carried by the n_a- and n_b-collinear fields.

We write the momentum of the incoming partons that are taken out of the proton as

$$\xi_a E_{\rm cm} \frac{n_a^\mu}{2} + \mathcal{O}(\Lambda_{\rm QCD})\,, \qquad \xi_b E_{\rm cm} \frac{n_b^\mu}{2} + \mathcal{O}(\Lambda_{\rm QCD})\,, \tag{7.16}$$

which defines the light-cone momentum fractions $\xi_{a,b}$ at which the PDFs are evaluated. The typical $\perp$-momenta of partons in the proton are $\mathcal{O}(\Lambda_{\rm QCD})$, while the small plus components are $\mathcal{O}(\Lambda_{\rm QCD}^2/E_{\rm cm})$. These momenta are much smaller than any soft or residual momenta in SCET$_{\rm I}$ and are expanded, which precisely corresponds to the OPE for the beam functions in Eq. (2.31) when matching them onto SCET$_{\rm II}$.

The momentum of the final-state remnant of the proton is thus given by

$$r_a^\mu = (1 - \xi_a) E_{\rm cm} \frac{n_a^\mu}{2}\,, \tag{7.17}$$

while the remnant of the initial-state jet radiated into the final state by the beam function

has momentum

$$b_a^\mu = (\xi_a - x_a)E_{\text{cm}} \frac{n_a^\mu}{2} + b_a^+ \frac{\bar{n}_a^\mu}{2} + b_{a\perp}^\mu \,, \tag{7.18}$$

and similarly for the n_b direction. The total n_a-collinear momentum in the final state is the sum of Eqs. (7.17) and (7.18), or equivalently, the difference between the proton momentum and Eq. (7.14),

$$b_a^\mu + r_a^\mu = P_a^\mu - p_a^\mu = (1 - x_a)E_{\text{cm}} \frac{n_a^\mu}{2} + b_a^+ \frac{\bar{n}_a^\mu}{2} + b_{a\perp}^\mu \,. \tag{7.19}$$

In addition to the collinear momenta, we define k_s^μ as the total four-momentum of the soft radiation in the final state. Hence, the total hadronic momentum in the final state is given by

$$p_X^\mu = (P_a^\mu - p_a^\mu) + (P_b^\mu - p_b^\mu) + k_s^\mu \,, \tag{7.20}$$

and we can write total momentum conservation $P_a^\mu + P_b^\mu = p_X^\mu + q^\mu$ as

$$p_a^\mu + p_b^\mu = q^\mu + k_s^\mu \,, \tag{7.21}$$

where q^μ is the total leptonic momentum.

The collinear and soft momenta, b_a^μ, b_b^μ, k_s^μ are not experimentally measurable quantities. Instead, the experiments can only measure hadronic quantities, such as the hemisphere momenta $B_a^+ = n_a \cdot B_a$ and $B_b^+ = n_b \cdot B_b$ introduced in Sec. 2.1. Splitting the total soft momentum into its contributions from each hemisphere, $k_s^\mu = k_a^\mu + k_b^\mu$ as shown in Fig. 2-2, we then have

$$B_a^\mu = b_a^\mu + r_a^\mu + k_a^\mu \,, \qquad B_b^\mu = b_b^\mu + r_b^\mu + k_b^\mu \,, \tag{7.22}$$

and defining $k_a^+ = n_a \cdot k_a$, $k_b^+ = n_b \cdot k_b$, we get

$$B_a^+ = n_a \cdot B_a = b_a^+ + k_a^+ \,, \qquad B_b^+ = n_b \cdot B_b = b_b^+ + k_b^+ \,. \tag{7.23}$$

In particular, the remnant momenta $r_{a,b}^\mu$ do not contribute to $B_{a,b}^+$. A physical argument for this was discussed in Sec. 2.1.

Next, we decompose the total leptonic momentum as

$$q^\mu = q^- \frac{n_a^\mu}{2} + q^+ \frac{n_b^\mu}{2} + q_\perp^\mu \,, \tag{7.24}$$

where $q_\perp^\mu$ contains the two components of q^μ transverse to the beam direction. Taking the z-axis along the $\vec{n}_a$ beam direction, we have

$$q^\pm = q^0 \mp q_z \,, \qquad q_\perp^\mu = (0, \vec{q}_T, 0) \,, \tag{7.25}$$

where $\vec{q}_T = (q_x, q_y)$ is a two-vector in the transverse x-y-plane. The total leptonic invariant mass and rapidity are

$$q^2 = q^+ q^- + q_\perp^2 = q^+ q^- - \vec{q}_T^{\,2} \,, \qquad Y = \frac{1}{2} \ln \frac{q^-}{q^+} \,, \tag{7.26}$$

with

$$q^\mp = e^{\pm Y} \sqrt{q^2 + \vec{q}_T^{\,2}} \,, \qquad \mathrm{d}^4 q = \frac{1}{2} \mathrm{d}q^+ \mathrm{d}q^- \, \mathrm{d}^2 \vec{q}_T = \frac{1}{2} \mathrm{d}q^2 \, \mathrm{d}Y \, \mathrm{d}^2 \vec{q}_T \,. \tag{7.27}$$

As we will see in the next section, the derivation of the factorization theorem requires us to be insensitive to the transverse components $\vec{q}_T$ such that we can freely integrate over them. Therefore, we have to expand the kinematics in the limit $\vec{q}_T = 0$. This expansion is justified because from Eq. (7.21) we have

$$q_\perp^\mu = -p_{X\perp}^\mu = -b_{a\perp}^\mu - b_{a\perp}^\mu - k_{s\perp}^\mu \sim \lambda Q \,. \tag{7.28}$$

A parametrically large $q_\perp^\mu \sim Q$ would require a separate jet at large $p_T \sim Q$ to balance the transverse momentum, which is not allowed in our setup. The kinematics of the hard matrix element in the factorization theorem is then given by the tree-level partonic kinematics, with the partonic momentum conservation

$$x_a E_{\mathrm{cm}} \frac{n_a^\mu}{2} + x_b E_{\mathrm{cm}} \frac{n_b^\mu}{2} = q = q^- \frac{n_a^\mu}{2} + q^+ \frac{n_b^\mu}{2} \,, \tag{7.29}$$

which implies

$$x_a E_{\mathrm{cm}} = q^- = \sqrt{q^2} \, e^Y \,, \qquad\qquad q^2 = q^+ q^- = x_a x_b E_{\mathrm{cm}}^2 \,,$$

$$x_b E_{\mathrm{cm}} = q^+ = \sqrt{q^2} \, e^{-Y} \,, \qquad\qquad Y = \frac{1}{2} \ln \frac{q^-}{q^+} = \frac{1}{2} \ln \frac{x_a}{x_b} \,. \tag{7.30}$$

Equations (7.28) and (7.29) imply that parametrically the leptons are back to back in the

122

transverse plane. Since q^+ and q^- can differ substantially, the leptons do not need to be back to back in three dimensions.

7.3 Derivation of Isolated Factorization Theorem

We now proceed to derive the isolated factorization theorem for generic processes $pp \to XL$, where the hadronic final state X has a restriction on the hemisphere momenta $B_{a,b}^+$. The derivation is carried out using SCET without Glauber degrees of freedom. The proof that Glauber effects are not required is given at the end of this section.

7.3.1 Cross Section in QCD

We will generically refer to properties of L as "leptonic", even though L can contain any non-strongly interacting particles. We only consider processes where the hard interaction couples the strong and electroweak sectors through one two-particle QCD current. (This includes for example Drell-Yan or Higgs production through gluon fusion with the Higgs decaying non-hadronically, but does not include electroweak Higgs production via vector-boson fusion.) Then, at leading order in the electroweak interactions, we can factorize the full-theory matrix element into its leptonic and hadronic parts

$$\mathcal{M}(pp \to XL) = \sum_J L_J \left\langle X | J | pp \right\rangle . \tag{7.31}$$

The sum runs over all relevant color-singlet two-particle QCD currents J, and L_J contains the corresponding electroweak matrix element, including the electroweak propagator coupling to J. For example, for Drell-Yan with $L = \ell^+ \ell^-$, the relevant currents are

$$J_{Vf}^\mu = \bar{q}_f \gamma^\mu q_f , \qquad J_{Af}^\mu = \bar{q}_f \gamma^\mu \gamma_5 q_f , \tag{7.32}$$

so in this case the sum over J in Eq. (7.31) includes the sums over the two Dirac structures, the vector index μ, and the quark flavor $f = \{u, d, \ldots\}$. The corresponding L_{Vf}^μ and L_{Af}^μ are given below in Eq. (7.71).

The cross section for some hadronic observable O in the center-of-mass frame of the

collision, averaged over proton spins, is

$$\frac{\mathrm{d}\sigma}{\mathrm{d}q^2\mathrm{d}Y\mathrm{d}O} = \frac{1}{2E_{\mathrm{cm}}^2} \int \frac{\mathrm{d}^2\vec{q}_T}{2(2\pi)^4} \int \mathrm{d}\Phi_L \, (2\pi)^4 \delta^4(q - p_L) \tag{7.33}$$

$$\times \frac{1}{4}\sum_{\mathrm{spins}}\sum_X |\mathcal{M}(pp \to XL)|^2 \, \delta[O - f_O(X)] \, (2\pi)^4\delta^4(P_a + P_b - q - p_X) \,.$$

Here, $P_{a,b}$ are the incoming proton momenta, p_X and p_L are the total hadronic and leptonic momenta, $\mathrm{d}\Phi_L$ denotes the leptonic phase space, and the phase-space integrations for the hadronic final states are included in the sum over X. The last δ function is overall momentum conservation. The function $f_O(X)$ inside the second δ function returns the value of the hadronic observable O for a given hadronic state X, so the δ function picks out all final states that contribute to a certain value of O. The $\delta^4(q - p_L)$ under the leptonic phase-space integral defines the measured q as the total leptonic momentum. Expanding this δ function for $\vec{q}_T = 0$, the leptonic part does not depend on $\vec{q}_T$ at leading order, and using Eq. (7.31), we can rewrite Eq. (7.33) as

$$\frac{\mathrm{d}\sigma}{\mathrm{d}q^2\mathrm{d}Y\mathrm{d}O} = \frac{1}{2E_{\mathrm{cm}}^2}\sum_{J,J'} L_{JJ'}(q^2, Y) \, W_{JJ'}(q^2, Y, O) \,. \tag{7.34}$$

The leptonic tensor is defined as

$$L_{JJ'}(q^2, Y) = \int \mathrm{d}\Phi_L \, L_J^\dagger L_{J'} \, (2\pi)^4\delta^4\left(q^-\frac{n_a}{2} + q^+\frac{n_b}{2} - p_L\right), \tag{7.35}$$

where $q^\pm = \sqrt{q^2}e^{\mp Y}$. The hadronic tensor contains the square of the hadronic matrix element

$$W_{JJ'}(q^2, Y, O) = \int \frac{\mathrm{d}^2\vec{q}_T}{2(2\pi)^4}\sum_X \langle pp|J^\dagger(0)|X\rangle\langle X|J'(0)|pp\rangle$$

$$\times (2\pi)^4\delta^4(P_a + P_b - q - p_X) \, \delta[O - f_O(X)] \,, \tag{7.36}$$

where as in Ch. 3 we keep the average over proton spins implicit in the matrix element. Since $W_{JJ'}$ is integrated over $\vec{q}_T$, it can only depend on q^2 and Y, as well as the hadronic observable O.

We are interested in the hadronic observables $B_a^+ = n_a \cdot B_a$ and $B_b^+ = n_b \cdot B_b$. The hemisphere hadronic momenta $B_{a,b}^\mu(X)$ can be obtained from the states $|X\rangle$ using the

124

hemisphere momentum operators $\hat{p}^{\mu}_{a,b}$

$$\hat{p}^{\mu}_a|X\rangle = B^{\mu}_a(X)|X\rangle\,, \qquad \hat{p}^{\mu}_b|X\rangle = B^{\mu}_b(X)|X\rangle\,. \tag{7.37}$$

A field-theoretic definition of $\hat{p}^{\mu}_{a,b}$ in terms of the energy-momentum tensor of the field theory was given in Ref. [32]. The hadronic tensor for $O \equiv \{B^+_a, B^+_b\}$ is

$$W_{JJ'}(q^2, Y, B^+_a, B^+_b) \tag{7.38}$$

$$= \int \frac{\mathrm{d}^2\vec{q}_T}{2(2\pi)^4} \int \mathrm{d}^4x\, e^{-iq\cdot x} \sum_X \langle pp|J^\dagger(x)|X\rangle\langle X|J'(0)|pp\rangle\, \delta[B^+_a - n_a\cdot B_a(X)]\, \delta[B^+_b - n_b\cdot B_b(X)]$$

$$= \int \frac{\mathrm{d}x^+\mathrm{d}x^-}{(4\pi)^2}\, e^{-i(q^+x^- + q^-x^+)/2} \left\langle pp\middle|J^\dagger\left(x - \frac{n_a}{2} + x^+\frac{n_b}{2}\right)\delta(B^+_a - n_a\cdot\hat{p}_a)\,\delta(B^+_b - n_b\cdot\hat{p}_b)J'(0)\middle|pp\right\rangle.$$

In the first line we used momentum conservation to shift the position of $J^\dagger$, and in the second line we performed the integral over $\vec{q}_T$, which sets $\vec{x}_T$ to zero. We also used Eq. (7.37) to eliminate the explicit dependence on X, allowing us to carry out the sum over all states X. The restriction on the states X is now implicit through the operator δ functions inside the matrix element.

7.3.2   Matching QCD onto SCET

In the next step, we match the QCD currents J onto SCET currents by integrating out fluctuations at the hard scale Q. At leading order in the power counting, the matching takes the form

$$J(x) = \sum_{n_1,n_2} \int \mathrm{d}\omega_1\, \mathrm{d}\omega_2\, e^{-i(\tilde{b}_1+\tilde{b}_2)\cdot x} \left[\sum_q C^{\alpha\beta}_{Jq\bar{q}}(\tilde{b}_1,\tilde{b}_2)\, O^{\alpha\beta}_{q\bar{q}}(\tilde{b}_1,\tilde{b}_2;x) \right.$$

$$\left. + C^{\mu\nu}_{Jgg}(\tilde{b}_1,\tilde{b}_2)\, O_{gg\,\mu\nu}(\tilde{b}_1,\tilde{b}_2;x) \right], \tag{7.39}$$

where α, β are spinor indices, μ, ν are vector indices, and the sum over q runs over all quark flavors $\{u, d, \ldots\}$. The Wilson coefficients and operators depend on the large label momenta

$$\tilde{b}^{\mu}_1 = \omega_1 \frac{n^{\mu}_1}{2}\,, \qquad \tilde{b}^{\mu}_2 = \omega_2 \frac{n^{\mu}_2}{2}\,. \tag{7.40}$$

They will eventually be set to either $q^- n^{\mu}_a/2$ or $q^+ n^{\mu}_b/2$ by momentum conservation, but at this point are unspecified, and the sums and integrals over n_1, n_2 and ω_1, ω_2 in Eq. (7.39)

run over all sets of distinct collinear directions and large label momenta. On the right-hand side of Eq. (7.39), the full x dependence of the current is separated into the x dependence appearing in the overall phase factor with large label momenta and the residual x dependence of the SCET operators.

The SCET operators $O_{q\bar{q}}^{\alpha\beta}(x)$ and $O_{gg}^{\mu\nu}(x)$ are constructed out of the collinear fields in Eq. (7.4). At leading order in the power counting they contain one field for each collinear direction. Since the QCD currents are color singlets, the leading operators that can contribute are

$$O_{q\bar{q}}^{\alpha\beta}(\tilde{b}_1, \tilde{b}_2; x) = \bar{\chi}_{n_1, -\omega_1}^{\alpha j}(x)\, \chi_{n_2, \omega_2}^{\beta j}(x)\,, \qquad O_{gg}^{\mu\nu}(\tilde{b}_1, \tilde{b}_2; x) = \sqrt{\omega_1\,\omega_2}\, \mathcal{B}_{n_1, -\omega_1\perp}^{\mu c}(x)\, \mathcal{B}_{n_2, -\omega_2\perp}^{\nu c}(x)\,,$$

(7.41)

where j and c are color indices in the fundamental and adjoint representations. We included appropriate minus signs on the labels, such that we always have $\omega_{1,2} > 0$ for incoming particles. Here, $\chi \equiv \chi_q$ is a quark field of flavor q, which for simplicity we keep implicit in our notation. Note that the entire spin and flavor structure of the current J is hidden in the label J on the matching coefficients in Eq. (7.39). The gluon operator is symmetric under interchanging both $\mu \leftrightarrow \nu$ and $\tilde{b}_1 \leftrightarrow \tilde{b}_2$, so its matching coefficient must have the same symmetry,

$$C_{Jgg}^{\nu\mu}(\tilde{b}_2, \tilde{b}_1) = C_{Jgg}^{\mu\nu}(\tilde{b}_1, \tilde{b}_2)\,. \tag{7.42}$$

We define the conjugate quark operator and matching coefficient with the usual factors of γ^0, i.e.,

$$O_{q\bar{q}}^{\dagger\beta\alpha}(\tilde{b}_1, \tilde{b}_2) = \bar{\chi}_{n_2, \omega_2}^{\beta j}(x)\, \chi_{n_1, -\omega_1}^{\alpha j}(x)\,, \qquad \bar{C}_{Jq\bar{q}}^{\beta\alpha}(\tilde{b}_1, \tilde{b}_2) = [\gamma^0 C_{Jq\bar{q}}^{\dagger}(\tilde{b}_1, \tilde{b}_2)\gamma^0]^{\beta\alpha}\,. \tag{7.43}$$

The matching coefficients are obtained by computing the renormalized matrix elements $\langle 0|...|q\bar{q}\rangle$ and $\langle 0|...|gg\rangle$ on both sides of Eq. (7.39) and comparing the results. In pure dimensional regularization for UV and IR divergences all loop graphs in SCET are scaleless and vanish, which means the UV and IR divergences in the bare matrix elements precisely cancel each other. The renormalized matrix elements of the right-hand side of Eq. (7.39) are then given by their tree-level expressions plus pure $1/\epsilon$ IR divergences, which cancel against those of the full-theory matrix elements $\langle 0|J|q\bar{q}\rangle$ and $\langle 0|J|gg\rangle$ of the left-hand side. Hence, the matching coefficients in $\overline{\text{MS}}$ are given in terms of the IR-finite parts of the renormalized

full-theory matrix elements computed in pure dimensional regularization.

7.3.3 Soft-Collinear Factorization

The field redefinitions in Eq. (7.10) introduce soft Wilson lines into the operators in Eq. (7.41),

$$O_{q\bar{q}}^{\alpha\beta}(x) = \bar{\chi}_{n_1,-\omega_1}^{(0)\alpha j}(x) \, T\big[Y_{n_1}^\dagger(x) \, Y_{n_2}(x)\big]^{jk} \chi_{n_2,\omega_2}^{(0)\beta k}(x) \,,$$

$$O_{gg}^{\mu\nu}(x) = \sqrt{\omega_1 \, \omega_2} \, \mathcal{B}_{n_1,-\omega_1\perp}^{(0)\mu c}(x) T\big[\mathcal{Y}_{n_1}^\dagger(x)\mathcal{Y}_{n_2}(x)\big]^{cd} \mathcal{B}_{n_2,-\omega_2\perp}^{(0)\nu d}(x) \,. \qquad (7.44)$$

The time ordering is required to ensure the proper ordering of the soft gluon fields inside the Wilson lines. It only affects the ordering of the field operators, while the ordering of the color generators is still determined by the (anti)path ordering of the Wilson lines. In the remainder, we use these redefined fields and drop the (0) superscript for convenience.

Since the momentum operator is linear in the Lagrangian, Eq. (7.12) allows us to write the hemisphere momentum operators as the sum of independent operators acting in the separate collinear and soft sectors,

$$\hat{p}_a = \hat{p}_{a,n_a} + \hat{p}_{a,n_b} + \hat{p}_{a,s} \,, \qquad \hat{p}_b = \hat{p}_{b,n_a} + \hat{p}_{b,n_b} + \hat{p}_{b,s} \,. \qquad (7.45)$$

The n_a (n_b) collinear sector cannot contribute momentum in the n_b (n_a) hemisphere. Thus, $\hat{p}_{a,n_b} = \hat{p}_{b,n_a} = 0$, while $\hat{p}_{a,n_a} = \hat{p}_{n_a}$ and $\hat{p}_{b,n_b} = \hat{p}_{n_b}$ reduce to the total momentum operators for each of the collinear sectors. For the soft sector, the distinction between the two hemisphere operators is important. We can now write

$$\delta(B_a^+ - n_a \cdot \hat{p}_a) = \int \mathrm{d}b_a^+ \, \mathrm{d}k_a^+ \, \delta(B_a^+ - b_a^+ - k_a^+) \, \delta(b_a^+ - n_a \cdot \hat{p}_{n_a}) \, \delta(k_a^+ - n_a \cdot \hat{p}_{a,s}) \,,$$

$$\delta(B_b^+ - n_b \cdot \hat{p}_b) = \int \mathrm{d}b_b^+ \, \mathrm{d}k_b^+ \, \delta(B_b^+ - b_b^+ - k_b^+) \, \delta(b_b^+ - n_b \cdot \hat{p}_{n_b}) \, \delta(k_b^+ - n_b \cdot \hat{p}_{b,s}) \,. \qquad (7.46)$$

Using Eq. (7.39) in the hadronic tensor in Eq. (7.38), the forward matrix element of the product of currents turns into the forward matrix element of the product of the operators in Eq. (7.44). Since the Lagrangian in Eq. (7.12) contains no interactions between the collinear and soft sectors after the field redefinition, we can use Eq. (7.46) to factorize the resulting matrix element into a product of independent n_a-collinear, n_b-collinear, and soft matrix elements.

We first look at the contribution from $O_{q\bar{q}}$. The x integral of the forward matrix element of $O_{q\bar{q}}$ becomes

$$
\int \frac{\mathrm{d}x^+ \mathrm{d}x^-}{(4\pi)^2}\, e^{-\mathrm{i}(q^+ x^- + q^- x^+)/2}\, e^{\mathrm{i}(\tilde{b}_1 + \tilde{b}_2)\cdot x}
$$

$$
\left\langle p_{n_a} p_{n_b} \middle| O_{q\bar{q}}^{\dagger\beta\alpha}(x)\, \delta(B_a^+ - n_a \cdot \hat{p}_a)\, \delta(B_b^+ - n_b \cdot \hat{p}_b)\, O_{q\bar{q}}^{\alpha'\beta'}(0) \middle| p_{n_a} p_{n_b} \right\rangle
$$

$$
= \int \frac{\mathrm{d}x^+ \mathrm{d}x^-}{(4\pi)^2}\, e^{-\mathrm{i}(q^+ x^- + q^- x^+)/2} \int \mathrm{d}b_a^+\, \mathrm{d}b_b^+\, \mathrm{d}k_a^+\, \mathrm{d}k_b^+\, \delta(B_a^+ - b_a^+ - k_a^+)\, \delta(B_b^+ - b_b^+ - k_b^+)
$$

$$
\times \int \mathrm{d}\omega_a\, \mathrm{d}\omega_b\, e^{\mathrm{i}(\omega_a x^+ + \omega_b x^-)/2}
$$

$$
\times \Bigg\{ \delta_{n_2 n_a}\, \delta(\omega_2 - \omega_a)\, \delta_{n_2' n_a}\, \delta(\omega_2' - \omega_a)\, \delta_{n_1 n_b}\, \delta(\omega_1 - \omega_b)\, \delta_{n_1' n_b}\, \delta(\omega_1' - \omega_b)
$$

$$
\times \left\langle 0 \middle| \overline{T} \left[Y_{n_a}^\dagger(x)\, Y_{n_b}(x) \right]^{kj} \delta(k_a^+ - n_a \cdot \hat{p}_{a,s})\, \delta(k_b^+ - n_b \cdot \hat{p}_{b,s})\, T \left[Y_{n_b}^\dagger(0)\, Y_{n_a}(0) \right]^{j'k'} \middle| 0 \right\rangle
$$

$$
\times \theta(\omega_a) \left\langle p_{n_a} \middle| \bar{\chi}_{n_a}^{\beta k}(x)\, \delta(b_a^+ - n_a \cdot \hat{p}_{n_a})\, \delta(\omega_a - \overline{\mathcal{P}}_{n_a})\, \chi_{n_a}^{\beta' k'}(0) \middle| p_{n_a} \right\rangle
$$

$$
\times \theta(\omega_b) \left\langle p_{n_b} \middle| \chi_{n_b}^{\alpha j}(x)\, \delta(b_b^+ - n_b \cdot \hat{p}_{n_b})\, \delta(\omega_b - \overline{\mathcal{P}}_{n_b})\, \bar{\chi}_{n_b}^{\alpha' j'}(0) \middle| p_{n_b} \right\rangle + (a \leftrightarrow b) \Bigg\}. \quad (7.47)
$$

Here, $|p_{n_a}\rangle$ and $|p_{n_b}\rangle$ are the proton states with momenta $P_{a,b}^\mu = E_{\mathrm{cm}} n_{a,b}^\mu / 2$ as in Eq. (7.13). The two terms in brackets in Eq. (7.47) arise from the different ways of matching up the fields with the external proton states. The restriction to have positive labels ω requires the fields in $O_{q\bar{q}}$ to be matched with the incoming proton states and the fields in $O_{q\bar{q}}^\dagger$ with the outgoing proton states. In principle, there are two more ways to match the fields and external states, yielding matrix elements with the structure $\langle p | \chi \chi | p \rangle$ and $\langle p | \bar{\chi} \bar{\chi} | p \rangle$, which vanish due to quark flavor number conservation in QCD. For the same reason, in the full product $(\sum_q O_{q\bar{q}}^\dagger)(\sum_{q'} O_{q'\bar{q}'})$ only the flavor-diagonal term with $q = q'$ survives.

We abbreviate the collinear and soft matrix elements in the last three lines of Eq. (7.47) as $M_{\omega_a}(x^-)$, $M_{\omega_b}(x^+)$, $M_s(x^+, x^-)$. The collinear matrix elements only depend on one light-cone coordinate because the label momenta $\omega_{a,b}$ are defined to be continuous. We could have also started with discrete label momenta, $\tilde{\omega}_{a,b}$, and then convert to continuous labels by absorbing the residual $k_{n_a}^-$ dependence as follows:

$$
\sum_{\tilde{\omega}_a} e^{\mathrm{i}\tilde{\omega}_a x^+/2}\, M_{\tilde{\omega}_a}(x^+, x^-) = \sum_{\tilde{\omega}_a} \int \mathrm{d}k_a^-\, e^{\mathrm{i}(\tilde{\omega}_a + k_{n_a}^-) x^+/2}\, M_{\tilde{\omega}_a + k_{n_a}^-}(x^-)
$$

$$
= \int \mathrm{d}\omega_a\, e^{\mathrm{i}\omega_a x^+/2}\, M_{\omega_a}(x^-), \quad (7.48)
$$

and analogously for $M_{\omega_b}(x^+)$. In the second step we used that by reparameterization invariance the Fourier-transformed matrix element can only depend on $\tilde{\omega}_a + k^-_{n_a} = \omega_a$.

As an aside, note that in the well-studied case where the collinear matrix elements are between vacuum states, giving rise to jet functions, the distinction between discrete and continuous labels is not as relevant. In that case, the SCET Feynman rules imply that the collinear matrix elements do not depend on the residual k^- (and $k_\perp$) components, and therefore the label momenta can be treated in either way. In our case, momentum conservation with the external state forces the collinear matrix elements to depend on k^-. Therefore, the only way to eliminate the residual k^- dependence is to absorb it into continuous ω labels. One can easily see this already at tree level. Replacing the proton states by quark states with momentum $p = \tilde{p} + p_r$, we get

$$
\int \frac{\mathrm{d}x^+ \, \mathrm{d}x^-}{(4\pi)^2} e^{-\mathrm{i}(k^- x^+ + k^+ x^-)/2} \left\langle q(p) \middle| \bar{\chi}_n(x^+, x^-) \, \delta_{\tilde{\omega}, \overline{\mathcal{P}}_n} \, \chi_n(0) \middle| q(p) \right\rangle
$$
$$
= \bar{u} u \, \delta_{\tilde{\omega}, \tilde{p}^-} \, \delta(k^- - p_r^-) \, \delta(k^+ - p_r^+) , \tag{7.49}
$$

and the label and residual minus momenta are combined using $\delta_{\tilde{\omega}, \tilde{p}^-} \, \delta(k^- - p_r^-) = \delta(\omega - p^-)$. Our continuous ω is physical and corresponds to the momentum fraction of the quark in the proton.

Returning to our discussion, to perform the x integral in Eq. (7.47), we take the residual Fourier transforms of the matrix elements,

$$
M_{\omega_a}(x^-) = \int \frac{\mathrm{d}k^+}{2\pi} e^{\mathrm{i}k^+ x^-/2} \, \widetilde{M}_{\omega_a}(k^+) , \qquad M_{\omega_b}(x^+) = \int \frac{\mathrm{d}k^-}{2\pi} e^{\mathrm{i}k^- x^+/2} \, \widetilde{M}_{\omega_b}(k^-) ,
$$
$$
M_s(x^-, x^+) = \int \frac{\mathrm{d}k_s^+ \, \mathrm{d}k_s^-}{(2\pi)^2} e^{\mathrm{i}(k_s^+ x^+ + k_s^- x^+)/2} \, \widetilde{M}_s(k_s^+, k_s^-) . \tag{7.50}
$$

Just as $x^\pm$, the residual momenta $k^\pm$ and $k_s^\pm$ here are all defined with respect to the common $n = n_a$. The x integral in Eq. (7.47) now becomes

$$
\int \frac{\mathrm{d}x^+ \mathrm{d}x^-}{(4\pi)^2} e^{\mathrm{i}(\omega_a - q^-)x^+/2} e^{\mathrm{i}(\omega_b - q^+)x^-/2} M_{\omega_a}(x^-) \, M_{\omega_b}(x^+) \, M_s(x^+, x^-)
$$
$$
= \int \frac{\mathrm{d}k^+}{2\pi} \frac{\mathrm{d}k^-}{2\pi} \frac{\mathrm{d}k_s^+ \, \mathrm{d}k_s^-}{(2\pi)^2} \, \widetilde{M}_{\omega_a}(k^+) \, \widetilde{M}_{\omega_b}(k^-) \, \widetilde{M}_s(k_s^+, k_s^-)
$$
$$
\times \, \delta(\omega_a - q^- + k^- + k_s^-) \, \delta(\omega_b - q^+ + k^+ + k_s^+)
$$
$$
= \delta(\omega_a - q^-) \, \delta(\omega_b - q^+) \, M_{\omega_a}(0) \, M_{\omega_b}(0) \, M_s(0) . \tag{7.51}
$$

In the last step we expanded $q^\pm - k^\pm - k_s^\pm = q^\pm[1 + \mathcal{O}(\lambda^2)]$. The remaining residual integrations are then simply the Fourier transforms of the matrix elements at $x = 0$.

Note that without the integration over $\vec{q}_T$ in the hadronic tensor Eq. (7.38), the currents would depend on $x_\perp$, which would require us to include perpendicular components $b_{a,b\perp}$ in the label momenta, and the soft matrix element would depend on $x_\perp$, too. (The residual $k_\perp$ dependence in the collinear matrix elements can again be absorbed into continuous $b_{a,b\perp}$.) The corresponding $x_\perp$ integration in Eq. (7.51) would yield an additional δ function $\delta^2(\vec{b}_{a\perp} + \vec{b}_{b\perp} + \vec{q}_T - \vec{k}_{s\perp})$. Integrating over $\vec{q}_T$ effectively eliminates this δ function, which would otherwise force us to introduce an explicit dependence on $b_{a,b\perp}$ in the beam functions. If one considers the q_T spectrum of the dileptons for $q_T^2 \ll q^2$, our analysis here provides a starting point but requires further study. One cannot just use p_T in place of $B_{a,b}^+$ with our arguments to impose an analogous restriction on the final state, because at $\mathcal{O}(\alpha_s^2)$ one can have two jets at high $\vec{p}_T$ that still have small total $\vec{p}_T$.

The n_a-collinear matrix element now reduces to the quark beam functions defined in Eq. (3.10),

$$
\begin{aligned}
M_{\omega_a}(0) &= \theta(\omega_a)\Big\langle p_{n_a}\Big|\bar{\chi}_{n_a}^{\beta k}(0)\,\delta(b_a^+ - n_a\cdot\hat{p}_{n_a})\,\delta(\omega_a - \overline{\mathcal{P}}_{n_a})\,\chi_{n_a}^{\beta'k'}(0)\Big|p_{n_a}\Big\rangle \\
&= \frac{\slashed{n}_a^{\beta'\beta}}{4}\frac{\delta^{k'k}}{N_c}\theta(\omega_a)\Big\langle p_{n_a}\Big|\bar{\chi}_{n_a}(0)\,\delta(b_a^+ - n_a\cdot\hat{p}_{n_a})\,\delta(\omega_a - \overline{\mathcal{P}}_{n_a})\frac{\slashed{\bar{n}}_a}{2}\chi_{n_a}(0)\Big|p_{n_a}\Big\rangle \\
&= \frac{\slashed{n}_a^{\beta'\beta}}{4}\frac{\delta^{k'k}}{N_c}\theta(\omega_a)\int\frac{dy^-}{4\pi}\,e^{ib_a^+y^-/2} \\
&\quad \times \Big\langle p_{n_a}\Big|e^{-i\hat{p}_{n_a}^+y^-/2}\,e^{i\hat{p}_{n_a}^+y^-/2}\,\bar{\chi}_{n_a}(0)\,e^{-i\hat{p}_{n_a}^+y^-/2}\,\delta(\omega_a - \overline{\mathcal{P}}_{n_a})\frac{\slashed{\bar{n}}_a}{2}\chi_{n_a}(0)\Big|p_{n_a}\Big\rangle \\
&= \frac{\slashed{n}_a^{\beta'\beta}}{4}\frac{\delta^{k'k}}{N_c}\,\omega_a B_q(\omega_a b_a^+, \omega_a/P_a^-)\,.
\end{aligned}
\tag{7.52}
$$

We abbreviated $\hat{p}_{n_a}^+ = n_a \cdot \hat{p}_{n_a}$, and in the last step we used $e^{i\hat{p}_n^+y^-/2}\bar{\chi}_n(0)\,e^{-i\hat{p}_n^+y^-/2} = \bar{\chi}_n(y^-n/2)$ and $\hat{p}_n^+|p_n\rangle = 0$. Similarly, for the antiquark beam function we have

$$
\begin{aligned}
M_{\omega_b}(0) &= \theta(\omega_b)\Big\langle p_{n_b}\Big|\chi_{n_b}^{\alpha j}(x)\,\delta(b_b^+ - n_b\cdot\hat{p}_b)\,\delta(\omega_b - \overline{\mathcal{P}}_{n_b})\,\bar{\chi}_{n_b}^{\alpha'j'}(0)\Big|p_{n_b}\Big\rangle \\
&= \frac{\slashed{n}_b^{\alpha\alpha'}}{4}\frac{\delta^{jj'}}{N_c}\,\omega_b B_{\bar{q}}(\omega_b b_b^+, \omega_b/P_b^-)\,.
\end{aligned}
\tag{7.53}
$$

Since the collinear matrix elements are color diagonal, the soft matrix element reduces

to an overall color-singlet trace, which defines the $q\bar{q}$ incoming hemisphere soft function,

$$S^{q\bar{q}}_{\text{ihemi}}(k_a^+, k_b^+) = \frac{1}{N_c} \text{tr} \langle 0| \overline{T}[Y_{n_a}^\dagger(0) \, Y_{n_b}(0)] \delta(k_a^+ - n_a \hat{p}_{a,s}) \, \delta(k_b^+ - n_b \hat{p}_{b,s}) \, T[Y_{n_b}^\dagger(0) \, Y_{n_a}(0)] |0\rangle.$$

$$(7.54)$$

The trace is over color and the factor of $1/N_c$ is included by convention, such that at tree level we have $S^{q\bar{q},\text{tree}}_{\text{ihemi}}(k_a^+, k_b^+) = \delta(k_a^+) \delta(k_b^+)$. The soft matrix element in the second term of Eq. (7.47) with $a \leftrightarrow b$ interchanged is equal to the above one due to charge conjugation invariance of QCD. Under charge conjugation, the Wilson lines transform as $\text{C}^{-1} Y_n^{ij} \text{C} = T[Y_n^{\dagger ji}]$. The explicit time ordering is required because the fields in Y_n are time-ordered by default, and charge conjugation only changes the ordering of the color generators but not of the field operators. For us this is not relevant, because the ordering of the fields is determined by the overall (anti-)time ordering in the matrix element. Thus, for the soft matrix element with $a \leftrightarrow b$ interchanged, we find

$$\text{tr} \langle 0| \overline{T}[Y_{n_b}^\dagger Y_{n_a}] \delta(k_a^+ - n_a \cdot \hat{p}_{a,s}) \, \delta(k_b^+ - n_b \cdot \hat{p}_{b,s}) \, T[Y_{n_a}^\dagger Y_{n_b}] |0\rangle \tag{7.55}$$

$$\overset{\text{C}}{=} \text{tr} \langle 0| \overline{T}[Y_{n_b}^T Y_{n_a}^{\dagger T}] \delta(k_a^+ - n_a \cdot \hat{p}_{a,s}) \, \delta(k_b^+ - n_b \cdot \hat{p}_{b,s}) \, T[Y_{n_a}^T Y_{n_b}^{\dagger T}] |0\rangle = S^{q\bar{q}}_{\text{ihemi}}(k_a^+, k_b^+),$$

where the transpose refers to the color indices. In the last step we used $\text{tr}[A^T B^T C^T D^T] = \text{tr}[BADC]$ and the fact that the fields in $Y_{n_b}^\dagger$ and Y_{n_a} are spacelike separated and thus commute. Under parity, we have $\text{P}^{-1} Y_{n_a} \text{P} = Y_{n_b}$ and $\text{P}^{-1} n_a \cdot \hat{p}_{a,s} \text{P} = n_b \cdot \hat{p}_{b,s}$. Therefore, CP invariance implies that $S^{q\bar{q}}_{\text{ihemi}}$ is symmetric in its arguments,

$$S^{q\bar{q}}_{\text{ihemi}}(k_a^+, k_b^+) \overset{\text{CP}}{=} \frac{1}{N_c} \text{tr} \langle 0| \overline{T}[Y_{n_a}^\dagger Y_{n_b}] \delta(k_a^+ - n_b \cdot \hat{p}_{b,s}) \, \delta(k_b^+ - n_a \cdot \hat{p}_{a,s}) \, T[Y_{n_b}^\dagger Y_{n_a}] |0\rangle$$

$$= S^{q\bar{q}}_{\text{ihemi}}(k_b^+, k_a^+). \tag{7.56}$$

Having worked out the different terms in Eq. (7.47), we are ready to include the remaining pieces from Eqs. (7.38) and (7.39). The $q\bar{q}$ contribution to W becomes

$$W_{JJ'q\bar{q}}(q^2, Y, B_a^+, B_b^+)$$

$$= \int d\omega_a \, d\omega_b \, \delta(\omega_a - q^-) \, \delta(\omega_b - q^+) \sum_{n_1, n_2, n_1', n_2'} \int d\omega_1 \, d\omega_2 \, d\omega_1' \, d\omega_2' \, \bar{C}^{\beta\alpha}_{Jq\bar{q}}(\tilde{b}_1, \tilde{b}_2) \, C^{\alpha'\beta'}_{J'q\bar{q}}(\tilde{b}_1', \tilde{b}_2')$$

$$\times \left\{ \delta_{n_2 n_a} \, \delta(\omega_2 - \omega_a) \, \delta_{n_2' n_a} \, \delta(\omega_2' - \omega_a) \, \delta_{n_1 n_b} \, \delta(\omega_1 - \omega_b) \, \delta_{n_1' n_b} \, \delta(\omega_1' - \omega_b) \right.$$

$$\times \frac{\eta_a^{\beta'\beta}}{4} \frac{\eta_b^{\alpha\alpha'}}{4} \frac{1}{N_c} \int \mathrm{d}k_a^+ \, \mathrm{d}k_b^+ \, q^2 B_q[x_a E_{\mathrm{cm}}(B_a^+ - k_a^+), x_a] \, B_{\bar{q}}[x_b E_{\mathrm{cm}}(B_b^+ - k_b^+), x_b]$$

$$\times S_{\mathrm{ihemi}}^{q\bar{q}}(k_a^+, k_b^+) + (a \leftrightarrow b) \bigg\}$$

$$= H_{JJ'q\bar{q}}(\tilde{b}_a, \tilde{b}_b) \int \mathrm{d}k_a^+ \mathrm{d}k_b^+ \, q^2 B_q[x_a E_{\mathrm{cm}}(B_a^+ - k_a^+), x_a] \, B_{\bar{q}}[x_b E_{\mathrm{cm}}(B_b^+ - k_b^+), x_b]$$

$$\times S_{\mathrm{ihemi}}^{q\bar{q}}(k_a^+, k_b^+) + (q \leftrightarrow \bar{q}) \,. \tag{7.57}$$

All label sums and integrations from Eq. (7.39) eliminate the label δ's from Eq. (7.47). In the second step we defined

$$\tilde{b}_a^\mu = x_a E_{\mathrm{cm}} \frac{n_a^\mu}{2} \,, \qquad\qquad \tilde{b}_b^\mu = x_b E_{\mathrm{cm}} \frac{n_b^\mu}{2}$$

$$x_a \equiv \frac{\omega_a}{E_{\mathrm{cm}}} = \frac{q^-}{E_{\mathrm{cm}}} = \frac{\sqrt{q^2}\, e^Y}{E_{\mathrm{cm}}} \,, \qquad x_b \equiv \frac{\omega_b}{E_{\mathrm{cm}}} = \frac{q^+}{E_{\mathrm{cm}}} = \frac{\sqrt{q^2}\, e^{-Y}}{E_{\mathrm{cm}}} \,, \tag{7.58}$$

as in Eq. (7.30), and introduced the hard functions

$$H_{JJ'q\bar{q}}(\tilde{b}_a, \tilde{b}_b) = \frac{1}{N_c} \frac{1}{4} \mathrm{tr}_{\mathrm{spins}} \left[\frac{\not{n}_a}{2} \bar{C}_{Jq\bar{q}}(\tilde{b}_b, \tilde{b}_a) \frac{\not{n}_b}{2} C_{J'q\bar{q}}(\tilde{b}_b, \tilde{b}_a) \right] \,,$$

$$H_{JJ'\bar{q}q}(\tilde{b}_a, \tilde{b}_b) = H_{JJ'q\bar{q}}(\tilde{b}_b, \tilde{b}_a) \,. \tag{7.59}$$

Equation (7.57) is the final factorized result for the $O_{q\bar{q}}$ contribution to the hadronic tensor.

Repeating the same steps for O_{gg}, we obtain for the forward matrix element

$$\int \frac{\mathrm{d}x^+ \mathrm{d}x^-}{(4\pi)^2} \, e^{-\mathrm{i}(q^+ x^- + q^- x^+)/2} \, e^{\mathrm{i}(\tilde{b}_1 + \tilde{b}_2)\cdot x}$$

$$\times \left\langle p_{n_a} p_{n_b} \middle| O_{gg}^{\dagger\nu\mu}(x) \, \delta(B_a^+ - n_a \cdot \hat{p}_{a,s}) \, \delta(B_b^+ - n_b \cdot \hat{p}_{b,s}) \, O_{gg}^{\mu'\nu'}(0) \middle| p_{n_a} p_{n_b} \right\rangle$$

$$= \int \mathrm{d}\omega_a \, \mathrm{d}\omega_b \, \delta(\omega_a - q^-) \, \delta(\omega_b - q^+)$$

$$\times \int \mathrm{d}b_a^+ \, \mathrm{d}b_b^+ \, \mathrm{d}k_a^+ \, \mathrm{d}k_b^+ \, \delta(B_a^+ - b_a^+ - k_a^+) \, \delta(B_b^+ - b_b^+ - k_b^+)$$

$$\times \left[\delta_{n_1 n_a} \, \delta(\omega_1 - \omega_a) \, \delta_{n_2 n_b} \, \delta(\omega_2 - \omega_b) + (a \leftrightarrow b) \right]$$

$$\times \left[\delta_{n_1' n_a} \, \delta(\omega_1' - \omega_a) \, \delta_{n_2' n_b} \, \delta(\omega_2' - \omega_b) + (a \leftrightarrow b) \right]$$

$$\times \left\langle 0 \middle| \bar{T} \left[\mathcal{Y}_{n_a}^\dagger(0) \, \mathcal{Y}_{n_b}(0) \right]^{cd} \delta(k_a^+ - n_a \cdot \hat{p}_{a,s}) \, \delta(k_b^+ - n_b \cdot \hat{p}_{b,s}) \, T \left[\mathcal{Y}_{n_b}^\dagger(0) \, \mathcal{Y}_{n_a}(0) \right]^{d'c'} \middle| 0 \right\rangle$$

$$\times \omega_a \, \theta(\omega_a) \left\langle p_{n_a} \middle| \mathcal{B}_{n_a \perp}^{\mu c}(0) \, \delta(b_a^+ - n_a \cdot \hat{p}_{n_a}) \, \delta(\omega_a - \overline{\mathcal{P}}_{n_a}) \, \mathcal{B}_{n_a \perp}^{\mu' c'}(0) \middle| p_{n_a} \right\rangle$$

$$\times \omega_b \, \theta(\omega_b) \left\langle p_{n_b} \middle| \mathcal{B}_{n_b \perp}^{\nu d}(0) \, \delta(b_b^+ - n_b \cdot \hat{p}_{n_b}) \, \delta(\omega_b - \overline{\mathcal{P}}_{n_b}) \, \mathcal{B}_{n_b \perp}^{\nu' d'}(0) \middle| p_{n_b} \right\rangle \,, \tag{7.60}$$

where we already performed the integral over x. The four terms in the third line correspond to the four different ways to match up the gluon fields with the incoming proton states. The collinear matrix elements reduce to the gluon beam function defined in Eq. (3.10),

$$
\omega_a\,\theta(\omega_a)\left\langle p_{n_a}\left|\mathcal{B}^{\mu c}_{n_a\perp}(0)\,\delta(b_a^+ - n_a\cdot\hat{p}_{n_a})\,\delta(\omega_a - \overline{\mathcal{P}}_{n_a})\,\mathcal{B}^{\mu'c'}_{n_a\perp}(0)\right|p_{n_a}\right\rangle
$$
$$
= \frac{g^{\mu\mu'}_\perp}{2}\,\frac{\delta^{cc'}}{N_c^2 - 1}\,\omega_a B_g(\omega_a b_a^+, \omega_a/P_a^-)\,. \tag{7.61}
$$

Including the color traces from the beam functions, the soft matrix element defines the gluonic incoming hemisphere soft function,

$$
S^{gg}_{\text{ihemi}}(k_a^+, k_b^+) \tag{7.62}
$$
$$
= \frac{1}{N_c^2 - 1}\left\langle 0\left|\text{tr}_{\text{color}}\left\{\overline{T}\left[\mathcal{Y}^\dagger_{n_a}(0)\mathcal{Y}_{n_b}(0)\right]\delta(k_a^+ - n_a\cdot\hat{p}_{a,s})\,\delta(k_b^+ - n_b\cdot\hat{p}_{b,s})\,T\left[\mathcal{Y}^\dagger_{n_b}(0)\mathcal{Y}_{n_a}(0)\right]\right\}\right|0\right\rangle,
$$

where the normalization is again convention. Putting everything together, the gluon contribution to the hadronic tensor becomes

$$
W_{JJ'gg}(q^2, Y, B_a^+, B_b^+) = H_{JJ'gg}(\tilde{b}_a, \tilde{b}_b)\int \mathrm{d}k_a^+\mathrm{d}k_b^+\,q^2 B_g[x_a E_{\text{cm}}(B_a^+ - k_a^+), x_a]
$$
$$
\times\,B_g[x_b E_{\text{cm}}(B_b^+ - k_b^+), x_b]\,S^{gg}_{\text{ihemi}}(k_a^+, k_b^+)\,, \tag{7.63}
$$

with the hard function

$$
H_{JJ'gg}(\tilde{b}_a, \tilde{b}_b) = \frac{1}{N_c^2 - 1}\,\frac{1}{2}\left(g_{\perp\,\mu\mu'}\,g_{\perp\,\nu\nu'} + g_{\perp\,\mu\nu'}\,g_{\perp\,\nu\mu'}\right)C^{\dagger\,\nu\mu}_{Jgg}(\tilde{b}_a, \tilde{b}_b)\,C^{\mu'\nu'}_{J'gg}(\tilde{b}_a, \tilde{b}_b)\,. \tag{7.64}
$$

Here we have used the symmetry of the Wilson coefficients in Eq. (7.42) to simplify the four terms that arise from interchanging $a \leftrightarrow b$ in Eq. (7.60).

To obtain the full result for the hadronic tensor all we have to do now is to add up the contributions from the different quark flavors and the gluon,

$$
W_{JJ'}(q^2, Y, B_a^+, B_b^+) = \sum_q W_{JJ'q\bar{q}}(q^2, Y, B_a^+, B_b^+) + W_{JJ'gg}(q^2, Y, B_a^+, B_b^+)\,. \tag{7.65}
$$

Inserting this back into Eq. (7.34), the final result for the factorized cross section becomes

$$
\frac{d\sigma}{dq^2 dY dB_a^+ dB_b^+} = \sum_{ij} H_{ij}(q^2, Y) \int dk_a^+ \, dk_b^+ \, q^2 B_i[x_a E_{\rm cm}(B_a^+ - k_a^+), x_a]
$$

$$
\times B_j[x_b E_{\rm cm}(B_b^+ - k_b^+), x_b] \, S_{\rm ihemi}^{ij}(k_a^+, k_b^+), \tag{7.66}
$$

with $x_{a,b} E_{\rm cm} = \sqrt{q^2} e^{\pm Y}$ as in Eqs. (7.30) and (7.58) and the hard function

$$
H_{ij}(q^2, Y) = \frac{1}{2E_{\rm cm}^2} \sum_{J,J'} L_{JJ'}(q^2, Y)
$$

$$
\times H_{JJ'ij}\left(x_a E_{\rm cm}\frac{n_a}{2}, x_b E_{\rm cm}\frac{n_b}{2}\right). \tag{7.67}
$$

The sum in Eq. (7.66) runs over parton species $ij = \{gg, u\bar{u}, \bar{u}u, d\bar{d}, \ldots\}$, where B_i is the beam function for parton i in beam a and B_j for parton j in beam b. Equation (7.66) is the final factorization theorem for the isolated $pp \to XL$ and $p\bar{p} \to XL$ processes. In Sec. 7.4 below we will apply it to the case of Drell-Yan, which will yield Eq. (2.16).

The beam functions in Eq. (7.66) are universal and take into account collinear radiation for isolated processes with x away from one. Since the soft function only depends on the color representation, but not on the specific quark flavor, there are only two independent soft functions $S_{\rm ihemi}^{q\bar{q}}$ and $S_{\rm ihemi}^{gg}$. In the sum over ij in Eq. (7.66), there are no mixed terms with ij corresponding to beam functions of two different quark flavors. Likewise, there are no mixed terms with quark and gluon beam functions. For example, a graph like Fig. 2-5(e) is part of the $ij = q\bar{q}$ term in the sum. Thus, cross terms between quark and gluon PDFs only appear via the contributions of different PDFs to a given beam function, as shown in Eq. (2.31).

The only process dependence in Eq. (7.66) arises through the hard functions $H_{ij}(q^2, Y)$, and one can study any desired leptonic observables by inserting the appropriate projections in the leptonic phase-space integrations inside $L_{JJ'}(q^2, Y)$. Since the hard function $H_{JJ'ij}$ corresponds to the partonic matrix element $\langle ij|J^\dagger|0\rangle\langle 0|J'|ij\rangle$ and $L_{JJ'}$ is given by the square of the relevant electroweak matrix elements $L_J^\dagger L_{J'}$, $H_{ij}(q^2, Y)$ can be determined from calculations of the partonic cross section $ij \to L$. Furthermore, $H_{ij}(q^2, Y)$ is identical to the hard function in threshold factorization theorems and hence in many cases is known from existing computations.
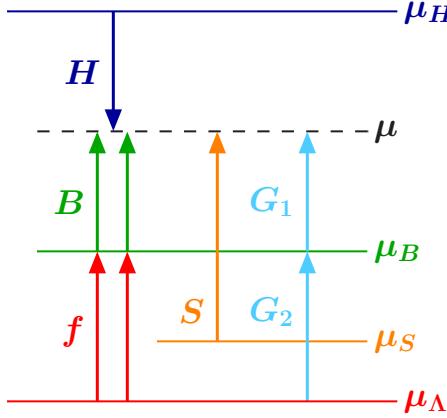
Figure 7-2: RGE running including potential Glauber modes.

7.3.4 Cancellation of Glauber Gluons

In the above derivation we have implicitly assumed that contributions from Glauber gluons cancel in the final cross section, so that we do not need Glauber interactions in the effective theory. To complete the proof of factorization, we now argue that this is indeed the case.

In principle, Glauber interactions add an additional term $\mathcal{L}_G$ to the SCET Lagrangian

$$\mathcal{L}_{\text{SCET}} = \mathcal{L}_{n_a}(\chi_{n_a}, A_s) + \mathcal{L}_{n_b}(\chi_{n_b}, A_s) + \mathcal{L}_s(A_s) + \mathcal{L}_G(A_G, \chi_{n_a}, \chi_{n_b}, A_s). \tag{7.68}$$

Glauber interactions in SCET have been considered in Refs. [90, 119], but we will not require an explicit construction of $\mathcal{L}_G$ here. Our arguments will be based on the one hand, on the consistency with processes where it has been proven that Glauber interactions cancel, and on the other hand on systematic scale separation in the language of effective field theory. The scale separation is valid independently of whether it leads to a factorization into simple matrix elements, or whether it leads to a non-factorizable matrix element with complicated dynamics.

The possible danger of the Glauber modes comes from the fact that they couple the two collinear sectors n_a and n_b with momentum scaling $Q(\lambda^2, 1, \lambda)$ and $Q(1, \lambda^2, \lambda)$. With $\mathcal{L}_G$, there will still be interactions between soft and collinear modes present in the Lagrangian even after the field redefinition, so we cannot a priori factorize the full matrix element into independent soft and collinear matrix elements. Therefore, we have to revisit each step in our derivation with $\mathcal{L}_G$ in mind.

Our argument will be divided into three steps: (i) above the scale μ_B, (ii) at the scale

μ_B, and (iii) below the scale μ_B. For (i) and (ii) we have to consider Glauber modes with momentum scaling $Q(\lambda^2, \lambda^2, \lambda)$, which we call G_1 modes. Since they have virtuality $\sim \mu_B^2$ they are integrated out at this scale. Any residual effects of Glauber interactions below μ_B could occur from modes with momentum scaling $Q(\lambda^4, \lambda^4, \lambda^2)$, which we call G_2. These modes are illustrated in Fig. 7-2.

Above the hard scale $\mu_H \simeq Q$, we have full QCD and no distinction between different modes is required, so in step (i) we are concerned with contributions of G_1 in the region $\mu_H > \mu > \mu_B$. At the scale μ_H, we integrate out hard modes with virtualities Q^2 or higher by matching the QCD currents onto SCET currents. For our process, the leading operators are given in Eq. (7.41), which contain only one field per collinear direction. For the theory in Eq. (7.68), all other possible operators are power suppressed. The matching onto these currents is valid at an operator level and can be performed with quark and gluon states. It is independent of the hadronic matrix element we are going to take later on. The key point is that the exact same matching calculation and resulting Wilson coefficients C occur for threshold Drell-Yan and $e^+e^- \to 2$ jets. For these cases it is known [77, 79] that G_1 modes do not affect the matching of the hard function $H \sim |C|^2$ at μ_H or the running of H in the region $\mu_H > \mu > \mu_B$ shown in Figs. 2-6(b) or 2-6(c). The hard function H gives a complete description of the physics down to the scale μ_B whether or not the modes in the SCET matrix elements factorize further. In Fig. 7-2, this corresponds to taking the scale $\mu = \mu_B$. Therefore, the G_1 modes can give neither large $\ln(\mu_B/\mu_H)$ terms nor finite contributions above μ_B.

In step (ii), we integrate out modes with virtualities $Q^2\lambda^2$ at the scale μ_B, which may involve matrix elements with G_1 modes exchanged. This matching affects the n_a-collinear, n_b-collinear, and G_1 modes, whose momentum scaling below μ_B changes to $Q(\lambda^4, 1, \lambda^2)$, $Q(1, \lambda^4, \lambda^2)$, and $Q(\lambda^4, \lambda^4, \lambda^2)$, respectively. Here we consider the theory right above μ_B including G_1 modes, leaving the discussion of the theory just below μ_B and G_2 modes to step (iii). Thus, we have to consider the matrix element of the composite operator

$$\left[\bar{\chi}_{n_a} \chi_{n_b} \right](x^+, x^-) \, \delta(B_a^+ - n_a \cdot \hat{p}_a) \, \delta(B_b^+ - n_b \cdot \hat{p}_b) \delta(\omega_a - \overline{\mathcal{P}}_{n_a}) \, \delta(\omega_b - \overline{\mathcal{P}}_{n_b}) \left[\bar{\chi}_{n_b} \chi_{n_a} \right](0) \,,$$

$$(7.69)$$

where we suppressed all spin and color indices for simplicity, and these collinear fields still couple to soft fields in their Lagrangians. Since μ_B is a perturbative scale, we can carry

out the matching onto the theory below μ_B at the operator level and do not yet have to consider proton states. Since the Glauber gluons are spacelike, they cannot cross the final-state cut indicated by the δ functions and only appear in virtual subdiagrams. We can therefore make a correspondence with the calculation in step (i) as follows. For any given final state with collinear and soft particles, the SCET computation for (ii) is identical to the SCET computation carried out for the matching in step (i) but using this particular choice of external states.[2] Since that SCET computation cannot induce any dependence on G_1 in step (i), there can also be no contributions from G_1 for the forward matrix-element computation here. The result of the step (ii) matching is thus given by a Wilson coefficient times an operator of the form

$$
\int dk_a^+ \, dk_b^+ \, C(x^+, x^-, B_a^+ - k_a^+, B_b^+ - k_b^+) \bar{\chi}'_{n_a}(0) \, \overline{T}\big[Y_{n_a}^\dagger Y_{n_b}\big] \chi'_{n_b}(0) \, \delta(k_a^+ - n_a \cdot \hat{p}_a)
$$
$$
\times \, \delta(k_b^+ - n_b \cdot \hat{p}_b) \, \delta(\omega_a - \overline{\mathcal{P}}_{n_a}) \, \delta(\omega_b - \overline{\mathcal{P}}_{n_b}) \bar{\chi}'_{n_b}(0) \, T\big[Y_{n_b}^\dagger Y_{n_a}\big] \chi'_{n_a}(0) \,, \tag{7.70}
$$

where the primed collinear fields have scaling $Q(\lambda^4, 1, \lambda^2)$ and $Q(1, \lambda^4, \lambda^2)$, and the soft fields in the Y Wilson lines have scaling $Q(\lambda^2, \lambda^2, \lambda^2)$.

For step (iii) below μ_B, we have to consider the $\langle pp| \cdots |pp\rangle$ matrix element of Eq. (7.70) and possible contributions from G_2 Glauber gluons, which can now also connect to spectator lines in the proton (which are primed collinear modes). The G_2 gluons may spoil the factorization of the two collinear sectors. To argue that this is not the case, we rely heavily on the original proof of the cancellation of Glauber gluons for inclusive Drell-Yan in Ref. [78]. By construction, for our observables the $k_{a,b}^+$ variables in Eq. (7.70) are of $\mathcal{O}(Q\lambda^2)$ and thus only get contributions from the soft gluons. Hence, we are fully inclusive in the Hilbert space of the primed collinear fields. Therefore, the G_2 modes as well as possible "ultrasoft" $Q(\lambda^4, \lambda^4, \lambda^4)$ gluons cancel in the sum over states, just as in the inclusive case. This discussion for the cancellation of G_2 modes is identical to Ref. [22], where arguments were presented for the cancellation of G_2 gluons up to the scale induced by the measurement on the final state, which in our case is μ_B.

Physically, one could imagine that Glauber modes kick the spectators in the proton remnant such that they can contribute to $B_{a,b}^+$. The above arguments show that this is

---

[2]In practice one would never make such a complicated choice, but if one does, it must give the same result as picking a minimal state for the matching.

not the case, so that our treatment of the proton and its remnant in the derivation of the factorization is correct.

Note that the above arguments do not suffice to show that Glauber interactions cancel when there are additional hard central jets in the final state.

7.4   Final Results for Drell-Yan

In this section, we present the final results for the isolated Drell-Yan cross section. Our discussion is split into four parts: the leptonic tensor, the hard function, the soft function, and the final cross section for beam thrust.

7.4.1   The Leptonic Tensor

To give an explicit example, we now apply the final factorization result in Eq. (7.66) to the Drell-Yan process with $L = \ell^+\ell^-$. The relevant QCD currents are the vector and axial-vector currents J_{hf}^{μ} with $h = \{V, A\}$, already given in Eq. (7.32). The corresponding leptonic contributions are

$$
L_{Vf}^{\mu}(p_1, p_2) = \frac{4\pi\alpha_{\rm em}}{q^2}\left[-Q_f\,\bar{u}(p_2)\gamma^{\mu}v(p_1) + \frac{v_f}{1 - m_Z^2/q^2}\,\bar{u}(p_2)\gamma^{\mu}(v_\ell - a_\ell\gamma_5)v(p_1)\right],
$$
$$
L_{Af}^{\mu}(p_1, p_2) = \frac{4\pi\alpha_{\rm em}}{q^2}\frac{-a_f}{1 - m_Z^2/q^2}\bar{u}(p_2)\gamma^{\mu}(v_\ell - a_\ell\gamma_5)v(p_1)\,, \tag{7.71}
$$

where in this section $p_1 = p_{\ell^+}$ and $p_2 = p_{\ell^-}$ are the lepton momenta, Q_f is the quark charge (in units of $|e|$), and $v_{\ell,f}$, $a_{\ell,f}$ are the standard vector and axial couplings of the leptons and quarks of flavor f to the Z boson. We will include the width of the Z later in Eq. (7.81).

The leptonic phase space integral is

$$
\int \frac{{\rm d}^4p_1\,{\rm d}^4p_2}{(2\pi)^2}\,\delta(p_1^2)\,\delta(p_2^2)\,\delta^4\left(q^- \frac{n_a}{2} + q^+ \frac{n_b}{2} - p_1 - p_2\right) = \frac{1}{32\,\pi^2}\int\frac{{\rm d}\Delta y\,{\rm d}\varphi}{1 + \cosh\Delta y}\,, \tag{7.72}
$$

where φ is the azimuthal angle of the leptons in the transverse plane and Δy is the rapidity difference of the two leptons:

$$
y_i = \frac{1}{2}\ln\frac{n_b\cdot p_i}{n_a\cdot p_i}\,, \quad \Delta y = y_1 - y_2\,. \tag{7.73}
$$

Since we expanded $\vec{q}_T = 0$, the leptons are back to back in the transverse plane, which

138

implies that at the order we are working

$$\frac{p_1^+}{p_2^-} = \frac{p_2^+}{p_1^-} = \frac{q^+}{q^-}\,, \qquad\qquad Y = \frac{1}{2}\left(y_1 + y_2\right),$$

$$\vec{p}_{1T} = -\vec{p}_{2T}\,, \qquad\qquad \vec{p}_{1T}^{\,2} = \vec{p}_{2T}^{\,2} = \frac{q^2}{2(1 + \cosh \Delta y)}\,. \qquad (7.74)$$

Thus, the leptonic kinematics is described by the four independent variables $\{q^2, Y, \Delta y, \varphi\}$, with $\{Y, \Delta y\}$ being equivalent to $\{y_1, y_2\}$. For simplicity, we assume that we do not distinguish the two leptons, as one would for example by measuring their rapidities y_i or transverse momenta p_{iT}. We can then integrate over $0 \leq \varphi \leq 2\pi$ and $-\infty < \Delta y < \infty$ in Eq. (7.72), giving an overall factor of 4π. The leptonic tensor, Eq. (7.35), now becomes

$$L^{\mu\nu}_{hh'ff'}(q^2, Y) = \frac{1}{32\pi^2} \int \frac{\mathrm{d}\Delta y\, \mathrm{d}\varphi}{1 + \cosh \Delta y} \sum_{\text{spins}} L^{\dagger\mu}_{hf}(p_1, p_2)\, L^{\nu}_{h'f'}(p_1, p_2)$$

$$= \frac{8\pi\alpha_{\text{em}}^2}{3q^2}\left(\frac{q^\mu q^\nu}{q^2} - g^{\mu\nu}\right) L_{hh'ff'}(q^2)\,, \qquad (7.75)$$

where

$$L_{VVff'}(q^2) = Q_f Q_{f'} - \frac{(Q_f v_{f'} + v_f Q_{f'})v_\ell}{1 - m_Z^2/q^2} + \frac{v_f v_{f'}(v_\ell^2 + a_\ell^2)}{(1 - m_Z^2/q^2)^2}\,,$$

$$L_{AAff'}(q^2) = \frac{a_f a_{f'}(v_\ell^2 + a_\ell^2)}{(1 - m_Z^2/q^2)^2}\,,$$

$$L_{AVff'}(q^2) = \frac{-a_f}{1 - m_Z^2/q^2}\left[-Q_{f'}v_\ell + \frac{v_{f'}(v_\ell^2 + a_\ell^2)}{1 - m_Z^2/q^2}\right]$$

$$= L_{VAf'f}(q^2)\,. \qquad (7.76)$$

7.4.2 The Hard Function

Using parity and charge conjugation invariance of QCD, the matching coefficients for the vector and axial-vector QCD currents can be written as

$$C^{\mu\,\alpha\beta}_{Vf\,q\bar{q}}(\tilde{b}_a, \tilde{b}_b) = C_{Vfq}(q^2)\,(\gamma_\perp^\mu)^{\alpha\beta}\,,$$

$$C^{\mu\,\alpha\beta}_{Af\,q\bar{q}}(\tilde{b}_a, \tilde{b}_b) = C_{Afq}(q^2)\,(\gamma_\perp^\mu \gamma_5)^{\alpha\beta}\,,$$

$$C^{\mu\,\rho\sigma}_{Af\,gg}(\tilde{b}_a, \tilde{b}_b) = C_{Ag}(q^2)\,(\tilde{b}_a + \tilde{b}_b)^\mu\,\mathrm{i}\epsilon^{\rho\sigma}{}_{\lambda\kappa}\tilde{b}_a^\lambda \tilde{b}_b^\kappa\,. \qquad (7.77)$$

By Lorentz invariance (or reparameterization invariance of $n_{a,b}$ and $\bar{n}_{a,b}$ [139]), the scalar coefficients can only depend on $\tilde{b}_a \cdot \tilde{b}_b = x_a x_b E_{\text{cm}}^2 = q^2$. In principle, parity and charge conjugation would also allow the Dirac structures $(\tilde{b}_a - \tilde{b}_b)^\mu \, \delta^{\alpha\beta}$ and $(\tilde{b}_a - \tilde{b}_b)^\mu \, (\gamma_5)^{\alpha\beta}$. However, as the vector and axial-vector currents are chiral even and the matching from QCD conserves chirality for massless quarks, these cannot be generated. For the gluon operator, the symmetry of the Wilson coefficient [see Eq. (7.42)] requires it to be proportional to $q^\mu = \tilde{b}_a^\mu + \tilde{b}_b^\mu$. Current conservation for the vector current requires $q_\mu C_{Vfq\bar{q}}^\mu = 0$, which eliminates this term. Thus, as expected, the only contribution for the gluon operator is due to the axial anomaly, coming from the diagram in Fig. 2-5(b). Since we neglect the lepton masses, $q_\mu L_{Af}^\mu = 0$, and thus C_{Afgg} does not survive the contraction of the leptonic and hadronic tensors for $L = \ell^+\ell^-$. Hence, the gluon beam functions do not contribute to Drell-Yan, and the gluon PDF only appears through its contribution to the quark beam functions. Inserting Eq. (7.77) into the general expression for the hard function in Eq. (7.59), we obtain

$$
\begin{aligned}
H_{hh'ff'\,q\bar{q}}^{\mu\nu}(\tilde{b}_a, \tilde{b}_b) &= -\frac{1}{2N_c}\left[g^{\mu\nu} - \frac{1}{2}(n_a^\mu n_b^\nu + n_a^\nu n_b^\mu)\right] C_{hfq}^*(q^2) C_{h'f'q}(q^2) \quad (\text{for } hh' = \{VV, AA\})\,, \\
H_{hh'ff'\,q\bar{q}}^{\mu\nu}(\tilde{b}_a, \tilde{b}_b) &= \frac{1}{4N_c}\, i\epsilon^{\mu\nu}{}_{\lambda\kappa} n_a^\lambda n_b^\kappa \, C_{hfq}^*(q^2) C_{h'f'q}(q^2) \quad\quad\quad\quad\quad (\text{for } hh' = \{VA, AV\})\,.
\end{aligned}
$$

$$(7.78)$$

At one loop, the vector and axial-vector coefficients are equal and diagonal in flavor and the SCET matching computation was performed in Refs. [33, 138], in agreement with the one-loop form factors

$$
\begin{aligned}
C_{Vfq}(q^2) &= C_{Afq}(q^2) = \delta_{fq} C(q^2)\,, \\
C(q^2, \mu) &= 1 + \frac{\alpha_s(\mu)\, C_F}{4\pi}\left[-\ln^2\left(\frac{-q^2 - i0}{\mu^2}\right) + 3\ln\left(\frac{-q^2 - i0}{\mu^2}\right) - 8 + \frac{\pi^2}{6}\right]\,.
\end{aligned}
$$

$$(7.79)$$

The vector current coefficient at two loops was obtained in Refs. [41, 118] from the known two-loop quark form factor [100, 130, 144, 145]. Starting at three loops, it can have a contribution that is not diagonal in flavor, i.e., is not proportional to δ_{fq}. The axial-vector coefficient can also receive additional diagonal and nondiagonal contributions starting at two loops from the axial anomaly [51, 122, 123]. The anomaly contributions cancel in the final result in the sum over f as long as one sums over massless quark doublets. Therefore, they will cancel when the hard matching scale is much larger than the top-quark mass, in

which case the top quark can be treated as massless. On the other hand, they have to be taken into account when the matching scale is below the top-quark mass, in which case the top quark is integrated out during the matching step and its mass cannot be neglected.

Combining Eqs. (7.78) and (7.79) with Eqs. (7.75) and (7.76), the coefficients $H_{ij}(q^2, Y)$ in Eq. (7.67) become

$$\frac{1}{2E_{\text{cm}}^2} \frac{8\pi \alpha_{\text{em}}^2}{3q^2} \frac{1}{N_c} \sum_{ff'} \left[L_{VVff'}(q^2) C_{Vfq}^*(q^2) C_{Vf'q}(q^2) + L_{AAff'}(q^2) C_{Afq}^*(q^2) C_{Af'q}(q^2) \right]$$

$$\equiv \sigma_0 H_{q\bar{q}}(q^2, \mu), \tag{7.80}$$

where at one loop

$$\sigma_0 = \frac{4\pi \alpha_{\text{em}}^2}{3 N_c E_{\text{cm}}^2 q^2}, \tag{7.81}$$

$$H_{q\bar{q}}(q^2, \mu) = H_{\bar{q}q}(q^2, \mu) = \left[Q_q^2 + \frac{(v_q^2 + a_q^2)(v_\ell^2 + a_\ell^2) - 2Q_q v_q v_\ell (1 - m_Z^2/q^2)}{(1 - m_Z^2/q^2)^2 + m_Z^2 \Gamma_Z^2/q^4} \right] |C(q^2, \mu)|^2,$$

with $|C(q^2, \mu)|^2$ given by Eq. (7.79), and where we also included the nonzero width of the Z. The RGE for the hard function $H_{q\bar{q}}(q^2, \mu)$ is

$$\mu \frac{\mathrm{d} H_{q\bar{q}}(q^2, \mu)}{\mathrm{d}\mu} = \gamma_H(q^2, \mu) \, H_{q\bar{q}}(q^2, \mu), \quad \gamma_H(q^2, \mu) = 2 \, \Gamma_{\text{cusp}}[\alpha_s(\mu)] \ln \frac{q^2}{\mu^2} + \gamma_H[\alpha_s(\mu)], \tag{7.82}$$

where Γ_{cusp} is the universal cusp anomalous dimension [127], and the one-loop non-cusp term is $\gamma_H[\alpha_s(\mu)] = -3\alpha_s(\mu) \, C_F/\pi$ [138]. The solution of Eq. (7.82) has the standard form

$$H_{q\bar{q}}(q^2, \mu) = H_{q\bar{q}}(q^2, \mu_0) \, U_H(q^2, \mu_0, \mu), \qquad U_H(q^2, \mu_0, \mu) = e^{K_H(\mu_0, \mu)} \left(\frac{q^2}{\mu_0^2} \right)^{\eta_H(\mu_0, \mu)}, \tag{7.83}$$

where $K_H(\mu_0, \mu)$ and $\eta_H(\mu_0, \mu)$ are

$$K_H(\mu_0, \mu) = \int_{\alpha_s(\mu_0)}^{\alpha_s(\mu)} \frac{\mathrm{d}\alpha_s}{\beta(\alpha_s)} \left[-4 \, \Gamma_{\text{cusp}}(\alpha_s) \int_{\alpha_s(\mu_0)}^{\alpha_s} \frac{\mathrm{d}\alpha_s'}{\beta(\alpha_s')} + \gamma_H(\alpha_s) \right],$$

$$\eta_H(\mu_0, \mu) = 2 \int_{\alpha_s(\mu_0)}^{\alpha_s(\mu)} \frac{\mathrm{d}\alpha_s}{\beta(\alpha_s)} \Gamma_{\text{cusp}}(\alpha_s). \tag{7.84}$$

Together, Eqs. (7.83) and (7.84) sum the large logarithms occurring in isolated Drell-Yan between the scales μ_H and μ_B. Electroweak corrections to the hard function $H_{q\bar{q}}(q^2, \mu)$ can be included using the results of Refs. [71–73].

7.4.3 The $q\bar{q}$ Soft Function

The incoming hemisphere soft function contains incoming Wilson lines stretching from $-\infty$ to 0 along n_a and n_b. Under time reversal, each incoming Wilson line transforms into a corresponding outgoing Wilson line stretching from 0 to ∞ along the opposite direction,

$$\mathrm{T}^{-1} Y_{n_a} \mathrm{T} = \overline{P} \exp\left[-\mathrm{i}g \int_0^\infty \mathrm{d}s\, n_b \cdot A_s(s\, n_b)\right] = \widetilde{Y}_{n_b}\,, \tag{7.85}$$

where $\overline{P}$ denotes anti-path ordering. Since T itself does not affect the original ordering of the field operators, time ordering turns into anti-time ordering and vice versa. In addition $\mathrm{T}\, n_a \cdot \hat{p}_{a,s}\, \mathrm{T}^{-1} = n_b \cdot \hat{p}_{b,s}$. Therefore, time-reversal invariance implies

$$
\begin{aligned}
S^{q\bar{q}}_{\mathrm{ihemi}}(k_a^+, k_b^+) &\stackrel{\mathrm{T}}{=} \frac{1}{N_c} \operatorname{tr} \left\langle 0 \big| T\big[\widetilde{Y}^\dagger_{n_b} \widetilde{Y}_{n_a}\big] \delta(k_a^+ - n_b\cdot\hat{p}_{b,s})\, \delta(k_b^+ - n_a\cdot\hat{p}_{a,s})\, \overline{T}\big[\widetilde{Y}^\dagger_{n_a} \widetilde{Y}_{n_b}\big] \big|0\right\rangle^* \\
&= \frac{1}{N_c} \operatorname{tr} \left\langle 0 \big| T\big[\widetilde{Y}^\dagger_{n_a} \widetilde{Y}_{n_b}\big] \delta(k_a^+ - n_a\cdot\hat{p}_{a,s})\, \delta(k_b^+ - n_b\cdot\hat{p}_{b,s})\, \overline{T}\big[\widetilde{Y}^\dagger_{n_b} \widetilde{Y}_{n_a}\big] \big|0\right\rangle. \tag{7.86}
\end{aligned}
$$

In the second step, the complex conjugation has no effect since the matrix element is real, and we used parity to switch $n_{b,a}$ back to $n_{a,b}$. For comparison, the hemisphere soft function with outgoing Wilson appearing in the double-differential hemisphere invariant-mass distribution in $e^+e^- \to 2$ jets [93, 94, 116, 128, 129, 157] is

$$S^{q\bar{q}}_{\mathrm{hemi}}(k_a^+, k_b^+) = \frac{1}{N_c} \operatorname{tr} \left\langle 0 \big| \overline{T}\big[\widetilde{Y}^\dagger_{n_a} \widetilde{Y}_{n_b}\big] \delta(k_a^+ - n_a\cdot\hat{p}_{a,s})\, \delta(k_b^+ - n_b\cdot\hat{p}_{b,s})\, T\big[\widetilde{Y}^\dagger_{n_b} \widetilde{Y}_{n_a}\big] \big|0\right\rangle. \tag{7.87}$$

This is almost the same as Eq. (7.86), the only difference being the opposite time ordering. Thus, S_{ihemi} and S_{hemi} are equal at one loop, where the time ordering is still irrelevant. Beyond one loop, S_{ihemi} and S_{hemi} may in general be different. However, since the beam and jet functions have the same anomalous dimension, the combined anomalous dimension of the hard and beam functions in isolated Drell-Yan agrees with that of the hard and jet functions for the e^+e^- hemisphere invariant-mass distribution. The consistency of the RGE in both cases then requires that S_{ihemi} and S_{hemi} have the same anomalous dimension to all orders in perturbation theory. In addition, the purely virtual contributions, obtained by inserting the vacuum state, are the same in both cases,

$$S^{q\bar{q},\mathrm{virtual}}_{\mathrm{ihemi}}(k_a^+, k_b^+) = \frac{1}{N_c}\, \delta(k_a^+)\, \delta(k_b^+)\, \operatorname{tr} \big|\langle 0 | T\big[\widetilde{Y}^\dagger_{n_a} \widetilde{Y}_{n_b}\big] |0\rangle\big|^2 = S^{q\bar{q},\mathrm{virtual}}_{\mathrm{hemi}}(k_a^+, k_b^+). \tag{7.88}$$

Hence, S_{ihemi} and S_{hemi} can only differ by finite real-emission corrections at each order in perturbation theory.

Using the one-loop results for $S_{\text{hemi}}^{q\bar{q}}$ from Refs. [94, 157], we have

$$
\begin{aligned}
S_{\text{ihemi}}^{q\bar{q}}(k_a^+, k_b^+) &= \delta(k_a^+)\,\delta(k_b^+) + \delta(k_a^+)\,S^{\text{1loop}}(k_b^+) + S^{\text{1loop}}(k_a^+)\,\delta(k_b^+)\,, \\
S^{\text{1loop}}(k^+) &= \frac{\alpha_s(\mu)\,C_F}{4\pi}\left\{ -\frac{8}{\mu}\left[\frac{\theta(k^+/\mu)\ln(k^+/\mu)}{k^+/\mu}\right]_+ + \frac{\pi^2}{6}\,\delta(k^+)\right\}.
\end{aligned}
\tag{7.89}
$$

The plus distribution is defined in Eq. (B.1). The one-loop soft function for beam thrust in Eq. (2.23) then becomes $S_B(k^+, \mu) = \delta(k^+) + 2\,S^{\text{1loop}}(k^+)$.

7.4.4 Final Cross Section for Beam Thrust

The differential cross section for beam thrust in Eq. (2.29) including the RGE running is

$$
\begin{aligned}
&\frac{\mathrm{d}\sigma}{\mathrm{d}q^2\,\mathrm{d}Y\,\mathrm{d}\tau_B} \tag{7.90} \\
&= \sigma_0 \sum_{ij} H_{ij}(q^2, \mu_H)\,U_H(q^2, \mu_H, \mu_S)\int \mathrm{d}t_a\,\mathrm{d}t_b\,Q\,S_B\!\left(Q\,\tau_B - \frac{t_a + t_b}{Q}, \mu_S\right) \\
&\quad \times \int \mathrm{d}t_a'\,B_i(t_a - t_a', x_a, \mu_B)\,U_B(t_a', \mu_B, \mu_S)\int \mathrm{d}t_b'\,B_j(t_b - t_b', x_b, \mu_B)\,U_B(t_b', \mu_B, \mu_S)\,.
\end{aligned}
$$

We now consider its fixed-order α_s expansion. To our knowledge $\mathrm{d}\sigma/\mathrm{d}q^2\mathrm{d}Y\mathrm{d}\tau_B$ has not been considered in perturbation theory in full QCD even at one loop. To obtain an expression for $\mathrm{d}\sigma/\mathrm{d}q^2\mathrm{d}Y\mathrm{d}\tau_B$ at NLO in α_s and leading order in the power counting, we drop the evolution factors U_H and U_B and expand all functions to NLO at a common scale μ. From the above NLO results for the hard and soft functions and the NLO results for the beam functions from Ch. 3, we find

$$
\begin{aligned}
\frac{\mathrm{d}\sigma}{\mathrm{d}q^2\,\mathrm{d}Y\,\mathrm{d}\tau_B} &= \sigma_0 \sum_{i,j}\left[Q_i^2 + \frac{(v_i^2 + a_i^2)(v_\ell^2 + a_\ell^2) - 2Q_i v_i v_\ell(1 - m_Z^2/q^2)}{(1 - m_Z^2/q^2)^2 + m_Z^2\Gamma_Z^2/q^4}\right] \\
&\quad \times \int \frac{\mathrm{d}\xi_a}{\xi_a}\frac{\mathrm{d}\xi_b}{\xi_b}\,C_{ij}\!\left(\frac{x_a}{\xi_a}, \frac{x_b}{\xi_b}, q^2, \tau_B, \mu\right)f_{i/a}(\xi_a, \mu)\,f_{j/b}(\xi_b, \mu)\,.
\end{aligned}
\tag{7.91}
$$

Here, $f_{i/a}(\xi_a, \mu)$ and $f_{j/b}(\xi_b, \mu)$ are the PDFs for parton i in proton a and parton j in (anti-)proton b. At tree level, the nonzero coefficients are

$$
C_{q\bar{q}}^{\text{tree}}(z_a, z_b, q^2, \tau_B, \mu) = C_{\bar{q}q}^{\text{tree}}(z_a, z_b, q^2, \tau_B, \mu) = \delta(\tau_B)\,\delta(1 - z_a)\,\delta(1 - z_b)\,.
\tag{7.92}
$$

At one loop, we obtain

$$
C_{q\bar{q}}^{1\text{loop}}(z_a, z_b, q^2, \tau_B, \mu)
$$

$$
= \frac{\alpha_s(\mu)\, C_F}{2\pi}\, \delta(1 - z_a)\, \theta(z_b)\Bigg\{ \left[-2\left[\frac{\theta(\tau_B)\ln\tau_B}{\tau_B} \right]_+ - \frac{3}{2}\left[\frac{\theta(\tau_B)}{\tau_B} \right]_+ - \delta(\tau_B)\left(4 - \frac{\pi^2}{2} \right) \right]\delta(1 - z_b)
$$

$$
+ \left[\left[\frac{\theta(\tau_B)}{\tau_B} \right]_+ + \delta(\tau_B)\ln\frac{q^2}{\mu^2} \right]\left[\theta(1 - z_b)\frac{1 + z_b^2}{1 - z_b} \right]_+ + \delta(\tau_B)\left[\left[\frac{\theta(1 - z_b)\ln(1 - z_b)}{1 - z_b} \right]_+ (1 + z_b^2) \right.
$$

$$
+ \theta(1 - z_b)\left(1 - z_b - \frac{1 + z_b^2}{1 - z_b}\ln z_b \right) \Bigg] \Bigg\} + (z_a \leftrightarrow z_b)\,,
$$

$$
C_{\bar{q}q}^{1\text{loop}}(z_a, z_b, q^2, \tau_B, \mu) = C_{q\bar{q}}^{1\text{loop}}(z_a, z_b, q^2, \tau_B, \mu)\,,
$$

$$
C_{qg}^{1\text{loop}}(z_a, z_b, q^2, \tau_B, \mu)
$$

$$
= \frac{\alpha_s(\mu)\, T_F}{2\pi}\, \delta(1 - z_a)\, \theta(z_b)\, \theta(1 - z_b)\Bigg\{ \left[\left[\frac{\theta(\tau_B)}{\tau_B} \right]_+ + \delta(\tau_B)\ln\frac{q^2}{\mu^2} \right]\left[z_b^2 + (1 - z_b)^2 \right]
$$

$$
+ \delta(\tau_B)\left[\ln\frac{1 - z_b}{z_b}\left[z_b^2 + (1 - z_b)^2 \right] + 2z_b(1 - z_b) \right] \Bigg\}\,,
$$

$$
C_{\bar{q}g}^{1\text{loop}}(z_a, z_b, q^2, \tau_B, \mu) = C_{qg}^{1\text{loop}}(z_a, z_b, q^2, \tau_B, \mu)\,,
$$

$$
C_{gq}^{1\text{loop}}(z_a, z_b, q^2, \tau_B, \mu) = C_{g\bar{q}}^{1\text{loop}}(z_a, z_b, q^2, \tau_B, \mu) = C_{qg}^{1\text{loop}}(z_b, z_a, q^2, \tau_B, \mu)\,. \tag{7.93}
$$

The single logarithms of q^2/μ^2 are multiplied by the QCD splitting kernels and are re-summed by the PDFs. Thus, in fixed-order perturbation theory the PDFs should be evaluated at the hard scale $\mu = Q$, such that there are no large logarithms when integrating over $0 \leq \tau_B \lesssim 1$. However, if the integration is restricted to $\tau_B \leq \tau_B^{\text{cut}} \ll 1$, the plus distributions in τ_B produce large logarithms $\ln^2\tau_B^{\text{cut}}$ and $\ln\tau_B^{\text{cut}}$, which make a fixed-order expansion un-reliable. These are precisely the logarithms that are resummed by the combined RGE of hard, jet, and soft functions in Eq. (7.90).

Chapter 8

Beam Thrust Cross Section for Drell-Yan

In this chapter we present and discuss results for the Drell-Yan beam thrust cross section, to appear in Ref. [169]. Beam thrust was defined in Eq. (2.25) and may be written as

$$\tau_B = \frac{1}{Q} \sum_k |\vec{p}_{kT}| e^{-|\eta_k - Y|} \,, \tag{8.1}$$

where Q^2 and Y are the dilepton invariant mass and rapidity. The sum runs over all (pseudo)particles in the final state except the two signal leptons, where $|\vec{p}_{kT}|$ and η_k are the measured transverse momenta and rapidities with respect to the beam axis (for simplicity we took all particles to be massless). Beam thrust is the analog of thrust for $e^+ e^- \to$ jets with the thrust axis fixed to the proton beam axis. For $\tau_B \ll 1$, the hadronic final state consists of two back-to-back jets along the beam axis due to the initial state radiation. The measurement of τ_B can provide a test of our understanding of the initial state at the Tevatron and LHC.

Experimentally, beam thrust is one of the simplest hadronic observables at a hadron collider. It requires no jet algorithms, is boost invariant along the beam axis, and can be directly compared to theory predictions without utilizing parton showering or hadronization from Monte Carlos.

Beam thrust is also theoretically clean. It is infrared safe, and simple enough to include in theoretical calculations. In Sec. 7.3 we derived an all-orders factorization theorem for

the Drell-Yan beam thrust cross section for small τ_B

$$\frac{\mathrm{d}\sigma}{\mathrm{d}Q\mathrm{d}Y\mathrm{d}\tau_B} \tag{8.2}$$
$$= \frac{8\pi\alpha_{\mathrm{em}}^2}{3N_cE_{\mathrm{cm}}^2}\sum_{ij} H_{ij}(Q^2,\mu_H)\, U_H(Q^2,\mu_H,\mu)\int \mathrm{d}t_a\mathrm{d}t_a'\, B_i(t_a - t_a', x_a, \mu_B)\, U_B^i(t_a', \mu_B, \mu)$$
$$\times \int \mathrm{d}t_b\mathrm{d}t_b'\, B_j(t_b - t_b', x_b, \mu_B)\, U_B^j(t_b', \mu_B, \mu)\int \mathrm{d}k\, S_B\Big(\tau_B Q - \frac{t_a + t_b}{Q} - k, \mu_S\Big) U_S(k, \mu_S, \mu)\,,$$

where $x_a = (Q/E_{\mathrm{cm}})e^Y$ and $x_b = (Q/E_{\mathrm{cm}})e^{-Y}$ are the partonic momentum fractions trans-
ferred to the leptons, and the sum runs over quark flavors $ij = \{u\bar{u}, \bar{u}u, d\bar{d}, \ldots\}$. The hard
function $H_{ij}(Q^2, \mu_H)$ contains hard virtual radiation at the hard scale $\mu_H \simeq Q$ (and also
includes the leptonic decay). The soft function $S_B(k, \mu_S)$ encodes the effect of soft virtual
and real radiation on the measurement of τ_B and is sensitive to the soft scale $\mu_S \simeq \tau_B Q$.
The beam functions $B_i(t_a, x_a, \mu_B)$ and $B_j(t_b, x_b, \mu_B)$ describe extracting the colliding par-
tons out of the proton and the formation of the initial state jets. As we showed in Sec. 3.3,
they can be matched onto PDFs $B_i = \sum_k \mathcal{I}_{ik} \otimes f_k$ at the beam scale $\mu_B \simeq \sqrt{t_{a,b}} \simeq \sqrt{\tau_B}Q$.

The cross section for small $\tau_B \ll 1$ contains large double logarithms $\alpha_s^n \ln^m \tau_B$ with
$m \leq 2n$. These are summed to all orders in Eq. (8.2) by evaluating the hard, beam, and
soft functions at their natural scale where they contain no large logarithms and using the
RG evolution kernels U_H, $U_B^{i,j}$, and U_S to run them to a common scale μ. The combination
of the evolution kernels is μ independent and sums the logarithms of τ_B. At NNLL we
need the next-to-leading order (NLO) expressions for H_{ij}, $\mathcal{I}_{ik}$, and S_B, as well as the NNLL
expressions for U_H, $U_B^{i,j}$, and U_S, given in Sec. 7.4 and App. E. The required convolutions
in Eq. (8.2) are carried out analytically following Ref. [135]. We use the MSTW2008 [143]
parton distribution functions at NLO for $\alpha_s(m_Z) = 0.117$ and with two-loop, five-flavor
running for $\alpha_s(\mu)$. Details on our order counting, as well as a technical point related to the
running of $\alpha_s(\mu)$, can be found at the beginning of Ch. 6.

To estimate the perturbative uncertainties we use the minimum and maximum variation
under the following separate scale variations

$$\text{a)} \qquad \mu_H = rQ\,,\ \mu_B = r\sqrt{\tau_B}Q\,,\ \mu_S = r\tau_B Q\,,$$

$$\text{b)} \qquad \mu_H = Q\,,\ \mu_B = r^{-(\ln\tau_B)/4}\sqrt{\tau_B}Q\,,\ \mu_S = \tau_B Q\,,$$

$$\text{c)} \qquad \mu_H = Q\,,\ \mu_B = \sqrt{\tau_B}Q\,,\ \mu_S = r^{-(\ln\tau_B)/4}\tau_B Q\,, \tag{8.3}$$
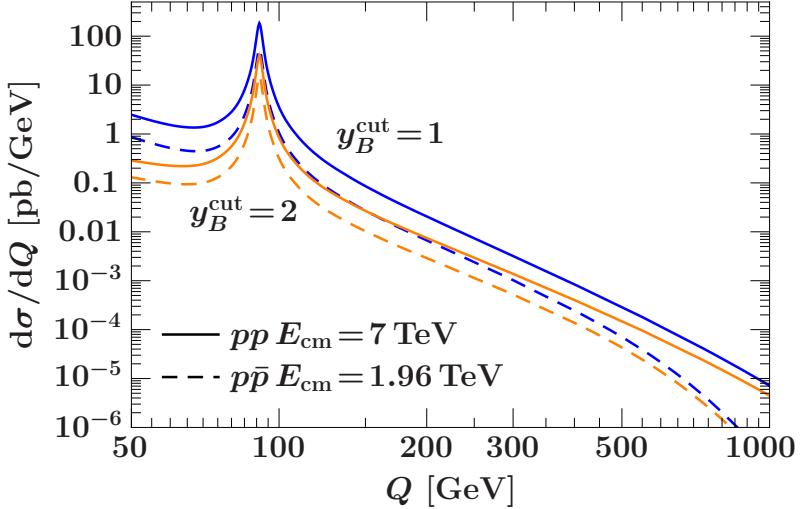
Figure 8-1: Drell-Yan cross section $d\sigma/dQ$ at NNLL with a cut on beam thrust $\tau_B \leq \exp(-2y_B^{\text{cut}})$ with $y_B^{\text{cut}} = 1, 2$. The solid lines show the cross section at the LHC with $E_{\text{cm}} = 7\,\text{TeV}$ and the dashed lines the cross section at the Tevatron.

with $r = \{1/2, 2\}$, and $r = 1$ corresponds to the central value. Only considering the simultaneous variation in a) produces unnaturally small scale uncertainties due to cancelations between the running of the hard, beam, and soft functions. The exponent of r for cases b) and c) is chosen such that for $\tau_B = e^{-4}$ the scales μ_B or μ_S vary by factors of two, with smaller variations for increasing τ_B and no variation for $\tau_B \to 1$. In this limit, there should only be a single scale $\mu_H = \mu_B = \mu_S$, and thus the only scale variation should be case a). For the cross section integrated up to $\tau_B \leq \tau_B^{\text{max}}$, the scales are chosen by replacing τ_B with τ_B^{max} in Eq. (8.3).

As already mentioned, small τ_B describes events with energetic initial-state radiation in the forward direction but no hard jets at central rapidities. More explicitly, a cut on $\tau_B \leq \exp(-2y_B^{\text{cut}})$ vetos energetic radiation with total energy $\gtrsim Q$ in the rapidity region $|y-Y| \lesssim y_B^{\text{cut}}$, while allowing energetic radiation for $|y-Y| \gtrsim y_B^{\text{cut}}$ with a smooth transition between the two regions. In Fig. 8-1 we show the Drell-Yan cross section $d\sigma/dQ$ at NNLL for $y_B^{\text{cut}} = 1$ and 2 at the LHC with $E_{\text{cm}} = 7\,\text{TeV}$ and the Tevatron. Increasing the restriction on the hadronic final state from $y_B^{\text{cut}} = 1$ to 2 reduces the cross section by a factor of few at larger Q which becomes a factor of 10 at small Q. The Z resonance is visible around $Q = 90\,\text{GeV}$.

Figure 8-2 shows the same cross section for $y_B^{\text{cut}} = 1$ normalized relative to the NLL result at the LHC with $E_{\text{cm}} = 7\,\text{TeV}$ (left panel) and the Tevatron (right panel). The bands

147
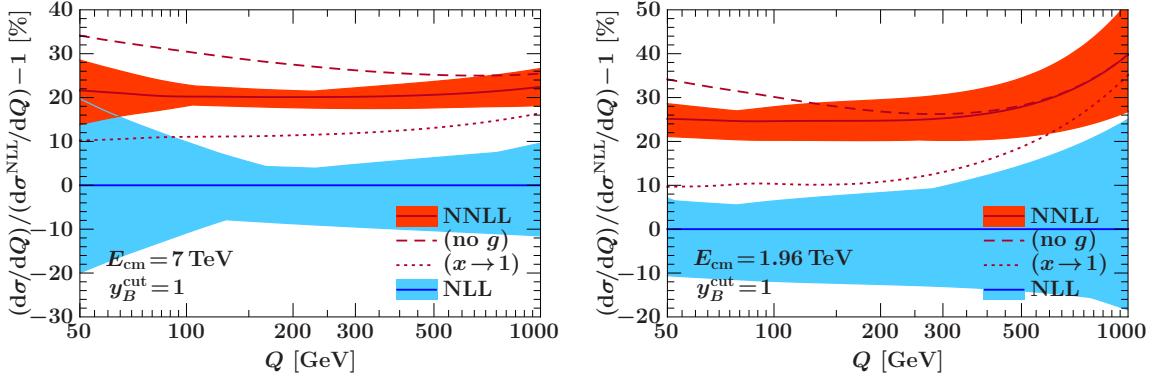
Figure 8-2: The Drell-Yan cross section $d\sigma/dQ$ at NNLL with a cut on beam thrust $\tau_B \leq \exp(-2y_B^{\rm cut})$ with $y_B^{\rm cut} = 1$ at the LHC with $E_{\rm cm} = 7\,{\rm TeV}$ (left panel) and the Tevatron (right panel). All results are normalized relative to the NLL result. Shown are the full NNLL result (solid), NNLL without the gluon contribution (dashed), and NNLL in the threshold limit (dotted). The bands show the scale uncertainties at NLL and NNLL as explained in the text.

show the perturbative uncertainties at NLL (medium blue band) and NNLL (dark orange band). From NLL to NNLL they are reduced by about a factor of two. As illustration, the dashed line shows the NNLL result without the contribution of the gluon PDF to the quark beam function, $\mathcal{I}_{qg}$ in Eq. (3.37). The dotted line shows the NNLL result in the threshold limit $x \to 1$, where in addition to neglecting the gluon contribution we only keep the leading terms as $x \to 1$ in the quark contribution $\mathcal{I}_{qq}$, shown in Eq. (6.1). Hence, the quark non-threshold contributions shift the result from the dotted to the dashed line, and the (non-threshold) gluon contributions shift it from the dashed to the solid line. At the LHC, there is a noticable cancelation between the non-threshold quark and gluon contributions, which is less prominent at the Tevatron. The reason is that the gluon PDF has a much larger effect on the antiquark beam function than the quark beam function. The non-threshold quark contributions are as large or larger than the threshold quark contributions, so there is no indication that the threshold terms are numerically dominant. The only exception is for the Tevatron, where because of the lower center-of-mass energy the threshold corrections dominate for large $Q \sim 1\,{\rm TeV}$, corresponding to $x \sim 0.5$. In this region the absolute cross section in Fig. 8-1 however is very small.

The left panel of Fig. 8-3 shows the beam thrust cross section $d\sigma/dQ\,dY\,d\tau_B$ at the LHC for small τ_B and at fixed $Y = 0$ and $Q = 100\,{\rm GeV}$. The bands show the perturbative uncertainties and results are shown at NNLL (dark orange), NLL (medium blue), and fixed
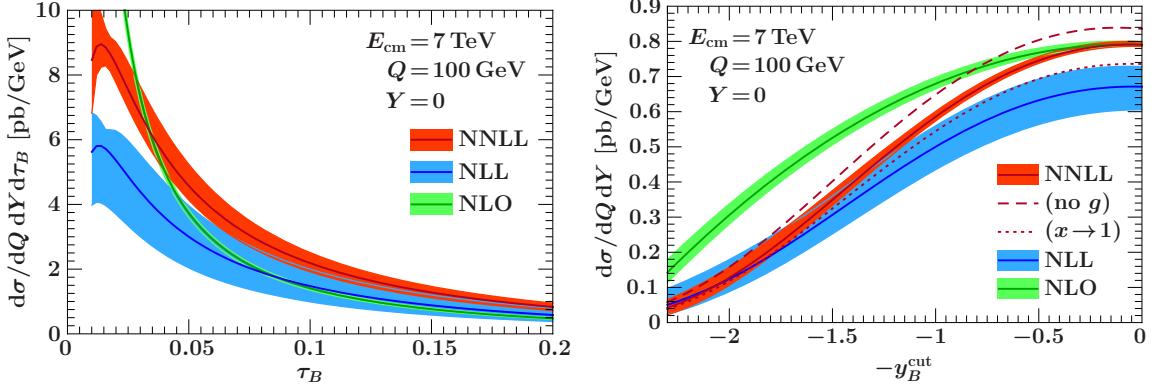
Figure 8-3: The beam thrust cross section for fixed $Q = 100\,\mathrm{GeV}$ and $Y = 0$ at the LHC with $E_{\mathrm{cm}} = 7\,\mathrm{TeV}$ at NLO, NLL, and NNLL. The bands indicate the perturbative scale uncertainties as explained in the text. Left: The differential cross section at small τ_B. Right: The cross section integrated up to $\tau_B \leq \exp(-2y_B^{\mathrm{cut}})$ as function of y_B^{cut}. Also shown are the NNLL results in the threshold limit $x \to 1$ (dotted) and without the gluon contribution (dashed).

order NLO (light green). The NLO result is obtained from Eq. (8.2) by using a common fixed scale $\mu_H = \mu_B = \mu_S = \mu$, with central value $\mu = Q$ and varying $\mu = \{2Q, Q/2\}$. This reproduces the leading singular terms for $\tau_B \to 0$ shown in Eq. (7.91). The full NLO result, which is not yet known, contains additional nonsingular terms that are relevant for $\tau_B \sim 1$, but for $\tau_B \ll 1$ constitute power corrections and are neglected in Eq. (8.2). The summation has a large effect at small τ_B and effectively regularizes the IR singularity in the fixed-order result. The curves are not plotted for $\tau_B \leq 0.01$, because at this point the soft scale drops below $1\,\mathrm{GeV}$. Near this cutoff, the soft function becomes nonperturbative and so we expect large corrections to our purely perturbative results.

In the right panel of Fig. 8-3 we plot the corresponding cross section integrated up to $\tau_B \leq \exp(-2y_B^{\mathrm{cut}})$ as function of y_B^{cut}. For nonzero y_B^{cut} (small τ_B^{max}) the summation is again important, while for $y_B^{\mathrm{cut}} \to 0$ ($\tau_B^{\mathrm{max}} \to 1$) no summation is necessary. The full NNLL result provides a smooth interpolation between these two regimes, approaching the singular NLO result for $y_B^{\mathrm{cut}} \to 0$ and the NLL result for $y_B^{\mathrm{cut}} \gtrsim 1.5$.

In conclusion, beam thrust in Drell-Yan provides an experimentally and theoretically clean measure of initial-state radiation in $q\bar{q} \to e^+e^-$, similar to how usual thrust measures final-state radiation in $e^+e^- \to q\bar{q}$. The experimental measurement of beam thrust will contribute very valuable information to our understanding of initial-state radiation at hadron colliders. It should be a priority in the early LHC runs when backgrounds from pile-up

effects are still small. We have presented theoretical results for the Drell-Yan beam thrust cross section at NNLL, showing that the effects of initial-state radiation in quark initiated processes are important but also under good theoretical control. We will see an example of a gluon initiated process in the next chapter.

Chapter 9

Beam Thrust Cross Section for Higgs Production

In this chapter we apply the factorization theorem of Ch. 7 to Higgs production through gluon fusion. In Sec. 9.1 we discuss the experimental relevance of a central jet veto for Higgs searches in the $H \to W^+W^- \to \ell^+\nu\ell^-\bar{\nu}$ and $H \to \gamma\gamma$ channel and present the corresponding factorization theorems. Plots for the cross section are shown and discussed in Sec. 9.2. These results will appear in Ref. [48].

9.1 Introduction

The discovery of the Higgs boson is a major goal of the Large Hadron Collider (LHC) and current analyses at the Tevatron. The $H \to W^+W^- \to \ell^+\nu\ell^-\bar{\nu}$ channel has strong discovery potential and plays a very important role for early searches that are statistics limited. It is the dominant channel in the current Tevatron exclusion limit [5]. The presence of the final-state neutrinos does not allow the reconstruction of the Higgs invariant mass, and hence for this channel sideband methods cannot be used to determine the backgrounds directly from data. At the LHC, $t\bar{t} \to W^+W^-b\bar{b}$ events constitute by far the largest background, dominating the signal by a factor of more than $30 : 1$ after applying lepton selection criteria [3, 4] (see Ref. [49] for a sensitivity update at $7\,\mathrm{TeV}$). Requiring a minimum missing energy is not effective against this background since it also contains two neutrinos. To eliminate the huge background from top-quark decays one imposes a stringent jet veto to define a 0-jet sample for the search. For example, ATLAS rejects all events that contain any

hard jet with $p_T > 20\,\text{GeV}$ and pseudorapidity $|\eta| < 4.8$, which reduces the $t\bar{t}$ background by a factor of more than 300 [4]. After the jet veto, the main background is from the direct production $pp \to W^+W^-$, which at this point still dominates the signal by a factor of $4:1$, and the final background discrimination is achieved by a fit to several kinematic variables.

Theoretically, the inclusive Higgs production cross section has been studied extensively in the literature and is known to NNLO [16, 85, 87, 113, 114, 153, 155, 163] (for reviews and additional references see e.g. Refs. [54, 88]). However, Higgs production in a 0-jet sample differs substantially from inclusive Higgs production. In particular, the jet veto induces large double logarithms that are not present in the inclusive cross section, and also induces dependence on the choice of jet algorithm used to define the veto. The current method employed by experiments to study the effect of the jet veto and the accompanying large logarithms is to use parton-shower Monte Carlos, such as MC@NLO [98, 99] and Pythia [160]. This allows one to take into account the dependence of the 0-jet sample on the choice of jet algorithm, but for the large logarithms it limits the accuracy to the leading-logarithmic summation inherent to parton showers.

Theoretical studies of the jet veto at fixed NNLO [17, 65, 84] and including additional kinematic selection cuts [11–13, 106] are available (see also Ref. [49]). The comparison [11, 13, 84] of the fixed NLO results with MC@NLO, which combines NLO with a LL parton-shower resummation, shows indeed discrepancies that indicate the importance of resumming the phase-space logarithms caused by the jet veto. The disagreements are reduced but not eliminated when the fixed NNLO prediction is compared with those from MC@NLO, Herwig [80, 81], and Pythia (reweighted to the same inclusive NNLO cross section). There are also notable differences between the Herwig and Pythia parton-level results, which is another indication that subleading phase-space logarithms are important.

Theoretically, one can also study the Higgs production as a function of the Higgs transverse momentum, p_T^H, both in fixed-order perturbation theory for large p_T^H [18, 86, 105, 154] and with a resummation of logarithms of p_T^H at small p_T^H [25, 50, 55, 56, 76, 131, 142]. The latter is motivated by the fact that the jet veto automatically forces p_T^H to be small, see e.g. Refs. [11, 13, 83]. However, a restriction to small p_T^H by itself does not provide a jet veto as it still allows for configurations with back-to-back hard final-state jets, so a study of the small-p_T^H spectrum can only provide a qualitative template for the effect of the jet veto.

Here, we use beam thrust to impose the jet veto in $pp \to HX$ and $p\bar{p} \to HX$. This

allows us to directly predict a 0-jet Higgs production cross section, including higher-order logarithmic resummation and without relying on parton showers or hadronization models from Monte Carlo. The corresponding cross section for the $pp \to WW + 0j$ background can be computed in a similar manner, which is left for future work.

While $H \to WW$ provides the most obvious motivation for studying the effect of jet vetos, we will also consider the case of $H \to \gamma\gamma$. Here, sideband methods are available to experimentally control the overwhelming QCD background (which is up to six orders of magnitude larger than the signal at the LHC), but it may still be interesting to study sidebands in combination with an explicit jet veto using an inclusive variable such as beam thrust. By suppressing the backgrounds from $pp \to jj$ and $pp \to j\gamma$ this could reduce the sensitivity of the measurement to the details of the photon isolation cuts. For our purposes, we use this channel to study the effect of the jet veto for the case where the Higgs invariant mass distribution and rapidity can be measured. With the ability to measure these variables the optimal beam thrust variable for $H \to \gamma\gamma$ differs slightly from that for $H \to WW$, as we discuss below.

It should be emphasized that Tevatron Higgs searches, which exclude the range $m_H = 162 - 166 \, \text{GeV}$ at 95% confidence level [5–7], already analyse their data using a jet algorithm and Monte Carlo to implement a jet veto on jets with $p_T \geq 15 \, \text{GeV}$ and $|\eta_j| \leq 2.4 - 2.5$. The motivation is again to eliminate backgrounds with additional jets. The CDF analysis [6] explicitly uses separate 0-jet, 1-jet, and $\geq$ 2-jet signal samples, where the latter are included to maximize the discovery reach due to the presence of ZH, WH, and vector boson fusion production channels. The D0 search previously used a $(0 + 1)$-jet sample, where in the latest update [7] the number of jets is used as input to a neural network. Even though the different jet samples are combined in the final exclusion limit, they are likely to have different efficiencies and systematics, with most of the sensitivity coming from the 0-jet sample. Hence, it is important to have a theoretical handle on the 0-jet production cross section also at the Tevatron. Furthermore, it will be important to use the available Tevatron data to test our method in preparation for the LHC searches.

At the LHC, the Higgs plus 2-jet channel with $H \to WW$ is also considered. In this thesis we restrict ourselves to studying an inclusive 0-jet veto using beam thrust. An analogous inclusive variable, N-jettiness, that works in the presence of N-signal jets will be discussed in Ch. 10 and can be used to study the exclusive $H + 1j$ and $H + 2j$ cross section.

To implement a jet veto in $H \to WW$ where missing energy plays an important role, the appropriate version of beam thrust is defined in the hadronic center-of-mass frame

$$\tau_B^{\text{cm}} = \frac{\mathcal{T}_B^{\text{cm}}}{m_H}, \qquad \mathcal{T}_B^{\text{cm}} = \sum_k |\vec{p}_{kT}| \, e^{-|\eta_k|}. \tag{9.1}$$

For the case studied here where the mass of the Higgs is unknown, the dimension-one variable $\mathcal{T}_B^{\text{cm}}$ is more convenient than the dimensionless τ_B^{cm}. The sum over k runs over all particles in the final state, with $\vec{p}_{kT}$ and η_k the measured transverse momentum and rapidity of each particle, excluding the signal leptons from the W decays. For simplicity we take all particles to be massless.

The production cross section from gluon fusion, $gg \to H$, for $\mathcal{T}_B \ll m_H$ (i.e. $\tau_B^{\text{cm}} \ll 1$) is given by the factorization theorem [see Eq. (2.22)]

$$\frac{d\sigma}{d\mathcal{T}_B^{\text{cm}}} = \sigma_0 \, H_{gg}(m_H, m_t, \mu) \int dY \int dt_a \, dt_b \, B_i(t_a, x_a, \mu) \, B_j(t_b, x_b, \mu)$$
$$\times S_B^{gg}\left(\mathcal{T}_B^{\text{cm}} - \frac{e^{-Y} t_a + e^Y t_b}{m_H}, \mu\right) \left[1 + \mathcal{O}\left(\frac{\Lambda_{\text{QCD}}}{m_H}, \tau_B^{\text{cm}}\right)\right], \tag{9.2}$$

where

$$x_a = \frac{m_H}{E_{\text{cm}}} e^Y, \qquad x_b = \frac{m_H}{E_{\text{cm}}} e^{-Y}, \qquad \sigma_0 = \frac{\sqrt{2} G_F \, m_H^2}{72\pi(N_c^2 - 1) E_{\text{cm}}^2}, \tag{9.3}$$

and the limits on the Y integration are $\ln(m_H/E_{\text{cm}}) \leq Y \leq -\ln(m_H/E_{\text{cm}})$.

For $H \to \gamma\gamma$ the rapidity Y of the Higgs is measurable and provides an estimate of the boost of the partonic hard collision relative to the hadronic center-of-mass frame. In this case it makes sense to account for the boost of the hard collision when imposing the jet veto. Therefore we use the usual beam thrust

$$\tau_B = \frac{\mathcal{T}_B}{m_H}, \qquad \mathcal{T}_B = \sum_k |\vec{p}_{kT}| \, e^{-|\eta_k - Y|}. \tag{9.4}$$

In this case, the factorization theorem for the production cross section is

$$\frac{d\sigma}{dY \, d\mathcal{T}_B} = \sigma_0 \, H_{gg}(m_t, m_H, \mu) \int dt_a \, dt_b \, B_g(t_a, x_a, \mu) \, B_g(t_b, x_b, \mu)$$
$$\times S_B^{gg}\left(\mathcal{T}_B - \frac{t_a + t_b}{m_H}, \mu\right) \left[1 + \mathcal{O}(\frac{\Lambda_{\text{QCD}}}{m_H}, \tau_B)\right]. \tag{9.5}$$

We will focus on the Higgs production cross section. The leptonic decay of the Higgs,

which is of course important in practical applications, does not alter the structure of the factorization theorem. It can be included straightforwardly as was done in Ref. [166] for the simpler case of $pp \to Z/\gamma \to \ell^+\ell^-$. In the narrow width approximation one can simply multiply the production cross section by the relevant differential branching fraction.

9.2 Plots

We will now show results for the 0-jet Higgs production cross section from gluon fusion. We restrict ourselves to the cross section for $\mathcal{T}_B$ in Eq. (9.5), because there is no distinction between $\mathcal{T}_B$ and $\mathcal{T}_B^{\mathrm{cm}}$ at NLL and the difference at NNLL is very small for the cross section integrated over Y (the distinction is important for large Y but this only gives a small contribution to the total cross section). We evaluate the hard, beam and soft functions at their natural scale, where they contain no large logarithms, and run them to a common scale μ using their RGE, which effectively sums the large logarithms. All the necessary perturbative results are collected in App. E, and we evaluate the convolutions of plus distributions using the identities from App. B of Ref. [135]. We use the MSTW2008 [143] parton distributions at NLO for $\alpha_s(m_Z) = 0.12$ and with two-loop, five-flavor running for $\alpha_s(\mu)$.

The perturbative uncertainty bands in the plots are estimated by taking the envelope of the following three separate scale variations

$$
\begin{aligned}
\text{a)} \qquad & \mu_H = r m_H \,, \ \mu_B = r\sqrt{\mathcal{T}_B m_H}\,, \ \mu_S = r\mathcal{T}_B \,, \\
\text{b)} \qquad & \mu_H = m_H \,, \ \mu_B = r^{-(\ln \mathcal{T}_B/m_H)/4}\sqrt{\mathcal{T}_B m_H}\,, \ \mu_S = \mathcal{T}_B \,, \\
\text{c)} \qquad & \mu_H = m_H \,, \ \mu_B = \sqrt{\mathcal{T}_B m_H}\,, \ \mu_S = r^{-(\ln \mathcal{T}_B/m_H)/4}\mathcal{T}_B \,,
\end{aligned}
\tag{9.6}
$$

with $r = \{1/2, 2\}$, and $r = 1$ corresponds to the central value. This procedure for estimating the uncertainties is identical to Drell-Yan and is discussed further around Eq. (8.3). For the cross section integrated up to $\mathcal{T}_B \leq \mathcal{T}_B^{\mathrm{cut}}$, the scales are chosen by replacing $\mathcal{T}_B$ with $\mathcal{T}_B^{\mathrm{cut}}$ in Eq. (9.6).

In Fig. 9-1 we show the Higgs production cross section from gluon fusion at the LHC with $E_{\mathrm{cm}} = 7\,\mathrm{TeV}$ (left panel) and the Tevatron (right panel), where we imposed the jet veto by requiring $\mathcal{T}_B < 20\,\mathrm{GeV}$. The large shift from NLL to NNLL is due to the large NLO corrections rather than NNLL resummation. This is clear from the NLL$'$ result (dashed),
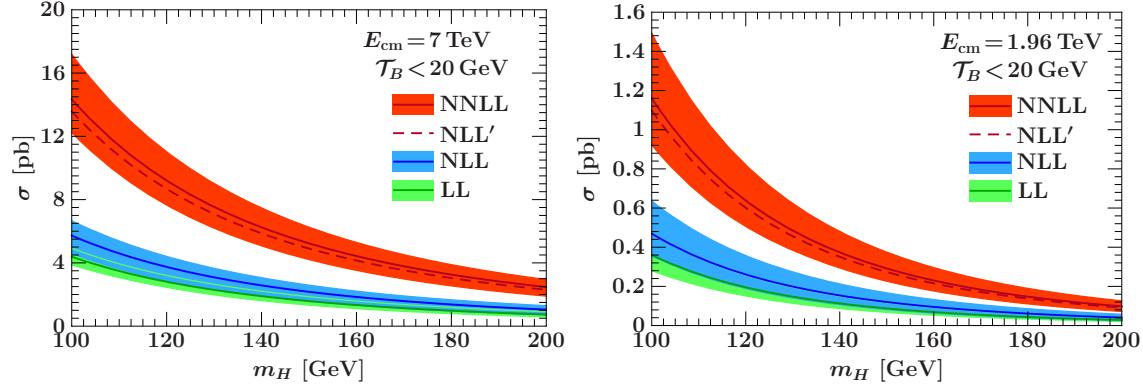
Figure 9-1: The Higgs production cross section from gluon fusion at the LHC with $E_{cm} = 7\,\text{TeV}$ (left panel) and the Tevatron (right panel) with a cut on beam thrust $\mathcal{T}_B < 20\,\text{GeV}$. Shown are the LL, NLL and NNLL results with perturbative uncertainties as well as the NLL$'$ results, which combine NLO fixed order corrections with NLL resummation.

which combines the fixed order NLO corrections with NLL resummation and accounts for almost the entire shift. These large perturbative corrections are well-known from fixed order calculations. Although it is not very visible, the relative uncertainties decrease slightly when going from NLL to NNLL. The larger relative uncertainties compared to Drell-Yan are not surprising since $C_A/C_F = 9/4$.

Figure 9-2 shows the beam thrust dependence of the production cross section for a Higgs with mass $m_H = 165\,\text{GeV}$ at the LHC with $E_{cm} = 7\,\text{TeV}$ (left column) and the Tevatron (right column). In these plots we include the singular NLO result, which corresponds to evaluating the factorization theorem in Eq. (9.5) at $\mu = Q$ without any running, i.e. without any resummation. The top row of Fig. 9-2 shows the cross section as function of $\mathcal{T}_B$. We observe that the resummation of logarithms regularizes the IR singularity for $\mathcal{T}_B \to 0$ in the fixed-order NLO result, as was the case for Drell-Yan. Compared to the Drell-Yan result in the left panel of Fig. 8-3, the peak occurs at a larger value of $\mathcal{T}_B$ and the tail is larger as well. This implies that there is more initial state radiation, gluons radiate more than quarks. We did not plot the curves for $\mathcal{T}_B \leq 1\,\text{GeV}$, because $\mu_S = \mathcal{T}_B$ and we therefore expect large corrections to our perturbative soft function in that region.

The bottom row in Fig. 9-2 shows the corresponding cross sections integrated up to $\mathcal{T}_B < \mathcal{T}_B^{\text{cut}}$ as a function of $\mathcal{T}_B^{\text{cut}}$. For $\mathcal{T}_B^{\text{cut}} \to 0$ the resummation is most important, while for large $\mathcal{T}_B^{\text{cut}}$ the perturbative corrections are most important. We see that the NNLL result interpolates between these regions, approaching the singular NLO result as $\mathcal{T}_B^{\text{cut}}$ becomes
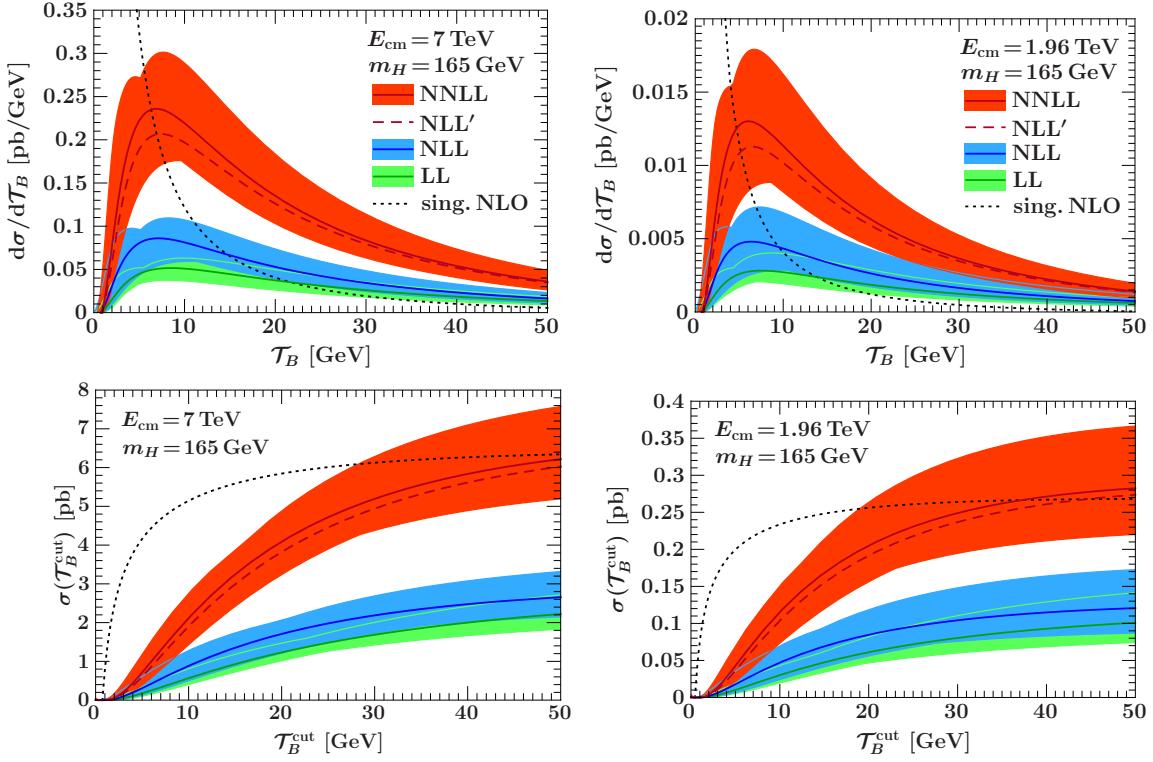
Figure 9-2: The Higgs production cross section though gluon fusion for $m_H = 165\,\text{GeV}$ at the LHC with $E_{\text{cm}} = 7\,\text{TeV}$ (left column) and the Tevatron (right column). Top row: The cross section differential in $\mathcal{T}_B$. Bottom row: The cross section integrated up to $\mathcal{T}_B < \mathcal{T}_B^{\text{cut}}$ as function of $\mathcal{T}_B^{\text{cut}}$. Shown are the LL, NLL and NNLL results with perturbative uncertainties and the NLL$'$ and singular NLO result.

large and the NLL and LL result for $\mathcal{T}_B^{\text{cut}} \to 0$. Compared to the results for Drell-Yan shown in the right panel of Fig. 8-3, the size of the α_s corrections as well as the effect of resummation is much larger.

Chapter 10

N-Jettiness: An Inclusive Event Shape to Veto Jets

In this chapter we will extend our work to events with N signal jets and consider the veto on additional unwanted jets. We introduce a global event shape "N-jettiness" τ_N to impose this veto, which for $N = 0$ reduces to the beam thrust. We discuss the experimental relevance of jet vetos and the benefits of using τ_N in theory calculations. In particular, τ_N allows us to sum large logarithms due to phase space restrictions and leads to a factorization formula with inclusive jet and beam functions. The work presented in this chapter was first reported in Ref. [167].

10.1   Introduction

At the LHC or Tevatron, hard interactions involving Higgs or new-physics particles are identified by looking for signals with a characteristic number of energetic jets, leptons, or photons [2, 39]. The backgrounds come from Standard Model processes producing the same signature of hard objects possibly with additional jets. An example are top quarks decaying into W plus b-jet, which is a major background for $H \to WW$ [5]. When reconstructing masses and decay chains of new-physics particles additional jets can cause large combinatorial backgrounds. Standard Model processes can also fake a signal when a jet is misidentified as lepton or photon, a typical example being $H \to \gamma\gamma$.

   Thus, a veto on additional undesired jets is an effective and sometimes necessary method to clean up the events and discriminate signal and the various backgrounds. More generally,

one would like to measure an "exclusive" N-jet cross section, $pp \to XL(Nj)$, to produce N signal jets j where the remaining X contains no hard (central) jets. Here, $N \geq 0$ and L denotes the hard leptons or photons required as part of the signal.

We introduce an inclusive event shape "N-jettiness", denoted τ_N and defined below in Eq. (10.1). For an event with at least N energetic jets, τ_N provides an inclusive measure of how N-jet-like the event looks. In the limit $\tau_N \to 0$ the event contains exactly N infinitely narrow jets. For $\tau_N \sim 1$ the event has hard radiation between the N signal jets. Requiring $\tau_N \ll 1$ constrains the radiation outside the signal and beam jets, providing an inclusive way to veto additional central jets. It yields an inclusive definition of an exclusive N-jet cross section with a smooth transition between the case of no jet veto, $\tau_N \sim 1$, and the extremely exclusive case $\tau_N \to 0$.

Vetoing additional jets imposes a phase-space restriction on the underlying inclusive N-jet cross section to produce N or more jets with the same L. Irrespectively of its precise definition, the jet veto introduces a jet resolution scale μ_J that characterizes this restriction, i.e. the distinction between N and $N+1$ jets. Hence, the exclusive N-jet cross section contains phase-space logarithms $\alpha_s^n \ln^m(\mu_J^2/\mu_H^2)$, where $m \leq 2n$ and μ_H is the scale of the hard interaction. For τ_N, $\mu_J^2/\mu_H^2 \simeq \tau_N \ll 1$. Generically there is always a hierarchy $\mu_J \ll \mu_H$, which becomes larger the stronger the restrictions are. These large logarithms must be summed to obtain reliable predictions.

Jet vetoes are typically implemented by using a jet algorithm to find all jets in the event and vetoing events with too many energetic jets. Jet algorithms are good tools to identify the signal jets. However, they are not necessarily well-suited to veto unwanted jets, because the corresponding phase-space restrictions are complicated and depend in detail on the algorithm. This makes it difficult to incorporate the jet veto into explicit theoretical calculations and in particular inhibits a systematic summation of the resulting large logarithms. In this case, usually the only way to predict the corresponding exclusive N-jet cross section is to rely on parton shower Monte Carlos to sum the leading logarithmic (LL) series.

In contrast, vetoing jets by cutting on an inclusive variable like τ_N has several advantages. First, we can go beyond LL order, because the logarithms from the phase-space restriction, $\alpha_s^n \ln^m \tau_N$, are simple enough to allow their systematic summation to higher orders. Moreover, the theory predictions with factorization can be directly compared with

(a) $e^+e^- \to 2$ jets.

(b) Isolated Drell-Yan.

(c) $pp \to$ leptons plus jets.
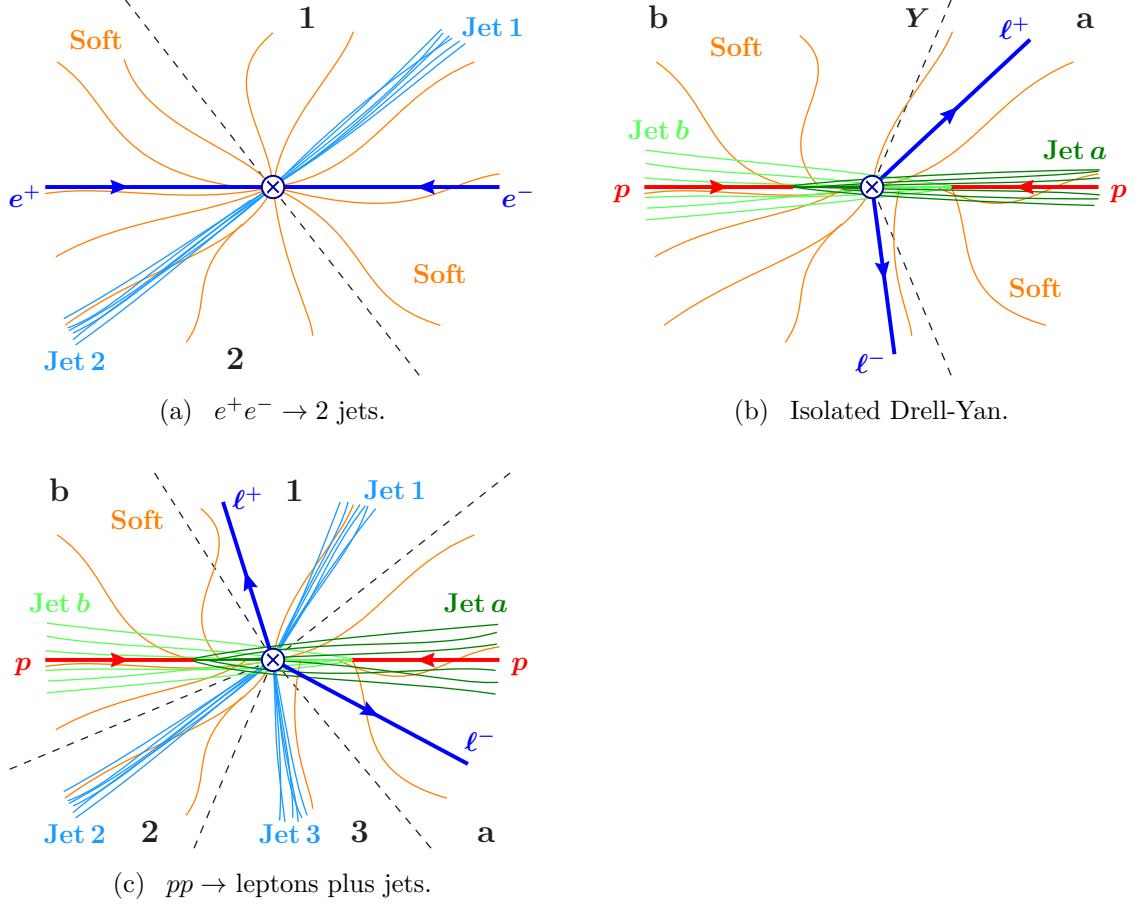
Figure 10-1: Different situations for the application of N-jettiness.

experiment without having to utilize Monte Carlos for parton showering or hadronization. Experimentally, τ_N reduces the dependence on jet algorithms and might help improve the background rejection.

10.2   Definition

N-jettiness is defined as

$$\tau_N = \frac{2}{Q^2} \sum_k \min\left\{ q_a \cdot p_k,\, q_b \cdot p_k,\, q_1 \cdot p_k,\, \ldots,\, q_N \cdot p_k \right\}. \tag{10.1}$$

As we discuss below, this definition of τ_N yields a factorization formula with inclusive jet and beam functions and allows the summation of logarithms to next-to-next-to-leading logarithmic (NNLL) order. The sum over k in Eq. (10.1) runs over the momenta p_k of all

measured (pseudo-)particles in the final state excluding the signal leptons or photons in L. (Any other leptons or photons, e.g. from hadronic decays, are included in the sum.) For simplicity we take all p_k to be massless. The q_a, q_b, and q_1, ..., q_N are a fixed set of massless reference momenta for the two beams and the N signal jets,

$$q_{a,b}^\mu = \tfrac{1}{2} x_{a,b} E_{\rm cm}\, n_{a,b}^\mu\,, \qquad\qquad n_a^\mu = (1,0,0,1)\,, \quad n_b^\mu = (1,0,0,-1)\,,$$
$$q_J^\mu = E_J(1,\hat{n}_J)\,, \qquad\qquad J = \{1,\ldots,N\}\,. \qquad\qquad (10.2)$$

The E_J and $\hat{n}_J$ correspond to the energies and directions of the N signal jets. Their choice is discussed below. The beam reference momenta q_a and q_b are the large momentum components of the colliding partons along the beam axis (taken to be the z axis). They are defined by

$$x_a E_{\rm cm} = n_b \cdot (q_1 + \cdots + q_N + q)\,, \qquad\qquad (10.3)$$

and analogously for x_b with $a \leftrightarrow b$. Here, q is the total momentum of the non-hadronic signal L. In Eq. (10.1), $Q^2 = x_a x_b E_{\rm cm}^2$ is the hard interaction scale, and the distance of a particle with momentum p_k from the jets or beams is measured by $q_m \cdot p_k$. If L contains missing energy, so q and $x_{a,b}$ are not known, one can use a modified distance measure as we discuss below Eq. (10.11).

The minimum for each k in Eq. (10.1) associates the particle with the closest beam or jet, appropriately dividing the hadronic initial-state radiation (ISR) and final-state radiation (FSR). Soft particles and energetic particles near any jet or beam only give small contributions to the sum. For $2 \to N$ scattering of massless partons, $\tau_N = 0$. Energetic particles far away from all jets and beams give large contributions. Hence, for $\tau_N \ll 1$ the final state has N jets, two forward beam jets, and only soft radiation between them. In this limit $x_{a,b}$ are the momentum fractions of the annihilated partons, and $Y = \ln(x_a/x_b)/2$ is the boost of the partonic center-of-mass frame.

10.2.1 $N = 2$ for $e^+e^- \to$ Jets.

In e^+e^- collisions there is no hadronic ISR, so we drop the $q_{a,b} \cdot p_k$ entries in Eq. (10.1). Now Q^2 is the total invariant mass of the leptons and $Y = 0$. In the two-jet limit, the jet

directions are close to the thrust axis $\hat{t}$, so we can choose

$$q_1^\mu = \frac{1}{2} Q\,(1, \hat{t})\,, \qquad q_2^\mu = \frac{1}{2} Q\,(1, -\hat{t}\,) \tag{10.4}$$

as reference momenta, and Eq. (10.1) becomes

$$\tau_2^{ee} = \frac{1}{Q} \sum_k E_k \min\{1 - \cos\theta_k,\, 1 + \cos\theta_k\}\,, \tag{10.5}$$

where θ_k is the angle between $\vec{p}_k$ and $\hat{t}$. The minimum divides all particles into the two hemispheres perpendicular to $\hat{t}$ as shown in Fig. 10-1(a). For $\tau_2^{ee} \ll 1$, the total invariant mass in each hemisphere is much smaller than Q, so the final state contains two narrow jets. In this limit, $\tau_2^{ee} = 1 - T$, where T is thrust, and a factorization theorem exists for $d\sigma/d\tau_2^{ee}$, which can be used to sum logarithms of τ_2^{ee} [43, 64, 129].

10.2.2 $N = 0$ for Drell-Yan

Next, consider isolated Drell-Yan, $pp \to X\ell^+\ell^-$ with no hard central jets, shown in Fig. 10-1(b). We now have ISR from the incoming partons, but no FSR from jets. From Eq. (10.3) we have

$$x_a E_{\rm cm} = e^{+Y}\sqrt{q^2 + \vec{q}_T^{\,2}}\,, \quad x_b E_{\rm cm} = e^{-Y}\sqrt{q^2 + \vec{q}_T^{\,2}}\,, \tag{10.6}$$

where q^2 and $\vec{q}_T$ are the dilepton invariant mass and transverse momentum, and Y equals the dilepton rapidity. Now, $Q^2 = q^2 + \vec{q}_T^{\,2}$ and Eq. (10.1) becomes

$$\tau_0 = \frac{1}{Q} \sum_k |\vec{p}_{kT}| \min\{e^{Y - \eta_k},\, e^{-Y + \eta_k}\}\,. \tag{10.7}$$

Thus, the q_a and q_b dependence in Eq. (10.1) explicitly accounts for the boost of the partonic center-of-mass frame. For $Y = 0$, the minimum in Eq. (10.7) divides all particles into two hemispheres perpendicular to the beam axis (analogous to the thrust axis in e^+e^-). For $Y \neq 0$, the hemispheres are boosted with their boundary now at Y, and the beam jet in the direction of the boost is narrower than the other, as depicted in Fig. 10-1(b). Contributions to τ_0 from large rapidities are exponentially suppressed by $|\vec{p}_{kT}|e^{-|\eta_k|} \approx 2E_k e^{-2|\eta_k|}$, so particles beyond the detector's rapidity reach give negligible contributions.

Beam thrust is given by $\tau_B = \sqrt{1 + \vec{q}_T^{\,2}/q^2}\,\tau_0$. It is obtained by choosing $x_{a,b} E_{\rm cm} =$

$\sqrt{q^2}e^{\pm Y}$ in case q^2 and Y are measured rather than the longitudinal components $n_{a,b} \cdot q$ in Eq. (10.6). For $\tau_0 \ll 1$ the hadronic final state can only contain soft radiation plus energetic radiation in the forward directions. In this limit the leptons become back-to-back in the transverse plane, $\vec{q}_T \ll Q$, so $\tau_B = \tau_0$. In Ch. 7 we derived a factorization theorem for $d\sigma/d\tau_B$ at small τ_B, which we used to sum logarithms of τ_B to NNLL.

10.2.3   General Case

For $pp \rightarrow XL(Nj)$ we have both ISR and FSR. We select candidate signal events by measuring L and running a jet algorithm to find the N signal jets and their momenta p_J. The conditions on the jets and L that define the signal are encoded in the cross section by a measurement function $F_N(\{p_J\}, L)$. Generically, F_N will enforce that there are at least N energetic jets that are sufficiently separated from each other and the beams. We now use the measured jet energies and directions to define the jet reference momenta q_J in Eq. (10.2),

$$E_J = p_J^0\,, \qquad \hat{n}_J = \vec{p}_J/|\vec{p}_J|\,, \tag{10.8}$$

while q_a and q_b are given by Eqs. (10.2) and (7.30).

Taking the minimum in Eq. (10.1) combines the previous cases in Eqs. (10.5) and (10.7). It divides all particles into jet and beam regions that are unique for a given set of reference momenta and whose union covers all of phase space, as illustrated in Fig. 10-1(c). The boundary between any two neighboring regions is part of a cone and is such that the sum of the total invariant masses in the regions is minimized (or in case of a beam region the virtuality of the incoming colliding parton).

For events with small τ_N all jet algorithms should agree how energetic radiation is split up between the jets and beams, and only differ in their treatment of softer particles. Thus, they all give the same $\hat{n}_J$ and E_J up to power corrections, while the split up of the soft radiation is determined by τ_N itself. Hence, the dependence of τ_N on the jet algorithm is formally power suppressed, $\tau_N^{\text{alg.1}} = \tau_N^{\text{alg.2}} + \mathcal{O}(\tau_N^2)$, as seen in Eq. (10.14) below.

To measure τ_N, we still rely on having a suitable jet algorithm to find the N signal jets but not more so than if we were not measuring τ_N. Imagine the jet size in the algorithm is chosen too small such that the algorithm divides what should be a single signal jet into

several narrow jets [1]. In this case, the jet algorithm yields a poorly reconstructed signal irrespective of measuring τ_N.

Since the jet veto is now provided by τ_N, this situation can be avoided because we do not have to rely on the jet algorithm to identify additional jets and so can use an algorithm that can be forced to always yield at most N jets. This is in fact the most natural thing to do when one is looking for N jets. Therefore, using τ_N as jet veto could also help improve the signal reconstruction.

10.2.4   Generalizations

We can generalize τ_N to

$$\tau_N^d = \sum_k \min\big\{d_a(p_k), d_b(p_k), d_1(p_k), \ldots, d_N(p_k)\big\}, \tag{10.9}$$

where $d_m(p_k)$ can be any infrared-safe distance measure. In Eq. (10.1), $d_m(p_k) = 2q_m\cdot p_k/Q^2$ with

$$2q_a \cdot p_k = |\vec{p}_{kT}|\, Q\, e^{Y-\eta_k}\,,$$
$$2q_J \cdot p_k = |\vec{p}_{kT}|\, |\vec{q}_{JT}|\, (2\cosh\Delta\eta_{Jk} - 2\cos\Delta\phi_{Jk})\,. \tag{10.10}$$

Here, $\Delta\eta_{Jk}$ and $\Delta\phi_{Jk}$ are the rapidity and azimuthal distances between q_J and p_k. If these are small, the factor in brackets reduces to the familiar $R^2 = (\Delta\eta)^2 + (\Delta\phi)^2$.

Raising a given measure to a power, $d_m(p_k)^{\alpha_m}$ changes the relative weight between the region's center and periphery in the sum over k, while the powers α_m can be used to change the division between beams and jets. Different measures that are boost-invariant along the beam axis can be obtained by raising each factor in Eq. (10.10) to a different power. A geometric measure, which is independent of $|\vec{q}_{JT}|$, is

$$d_a(p_k) = \frac{|\vec{p}_{kT}|}{Q}\, e^{Y-\eta_k}\,, \qquad d_b(p_k) = \frac{|\vec{p}_{kT}|}{Q}\, e^{-Y+\eta_k}\,,$$
$$d_J(p_k) = \frac{|\vec{p}_{kT}|}{Q}\, (2\cosh\Delta\eta_{Jk} - 2\cos\Delta\phi_{Jk})\,. \tag{10.11}$$

---

[1]This can be tested by comparing the total energy in each region defined by τ_N with the energy from the jet algorithm. If these are very different, but at the same time τ_N is small, then there are additional energetic particles near the signal jets that the algorithm should have included.

It evenly divides the area rather than invariant mass between neighboring regions, such that more energetic jets also get more invariant mass.

If L contains missing energy, $x_{a,b}$ in Eq. (10.3) and thus Q and Y are not known. For Q, one can use any hard scale, like the $|\vec{q}_{JT}|$ of the hardest jet, since it only serves as an overall normalization. In the beam measures $d_{a,b}(p_k)$ in Eq. (10.11) we can simply set $Y = 0$, which defines them in the hadronic center-of-mass frame and effectively averages over all possible boosts Y.

N-jettiness does not split events into N, $N + 1$, $N + 2$, etc. jets like a traditional jet algorithm. But we can consider using τ_N to define an "exclusive N-jet algorithm" as follows: First, we use a geometric measure and find the directions $\hat{n}_J$ and boost Y that minimize τ_N. This is analogous to determining the thrust axis in $e^+e^- \to$ jets. It might actually allow one to get an estimate of Y even in the case of missing energy by exploiting the asymmetry in the beam jets. Second, we determine the jet energies by summing over the particles in each jet region. (To reduce the sensitivity to the underlying event and pile-up, one can weigh the sum over energies by the distance from $\hat{n}_J$.)

10.3   Factorization formula

For simplicity, we now use τ_N again as defined in Eq. (10.1). For $\tau_N \ll 1$, QCD ISR and FSR can be described in soft-collinear effective theory [29–31, 35, 37] at leading power by $N + 2$ independent sectors for collinear particles close to each q_m with $m = \{a, b, J\}$ and a separate sector for soft particles. By power counting, J-collinear particles are closest to q_J, so the sum over k for the J-collinear sector is

$$\sum_{k \in \text{coll}_J} \min_m \{2q_m \cdot p_k\} = \sum_{k \in \text{coll}_J} 2q_J \cdot p_k = s_J, \qquad (10.12)$$

where (up to power corrections) s_J is the total invariant mass in the J-collinear sector. Similarly, the sum over the beam collinear sectors yields the total (transverse) virtuality of the colliding partons, t_a and t_b. Therefore,

$$\tau_N Q^2 = t_a + t_b + \sum_J s_J + \sum_{k \in \text{soft}} \min_m \{2q_m \cdot p_k\}. \qquad (10.13)$$

The sum in the last term is now restricted to the soft sector. Combining Eq. (10.13) with the analyses in Ref. [32] and Ch. 7 yields the factorization formula for N-jettiness [2]

$$
\frac{\mathrm{d}\sigma}{\mathrm{d}\tau_N} = \int \mathrm{d}x_a \mathrm{d}x_b \int \mathrm{d}^4 q \, \mathrm{d}\Phi_L(q) \int \mathrm{d}\Phi_N(\{q_J\}) F_N(\{q_m\}, L) \, (2\pi)^4 \delta^4 \Big(q_a + q_b - \sum_J q_J - q \Big)
$$
$$
\times \sum_{ij,\kappa} \mathrm{tr} \, \widehat{H}_{ij\to\kappa}(\{q_m\}, L, \mu) \int \mathrm{d}t_a \, B_i(t_a, x_a, \mu) \int \mathrm{d}t_b \, B_j(t_b, x_b, \mu) \prod_J \int \mathrm{d}s_J \, J_{\kappa_J}(s_J, \mu)
$$
$$
\times \widehat{S}_N^{ij\to\kappa} \Big(\tau_N - \frac{t_a + t_b + \sum_J s_J}{Q^2}, \{q_m\}, \mu \Big). \tag{10.14}
$$

$\widehat{H}_{ij\to\kappa}(\{q_m\}, L)$ contains the underlying hard process $i(q_a)j(q_b) \to L(q)\kappa_1(q_1)\cdots\kappa_N(q_N)$, where i, j, κ_J denote the parton types, and the sum over ij, κ is over all relevant partonic channels. It is a matrix in color space given by the IR-finite parts (in pure dim. reg.) of the squared partonic matrix elements in each channel. The N-body phase space for the massless momenta q_J is denoted $\mathrm{d}\Phi_n(\{q_J\})$, and that for L by $\mathrm{d}\Phi_L(q)$.

The distributions in s_J and $t_{a,b}$ are described by inclusive jet and beam functions, $J_{\kappa_J}(s_J)$ and $B_{i,j}(t_{a,b}, x_{a,b})$. The last term in Eq. (10.13) is the contribution to τ_N from soft particles in the "underlying event". It is described by the soft function $\widehat{S}_N^{ij\to\kappa}(\tau_N^{\mathrm{soft}}, \{q_m\})$, which depends on the jet's angles $\hat{n}_l \cdot \hat{n}_m$ and energy fractions E_l/E_m. Like $\widehat{H}$, it is a color matrix, and the trace in Eq. (10.14) is over $\mathrm{tr}(\widehat{H}\widehat{S})$.

In Eq. (10.14), all functions are evaluated at the same renormalization scale μ. Large logarithms of τ_N in $\mathrm{d}\sigma/\mathrm{d}\tau_N$ are summed by first computing $\widehat{H}(\mu_H)$, $J(\mu_J)$, $B(\mu_B)$, $\widehat{S}(\mu_S)$ at the scales $\mu_H \simeq Q$, $\mu_J \simeq \mu_B \simeq \sqrt{\tau_N}Q$, $\mu_S \simeq \tau_N Q$, where the functions contain no large logarithms, and then evolving them to the scale μ. This evolution is known analytically [94, 135, 151] and the required anomalous dimensions are already known to NNLL [92, 112, 127, 130, 146, 147], because we have inclusive jet and beam functions. NNLL also requires the $\mathcal{O}(\alpha_s)$ corrections for each function, which are known for J and B. The $\mathcal{O}(\alpha_s)$ hard function is determined by the one-loop QCD matrix elements. For $\tau_N \gg \Lambda_{\mathrm{QCD}}/Q$, $\widehat{S}(\mu_S)$ can be computed perturbatively and will be given in a future publication.

---

[2] Here, F_N enforces distinct collinear sectors with $1 - \hat{n}_l \cdot \hat{n}_m \gg \tau_N$ and $E_m/Q \gg \tau_N$. We assume F_N only depends on the large components q_J of the jet momenta, $p_J = q_J[1 + \mathcal{O}(\tau_N)]$, and that L only couples to the QCD subprocess via a hard interaction. We also assume that Glauber gluons do not spoil this factorization.

Chapter 11

Conclusions and Outlook

Typical Higgs and new physics searches at the LHC or Tevatron require a certain number of hard jets, leptons and photons. Jet algorithms are good for identifying jets, but, as we have seen, a veto on additional unwanted jets is most easily incorporated in theory calculations by using an event shape. This approach allowed us to sum the corresponding large phase space logarithms and make predictions without relying on Monte Carlo programs for parton showers or hadronization models.

A lot of our work has focussed on the 0-jet case, for which we implemented the jet veto by restricting the beam thrust variable $\tau_B \ll 1$. A central jet veto is needed to reduce the large background in $H \to WW \to \ell\nu\ell\bar\nu$ from top quarks decaying into a W plus b-jet. We derived a factorization theorem that allowed us to sum the large phase space logarithms $\alpha_s^n \ln^m \tau_B$. The central jet veto also probes the initial-state radiation, which requires beam function to describe the initial state. Beam functions describe extracting a parton out of the proton as well as the formation of an initial-state jet. They can be related to PDFs through a perturbative matching calculation, which we carried out at one loop. Our calculations allow us to study the effect of initial-state radiation in perturbation theory and the next step is to compare our analytical results with Monte Carlo programs. Another interesting extension of our work would be to include the measurement of the recoil of the initial-state jets, which requires p_T dependent beam functions.

We concluded this thesis by considering the extension to N signal jets, for which we introduced the event shape N-jettiness to veto unwanted additional jets. Many of the features of the 0-jet case carry over, including the resummation of large logarithms and the

presence of beam functions. In the 0-jet case there was no jet algorithm dependence, in this case a jet algorithm is used to identify the jets but the dependence on the choice of jet algorithm is power suppressed. We still need to show the cancellation of Glauber gluons. Once the one-loop soft function has been calculated we can use our factorization formula to determine cross sections for processes with final state jets at NNLL. This will allow us to study the jet energies and directions, which are of interest to new physics searches. To study other properties of the jets, such as their invariant masses, requires an extension of our factorization formula.

Appendix A

Notation Cheat Sheet

A.1 Lightcone Coordinates

We use lightcone vectors n^μ and $\bar{n}^\mu$ with $n^2 = \bar{n}^2 = 0$ and $\bar{n}\cdot n = 2$ to decompose four-vectors $p^\mu = (p^+, p^-, p_\perp^\mu)$

$$p^\mu = p^- \frac{n^\mu}{2} + p^+ \frac{\bar{n}^\mu}{2} + p_\perp^\mu \,, \qquad p^+ = n\cdot p \,, \qquad p^- = \bar{n}\cdot p \,. \qquad (A.1)$$

We have two collinear directions $n_a^\mu = (1, 0, 0, 1)$ and $n_b^\mu = (1, 0, 0, -1)$ corresponding to the directions of the incoming protons, and take $n_b = \bar{n}_a$ and $n_a = \bar{n}_b$. Lightcone coordinates of a momentum with subscript a or b will be with respect to n_a or n_b, e.g. $B_a^+ = n_a \cdot B_a$, $B_b^+ = n_b \cdot B_b$. We will sometimes write $p_T = p_\perp$.

For an energetic particle collinear to the n^μ direction we separate its momentum p^μ into a (discrete) large $\tilde{p}^\mu$ and (continuous) small momentum p_r^μ in SCET, $p^\mu = \tilde{p}^\mu + p_r^\mu$. The large momentum $\tilde{p}^\mu = (0, \tilde{p}^-, \tilde{p}_\perp^\mu)$ has components $\tilde{p}^- = \bar{n}\cdot p$ and $\tilde{p}_\perp^\mu \sim \lambda p^-$, where λ is the power counting parameter. The continuous small momentum has scaling $p_r^\mu = \lambda^2 \tilde{p}^-$. The large momentum appears as a label on the field and is picked out by the label operator $\mathcal{P}$. The small momentum is picked out by $\hat{p}$ and is often written in the conjugate position space coordinate y. We absorb the residual p_r^- and $p_{r\perp}^\mu$ into the label $\tilde{p}$, to give continuous labels. This leaves us with just one residual coordinate y^-. More details on SCET can be found in Secs. 1.4, 3.1 and 7.1.

A.2 Symbols

Below we list the most common symbols and their definition. Whenever there is a subscript a there will be a corresponding symbol with a subscript b, corresponding to the other proton, parton or hemisphere. The subscripts i and j run over flavors (quark or gluon).

	Symbol	Definition
General	ε	polarization vector
	L	non-hadronic final state ($\ell^+\ell^-$ for Drell-Yan)
	n_a^μ	lightcone vectors in the direction of the incoming protons
	p_n	n-collinear proton
	$u_n(p)$	n-collinear spinor
	X	total hadronic final state
Momenta	b_a^μ	collinear radiation from the incoming parton a
	B_a^μ	hadronic momentum in hemisphere a, $B_a^\mu = b_a^\mu + r_a^\mu + k_a^\mu$
	k_a^μ	soft momentum in the hemisphere a
	P_a^μ	momentum of proton a, $P_a^\mu = E_{\rm cm} n_a^\mu/2$
	p_a^μ	momenta of incoming parton a
	$p_{1,2}^\mu$	momenta of the leptons for Drell-Yan
	r_a^μ	momentum of the proton remnant for proton a
	q^μ	total non-hadronic momentum ($q^\mu = p_1^\mu + p_2^\mu$ for Drell-Yan)
Kinematics	$\omega_{a,b}$	large momentum component of incoming parton, $\omega_a = p_a^-$
	Q	inv. mass of non-hadronic particles, hard scale, $Q = \sqrt{q^2}$
	t	transverse virtuality of incoming parton, $t_a = \omega_a b_a^+$
	τ	$\tau = q^2/E_{\rm cm}^2$
	τ_B	beam thrust
	x_a	momentum fraction of parton, $x_a = \omega_a/P_a^-$
	ξ_a	momentum fraction of parton in the PDF
	$y_B^{\rm cut}$	rapidity "cut" corresponding to beam thrust, $\tau_B \leq \exp(-2y_B^{\rm cut})$
	Y	total rapidity of non-hadronic particles
	z	parton momentum fraction of in partonic calculation
Scales	μ_B	beam scale, $\mu_B \sim \sqrt{\tau_B}Q$ for beam thrust
	μ_H	hard scale, $\mu_H \sim Q$
	μ_Λ	low scale at which the PDFs are defined
	μ_S	soft scale, $\mu_S \sim \tau_B Q$ for beam thrust

	Symbol	Definition
Factor-ization	B_i	beam function
	$\widetilde{B}_i$	beam function integrated up to $t \leq t_{\max}$
	f_i	parton distribution function
	H_{ij}	hard function (same for threshold and isolated processes)
	$\mathcal{I}_{ij}$	Wilson coefficient for initial state jet, $\mathcal{B} = \mathcal{I} \otimes f$
	J_i	(final state) jet function
	λ	power counting parameter, $\lambda \sim B^+/Q \sim \tau_B$
	$\mathcal{O}_i$	beam function operator, $B_i = \langle P^- | \mathcal{O}_i | P^- \rangle$
	$\mathcal{Q}_i$	PDF operator, $f_i = \langle P^- | \mathcal{Q}_i | P^- \rangle$
	S^{ij}	soft function (differs between threshold and isolated)
	σ_0	Born cross section
Renorm-alization	η_Γ	shows up in RGE solution for cusp piece
	$\gamma(\dots, \mu)$	anomalous dimension
	$\gamma(\alpha_s)$	non-cusp anomalous dimension
	Γ_{cusp}	cusp anomalous dimension
	K_Γ	exponent in RGE solution for cusp piece
	K_γ	exponent in RGE solution for non-cusp piece
	$P_{jk}(z)$	splitting functions in PDF evolution
	U	evolution function
	Z	renormalization factor
SCET	A_n	n-colinear gluon field
	A_s	soft gluon field
	$\mathcal{B}_{n\perp}$	gauge invariant collinear gluon field
	χ_n	gauge invariant n-collinear quark field, $\chi_n(y) = W_n^\dagger(y)\xi_n(y)$
	λ	power counting parameter, $\lambda \sim B^+/Q \sim \tau_B$
	$\hat{p}^\mu$	residual momentum operator
	$\mathcal{P}^\mu$	label momentum operator, $\mathcal{P}^\mu \xi_{n,\tilde{p}}(y) = \tilde{p}^\mu \xi_{n,\tilde{p}}(y)$
	$\overline{\mathcal{P}}$	minus label momentum operator, $\overline{\mathcal{P}} = \mathcal{P}^-$
	W_n	n-collinear Wilson line
	ξ_n	n-collinear quark field
	y^-	residual minus position coordinate
	Y_n	soft Wilson line along the n^μ direction (fundamental repr.)
	$\mathcal{Y}_n$	soft Wilson line along the n^μ direction (adjoint repr.)

Appendix B

Plus Distributions and Discontinuities

The standard plus distribution for some function $g(x)$ can be defined as

$$\big[\theta(x)g(x)\big]_+ = \lim_{\beta \to 0} \frac{\mathrm{d}}{\mathrm{d}x}\big[\theta(x-\beta)\,G(x)\big] \qquad \text{with} \qquad G(x) = \int_1^x \mathrm{d}x'\, g(x')\,, \tag{B.1}$$

satisfying the boundary condition $\int_0^1 \mathrm{d}x\,[\theta(x)g(x)]_+ = 0$. Two special cases we need are

$$\mathcal{L}_n(x) \equiv \left[\frac{\theta(x)\ln^n x}{x}\right]_+ = \lim_{\beta \to 0}\left[\frac{\theta(x-\beta)\ln^n x}{x} + \delta(x-\beta)\frac{\ln^{n+1}\beta}{n+1}\right],$$

$$\mathcal{L}^\eta(x) \equiv \left[\frac{\theta(x)}{x^{1-\eta}}\right]_+ = \lim_{\beta \to 0}\left[\frac{\theta(x-\beta)}{x^{1-\eta}} + \delta(x-\beta)\frac{x^\eta - 1}{\eta}\right]. \tag{B.2}$$

In addition, we need the identity

$$\frac{\theta(x)}{x^{1+\epsilon}} = -\frac{1}{\epsilon}\,\delta(x) + \mathcal{L}_0(x) - \epsilon\mathcal{L}_1(x) + \mathcal{O}(\epsilon^2)\,, \tag{B.3}$$

the Fourier transform

$$\mathcal{L}_0(x) = -\int \frac{\mathrm{d}y}{2\pi}\, e^{\mathrm{i}xy}\,\ln\!\big[\mathrm{i}(y - \mathrm{i}0)e^{\gamma_E}\big]\,, \tag{B.4}$$

and the two limits

$$\lim_{\beta \to 0}\left[\frac{\theta(x-\beta)\ln(x-\beta)}{x} + \delta(x-\beta)\frac{1}{2}\ln^2\beta\right] = \mathcal{L}_1(x) - \frac{\pi^2}{6}\,\delta(x)\,,$$

$$\lim_{\beta \to 0}\frac{\theta(x-\beta)\,\beta}{x^2} = \delta(x)\,. \tag{B.5}$$

Away from $x = 0$ these relations are straightforward, while the behavior at $x = 0$ is obtained by taking the integral of both sides. General relations for the rescaling and convolutions of $\mathcal{L}_n(x)$ and $\mathcal{L}^\eta(x)$ can be found in App. B of Ref. [135].

The discontinuity of a function $g(x)$ is defined as

$$\operatorname{Disc}_x g(x) = \lim_{\beta \to 0} \left[g(x + i\beta) - g(x - i\beta) \right]. \tag{B.6}$$

If we are only interested in the discontinuity in some interval in x, we simply multiply the right-hand side with the appropriate θ functions, as in Eq. (3.54). If $g(x)$ is real then $\operatorname{Disc}_x g(x) = 2i \operatorname{Im} g(x + i0)$. Two useful identities are

$$\frac{i}{2\pi} \operatorname{Disc}_x \frac{1}{x^{n+1}} = \frac{(-1)^n}{n!} \delta^{(n)}(x), \qquad \frac{i}{2\pi} \operatorname{Disc}_x (-x)^{n-\epsilon} = (-1)^{n-1} \frac{\sin \pi \epsilon}{\pi} \theta(x) x^{n-\epsilon}. \tag{B.7}$$

To derive the last identity, note that

$$(-x - i0)^{n-\epsilon} = \exp[(n - \epsilon) \ln(-x - i0)] = |x|^{n-\epsilon} \exp[-i\pi(n - \epsilon)\theta(x)], \tag{B.8}$$

so taking the imaginary part gives $\operatorname{Im}(-x - i0)^{n-\epsilon} = (-1)^n \sin(\pi\epsilon)\, \theta(x)\, x^{n-\epsilon}$. To calculate the discontinuities of the various graphs in Sec. 5.3 we need the relations,

$$-\theta(z) \frac{i}{2\pi} \operatorname{Disc}_{t>0} \int_0^1 d\alpha\, \Delta^{-1-\epsilon} = \theta(z) \frac{\sin \pi \epsilon}{\pi \epsilon} \frac{\theta(t)}{t^{1+\epsilon}} \theta(1 - z) z^{1+\epsilon} (1 - z)^{-\epsilon}, \tag{B.9}$$

$$-\theta(z) \frac{i}{2\pi} \operatorname{Disc}_{t>0} \int_0^1 d\alpha\, (1 - \alpha)\Delta^{-1-\epsilon} = \theta(z) \frac{\sin \pi \epsilon}{\pi \epsilon (1 - \epsilon)} \frac{\theta(t)}{t^{1+\epsilon}} \theta(1 - z) z^{1+\epsilon} (1 - z)^{1-\epsilon},$$

$$-\theta(z) \frac{i}{2\pi} \operatorname{Disc}_{t>0} \int_0^1 d\alpha\, (1 - \alpha)\, t\Delta^{-2-\epsilon} = \theta(z) \frac{\sin \pi \epsilon}{\pi \epsilon (1 + \epsilon)} \frac{\theta(t)}{t^{1+\epsilon}} \theta(1 - z) z^{2+\epsilon} (1 - z)^{-\epsilon},$$

where $\Delta = t(1 - \alpha/z)$.

Appendix C

Renormalization Structure of the Beam Function

In this appendix we derive the general structure of the beam function RGE in Eq. (3.25) to all orders in perturbation theory, which was presented in Ref. [168]. The two essential ingredients will be the known all-order renormalization properties of lightlike Wilson lines [57, 124, 126, 127] and the factorization theorem for the isolated $pp \to XL$ cross section, where X is the hadronic and L the non-hadronic final state. In Ch. 7 we proved that to all orders in perturbation theory and leading order in the power counting this cross section factorizes as

$$\frac{\mathrm{d}\sigma}{\mathrm{d}q^2 \mathrm{d}Y \mathrm{d}B_a^+ \mathrm{d}B_b^+} = \sum_{ij} H_{ij}(q^2, Y, \mu) \int \mathrm{d}k_a^+ \, \mathrm{d}k_b^+ \, S_{\mathrm{ihemi}}^{ij}(k_a^+, k_b^+, \mu)$$

$$\times q^2 B_i[\omega_a(B_a^+ - k_a^+), x_a, \mu] B_j[\omega_b(B_b^+ - k_b^+), x_b, \mu] \,. \qquad \text{(C.1)}$$

The sum over ij runs over parton species $ij = \{gg, u\bar{u}, \bar{u}u, d\bar{d}, \bar{d}d, \ldots\}$. The soft function does not depend on the quark flavor, and its superscript only refers to the color representation.

The three ingredients in Eq. (C.1) are the renormalized hard, beam, and soft functions, $H_{ij}(q^2, Y, \mu)$, $B_i(t, x, \mu)$, $S_{\mathrm{ihemi}}^{ij}(k_a^+, k_b^+, \mu)$. Their dependence on the renormalization scale μ must cancel in Eq. (C.1), because the cross section must be μ independent. The structure of the RGE for the hard and soft functions thus uniquely determines the allowed structure of the beam function RGE.

The hard function is a contraction between the relevant leptonic matrix element squared

and the square of the Wilson coefficients of the color-singlet $q\bar{q}$ and gg local SCET currents (see Sec. 7.3.2)

$$O_{q\bar{q}}^{\alpha\beta} = \bar{\chi}_{n_a,-\omega_a}^{\alpha}\, \chi_{n_b,\omega_b}^{\beta}\,, \qquad O_{gg}^{\mu\nu} = \sqrt{\omega_a\, \omega_b}\, \mathcal{B}_{n_a,-\omega_a\perp}^{\mu c}\, \mathcal{B}_{\bar{n}_b,-\omega_b\perp}^{\nu c}\,, \tag{C.2}$$

where α and β are spin indices. In each collinear sector, total label momentum and fermion number for each quark flavor are conserved. Thus, the currents cannot mix with each other and are multiplicatively renormalized. Furthermore, RPI-III invariance implies that the RGE for the currents can only depend on $q^2 = \omega_a\omega_b$. The renormalization of these SCET currents also does not depend on their spin structure, so the RGE for the hard function must have the same structure as for the currents. Therefore, to all orders in perturbation theory we have (with no sum on ij)

$$\mu\frac{\mathrm{d}}{\mathrm{d}\mu}H_{ij}(q^2, Y, \mu) = \gamma_H^{ij}(q^2, \mu)\, H_{ij}(q^2, Y, \mu)\,. \tag{C.3}$$

Next, the incoming hemisphere soft function, $S_{\text{ihemi}}^{ij}(k_a^+, k_b^+, \mu)$, is given by the vacuum matrix element of incoming soft lightlike Wilson lines along the n_a and n_b directions. In position space,

$$\widetilde{S}_{\text{ihemi}}^{ij}(y_a^-, y_b^-, \mu) = \int \mathrm{d}k_a^+ \mathrm{d}k_b^+\, e^{-\mathrm{i}(k_a^+ y_a^- + k_b^+ y_b^-)/2}\, S_{\text{ihemi}}^{ij}(k_a^+, k_b^+, \mu) \tag{C.4}$$

has two cusps, one at spacetime position 0 and one at $y = y_a^- n_a/2 + y_b^- n_b/2$. The renormalization properties of lightlike Wilson lines with cusps [57, 124, 126, 127] then imply that to all orders in perturbation theory,

$$\mu\frac{\mathrm{d}}{\mathrm{d}\mu}\widetilde{S}_{\text{ihemi}}^{ij}(y_a^-, y_b^-, \mu) = \tilde{\gamma}_S^{ij}(y_a^-, y_b^-, \mu)\, \widetilde{S}_{\text{ihemi}}^{ij}(y_a^-, y_b^-, \mu)\,, \tag{C.5}$$

$$\tilde{\gamma}_S^{ij}(y_a^-, y_b^-, \mu) = 2\Gamma_{\text{cusp}}^i(\alpha_s)\left[-\ln\left(\mathrm{i}\frac{y_a^- - \mathrm{i}0}{2}\mu e^{\gamma_E}\right) - \ln\left(\mathrm{i}\frac{y_b^- - \mathrm{i}0}{2}\mu e^{\gamma_E}\right)\right] + \gamma_S^{ij}(\alpha_s)\,,$$

where Γ_{cusp}^i is the cusp anomalous dimension for quarks/antiquarks or gluons, and $\gamma_S^{ij}[\alpha_s(\mu)]$ and $\Gamma_{\text{cusp}}^i[\alpha_s(\mu)]$ depend only indirectly on μ via $\alpha_s(\mu)$. Dimensional analysis and RPI-III invariance imply that the single logarithm multiplying $2\Gamma_{\text{cusp}}^i$ scales like $\ln(y_a^- y_b^- \mu^2)$. (The additional dimensionless factors are chosen for convenience. Any change in them can be absorbed into $\gamma_S^{ij}(\alpha_s)$.) The correct overall sign and i0 prescription for the logarithms can

be deduced from the explicitly known one-loop result see Eq. (7.89) and [94, 157].

Taking the Fourier transform of the cross section in Eq. (C.1) with respect to B_a^+ and B_b^+ and differentiating the result with respect to μ yields

$$
\begin{aligned}
0 &= \mu \frac{\mathrm{d}}{\mathrm{d}\mu} \left[\sum_{ij} H_{ij}(q^2, Y, \mu) \widetilde{B}_i\left(\frac{y_a^-}{2\omega_a}, x_a, \mu\right) \widetilde{B}_j\left(\frac{y_b^-}{2\omega_b}, x_b, \mu\right) \widetilde{S}_{\mathrm{ihemi}}^{ij}(y_a^-, y_b^-, \mu) \right] \\
&= \sum_{ij} H_{ij}(q^2, Y, \mu) \widetilde{S}_{\mathrm{ihemi}}^{ij}(y_a^-, y_b^-, \mu) \\
&\quad \times \left[\gamma_H^{ij}(\omega_a\omega_b, \mu) + \tilde{\gamma}_S^{ij}(y_a^-, y_b^-, \mu) + \mu\frac{\mathrm{d}}{\mathrm{d}\mu} \right] \widetilde{B}_i\left(\frac{y_a^-}{2\omega_a}, x_a, \mu\right) \widetilde{B}_j\left(\frac{y_b^-}{2\omega_b}, x_b, \mu\right) . \quad \text{(C.6)}
\end{aligned}
$$

The factorization theorem for the cross section neither depends on the choice of L, which affects the form of H_{ij} for different ij, nor the type of the colliding hadrons. This implies that each term in the sum over ij must vanish separately. (For example, choosing Drell-Yan, $L = \ell^+\ell^-$, there is no contribution from $ij = gg$, so the quark and gluon contributions are separately zero. Then, by assigning arbitrary electroweak quark charges, the contribution from each quark flavor must vanish separately. Finally, the $ij = q\bar{q}$ and $ij = \bar{q}q$ contributions for a single quark flavor q must vanish separately by choosing various different incoming hadrons.) Therefore, the RGE for the product of the two beam functions is

$$
\left[\gamma_H^{ij}(\omega_a\omega_b, \mu) + \tilde{\gamma}_S^{ij}(y_a^-, y_b^-, \mu) + \mu\frac{\mathrm{d}}{\mathrm{d}\mu} \right] \widetilde{B}_i\left(\frac{y_a^-}{2\omega_a}, x_a, \mu\right) \widetilde{B}_j\left(\frac{y_b^-}{2\omega_b}, x_b, \mu\right) = 0 , \quad \text{(C.7)}
$$

which shows that the beam functions in position space renormalize multiplicatively and independently of $x_{a,b}$. The RGE for each individual beam function can only depend on the RPI-III invariant $y^-/2\omega$ and obviously cannot depend on the variables of the other beam function. Hence, we find that to all orders in perturbation theory

$$
\mu\frac{\mathrm{d}}{\mathrm{d}\mu} \widetilde{B}_i\left(\frac{y^-}{2\omega}, x, \mu\right) = \tilde{\gamma}_B^i\left(\frac{y^-}{2\omega}, \mu\right) \widetilde{B}_i\left(\frac{y^-}{2\omega}, x, \mu\right) , \quad \text{(C.8)}
$$

which is the result we set out to prove in this Appendix. Using Eq. (C.8) together with Eq. (C.7), the anomalous dimensions must satisfy the consistency condition

$$
0 = \gamma_H^{ij}(\omega_a\omega_b, \mu) + \tilde{\gamma}_S^{ij}(y_a^-, y_b^-, \mu) + \tilde{\gamma}_B^i\left(\frac{y_a^-}{2\omega_a}, \mu\right) + \tilde{\gamma}_B^j\left(\frac{y_b^-}{2\omega_b}, \mu\right) . \quad \text{(C.9)}
$$

Given the form of $\tilde{\gamma}_S^{ij}$ in Eq. (C.5), it follows that the anomalous dimensions are given to

179

all orders by

$$\gamma_H^{ij}(\omega_a\omega_b, \mu) = 2\Gamma_{\text{cusp}}^i(\alpha_s) \ln \frac{\omega_a\omega_b}{\mu^2} + \gamma_H^{ij}(\alpha_s),$$

$$\tilde{\gamma}_B^i\left(\frac{y^-}{2\omega}, \mu\right) = 2\Gamma_{\text{cusp}}^i(\alpha_s) \ln\left(\mathrm{i}\frac{y^- - \mathrm{i}0}{2\omega}\mu^2 e^{\gamma_E}\right) + \gamma_B^i(\alpha_s),$$

$$\gamma_S^{ij}(\alpha_s) = -\gamma_H^{ij}(\alpha_s) - \gamma_B^i(\alpha_s) - \gamma_B^j(\alpha_s). \tag{C.10}$$

Taking the Fourier transform using Eq. (B.4), the momentum-space anomalous dimensions become

$$\gamma_S^{ij}(k_a^+, k_b^+, \mu) = 2\Gamma_{\text{cusp}}^i(\alpha_s)\left[\frac{1}{\mu}\mathcal{L}_0\left(\frac{k_a^+}{\mu}\right)\delta(k_b^+) + \delta(k_a^+)\frac{1}{\mu}\mathcal{L}_0\left(\frac{k_b^+}{\mu}\right)\right] + \gamma_S^{ij}(\alpha_s)\,\delta(k_a^+)\delta(k_b^+),$$

$$\gamma_B^i(t, \mu) = -2\Gamma_{\text{cusp}}^i(\alpha_s)\frac{1}{\mu^2}\mathcal{L}_0\left(\frac{t}{\mu^2}\right) + \gamma_B^i(\alpha_s)\,\delta(t). \tag{C.11}$$

The same all-order structure of the soft anomalous dimension as in Eq. (C.11) was obtained in Ref. [94] for the hemisphere soft function with outgoing Wilson lines in $e^+e^- \to 2$ jets using analogous consistency conditions. In fact, the hard SCET currents here and there are the same and in Sec. 3.2 we proved that the anomalous dimensions for the beam and jet function are the same, $\gamma_B^i = \gamma_J^i$. Hence, the hemisphere soft functions with incoming and outgoing Wilson lines have in fact identical anomalous dimensions to all orders.

Appendix D

Quark Beam Function Matching in Pure Dimensional Regularization

Here we repeat the NLO matching calculation from Ch. 4 using dimensional regularization for both the UV and IR, which was reported in Ref. [168]. Since we only change the IR regulator, the final results for the matching coefficients $\mathcal{I}_{ij}(t, z, \mu)$ should not be affected.

In pure dimensional regularization all the loop diagrams contributing to the bare matrix elements of $\mathcal{Q}_q$ vanish, since by dimensional analysis there is no Lorentz invariant quantity they can depend on. Hence, including the counter terms in Eq. (4.17) to subtract the UV divergences, the renormalized matrix elements consist of pure IR divergences with opposite signs to the UV divergences,

$$
\begin{aligned}
\langle q_n | \mathcal{Q}_q(\omega, \mu) | q_n \rangle^{(1)} &= -\frac{1}{\epsilon} \frac{\alpha_s(\mu) C_F}{2\pi} \theta(z) P_{qq}(z) \,, \\
\langle g_n | \mathcal{Q}_q(\omega, \mu) | g_n \rangle^{(1)} &= -\frac{1}{\epsilon} \frac{\alpha_s(\mu) T_F}{2\pi} \theta(z) P_{qg}(z) \,.
\end{aligned}
\tag{D.1}
$$

This shows explicitly that the conventional $\overline{\text{MS}}$ definition of the PDFs in QCD, which also yields Eq. (D.1), is indeed identical to the SCET definition used in our OPE for the beam function.

Considering the beam function matrix elements, the bare results for Figs. 4-2(c) and 4-2(d) now vanish, because their loop integrals are again scaleless. For the remaining diagrams we can reuse the intermediate results from Sec. 4.2 before carrying out the Feynman parameter integrals and taking the discontinuity. Setting $t' = 0$ the denominator in the

Feynman parameter integrals in Eq. (4.22) becomes $(1 - \alpha)A - \alpha B = t(1 - \alpha/z)$. In this case it easier to carry out the integral after taking the discontinuity. The discontinuity we need is

$$\frac{i}{2\pi} \mathrm{Disc}_{t>0} \Big[\Big(1 - \frac{\alpha}{z}\Big)t\Big]^{-1-\epsilon} = \frac{\sin \pi \epsilon}{\pi} \frac{\theta(t)}{t^{1+\epsilon}} \theta\Big(\frac{\alpha}{z} - 1\Big)\Big(\frac{\alpha}{z} - 1\Big)^{-1-\epsilon}, \qquad (D.2)$$

where we used Eq. (B.7). Since we require $z > 0$, the first θ function becomes $\theta(\alpha - z)$, and so we have

$$-\theta(z)\frac{i}{2\pi}\mathrm{Disc}_{t>0} I_1(A, B, \epsilon) = -\theta(z)\frac{\sin \pi \epsilon}{\pi}\frac{\theta(t)}{t^{1+\epsilon}}\int_0^1 d\alpha\, \theta(\alpha - z)\Big(\frac{\alpha}{z} - 1\Big)^{-1-\epsilon}$$

$$= \theta(z)\frac{\sin \pi \epsilon}{\pi \epsilon}\frac{\theta(t)}{t^{1+\epsilon}}\theta(1 - z)z^{1+\epsilon}(1 - z)^{-\epsilon},$$

$$-\theta(z)\frac{i}{2\pi}\mathrm{Disc}_{t>0} I_2(A, B, \epsilon) = \theta(z)\frac{\sin \pi \epsilon}{\pi \epsilon(1 - \epsilon)}\frac{\theta(t)}{t^{1+\epsilon}}\theta(1 - z)z^{1+\epsilon}(1 - z)^{1-\epsilon}. \qquad (D.3)$$

For Fig. 4-2(a), using Eqs. (4.23) and (D.3) we obtain

$$\langle q_n|\theta(\omega)\mathcal{O}_q^{\mathrm{bare}}(t, \omega)|q_n\rangle^{(a)}$$

$$= \frac{\alpha_s(\mu)C_F}{2\pi}\frac{\theta(z)}{z}\Gamma(1 + \epsilon)(e^{\gamma_E}\mu^2)^{\epsilon}(1 - \epsilon)^2\Big[-\frac{i}{2\pi}\mathrm{Disc}_{t>0} I_2(A, B, \epsilon)\Big]$$

$$= \frac{\alpha_s(\mu)C_F}{2\pi}\theta(z)\theta(1 - z)(1 - z)\Gamma(1 + \epsilon)(e^{\gamma_E}\mu^2)^{\epsilon}(1 - \epsilon)\frac{\sin \pi \epsilon}{\pi \epsilon}\frac{\theta(t)}{t^{1+\epsilon}}\Big(\frac{z}{1 - z}\Big)^{\epsilon}$$

$$= \frac{\alpha_s(\mu)C_F}{2\pi}\theta(z)\theta(1 - z)(1 - z)\Big\{\frac{1}{\mu^2}\mathcal{L}_0\Big(\frac{t}{\mu^2}\Big) + \delta(t)\Big(-\frac{1}{\epsilon} + \ln\frac{1 - z}{z} + 1\Big)\Big\}, \qquad (D.4)$$

where in the last step we used Eq. (B.3) to expand in ϵ. For Fig. 4-2(b), we start from the third line in Eq. (4.29) and using Eqs. (D.3) and (B.3) we get

$$\langle q_n|\theta(\omega)\mathcal{O}_q^{\mathrm{bare}}(t, \omega)|q_n\rangle^{(b)}$$

$$= \frac{\alpha_s(\mu)C_F}{\pi}\frac{\theta(z)}{1 - z}\Gamma(1 + \epsilon)(e^{\gamma_E}\mu^2)^{\epsilon}\Big[-\frac{i}{2\pi}\mathrm{Disc}_{t>0} I_1(A, B, \epsilon)\Big]$$

$$= \frac{\alpha_s(\mu)C_F}{\pi}\theta(z)\Gamma(1 + \epsilon)(e^{\gamma_E}\mu^2)^{\epsilon}\frac{\sin \pi \epsilon}{\pi \epsilon}\frac{\theta(t)}{t^{1+\epsilon}}\frac{\theta(1 - z)z^{1+\epsilon}}{(1 - z)^{1+\epsilon}}$$

$$= \frac{\alpha_s(\mu)C_F}{\pi}\theta(z)\Big\{\Big[-\frac{1}{\epsilon}\delta(t) + \frac{1}{\mu^2}\mathcal{L}_0\Big(\frac{t}{\mu^2}\Big)\Big]\Big[-\frac{1}{\epsilon}\delta(1 - z) + \mathcal{L}_0(1 - z)z\Big]$$

$$+ \frac{1}{\mu^2}\mathcal{L}_1\Big(\frac{t}{\mu^2}\Big)\delta(1 - z) + \delta(t)\Big[\mathcal{L}_1(1 - z)z - \mathcal{L}_0(1 - z)z\ln z - \frac{\pi^2}{12}\delta(1 - z)\Big]\Big\}. \qquad (D.5)$$

Adding up Eqs. (D.4) and (D.5), the bare quark matrix element in pure dimensional regu-

larization becomes

$$\langle q_n|\theta(\omega)\mathcal{O}_q^{\text{bare}}(t,\omega)|q_n\rangle^{(1)}$$

$$= \frac{\alpha_s(\mu)C_F}{2\pi}\,\theta(z)\Bigg\{\Big[\delta(t)\Big(\frac{2}{\epsilon^2}+\frac{3}{2\epsilon}\Big)-\frac{2}{\epsilon}\frac{1}{\mu^2}\mathcal{L}_0\Big(\frac{t}{\mu^2}\Big)\Big]\delta(1-z)-\frac{1}{\epsilon}\,\delta(t)P_{qq}(z)$$

$$+\frac{2}{\mu^2}\mathcal{L}_1\Big(\frac{t}{\mu^2}\Big)\delta(1-z)+\frac{1}{\mu^2}\mathcal{L}_0\Big(\frac{t}{\mu^2}\Big)\mathcal{L}_0(1-z)(1+z^2)$$

$$+\delta(t)\Big[\mathcal{L}_1(1-z)(1+z^2)-\frac{\pi^2}{6}\delta(1-z)+\theta(1-z)\Big(1-z-\frac{1+z^2}{1-z}\ln z\Big)\Big]\Bigg\}. \quad \text{(D.6)}$$

We can now proceed in two ways to obtain the matching coefficient $\mathcal{I}_{qq}(t,z,\mu)$.

First, we can subtract $\delta(t)$ times Eq. (D.1) from Eq. (D.6) to obtain the bare matching coefficient. This simply removes the $(1/\epsilon)\delta(t)P_{qq}(z)$ in the first line of Eq. (D.6). Assuming that the IR divergences between the PDF and beam function cancel (and including the vanishing zero-bin) the remaining poles in the first line are of UV origin and determine the necessary $\overline{\text{MS}}$ counter term, reproducing our previous result for $Z_B^q(t,\mu)$ in Eq. (4.40).

Alternatively, we can use our general result that the beam function has the same renormalization as the jet function. In this case, we subtract the one-loop counter term for $\mathcal{O}_q^{\text{bare}}$ in Eq. (4.40) (which is already known from the jet function's renormalization) from Eq. (D.6) to obtain the renormalized quark matrix element, which equals Eq. (D.6) without the $[...]\delta(1-z)$ term in the first line. The remaining $1/\epsilon$ pole must then be of IR origin, so we again have an explicit check that the IR divergences in the beam function match those of the PDF in Eq. (D.1). Either way, the finite terms in the last two lines of Eq. (D.6) determine the renormalized matching coefficient $\mathcal{I}_{qq}(t,z,\mu)$, which agrees with our previous result in Eq. (4.47).

For the gluon matrix element, Fig. 4-2(f) again does not contribute. For Fig. 4-2(e), starting from the third line of Eq. (4.37), we find

$$\langle g_n|\theta(\omega)\mathcal{O}_q^{\text{bare}}(t,\omega)|g_n\rangle^{(1)} \qquad\qquad\qquad\qquad\qquad\qquad\qquad\qquad\qquad \text{(D.7)}$$

$$= \frac{\alpha_s(\mu)T_F}{2\pi}\,\frac{\theta(z)}{z}\,\Gamma(1+\epsilon)(e^{\gamma_E}\mu^2)^\epsilon\Big(\frac{1-\epsilon}{1-z}-2z\Big)\Big[-\frac{i}{2\pi}\text{Disc}_{t>0}\,I_2(A,B,\epsilon)\Big]$$

$$= \frac{\alpha_s(\mu)T_F}{2\pi}\,\theta(z)\theta(1-z)\Gamma(1+\epsilon)(e^{\gamma_E}\mu^2)^\epsilon(1-2z+2z^2-\epsilon)\frac{\sin\pi\epsilon}{\pi\epsilon(1-\epsilon)}\frac{\theta(t)}{t^{1+\epsilon}}\Big(\frac{z}{1-z}\Big)^\epsilon$$

$$= \frac{\alpha_s(\mu)T_F}{2\pi}\,\theta(z)\Big\{\frac{1}{\mu^2}\mathcal{L}_0\Big(\frac{t}{\mu^2}\Big)P_{qg}(z)+\delta(t)\Big[P_{qg}(z)\Big(-\frac{1}{\epsilon}+\ln\frac{1-z}{z}-1\Big)+\theta(1-z)\Big]\Big\}.$$

The same discussion as for the quark matrix element above can be repeated for the gluon matrix element. The $(1/\epsilon)\delta(t)P_{qg}(z)$ term matches the IR divergence in the PDF in Eq. (D.1). Since there are no further poles, no UV renormalization is required and the quark and gluon operators do not mix. The finite terms in Eq. (D.7) then determine the matching coefficient $\mathcal{I}_{qg}(t, z, \mu)$, reproducing our previous result in Eq. (4.47).

Appendix E

Perturbative Results

In this appendix we collect perturbative results relevant for the Drell-Yan beam thrust cross section in Eq. (8.2) and the cross section for isolated Higgs production through gluon fusion in Eq. (9.5). These were included as appendices in Ref. [48, 168].

E.1 Fixed-Order Results for Drell-Yan

We summarize the results of Sec. 7.4. The one-loop hard function for Drell-Yan is given by the square of Wilson coefficients in SCET for which the relevant one-loop matching from QCD onto SCET was carried out in Refs. [33, 138]

$$
H_{q\bar{q}}(q^2, \mu) = H_{\bar{q}q}(q^2, \mu) = \left[Q_q^2 + \frac{(v_q^2 + a_q^2)(v_\ell^2 + a_\ell^2) - 2Q_q v_q v_\ell (1 - m_Z^2/q^2)}{(1 - m_Z^2/q^2)^2 + m_Z^2 \Gamma_Z^2/q^4} \right]
$$
$$
\times \left[1 + \frac{\alpha_s(\mu)\, C_F}{2\pi} \left(-\ln^2 \frac{q^2}{\mu^2} + 3\ln \frac{q^2}{\mu^2} - 8 + \frac{7\pi^2}{6} \right) \right]. \qquad \text{(E.1)}
$$

We included the prefactor from the leptonic matrix element, where Q_q is the quark charge in units of $|e|$, $v_{\ell,q}$ and $a_{\ell,q}$ are the standard vector and axial couplings of the leptons and quarks, and m_Z and Γ_Z are the mass and width of the Z boson. The beam thrust soft function can be extracted form the one-loop incoming hemisphere soft function [94, 157] and is given by

$$
S_B^{q\bar{q}}(k^+, \mu) = \delta(k^+) + \frac{\alpha_s(\mu)\, C_F}{2\pi} \left[-\frac{8}{\mu} \mathcal{L}_1\left(\frac{k^+}{\mu}\right) + \frac{\pi^2}{6}\, \delta(k^+) \right]. \qquad \text{(E.2)}
$$

Our one-loop results for the matching coefficients in the beam function OPE in Eq. (3.37) are for the quark beam function given in Eq. (4.47).

E.2   Fixed-Order Results for Higgs Production

For Higgs production through gluon fusion we will integrate out the top quark and hard off-shell modes in one step. This avoids the often used expansion $m_H \ll m_t$, but does not allow us to sum logarithms of m_H^2/m_t^2. In the narrow width approximation the virtuality of the Higgs is simply $q^2 = m_H^2$, but we will keep q^2 general in the below discussion. In pure dimensional regularization the matching coefficient $C_{ggH}(m_t, q^2)$ is given by the infrared-finite part of the on-shell ggH form factor [10, 111, 115, 152]. At NLO this yields

$$H_{ggH}(m_t, q^2, \mu) = \alpha_s^2(\mu)|F^{(0)}(\rho/4)|^2\left\{1 + \frac{\alpha_s(\mu)}{2\pi}\left[C_A\left(-\ln^2\frac{q^2}{\mu^2} + \frac{7\pi^2}{6}\right) + F^{(1)}(\rho)\right]\right\},$$

(E.3)

where $\rho = m_H^2/m_t^2$ and

$$F^{(0)}(x) = \frac{3}{2x} - \frac{3}{2x}\left|1 - \frac{1}{x}\right| \begin{cases} \arcsin^2(\sqrt{x}), & 0 < x \leq 1, \\ \ln^2[-i(\sqrt{x} + \sqrt{x-1})], & x > 1, \end{cases}$$

(E.4)

$$F^{(1)}(\rho) = \left(5 - \frac{19}{90}\rho - \frac{1289}{75600}\rho^2 - \frac{155}{72576}\rho^3 - \frac{5385047}{16765056000}\rho^4\right)C_A$$
$$+ \left(-3 + \frac{307}{360}\rho + \frac{25813}{302400}\rho^2 + \frac{3055907}{254016000}\rho^3 + \frac{659504801}{335301120000}\rho^4\right)C_F + \mathcal{O}(\rho^5).$$

For $\rho \to 0$ (corresponding to $m_t \to \infty$) we have $F^{(0)}(0) = 1$ and $F^{(1)}(0) = 5C_A - 3C_F$.

The gluon beam thrust soft function has Wilson lines in the adjoint rather than fundamental representation. At one loop we can simply replace C_F by C_A (Casimir scaling) in the quark result in Eq. (E.2)

$$S_B^{gg}(k^+, \mu) = \delta(k^+) + \frac{\alpha_s(\mu)\,C_A}{2\pi}\left\{-\frac{8}{\mu}\left[\frac{\theta(k^+/\mu)\ln(k^+/\mu)}{k^+/\mu}\right]_+ + \frac{\pi^2}{6}\delta(k^+)\right\}.$$

The one-loop coefficients for matching the gluon beam function onto PDFs are given in Eq. (5.29).

E.3 Renormalization Group Evolution

The RGE and anomalous dimension for the hard function are [see Eqs. (7.82) and (C.10)]

$$\mu\frac{\mathrm{d}}{\mathrm{d}\mu}H_{ij}(q^2,\mu) = \gamma_H^{ij}(q^2,\mu)H_{ij}(q^2,\mu)\,,$$

$$\gamma_H^{ij}(q^2,\mu) = 2\Gamma_{\mathrm{cusp}}^i(\alpha_s)\ln\frac{q^2}{\mu^2} + \gamma_H^{ij}(\alpha_s)\,. \tag{E.5}$$

The expansion coefficients of $\Gamma_{\mathrm{cusp}}^i(\alpha_s)$ and $\gamma_H^{ij}(\alpha_s)$ are given below in Eqs. (E.15) and (E.18). Note that $\Gamma_{\mathrm{cusp}}^q = \Gamma_{\mathrm{cusp}}^{\bar{q}}$ so $\Gamma_{\mathrm{cusp}}^i = \Gamma_{\mathrm{cusp}}^j$. The RGE in Eq. (7.82) has the standard solution

$$H_{ij}(q^2,\mu) = H_{ij}(q^2,\mu_0)\,U_H^{ij}(q^2,\mu_0,\mu)\,,$$

$$U_H^{ij}(q^2,\mu_0,\mu) = e^{K_H^{ij}(\mu_0,\mu)}\Big(\frac{q^2}{\mu_0^2}\Big)^{\eta_H^{ij}(\mu_0,\mu)}\,,$$

$$K_H^{ij}(\mu_0,\mu) = -4K_\Gamma^i(\mu_0,\mu) + K_{\gamma_H^{ij}}(\mu_0,\mu)\,, \qquad \eta_H^{ij}(\mu_0,\mu) = 2\eta_\Gamma^i(\mu_0,\mu)\,, \tag{E.6}$$

where the functions $K_\Gamma^i(\mu_0,\mu)$, $\eta_\Gamma^i(\mu_0,\mu)$ and K_γ are given below in Eq. (E.12).

The beam function RGE is [see Eqs. (3.25) and (3.26)]

$$\mu\frac{\mathrm{d}}{\mathrm{d}\mu}B_i(t,x,\mu) = \int\mathrm{d}t'\,\gamma_B^i(t-t',\mu)\,B_i(t',x,\mu)\,,$$

$$\gamma_B^i(t,\mu) = -2\Gamma_{\mathrm{cusp}}^i(\alpha_s)\frac{1}{\mu^2}\mathcal{L}_0\Big(\frac{t}{\mu^2}\Big) + \gamma_B^i(\alpha_s)\,\delta(t)\,, \tag{E.7}$$

and its solution is [26, 94, 135, 151] [see Eq. (3.28)]

$$B_i(t,x,\mu) = \int\mathrm{d}t'\,B_i(t-t',x,\mu_0)\,U_B^i(t',\mu_0,\mu)\,,$$

$$U_B^i(t,\mu_0,\mu) = \frac{e^{K_B^i-\gamma_E\,\eta_B^i}}{\Gamma(1+\eta_B^i)}\Big[\frac{\eta_B^i}{\mu_0^2}\mathcal{L}^{\eta_B^i}\Big(\frac{t}{\mu_0^2}\Big) + \delta(t)\Big]\,,$$

$$K_B^i(\mu_0,\mu) = 4K_\Gamma^i(\mu_0,\mu) + K_{\gamma_B^i}(\mu_0,\mu)\,, \qquad \eta_B^i(\mu_0,\mu) = -2\eta_\Gamma^i(\mu_0,\mu)\,. \tag{E.8}$$

The beam thrust soft function is given in terms of S_{ihemi}^{ij} by

$$S_B^{ij}(k^+,\mu) = \int\mathrm{d}k_a^+\,\mathrm{d}k_b^+\,S_{\mathrm{ihemi}}^{ij}(k_a^+,k_b^+,\mu)\,\delta(k^+-k_a^+-k_b^+)\,. \tag{E.9}$$

Its RGE is easily obtained by integrating Eqs. (C.5) and (C.11),

$$\mu\frac{\mathrm{d}}{\mathrm{d}\mu}S_B^{ij}(k^+,\mu) = \int\mathrm{d}\ell^+\,\gamma_S^{ij}(k^+-\ell^+,\mu)\,S_B^{ij}(\ell^+,\mu)\,, \tag{E.10}$$

$$\gamma_S^{ij}(k^+,\mu) = 4\,\Gamma_{\mathrm{cusp}}^i(\alpha_s)\,\frac{1}{\mu}\mathcal{L}_0\Big(\frac{k^+}{\mu}\Big) + \gamma_S^{ij}(\alpha_s)\,\delta(k^+)\,, \quad \gamma_S^{ij}(\alpha_s) = -\gamma_H^{ij}(\alpha_s) - 2\gamma_B^i(\alpha_s)\,,$$

whose solution is completely analogous to Eq. (E.8),

$$S_B^{ij}(k^+,\mu) = \int\mathrm{d}\ell^+\,S_B^{ij}(k^+-\ell^+,\mu_0)\,U_S^{ij}(\ell^+,\mu_0,\mu)\,,$$

$$U_S^{ij}(k^+,\mu_0,\mu) = \frac{e^{K_S^{ij}-\gamma_E\,\eta_S^{ij}}}{\Gamma(1+\eta_S^{ij})}\left[\frac{\eta_S^{ij}}{\mu_0}\mathcal{L}^{\eta_S^{ij}}\Big(\frac{k^+}{\mu_0}\Big) + \delta(k^+)\right],$$

$$K_S^{ij}(\mu_0,\mu) = -4K_\Gamma^i(\mu_0,\mu) + K_{\gamma_S^{ij}}(\mu_0,\mu)\,, \quad \eta_S^{ij}(\mu_0,\mu) = 4\eta_\Gamma^i(\mu_0,\mu)\,. \tag{E.11}$$

The functions $K_\Gamma^i(\mu_0,\mu)$, $\eta_\Gamma^i(\mu_0,\mu)$, $K_\gamma(\mu_0,\mu)$ in the above RGE solutions are defined as

$$K_\Gamma^i(\mu_0,\mu) = \int_{\alpha_s(\mu_0)}^{\alpha_s(\mu)}\frac{\mathrm{d}\alpha_s}{\beta(\alpha_s)}\Gamma_{\mathrm{cusp}}^i(\alpha_s)\int_{\alpha_s(\mu_0)}^{\alpha_s}\frac{\mathrm{d}\alpha_s'}{\beta(\alpha_s')}\,, \quad \eta_\Gamma^i(\mu_0,\mu) = \int_{\alpha_s(\mu_0)}^{\alpha_s(\mu)}\frac{\mathrm{d}\alpha_s}{\beta(\alpha_s)}\Gamma_{\mathrm{cusp}}^i(\alpha_s)\,,$$

$$K_\gamma(\mu_0,\mu) = \int_{\alpha_s(\mu_0)}^{\alpha_s(\mu)}\frac{\mathrm{d}\alpha_s}{\beta(\alpha_s)}\gamma(\alpha_s)\,. \tag{E.12}$$

Expanding the beta function and anomalous dimensions in powers of α_s,

$$\beta(\alpha_s) = -2\alpha_s\sum_{n=0}^{\infty}\beta_n\Big(\frac{\alpha_s}{4\pi}\Big)^{n+1}\,, \quad \Gamma_{\mathrm{cusp}}^i(\alpha_s) = \sum_{n=0}^{\infty}\Gamma_n^i\Big(\frac{\alpha_s}{4\pi}\Big)^{n+1}\,, \quad \gamma(\alpha_s) = \sum_{n=0}^{\infty}\gamma_n\Big(\frac{\alpha_s}{4\pi}\Big)^{n+1}\,, \tag{E.13}$$

their explicit expressions at NNLL are,

$$K_\Gamma(\mu_0,\mu) = -\frac{\Gamma_0}{4\beta_0^2}\left\{\frac{4\pi}{\alpha_s(\mu_0)}\Big(1-\frac{1}{r}-\ln r\Big) + \Big(\frac{\Gamma_1}{\Gamma_0}-\frac{\beta_1}{\beta_0}\Big)(1-r+\ln r) + \frac{\beta_1}{2\beta_0}\ln^2 r\right.$$

$$+\frac{\alpha_s(\mu_0)}{4\pi}\left[\Big(\frac{\beta_1^2}{\beta_0^2}-\frac{\beta_2}{\beta_0}\Big)\Big(\frac{1-r^2}{2}+\ln r\Big) + \Big(\frac{\beta_1\Gamma_1}{\beta_0\Gamma_0}-\frac{\beta_1^2}{\beta_0^2}\Big)(1-r+r\ln r)\right.$$

$$\left.\left.-\Big(\frac{\Gamma_2}{\Gamma_0}-\frac{\beta_1\Gamma_1}{\beta_0\Gamma_0}\Big)\frac{(1-r)^2}{2}\right]\right\}\,,$$

$$\eta_\Gamma(\mu_0,\mu) = -\frac{\Gamma_0}{2\beta_0}\left[\ln r + \frac{\alpha_s(\mu_0)}{4\pi}\Big(\frac{\Gamma_1}{\Gamma_0}-\frac{\beta_1}{\beta_0}\Big)(r-1)\right.$$

$$\left.+\frac{\alpha_s^2(\mu_0)}{16\pi^2}\Big(\frac{\Gamma_2}{\Gamma_0}-\frac{\beta_1\Gamma_1}{\beta_0\Gamma_0}+\frac{\beta_1^2}{\beta_0^2}-\frac{\beta_2}{\beta_0}\Big)\frac{r^2-1}{2}\right]\,,$$

$$K_\gamma(\mu_0, \mu) = -\frac{\gamma_0}{2\beta_0} \left[\ln r + \frac{\alpha_s(\mu_0)}{4\pi} \left(\frac{\gamma_1}{\gamma_0} - \frac{\beta_1}{\beta_0} \right)(r - 1) \right]. \tag{E.14}$$

Here $r = \alpha_s(\mu)/\alpha_s(\mu_0)$ and we have suppressed the superscript i on K_Γ^i, η_Γ^i and Γ_n^i.

Up to three loops, the coefficients of the beta function [133, 172] and cusp anomalous dimension [127, 147] in $\overline{\text{MS}}$ are

$$\beta_0 = \frac{11}{3} C_A - \frac{4}{3} T_F n_f, \tag{E.15}$$

$$\beta_1 = \frac{34}{3} C_A^2 - \left(\frac{20}{3} C_A + 4C_F \right) T_F n_f,$$

$$\beta_2 = \frac{2857}{54} C_A^3 + \left(C_F^2 - \frac{205}{18} C_F C_A - \frac{1415}{54} C_A^2 \right) 2T_F n_f + \left(\frac{11}{9} C_F + \frac{79}{54} C_A \right) 4T_F^2 n_f^2,$$

$$\Gamma_0^q = 4C_F,$$

$$\Gamma_1^q = 4C_F \left[\left(\frac{67}{9} - \frac{\pi^2}{3} \right) C_A - \frac{20}{9} T_F n_f \right],$$

$$\Gamma_2^q = 4C_F \left[\left(\frac{245}{6} - \frac{134\pi^2}{27} + \frac{11\pi^4}{45} + \frac{22\zeta_3}{3} \right) C_A^2 + \left(-\frac{418}{27} + \frac{40\pi^2}{27} - \frac{56\zeta_3}{3} \right) C_A T_F n_f \right.$$
$$\left. + \left(-\frac{55}{3} + 16\zeta_3 \right) C_F T_F n_f - \frac{16}{27} T_F^2 n_f^2 \right], \tag{E.16}$$

$$\Gamma_n^g = \frac{C_A}{C_F} \Gamma_n^q \quad \text{for } n \leq 2. \tag{E.17}$$

The $\overline{\text{MS}}$ non-cusp anomalous dimension for the hard function $H^{q\bar{q}}$ can be obtained [41, 118] from the IR divergences of the on-shell massless quark form factor which is known to three loops [148]. Similarly, the anomalous dimension for H^{gg} can be extracted [40] from the gluon form factor, which has also been calculated to three loops [149].

$$\gamma_{H0}^{q\bar{q}} = -12C_F,$$

$$\gamma_{H1}^{q\bar{q}} = -2C_F \left[\left(\frac{82}{9} - 52\zeta_3 \right) C_A + (3 - 4\pi^2 + 48\zeta_3) C_F + \left(\frac{65}{9} + \pi^2 \right) \beta_0 \right],$$

$$\gamma_{H2}^{q\bar{q}} = -4C_F \left[\left(\frac{66167}{324} - \frac{686\pi^2}{81} - \frac{302\pi^4}{135} - \frac{782\zeta_3}{9} + \frac{44\pi^2\zeta_3}{9} + 136\zeta_5 \right) C_A^2 \right.$$
$$+ \left(\frac{151}{4} - \frac{205\pi^2}{9} - \frac{247\pi^4}{135} + \frac{844\zeta_3}{3} + \frac{8\pi^2\zeta_3}{3} + 120\zeta_5 \right) C_F C_A$$
$$+ \left(\frac{29}{2} + 3\pi^2 + \frac{8\pi^4}{5} + 68\zeta_3 - \frac{16\pi^2\zeta_3}{3} - 240\zeta_5 \right) C_F^2$$
$$+ \left(-\frac{10781}{108} + \frac{446\pi^2}{81} + \frac{449\pi^4}{270} - \frac{1166\zeta_3}{9} \right) C_A \beta_0$$
$$\left. + \left(\frac{2953}{108} - \frac{13\pi^2}{18} - \frac{7\pi^4}{27} + \frac{128\zeta_3}{9} \right) \beta_1 + \left(-\frac{2417}{324} + \frac{5\pi^2}{6} + \frac{2\zeta_3}{3} \right) \beta_0^2 \right], \tag{E.18}$$

$$\gamma_{H\,0}^{gg} = -4\beta_0\,,$$

$$\gamma_{H\,1}^{gg} = \Big(-\frac{236}{9} + 8\zeta_3\Big)C_A^2 + \Big(-\frac{76}{9} + \frac{2\pi^2}{3}\Big)C_A\,\beta_0 - 4\beta_1\,,$$

$$\gamma_{H\,2}^{gg} = \Big(-\frac{60875}{81} + \frac{1268\pi^2}{81} + \frac{16\pi^4}{5} + \frac{3944\zeta_3}{9} - \frac{80\pi^2\zeta_3}{9} - 64\zeta_5\Big)C_A^3$$
$$+ \Big(\frac{7649}{27} + \frac{268\pi^2}{81} - \frac{122\pi^4}{45} - \frac{1000\zeta_3}{9}\Big)C_A^2\,\beta_0 + \Big(\frac{932}{81} + \frac{10\pi^2}{9} - \frac{56\zeta_3}{3}\Big)C_A\,\beta_0^2$$
$$+ \Big(-\frac{1819}{27} + \frac{2\pi^2}{3} + \frac{8\pi^4}{45} + \frac{304\zeta_3}{9}\Big)C_A\,\beta_1 - 4\beta_2\,. \tag{E.19}$$

Denoting γ_f^q the coefficient of the $\delta(1-z)$ in the quark PDF anomalous dimension, Eq. (3.17) (which gives the non-cusp part of the anomalous dimension in the threshold limit $z \to 1$), the factorization theorem for DIS at threshold implies that $\gamma_H + \gamma_J^q + \gamma_f^q = 0$, which was used in Ref. [41] to obtain γ_J^q at three loops from the known three-loop result for γ_f^q [147]. This argument can repeated for a gluons. As we showed in Sec. 3.2, the anomalous dimension for the beam function equals that of the jet function, $\gamma_B^i = \gamma_J^i$, so the three-loop result for γ_f^i together with Eq. (E.18) yield the non-cusp three-loop anomalous dimension for the beam functions

$$\gamma_{B\,0}^q = 6C_F\,,$$

$$\gamma_{B\,1}^q = C_F\Big[\Big(\frac{146}{9} - 80\zeta_3\Big)C_A + (3 - 4\pi^2 + 48\zeta_3)C_F + \Big(\frac{121}{9} + \frac{2\pi^2}{3}\Big)\beta_0\Big]\,,$$

$$\gamma_{B\,2}^q = 2C_F\Big[\Big(\frac{52019}{162} - \frac{841\pi^2}{81} - \frac{82\pi^4}{27} - \frac{2056\zeta_3}{9} + \frac{88\pi^2\zeta_3}{9} + 232\zeta_5\Big)C_A^2$$
$$+ \Big(\frac{151}{4} - \frac{205\pi^2}{9} - \frac{247\pi^4}{135} + \frac{844\zeta_3}{3} + \frac{8\pi^2\zeta_3}{3} + 120\zeta_5\Big)C_AC_F$$
$$+ \Big(\frac{29}{2} + 3\pi^2 + \frac{8\pi^4}{5} + 68\zeta_3 - \frac{16\pi^2\zeta_3}{3} - 240\zeta_5\Big)C_F^2$$
$$+ \Big(-\frac{7739}{54} + \frac{325}{81}\pi^2 + \frac{617\pi^4}{270} - \frac{1276\zeta_3}{9}\Big)C_A\beta_0$$
$$+ \Big(-\frac{3457}{324} + \frac{5\pi^2}{9} + \frac{16\zeta_3}{3}\Big)\beta_0^2 + \Big(\frac{1166}{27} - \frac{8\pi^2}{9} - \frac{41\pi^4}{135} + \frac{52\zeta_3}{9}\Big)\beta_1\Big]\,, \tag{E.20}$$

$$\gamma_{B\,0}^g = 2\beta_0\,,$$

$$\gamma_{B\,1}^g = \Big(\frac{182}{9} - 32\zeta_3\Big)C_A^2 + \Big(\frac{94}{9} - \frac{2\pi^2}{3}\Big)C_A\,\beta_0 + 2\beta_1\,,$$

$$\gamma_{B\,2}^g = \Big(\frac{49373}{81} - \frac{944\pi^2}{81} - \frac{16\pi^4}{5} - \frac{4520\zeta_3}{9} + \frac{128\pi^2\zeta_3}{9} + 224\zeta_5\Big)C_A^3$$
$$+ \Big(-\frac{6173}{27} - \frac{376\pi^2}{81} + \frac{13\pi^4}{5} + \frac{280\zeta_3}{9}\Big)C_A^2\,\beta_0 + \Big(-\frac{986}{81} - \frac{10\pi^2}{9} + \frac{56\zeta_3}{3}\Big)C_A\,\beta_0^2$$
$$+ \Big(\frac{1765}{27} - \frac{2\pi^2}{3} - \frac{8\pi^4}{45} - \frac{304\zeta_3}{9}\Big)C_A\,\beta_1 + 2\beta_2\,. \tag{E.21}$$

At NNLL, we only need the one- and two-loop coefficients of γ_B^i and γ_H^{ij}. The three-loop coefficients, $\gamma_{H\,2}^{ij}$ and $\gamma_{B\,2}^i$, are given here for completeness. They are required for the resummation at N^{3}LL, where one would also need the four-loop beta function and cusp anomalous dimension, the latter of which is has not been calculated so far. In addition, the full N^{3}LL would also require the two-loop fixed-order corrections, which are known for the hard function, but not yet for the beam and soft functions.

Bibliography

[1] Atlas detector and physics performance. technical design report. vol. 1. 1999. CERN-LHCC-99-14.

[2] Atlas detector and physics performance. technical design report. vol. 2. 1999. CERN-LHCC-99-15.

[3] Search Strategy for a Standard Model Higgs Boson Decaying to Two W Bosons in the Fully Leptonic Final State. 2009. CMS-PAS-HIG-08-006.

[4] G. Aad et al. Expected Performance of the ATLAS Experiment - Detector, Trigger and Physics. 2009.

[5] T. Aaltonen et al. Combination of Tevatron searches for the standard model Higgs boson in the W^+W^- decay mode. *Phys. Rev. Lett.*, 104:061802, 2010.

[6] T. Aaltonen et al. Inclusive Search for Standard Model Higgs Boson Production in the WW Decay Channel using the CDF II Detector. *Phys. Rev. Lett.*, 104:061803, 2010.

[7] V. M. Abazov et al. Search for Higgs boson production in dilepton and missing energy final states with 5.4fb^{-1} of $p\bar{p}$ collisions at $\sqrt{s} = 1.96$ TeV. *Phys. Rev. Lett.*, 104:061804, 2010.

[8] Guido Altarelli, R. Keith Ellis, and G. Martinelli. Large Perturbative Corrections to the Drell-Yan Process in QCD. *Nucl. Phys. B*, 157:461, 1979.

[9] Guido Altarelli and G. Parisi. Asymptotic Freedom in Parton Language. *Nucl. Phys. B*, 126:298, 1977.

[10] Charalampos Anastasiou, Stefan Beerli, Stefan Bucherer, Alejandro Daleo, and Zoltan Kunszt. Two-loop amplitudes and master integrals for the production of a Higgs boson via a massive quark and a scalar-quark loop. *JHEP*, 01:082, 2007.

[11] Charalampos Anastasiou, Guenther Dissertori, Massimiliano Grazzini, Fabian Stockli, and Bryan R. Webber. Perturbative QCD effects and the search for a $H \rightarrow WW \rightarrow \ell\nu\ell\nu$ signal at the Tevatron. *JHEP*, 08:099, 2009.

[12] Charalampos Anastasiou, Gunther Dissertori, and Fabian Stockli. NNLO QCD predictions for the $H \rightarrow WW \rightarrow \ell\nu\ell\nu$ signal at the LHC. *JHEP*, 09:018, 2007.

[13] Charalampos Anastasiou, Gunther Dissertori, Fabian Stockli, and Bryan R. Webber. QCD radiation effects on the $H \rightarrow WW \rightarrow \ell\nu\ell\nu$ signal at the LHC. *JHEP*, 03:017, 2008.

[14] Charalampos Anastasiou, Lance J. Dixon, Kirill Melnikov, and Frank Petriello. Dilepton rapidity distribution in the Drell-Yan process at NNLO in QCD. *Phys. Rev. Lett.*, 91:182002, 2003.

[15] Charalampos Anastasiou, Lance J. Dixon, Kirill Melnikov, and Frank Petriello. High precision QCD at hadron colliders: Electroweak gauge boson rapidity distributions at NNLO. *Phys. Rev. D*, 69:094008, 2004.

[16] Charalampos Anastasiou and Kirill Melnikov. Higgs boson production at hadron colliders in NNLO QCD. *Nucl. Phys.*, B646:220–256, 2002.

[17] Charalampos Anastasiou, Kirill Melnikov, and Frank Petriello. Higgs boson production at hadron colliders: Differential cross sections through next-to-next-to-leading order. *Phys. Rev. Lett.*, 93:262002, 2004.

[18] Charalampos Anastasiou, Kirill Melnikov, and Frank Petriello. Fully differential Higgs boson production and the di-photon signal through next-to-next-to-leading order. *Nucl. Phys. B*, 724:197–246, 2005.

[19] David Appell, George Sterman, and Paul B. Mackenzie. Soft Gluons and the Normalization of the Drell-Yan Cross Section. *Nucl. Phys. B*, 309:259, 1988.

[20] R. B. Appleby and M. H. Seymour. The resummation of inter-jet energy flow for gaps-between-jets processes at HERA. *JHEP*, 09:056, 2003.

[21] Christian M. Arnesen, Joydip Kundu, and Iain W. Stewart. Constraint equations for heavy-to-light currents in scet. *Phys. Rev. D*, 72:114002, 2005.

[22] S. Mert Aybat and George Sterman. Soft-Gluon Cancellation, Phases and Factorization with Initial-State Partons. *Phys. Lett. B*, 671:46–50, 2009.

[23] M. Bahr et al. Herwig++ Physics and Manual. *Eur. Phys. J. C*, 58:639–707, 2008.

[24] Manuel Bahr, Stefan Gieseke, and Michael H. Seymour. Simulation of multiple partonic interactions in Herwig++. *JHEP*, 07:076, 2008.

[25] C. Balazs and C. P. Yuan. Higgs boson production at the LHC with soft gluon effects. *Phys. Lett. B*, 478:192–198, 2000.

[26] Christopher Balzereit, Thomas Mannel, and Wolfgang Kilian. Evolution of the light-cone distribution function for a heavy quark. *Phys. Rev. D*, 58:114029, 1998.

[27] A. Banfi et al. Resummation (HERA-LHC workshop). 2005.

[28] Andrea Banfi, Gavin P. Salam, and Giulia Zanderighi. Resummed event shapes at hadron - hadron colliders. *JHEP*, 08:062, 2004.

[29] Christian W. Bauer, Sean Fleming, and Michael E. Luke. Summing Sudakov logarithms in $B \to X_s \gamma$ in effective field theory. *Phys. Rev. D*, 63:014006, 2000.

[30] Christian W. Bauer, Sean Fleming, Dan Pirjol, Ira Z. Rothstein, and Iain W. Stewart. Hard scattering factorization from effective field theory. *Phys. Rev. D*, 66:014017, 2002.

[31] Christian W. Bauer, Sean Fleming, Dan Pirjol, and Iain W. Stewart. An effective field theory for collinear and soft gluons: Heavy to light decays. *Phys. Rev. D*, 63:114020, 2001.

[32] Christian W. Bauer, Andrew Hornig, and Frank J. Tackmann. Factorization for generic jet production. *Phys. Rev. D*, 79:114013, 2009.

[33] Christian W. Bauer, Christopher Lee, Aneesh V. Manohar, and Mark B. Wise. Enhanced nonperturbative effects in Z decays to hadrons. *Phys. Rev. D*, 70:034014, 2004.

[34] Christian W. Bauer, Aneesh V. Manohar, and Mark B. Wise. Enhanced nonperturbative effects in jet distributions. *Phys. Rev. Lett.*, 91:122001, 2003.

[35] Christian W. Bauer, Dan Pirjol, and Iain W. Stewart. Soft-collinear factorization in effective field theory. *Phys. Rev. D*, 65:054022, 2002.

[36] Christian W. Bauer, Dan Pirjol, and Iain W. Stewart. Factorization and endpoint singularities in heavy-to-light decays. *Phys. Rev. D*, 67:071502(R), 2003.

[37] Christian W. Bauer and Iain W. Stewart. Invariant operators in collinear effective theory. *Phys. Lett. B*, 516:134–142, 2001.

[38] G. L. Bayatian et al. CMS physics: Technical design report. CERN-LHCC-2006-001.

[39] G. L. Bayatian et al. CMS technical design report, volume II: Physics performance. *J. Phys. G*, 34:995–1579, 2007.

[40] Thomas Becher and Matthias Neubert. On the Structure of Infrared Singularities of Gauge-Theory Amplitudes. *JHEP*, 06:081, 2009.

[41] Thomas Becher, Matthias Neubert, and Ben D. Pecjak. Factorization and momentum-space resummation in deep-inelastic scattering. *JHEP*, 01:076, 2007.

[42] Thomas Becher, Matthias Neubert, and Gang Xu. Dynamical Threshold Enhancement and Resummation in Drell-Yan Production. *JHEP*, 07:030, 2008.

[43] Thomas Becher and Matthew D. Schwartz. A Precise determination of α_s from LEP thrust data using effective field theory. *JHEP*, 07:034, 2008.

[44] Andrei V. Belitsky. Two-loop renormalization of Wilson loop for Drell-Yan production. *Phys. Lett. B*, 442:307–314, 1998.

[45] Mats Bengtsson, Torbjorn Sjostrand, and Maria van Zijl. Initial state radiation effects on W and jet production. *Z. Phys. C*, 32:67, 1986.

[46] Carola F. Berger, Tibor Kucs, and George Sterman. Energy flow in interjet radiation. *Phys. Rev. D*, 65:094031, 2002.

[47] Carola F. Berger, Tibor Kucs, and George Sterman. Event shape / energy flow correlations. *Phys. Rev. D*, 68:014012, 2003.

[48] Carola F. Berger, Claudio Marcantonini, Iain W. Stewart, Frank J. Tackmann, and Wouter J. Waalewijn. Higgs Production with a Central Jet Veto at NNLL+NNLO. *JHEP*, 1104:092.

[49] Edmond L. Berger, Qing-Hong Cao, C. B. Jackson, Tao Liu, and Gabe Shaughnessy. Higgs Boson Search Sensitivity in the $H \to WW$ Dilepton Decay Mode at $\sqrt{s} = 7$ and 10 TeV. 2010.

[50] Edmond L. Berger and Jian-wei Qiu. Differential cross section for Higgs boson production including all-orders soft gluon resummation. *Phys. Rev. D*, 67:034026, 2003.

[51] W. Bernreuther et al. Two-loop QCD corrections to the heavy quark form factors: Anomaly contributions. *Nucl. Phys. B*, 723:91–116, 2005.

[52] Geoffrey T. Bodwin. Factorization of the Drell-Yan Cross Section in Perturbation Theory. *Phys. Rev. D*, 31:2616, 1985.

[53] Roberto Bonciani, Stefano Catani, Michelangelo L. Mangano, and Paolo Nason. NLL resummation of the heavy-quark hadroproduction cross- section. *Nucl. Phys.*, B529:424–450, 1998.

[54] Radja Boughezal. Theoretical Status of Higgs Production at Hadron Colliders in the SM. 2009.

[55] G. Bozzi, S. Catani, D. de Florian, and M. Grazzini. The q_T spectrum of the Higgs boson at the LHC in QCD perturbation theory. *Phys. Lett. B*, 564:65–72, 2003.

[56] Giuseppe Bozzi, Stefano Catani, Daniel de Florian, and Massimiliano Grazzini. Transverse-momentum resummation and the spectrum of the Higgs boson at the LHC. *Nucl. Phys. B*, 737:73–120, 2006.

[57] Richard A. Brandt, Filippo Neri, and Masa aki Sato. Renormalization of Loop Functions for All Loops. *Phys. Rev. D*, 24:879, 1981.

[58] Gerhard Buchalla, Andrzej J. Buras, and Markus E. Lautenbacher. Weak decays beyond leading logarithms. *Rev. Mod. Phys.*, 68:1125–1144, 1996.

[59] Andrzej J. Buras. Weak Hamiltonian, CP violation and rare decays. 1998.

[60] J. M. Butterworth, Jeffrey R. Forshaw, and Michael H. Seymour. Multiparton interactions in photoproduction at HERA. *Z. Phys. C*, 72:637–646, 1996.

[61] Curtis G. Callan, Jr. Broken scale invariance in scalar field theory. *Phys. Rev.*, D2:1541–1547, 1970.

[62] John M. Campbell, J. W. Huston, and W. J. Stirling. Hard Interactions of Quarks and Gluons: A Primer for LHC Physics. *Rept. Prog. Phys.*, 70:89, 2007.

[63] S. Catani and L. Trentadue. Resummation of the QCD Perturbative Series for Hard Processes. *Nucl. Phys. B*, 327:323, 1989.

[64] S. Catani, L. Trentadue, G. Turnock, and B. R. Webber. Resummation of large logarithms in e^+e^- event shape distributions. *Nucl. Phys. B*, 407:3–42, 1993.

[65] Stefano Catani, Daniel de Florian, and Massimiliano Grazzini. Direct Higgs production and jet veto at the Tevatron and the LHC in NNLO QCD. *JHEP*, 01:015, 2002.

[66] Stefano Catani, Daniel de Florian, Massimiliano Grazzini, and Paolo Nason. Soft-gluon resummation for Higgs boson production at hadron colliders. *JHEP*, 07:028, 2003.

[67] Stefano Catani, Michelangelo L. Mangano, and Paolo Nason. Sudakov resummation for prompt photon production in hadron collisions. *JHEP*, 07:024, 1998.

[68] Stefano Catani, Michelangelo L. Mangano, Paolo Nason, and Luca Trentadue. The Resummation of Soft Gluon in Hadronic Collisions. *Nucl. Phys. B*, 478:273–310, 1996.

[69] Junegone Chay and Chul Kim. Collinear effective theory at subleading order and its application to heavy-light currents. *Phys. Rev. D*, 65:114016, 2002.

[70] Junegone Chay, Chul Kim, Yeong Gyun Kim, and Jong-Phil Lee. Soft Wilson lines in soft-collinear effective theory. *Phys. Rev. D*, 71:056001, 2005.

[71] Jui-yu Chiu, Andreas Fuhrer, Randall Kelley, and Aneesh V. Manohar. Factorization Structure of Gauge Theory Amplitudes and Application to Hard Scattering Processes at the LHC. *Phys. Rev. D*, 80:094013, 2009.

[72] Jui-yu Chiu, Frank Golf, Randall Kelley, and Aneesh V. Manohar. Electroweak corrections in high energy processes using effective field theory. *Phys. Rev. D*, 77:053004, 2008.

[73] Jui-yu Chiu, Randall Kelley, and Aneesh V. Manohar. Electroweak Corrections using Effective Field Theory: Applications to the LHC. *Phys. Rev. D*, 78:073006, 2008.

[74] John C. Collins and Davison E. Soper. Parton Distribution and Decay Functions. *Nucl. Phys. B*, 194:445, 1982.

[75] John C. Collins, Davison E. Soper, and George Sterman. Factorization for Short Distance Hadron - Hadron Scattering. *Nucl. Phys. B*, 261:104, 1985.

[76] John C. Collins, Davison E. Soper, and George Sterman. Transverse Momentum Distribution in Drell-Yan Pair and W and Z Boson Production. *Nucl. Phys. B*, 250:199, 1985.

[77] John C. Collins, Davison E. Soper, and George Sterman. Factorization of Hard Processes in QCD. *Adv. Ser. Direct. High Energy Phys.*, 5:1–91, 1988.

[78] John C. Collins, Davison E. Soper, and George Sterman. Soft gluons and factorization. *Nucl. Phys. B*, 308:833, 1988.

[79] John C. Collins and George Sterman. Soft partons in QCD. *Nucl. Phys. B*, 185:172, 1981.

[80] G. Corcella et al. Herwig 6: An event generator for hadron emission reactions with interfering gluons (including supersymmetric processes). *JHEP*, 01:010, 2001.

[81] G. Corcella et al. HERWIG 6.5 release note. 2002.

[82] M. Dasgupta and G. P. Salam. Resummation of non-global QCD observables. *Phys. Lett. B*, 512:323–330, 2001.

[83] G. Davatz, G. Dissertori, M. Dittmar, M. Grazzini, and F. Pauss. Effective K-factors for $gg \to H \to WW \to \ell\nu\ell\nu$ at the LHC. *JHEP*, 05:009, 2004.

[84] Giovanna Davatz et al. Combining Monte Carlo generators with next-to-next-to-leading order calculations: Event reweighting for Higgs boson production at the LHC. *JHEP*, 07:037, 2006.

[85] Sally Dawson. Radiative corrections to Higgs boson production. *Nucl. Phys. B*, 359:283–300, 1991.

[86] D. de Florian, M. Grazzini, and Z. Kunszt. Higgs production with large transverse momentum in hadronic collisions at next-to-leading order. *Phys. Rev. Lett.*, 82:5209–5212, 1999.

[87] A. Djouadi, M. Spira, and P. M. Zerwas. Production of Higgs bosons in proton colliders: QCD corrections. *Phys. Lett. B*, 264:440–446, 1991.

[88] Abdelhak Djouadi. The Anatomy of electro-weak symmetry breaking. I: The Higgs boson in the standard model. *Phys. Rept.*, 457:1–216, 2008.

[89] Yuri L. Dokshitzer. Calculation of the Structure Functions for Deep Inelastic Scattering and e^+e^- Annihilation by Perturbation Theory in Quantum Chromodynamics. (In Russian). *Sov. Phys. JETP*, 46:641–653, 1977.

[90] John F. Donoghue and Daniel Wyler. On Regge kinematics in SCET. 2009.

[91] Estia Eichten and Brian Russell Hill. An Effective Field Theory for the Calculation of Matrix Elements Involving Heavy Quarks. *Phys. Lett.*, B234:511, 1990.

[92] Andrea Ferroglia, Matthias Neubert, Ben D. Pecjak, and Li Lin Yang. Two-loop divergences of massive scattering amplitudes in non-abelian gauge theories. *JHEP*, 11:062, 2009.

[93] Sean Fleming, Andre H. Hoang, Sonny Mantry, and Iain W. Stewart. Jets from massive unstable particles: Top-mass determination. *Phys. Rev. D*, 77:074010, 2008.

[94] Sean Fleming, Andre H. Hoang, Sonny Mantry, and Iain W. Stewart. Top Jets in the Peak Region: Factorization Analysis with NLL Resummation. *Phys. Rev. D*, 77:114003, 2008.

[95] Sean Fleming, Adam K. Leibovich, and Thomas Mehen. Resumming the color-octet contribution to $e^+e^- \to J/\psi + X$. *Phys. Rev. D*, 68:094011, 2003.

[96] Sean Fleming, Adam K. Leibovich, and Thomas Mehen. Resummation of Large Endpoint Corrections to Color-Octet J/ψ Photoproduction. *Phys. Rev. D*, 74:114004, 2006.

[97] Jeffrey R. Forshaw, A. Kyrieleis, and M. H. Seymour. Super-leading logarithms in non-global observables in QCD. *JHEP*, 08:059, 2006.

[98] Stefano Frixione, Paolo Nason, and Bryan R. Webber. Matching NLO QCD and parton showers in heavy flavour production. *JHEP*, 08:007, 2003.

[99] Stefano Frixione and Bryan R. Webber. Matching NLO QCD computations and parton shower simulations. *JHEP*, 06:029, 2002.

[100] T. Gehrmann, T. Huber, and D. Maitre. Two-loop quark and gluon form factors in dimensional regularisation. *Phys. Lett. B*, 622:295–302, 2005.

[101] Murray Gell-Mann and F. E. Low. Quantum electrodynamics at small distances. *Phys. Rev.*, 95:1300–1312, 1954.

[102] H. Georgi. Effective field theory. *Ann. Rev. Nucl. Part. Sci.*, 43:209–252, 1993.

[103] Howard Georgi. An Effective Field Theory for Heavy Quarks at Low-Energies. *Phys. Lett.*, B240:447–450, 1990.

[104] Howard Georgi and H. David Politzer. Electroproduction scaling in an asymptotically free theory of strong interactions. *Phys. Rev. D*, 9:416–420, 1974.

[105] Christopher J. Glosser and Carl R. Schmidt. Next-to-leading corrections to the Higgs boson transverse momentum spectrum in gluon fusion. *JHEP*, 12:016, 2002.

[106] Massimiliano Grazzini. NNLO predictions for the Higgs boson signal in the $H \to WW \to \ell\nu\ell\nu$ and $H \to ZZ \to 4\ell$ decay channels. *JHEP*, 02:043, 2008.

[107] V. N. Gribov and L. N. Lipatov. Deep inelastic ep scattering in perturbation theory. *Sov. J. Nucl. Phys.*, 15:438–450, 1972.

[108] Benjamin Grinstein. The Static Quark Effective Theory. *Nucl. Phys.*, B339:253–268, 1990.

[109] David J. Gross and Frank Wilczek. Asymptotically free gauge theories. II. *Phys. Rev. D*, 9:980–993, 1974.

[110] R. Hamberg, W. L. van Neerven, and T. Matsuura. A Complete calculation of the order α_s^2 correction to the Drell-Yan K factor. *Nucl. Phys. B*, 359:343–405, 1991.

[111] Robert Harlander and Philipp Kant. Higgs production and decay: Analytic results at next-to- leading order QCD. *JHEP*, 12:015, 2005.

[112] Robert V. Harlander. Virtual corrections to $gg \to H$ to two loops in the heavy top limit. *Phys. Lett. B*, 492:74–80, 2000.

[113] Robert V. Harlander and William B. Kilgore. Next-to-next-to-leading order Higgs production at hadron colliders. *Phys. Rev. Lett.*, 88:201801, 2002.

[114] Robert V. Harlander, Hendrik Mantler, Simone Marzani, and Kemal J. Ozeren. Higgs production in gluon fusion at next-to-next-to-leading order QCD for finite top mass. *Eur. Phys. J. C*, 66:359–372, 2010.

[115] Robert V. Harlander and Kemal J. Ozeren. Top mass effects in Higgs production at next-to-next-to- leading order QCD: virtual corrections. *Phys. Lett.*, B679:467–472, 2009.

[116] Andre H. Hoang and Stefan Kluth. Hemisphere Soft Function at $O(\alpha_s^2)$ for Dijet Production in e^+e^- Annihilation. 2008.

[117] Andre H. Hoang and Iain W. Stewart. Designing Gapped Soft Functions for Jet Production. *Phys. Lett. B*, 660:483–493, 2008.

[118] Ahmad Idilbi, Xiang dong Ji, and Feng Yuan. Resummation of Threshold Logarithms in Effective Field Theory For DIS, Drell-Yan and Higgs Production. *Nucl. Phys. B*, 753:42–68, 2006.

[119] Ahmad Idilbi and Abhijit Majumder. Extending Soft-Collinear-Effective-Theory to describe hard jets in dense QCD media. *Phys. Rev. D*, 80:054022, 2009.

[120] Ahmad Idilbi and Thomas Mehen. On the equivalence of soft and zero-bin subtractions. *Phys. Rev. D*, 75:114017, 2007.

[121] Nikolaos Kidonakis, Gianluca Oderda, and George Sterman. Threshold resummation for dijet cross sections. *Nucl. Phys. B*, 525:299–332, 1998.

[122] Bernd A. Kniehl and Johann H. Kuhn. QCD Corrections to the Axial Part of the Z Decay Rate. *Phys. Lett. B*, 224:229, 1989.

[123] Bernd A. Kniehl and Johann H. Kuhn. QCD Corrections to the Z Decay Rate. *Nucl. Phys. B*, 329:547, 1990.

[124] I. A. Korchemskaya and G. P. Korchemsky. On lightlike Wilson loops. *Phys. Lett. B*, 287:169–175, 1992.

[125] G. P. Korchemsky. Power corrections in Drell-Yan production beyond the leading order. 1996.

[126] G. P. Korchemsky and G. Marchesini. Structure function for large x and renormalization of Wilson loop. *Nucl. Phys. B*, 406:225–258, 1993.

[127] G. P. Korchemsky and A. V. Radyushkin. Renormalization of the Wilson Loops Beyond the Leading Order. *Nucl. Phys. B*, 283:342–364, 1987.

[128] G. P. Korchemsky and S. Tafat. On power corrections to the event shape distributions in QCD. *JHEP*, 10:010, 2000.

[129] Gregory P. Korchemsky and George Sterman. Power corrections to event shapes and factorization. *Nucl. Phys. B*, 555:335–351, 1999.

[130] G. Kramer and B. Lampe. Two Jet Cross-Section in e^+e^- Annihilation. *Z. Phys. C*, 34:497, 1987. [Erratum-ibid. C **42**, 504 (1989)].

[131] Anna Kulesza, George Sterman, and Werner Vogelsang. Joint resummation for Higgs production. *Phys. Rev. D*, 69:014012, 2004.

[132] Eric Laenen, Gianluca Oderda, and George Sterman. Resummation of threshold corrections for single particle inclusive cross-sections. *Phys. Lett.*, B438:173–183, 1998.

[133] S. A. Larin and J. A. M. Vermaseren. The three-loop QCD β function and anomalous dimensions. *Phys. Lett. B*, 303:334–336, 1993.

[134] Christopher Lee and George Sterman. Momentum flow correlations from event shapes: Factorized soft gluons and soft-collinear effective theory. *Phys. Rev. D*, 75:014022, 2007.

[135] Zoltan Ligeti, Iain W. Stewart, and Frank J. Tackmann. Treating the b quark distribution function with reliable uncertainties. *Phys. Rev. D*, 78:114014, 2008.

[136] Lorenzo Magnea. All-order summation and two-loop results for the Drell-Yan cross section. *Nucl. Phys. B*, 349:703–713, 1991.

[137] Aneesh V. Manohar. Effective field theories. 1996.

[138] Aneesh V. Manohar. Deep inelastic scattering as $x \to 1$ using soft-collinear effective theory. *Phys. Rev. D*, 68:114019, 2003.

[139] Aneesh V. Manohar, Thomas Mehen, Dan Pirjol, and Iain W. Stewart. Reparameterization invariance for collinear operators. *Phys. Lett. B*, 539:59–66, 2002.

[140] Aneesh V. Manohar and Iain W. Stewart. The zero-bin and mode factorization in quantum field theory. *Phys. Rev. D*, 76:074002, 2007.

[141] Aneesh V. Manohar and Mark B. Wise. Heavy quark physics. *Camb. Monogr. Part. Phys. Nucl. Phys. Cosmol.*, 10:1–191, 2000.

[142] Sonny Mantry and Frank Petriello. Factorization and Resummation of Higgs Boson Differential Distributions in Soft-Collinear Effective Theory. 2009.

[143] A. D. Martin, W. J. Stirling, R. S. Thorne, and G. Watt. Uncertainties on α_s in global PDF analyses and implications for predicted hadronic cross sections. *Eur. Phys. J. C*, 64:653–680, 2009.

[144] T. Matsuura, S. C. van der Marck, and W. L. van Neerven. The Calculation of the Second Order Soft and Virtual Contributions to the Drell-Yan Cross-Section. *Nucl. Phys. B*, 319:570, 1989.

[145] T. Matsuura and W. L. van Neerven. Second order logarithmic corrections to the Drell-Yan cross-section. *Z. Phys. C*, 38:623, 1988.

[146] S. Mert Aybat, Lance J. Dixon, and George Sterman. The two-loop soft anomalous dimension matrix and resummation at next-to-next-to leading pole. *Phys. Rev. D*, 74:074004, 2006.

[147] S. Moch, J. A. M. Vermaseren, and A. Vogt. The three-loop splitting functions in QCD: The non-singlet case. *Nucl. Phys. B*, B688:101–134, 2004.

[148] S. Moch, J. A. M. Vermaseren, and A. Vogt. The quark form factor at higher orders. *JHEP*, 08:049, 2005.

[149] S. Moch, J. A. M. Vermaseren, and A. Vogt. Three-loop results for quark and gluon form factors. *Phys. Lett. B*, 625:245–252, 2005.

[150] S. Moch and A. Vogt. Higher-order soft corrections to lepton pair and Higgs boson production. *Phys. Lett. B*, 631:48–57, 2005.

[151] Matthias Neubert. Renormalization-group improved calculation of the $B \to X_s\gamma$ branching ratio. *Eur. Phys. J. C*, 40:165–186, 2005.

[152] Alexey Pak, Mikhail Rogal, and Matthias Steinhauser. Virtual three-loop corrections to Higgs boson production in gluon fusion for finite top quark mass. *Phys. Lett.*, B679:473–477, 2009.

[153] Alexey Pak, Mikhail Rogal, and Matthias Steinhauser. Finite top quark mass effects in NNLO Higgs boson production at LHC. *JHEP*, 02:025, 2010.

[154] V. Ravindran, J. Smith, and W. L. Van Neerven. Next-to-leading order QCD corrections to differential distributions of Higgs boson production in hadron hadron collisions. *Nucl. Phys. B*, 634:247–290, 2002.

[155] V. Ravindran, J. Smith, and W. L. van Neerven. NNLO corrections to the total cross section for Higgs boson production in hadron hadron collisions. *Nucl. Phys. B*, 665:325–366, 2003.

[156] Ira Z. Rothstein. TASI lectures on effective field theories. 2003.

[157] Matthew D. Schwartz. Resummation and NLO Matching of Event Shapes with Effective Field Theory. *Phys. Rev. D*, 77:014026, 2008.

[158] Torbjörn Sjöstrand. A Model for Initial State Parton Showers. *Phys. Lett. B*, 157:321, 1985.

[159] Torbjörn Sjöstrand, Stephen Mrenna, and Peter Skands. Pythia 6.4 physics and manual. *JHEP*, 05:026, 2006.

[160] Torbjörn Sjöstrand, Stephen Mrenna, and Peter Skands. A Brief Introduction to PYTHIA 8.1. *Comput. Phys. Commun.*, 178:852–867, 2008.

[161] Torbjörn Sjöstrand and Peter Z. Skands. Multiple interactions and the structure of beam remnants. *JHEP*, 03:053, 2004.

[162] Torbjörn Sjöstrand and Peter Z. Skands. Transverse-momentum-ordered showers and interleaved multiple interactions. *Eur. Phys. J. C*, 39:129–154, 2005.

[163] M. Spira, A. Djouadi, D. Graudenz, and P. M. Zerwas. Higgs boson production at the LHC. *Nucl. Phys. B*, 453:17–82, 1995.

[164] George Sterman. Mass divergences in annihilation processes. II. Cancellation of divergences in cut vacuum polarization diagrams. *Phys. Rev. D*, 17:2789, 1978.

[165] George Sterman. Summation of Large Corrections to Short Distance Hadronic Cross-Sections. *Nucl. Phys. B*, 281:310, 1987.

[166] Iain W. Stewart, Frank J. Tackmann, and Wouter J. Waalewijn. Factorization at the LHC: From PDFs to Initial State Jets. *Phys.Rev.*, D81:094035, 2010.

[167] Iain W. Stewart, Frank J. Tackmann, and Wouter J. Waalewijn. N-Jettiness: An Inclusive Event Shape to Veto Jets. *Phys.Rev.Lett.*, 105:092002, 2010.

[168] Iain W. Stewart, Frank J. Tackmann, and Wouter J. Waalewijn. The Quark Beam Function at NNLL. *JHEP*, 1009:005, 2010.

[169] Iain W. Stewart, Frank J. Tackmann, and Wouter J. Waalewijn. The Beam Thrust Cross Section for Drell-Yan at NNLL Order. *Phys.Rev.Lett.*, 106:032001, 2011.

[170] K. Symanzik. Small distance behavior in field theory and power counting. *Commun. Math. Phys.*, 18:227–246, 1970.

[171] Gerard 't Hooft. Dimensional regularization and the renormalization group. *Nucl. Phys.*, B61:455–468, 1973.

[172] O. V. Tarasov, A. A. Vladimirov, and A. Yu. Zharkov. The Gell-Mann-Low Function of QCD in the Three Loop Approximation. *Phys. Lett. B*, 93:429–432, 1980.

[173] Michael Trott. Jets in effective theory: Summing phase space logs. *Phys. Rev. D*, 75:054011, 2007.

[174] Steven Weinberg. New approach to the renormalization group. *Phys. Rev.*, D8:3497–3509, 1973.

[175] Kenneth G. Wilson and Wolfhart Zimmermann. Operator product expansions and composite field operators in the general framework of quantum field theory. *Comm. Math. Phys.*, 24:87–106, 1972.